The Nature and Evolution of High Redshift Dusty Star Forming Galaxies

Joshua Greenslade

Astrophysics Group
Department of Physics
Imperial College London

Thesis submitted for the Degree of Doctor of Philosophy to Imperial College London
- 2018 -

Abstract

DSFGs dominate the cosmic star formation rate (SFR) at $z > 0.7$, are 2 - 3 orders of magnitude more populous at $z = 2$ than locally, and have SFRs of tens to thousands of $M_\odot$ yr^{-1}. Despite their prodigious SFR, they are heavily dust obscured, with estimates suggesting that optical/UV surveys alone miss half the star formation in the Universe. Furthermore, DSFGs are believed to be the evolutionary progenitors to the massive elliptical galaxies that today inhabit the cores of massive galaxy clusters. DSFGs however remain poorly constrained, with few constraints on their contribution to the cosmic SFR density above $z > 4$, disagreement over whether single-dish observations accurately reflect the underlying population, and uncertainty about DSFGs in clusters, particularly whether they trace massive overdensities at their epoch. This thesis presents a series of results that set out to address some of these questions. To begin with, and by cross-matching Planck and Herschel data, we identify 27 candidate protoclusters by searching for overdensities of DSFGs. Their colours indicate they likely lie at $z = 2 - 3$, their flux density is 3x brighter than predicted from models, and fitting modified blackbodies to their photometry suggests they have total SFRs of several thousand $M_\odot$ yr^{-1}. We additionally present the results of an interferometric program targeting 36 single-dish DSFGs at $z \sim 4$. We assess their multiplicity, finding that whilst $\sim 45\%$ are blends of multiple sources, there are a number of highly luminous, possibly lensed, singular sources. Finally, we present the serendipitous detection of a SPIRE dropout, a source detected at 850 μm but not at any shorter wavelength, likely at $z > 6$, and we discuss the application of its selection to wider surveys. In closing, we discuss the future of FIR/sub-mm astronomy, new directions of the work begun here, and the challenges that remain for the field.

Acknowledgements

Of all of the words in this thesis, these are the hardest to write. To adequately credit all those who have borne me through to this point is simply an impossible task. Nevertheless, several of those countless individuals deserve space within these few lines.

First and foremost, I would like to thank my supervisor, Dave Clements, whose infinite patience, guidance, and care have not only supported me through this journey, but whose raw passion and clear enjoyment of his subject are constantly uplifting. Quite simply, without Dave, none of this would have been possible. I also wish to pay thanks to my academic brother Tai-An, whose insight and determination serve as an inspiration every day, and whose comments and questions have helped me to refine and polish every aspect of this thesis. I cannot pass by without mentioning my other academic siblings, in particular those who shared so much of this journey with me. Ciarân, Charlotte, Claude, Rhys, Hik and Nat, with whom I have all shared so my laughs, jokes, pints, puzzles and emergency tea, thank you for everything and for making this journey endurable. Special mention should also go out to everyone involved in the planetarium shows (thanks Cat for dumping that on my desk at the end of first year!), in particular to Tom, Dan, Charlotte, Hik, George, Wahid, Emily, and everyone who've I've inevitably forgotten to mention and who've been involved. Without you all, it would never had gotten to the point it is now, so thank you. It goes too, without saying, my thanks to those involved and who enjoy the cryptic puzzle group that has been springing up in the interaction area over the last few years. It is my great hope that someone else takes over the posting of new puzzles and clues, and my thanks to all who indulged in these interesting titbits.

To my friends, too numerous to mention but too extraordinary not to, yours has been the guiding light; each and every one of you a shimmering, blazing star in your own right, against the backdrop of what has been a long, dark nights sky for me. Yours, all of yours, are the lights which have guided me, comforted me, and given me hope. Special mention to those that have suffered me most: Henry Wearing, whose honesty and kinship gave me joy at the lowest of points, James Hickson, who together in mutual suffering we shared laughter and drunken despondence at our lot, Heather Thomas, whose shining love, altruistic care, and unwavering patience with my ups and downs have carried me more than any other through the last few years, and finally Chris Love, for whom no earthen language, script or motion possess the requisite intricacy to describe my unceasing gratitude for your friendship.

Finally, I would like to thank my brother Chris, my sister Faye, my mother Debra, my father Ian, my aunt NJ, my cousin Kai, my grandma Joan (Guv), and my grandma Valerie. They have all shown an inhuman level of patience with me as I've been writing this, picking up the slack whilst I effectively dropped off the radar for six months. Their continued words and actions of kindness and compassion serve as a constant reminder that whilst the Universe may hold infinite possibility, there is no place I would rather be than within their familial embrace.

Dedication

For Ian Stuart Greenslade.

A teacher of unparalleled passion,

A inquirer of unequalled eagerness,

And a father of indisputable devotion,

Whose hope, curiosity, and love,

Thunder into the cosmos.

The work contained herein is the result of the authors own work. Any work that is not the authors own is correctly referenced and attributed to its original source.

Contents

Abstract **1**

Acknowledgements **2**

Copyright Declaration **6**

Declaration of Originality **7**

1 Introduction **22**

1.1 The Infrared Sky 22

1.1.1 Cosmology 22

1.1.2 The Cosmic Infrared Background 24

1.1.3 Local Infrared Bright Galaxies 27

1.2 Infrared Astronomy 32

1.2.1 Atmospheric Opacity 32

1.2.2 Single Dish Observations 33

1.2.3 An Extremely Negative K-correction 36

1.2.4 Instrumentation 38

1.3 Dusty Star Forming Galaxies 40
1.3.1 Redshift Distributions 41
1.3.2 The Luminosity Evolution of Dusty Star Forming Galaxies 44
1.3.3 Scaled up Local (U)LIRGs 47
1.3.4 Multiplicity and Mergers 48
1.3.5 Environment 50
1.3.6 Models of DSFGs 51
1.3.7 Our Current Understanding of High-z DSFGs 53
1.4 This Thesis 54

2 Protoclusters of DSFGs at z > 1 **57**

2.1 Introduction and Motivation 57
2.2 The Data 64
2.2.1 The Planck Catalogues of Compact Sources 65
2.2.2 The Herschel Extragalactic Legacy Surveys 69
2.3 Selection and Identification of Sources 73
2.3.1 Source Selection 74
2.3.2 Source Identification 76
2.3.3 Diffuse and Dominated Sources 80
2.3.4 Variations between the ERCSC, PCCS1 and PCCS2 83
2.4 Photometry 84
2.4.1 Are the Planck and Herschel Photometry Consistent? 85

2.4.2 Are the Detected Herschel Sources Enough to Match the Planck Flux Density? . . . 87

2.5 Colours . . . 90

2.5.1 Planck Colours . . . 90

2.5.2 Herschel Colours . . . 95

2.6 The Candidate Protoclusters . . . 98

2.6.1 Line of Sight Effects . . . 98

2.6.2 Properties of the Protocluster Candidates . . . 100

2.6.3 Simulations of DSFGs in Clusters . . . 113

2.7 Discussion . . . 115

2.7.1 The HeLMS Field . . . 116

2.7.2 The Nature of the Planck Sources . . . 116

2.7.3 The Nature of the Candidate Protoclusters . . . 121

2.7.4 Future Work . . . 122

2.8 Conclusions . . . 123

3 Multiplicities of 500 Micron Risers **126**

3.1 Introduction and Motivation . . . 126

3.2 Target Selection . . . 129

3.3 Methods . . . 132

3.3.1 Interferometry . . . 132

3.3.2 Data Reduction . . . 134

3.3.3 Source Extraction . . . 135

3.3.4 The Detected Sources . . . 148

3.4 Extraction of Physical Properties . . . 153

3.5 Discussion . . . 158

3.5.1 Number Counts . . . 158

3.5.2 Lensing . . . 159

3.5.3 Blended Sources . . . 160

3.5.4 Extreme Luminosities . . . 161

3.5.5 Multi-Wavelength Counterparts . . . 162

3.6 Conclusions . . . 163

4 SPIRE dropouts 166

4.1 Introduction and Motivation . . . 166

4.2 Serendipitous Discovery of NGP6_D1 . . . 170

4.3 Photometric Observations . . . 173

4.3.1 SMA . . . 173

4.3.2 NIKA . . . 177

4.3.3 VLA . . . 177

4.3.4 SDSS, UKIDSS and WISE . . . 178

4.4 Spectroscopic Observations . . . 180

4.4.1 RSR . . . 180

4.4.2 EMIR . . . 183

4.4.3 NOEMA . . . 183
4.5 Photometric Analysis . . . 184
4.5.1 Template Fitting . . . 185
4.5.2 Fitting Modified Blackbodies . . . 188
4.5.3 The NIKA Observations . . . 196
4.5.4 The Statistics of $T_{dust}/(1+z)$ . . . 197
4.6 Spectroscopic Analysis . . . 198
4.6.1 Literature CO Values . . . 200
4.6.2 CO(1-0) Estimates . . . 201
4.7 Radio FIR Correlation . . . 204
4.8 Discussion . . . 205
4.8.1 Comparison to the Literature . . . 205
4.8.2 What do the SPIRE Dropouts Represent? . . . 207
4.8.3 SPIRE Dropouts Number Counts . . . 211
4.9 Conclusions . . . 213

5 Conclusion 216

5.1 Summary of Thesis Achievements . . . 216
5.2 Future Work . . . 217
5.2.1 Future Protocluster Detection . . . 217
5.2.2 The Optical/NIR Environments Around 500 μm Risers . . . 218
5.2.3 SPIRE dropouts in the JINGLE fields . . . 220

5.3 Concluding Remarks 223

A Planck Compact Sources Detected in the Herschel Extragalactic Fields 254

List of Tables

2.1 Herschel extragalactic fields containing a Planck source 75

2.2 Planck compact source identification statistics 77

2.3 Source identification as a function of Planck catalogue 83

3.1 Target properties 130

3.2 Detections per map 147

3.3 Properties of the detected sources 149

3.4 Derived properties of the detected sources 157

4.1 Observed properties of NGP6_D1 175

A.1 Planck compact sources at 857 GHz 255

A.2 Planck compact sources at 545 GHz 264

List of Figures

1.1 Cosmic Backgrounds 25

1.2 Typical galaxy SEDs 31

1.3 Atmospheric Opacity 33

1.4 Confusion 35

1.5 K-Correction 37

1.6 Redshift Distributions 43

1.7 IR luminosity function 45

2.1 Mexican-hat wavelets 68

2.2 Herschel source density distribution 78

2.3 Herschel flux density variance within a Planck source 81

2.4 Fractional contribution to a Planck source 82

2.5 Planck to Herschel aperture flux density ratios 86

2.6 Planck to Herschel discrete flux density ratios 89

2.7 Planck colours 91

2.8 Simulated Planck colours of protoclusters 94

2.9 Simulated SPIRE colours 96

2.10 Compact source SPIRE colours 97

2.11 Protocluster flux density distributions 103

2.12 Redshift vs SFR 107

2.13 Radial distribution of Herschel sources 110

2.14 Simulated protocluster predictions to observations 114

3.1 SMA maps and beam 136

3.2 Fake SMA sources 144

3.3 Reliability of detections 148

3.4 SMA-SPIRE colours 150

3.5 Fitted models to the SPIRE and SMA flux densities 154

3.6 Extended SMA observations 159

3.7 Detections as a function of Herschel flux 161

3.8 XMM-M7 in Spitzer 163

4.1 SPIRE and SCUBA-2 Maps of NGP6_D1 172

4.2 Expected SPIRE flux as a function of redshift 174

4.3 SMA 345 GHz map of NGP6_D1 176

4.4 VLA 6 GHz image of NGP6_D1 178

4.5 SDSS image of the region around NGP6_D1 179

4.6 Spectra of NGP6_D1 from the RSR and EMIR 182

4.7 NOEMA spectra of NGP6_D1 184

4.8 Fitting the ALESS average SED template to NGP6_D1 185

4.9 Template fitting to NGP6_D1 187

4.10 Photo-z Vs Spec-z for a variety of high-z DSFGs 189

4.11 Posteriors from fitting modified blackbodies to NGP6_D1 191

4.12 SED fits to NGP6_D1 192

4.13 Derived properties of NGP6_D1 194

4.14 NGP6_D1 without NIKA data 195

4.15 $\mathrm{T}_{Dust}/(1+z)$ 197

4.16 The luminosity constraints on SPIRE dropouts 199

4.17 Expected CO line flux densities 200

4.18 The L_{FIR} to L_{CO} correlation for LIRGS 203

4.19 FIR-Radio correlation 206

4.20 Luminosity limits of SPIRE dropouts and 500 μm risers 210

4.21 SPIRE dropouts number counts 213

5.1 CORE simulations 219

5.2 Optical / NIR counterparts to 500 μm risers 221

5.3 Jingle Dropout 222

"It is sometimes of great use in natural philosophy, to doubt of things that are commonly taken for granted; especially as the means of resolving any doubt, when once it is entertained, are often within our reach." - William Herschel, Phil. Trans. R. Soc. Lond. 1800 90, 255-283, published 1 January 1800.

Chapter 1

Introduction

1.1 The Infrared Sky

1.1.1 Cosmology

Today, our Universe appears to be homogeneous, isotropic, expanding, and expanding at an accelerating rate (Ade et al., 2016). The current best cosmological model which can explain these observations is commonly known as Λ-CDM, where Λ refers to a "cosmological constant" responsible for the accelerated expansion of the Universe, and CDM refers to a form of cold (i.e. non-relativistic) matter known as dark matter. The vast majority of the energy density of our Universe today is thought to be in one of these two forms. Specifically, 69% of the energy density is in the form of dark energy, a form of energy density that can be described as a perfect fluid with negative pressure that results in the observed accelerated expansion of the Universe, 26% in dark matter, a collisionless form of matter that appears to interact only through gravity and is required to explain a number of observations, for instance galaxy rotation curves and the gravitational lensing of light, 5% in baryons and $<< 1\%$ in radiation (Ade et al., 2016). Additionally, the Universe today contains significant baryonic structure, ranging from complex molecules to stars to galaxies to clusters of galaxies, all the way to a complex "cosmic web" of matter and dark matter, which links together these massive galaxy clusters.

Within the Λ-CDM cosmological paradigm, the Universe originated 13.8 billion years ago as a hot, dense, uniform, compact field of relativistic particle species, all in local thermodynamic equilibrium with one another, which then rapidly expanded and cooled. How did we get from the initial hot, compact, uniform Universe to the structure filled Universe we see today? The initial energy density of the Universe contained small perturbations, both overdense and underdense, both of which grew over time with the expansion of the Universe. The Universe today is observed to be spatially flat on average, and therefore the overdense regions acted like universes with positive curvature (i.e. act like closed universes). As such, they continued to expand at a slower rate than the general expansion of the Universe until they reached a maximum size, at which point they broke away from the general expansion and began to collapse under their own gravity. The dark matter, which is unable to decrease its total energy through the emission of photons, eventually virialised and reached a state of equilibrium. The baryons, on the other hand, were able to continue to collapse, eventually reaching sufficient pressures to initiate nuclear fusion and give rise to the first stars, and eventually the first galaxies.

Models of galaxy formation and evolution attempt to simulate these processes and explain their relative importance, in order to reproduce the observed properties of galaxies in our Universe throughout cosmic time. Whilst the dark matter, acting only under gravity, is reasonably easy to simulate, the baryonic processes include interactions that take place on the subatomic and atomic scale through nuclear fusion and molecular growth, on the stellar scale through the emission of ionising radiation, on galactic scale through black hole activity and supernova, all the way to the intergalactic scale through galaxy mergers and clusters. Much of the complexity in both the Universe and in galaxy formation and evolution models emerges principally due to these baryonic processes, their interactions, and their response to one another. By requiring these models to match our observations of the Universe, we can constrain the relative strengths of these processes, and gain physical insight into how the Universe today came to be. One of the best constraints on the relative strengths of these processes comes from the cosmic background radiation we observe today.

1.1.2 The Cosmic Infrared Background

The diffuse background radiation we observe today is formed from the integrated intensity of all astrophysical and cosmological phenomena that have taken place over the history of the Universe[1]. The most energetic part of this background spectrum is the well studied cosmic microwave background (CMB), which dominates between $\sim 400\ \mu m$ and ~ 1 m, accounts for roughly 95% of the total background energy density (Dole et al., 2006; Cooray, 2016), and originates from photons decoupling from baryons around $z = 1100$. The second most energetic backgrounds come jointly from the cosmic optical background between 0.1 and 5 μm (COB, Cooray (2016)), and the cosmic infrared background between 10 and 1000 μm (CIB, Puget et al. (1996); Fixsen et al. (1998); Dole et al. (2006)). These have comparable energy densities of 24 ± 4 and $30 \pm 10\ nW\ m^{-2}\ sr^{-1}$ respectively (Cooray, 2016), and together account for $\sim$ 5% of the bolometric background energy density. Both the CIB and COB have their origins in phenomena relating to the history of galaxy formation and evolution, namely in stellar nucleosynthesis and active galactic nuclei (AGN) activity throughout cosmic time. While the COB intensity is primarily from direct starlight, the CIB intensity results mostly from starlight that has been reprocessed by dust into the mid and far-infrared, with AGN contributing a small $\sim 10\%$ fraction to both (Hauser and Dwek, 2001; Andrews et al., 2018). This dust is thought to be primarily from silicates and carbon based[2] molecules (Draine, 2003), with the cross-section for dust absorption strongly peaking in the UV at $\sim 100\ nm$, and with photons with wavelengths $> 300\ nm$ more likely to be scattered by dust than absorbed (See Figure 9 of Draine (2003)). The implications of roughly equal energy densities in the COB and CIB are stark; half the energy from stellar nucleosynthesis (i.e. starlight) over the history of the Universe has been been reprocessed by dust into the infrared (IR). The CMB, CIB, COB, and other cosmic backgrounds and their relative strengths are shown in Figure 1.1.

These results contrast heavily with observations of the local Universe, where the infrared energy density is only $\sim 1/3$ that from the optical/UV energy density (Soifer and Neugebauer, 1991). This implies that the IR energy density must have been significantly higher in the early Universe.

[1] A comprehensive and up to date review of the various cosmic backgrounds is given by Cooray (2016).
[2] Mostly carbon by mass.

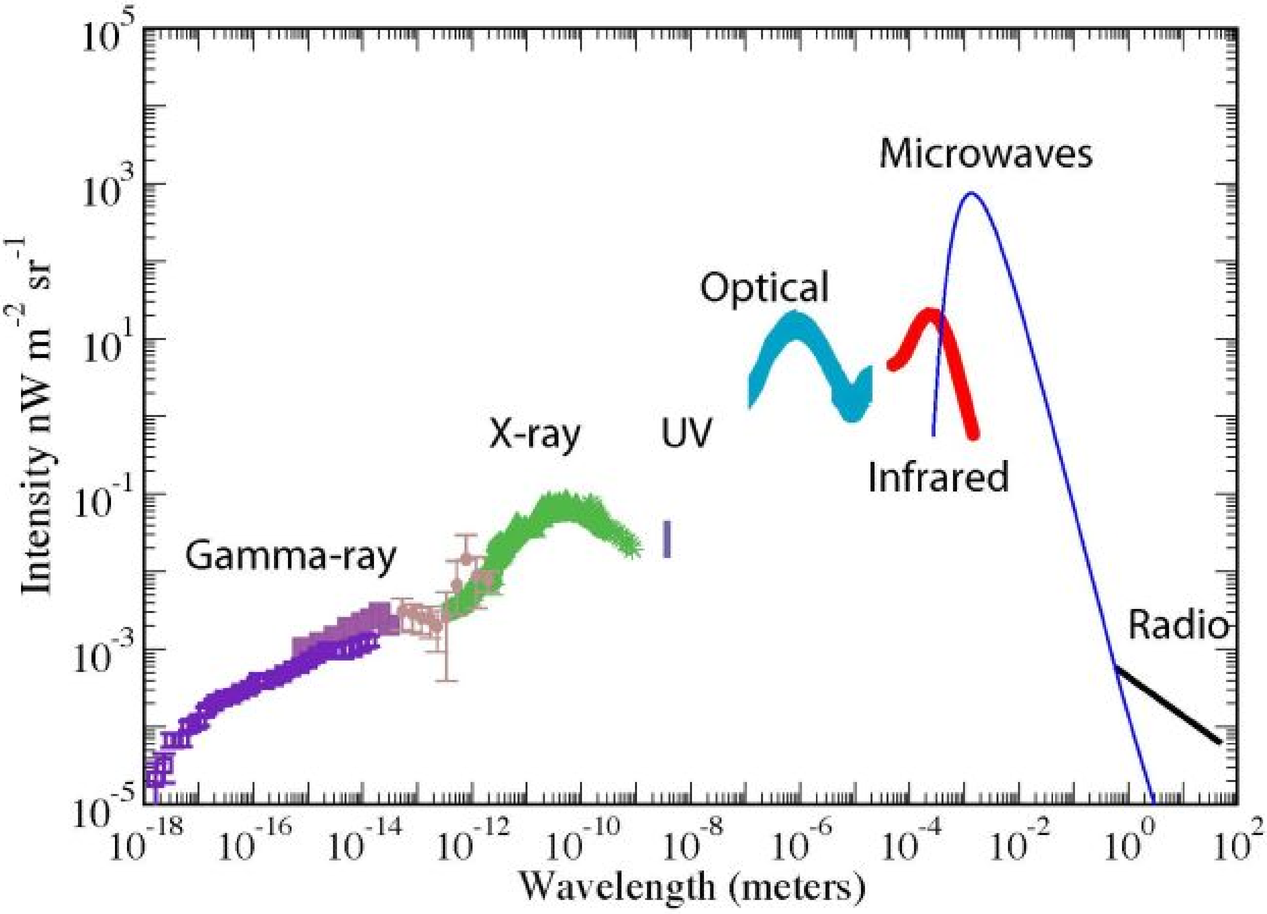

Figure 1.1: The intensity of the various cosmic backgrounds as a function of wavelength. Reproduced from Cooray (2016) under a creative commons licence (`https://creativecommons.org/licenses/by/4.0/`).

.

Furthermore, the long wavelength sub-mm and mm shape of the CIB has a particularly shallow slope, with $I_\nu \propto \nu^{1.4}$ (Gispert et al., 2000), where I_ν is the intensity per unit frequency and ν is the frequency. This is far shallower than, for instance, the frequency dependent thermal emission from the tail of a blackbody (the Rayleigh-Jeans law gives $I_\nu \propto \nu^2$), and variations on such blackbodies are often used to model the dust reprocessed emission from individual galaxies (Blain, 2002). As such, the sources which account for the peak of the CIB emission at around 100 μm are likely not the same as those which account for the sub-mm and mm emission, which probably lie at higher redshifts. For example, Elbaz et al. (2002) find that 15 μm selected galaxies, with a median redshift of $z = 0.7$, can account for 80% of the CIB at 15 μm and 66% of the CIB at 140 μm, but these same galaxies make little to no contribution to the sub-mm or mm CIB emission (Lagache et al., 2005).

Taken together, both the integrated intensity and long wavelength slope of the CIB directly imply that the IR output of the Universe must have not only evolved faster than the optical up to $z = 1$, but must have then remained constant out to at least $z = 3$ (Gispert et al., 2000; Lagache et al., 2005). This increased IR output can be directly related to recent star formation, as only the shortest lived, most massive stars emit a significant number of UV photons, where the cross-section for absorption by dust peaks. This dust then reprocesses the UV photons into the infrared through the collective thermal emission of individual dust grains, and therefore the dust emission can directly trace the recent star formation in a galaxy. The increase in the cosmic IR emission suggests that dusty star forming galaxies play a key role in the star formation history of the Universe, especially at $z > 1$. Indeed, comparison of the observed CIB+COB intensity to models has revealed that the cosmic star formation rate density at $z \sim 1.5$ must be a factor of 2 higher than predicted by purely optical and UV observations (Madau et al., 1998; Hauser et al., 1998; Lonsdale et al., 2006). In other words, *roughly half the star formation in the Universe is missed by purely optical and/or UV observations.*

What are the properties of the galaxies responsible for this obscured star formation? They must be heavily dust enshrouded, more numerous at high redshift than their population today, and are likely extremely far-infrared luminous[3]. Thus, to explain the star formation history

[3]Alternatively, rather than a few extremely far-infrared luminous galaxies, a large number of IR-faint galaxies

of our Universe, there is a need for a high-z population of galaxies, bright in the far-infrared and sub-mm but faint in the optical and UV, that are heavily dust obscured and prodigiously star-forming.

1.1.3 Local Infrared Bright Galaxies

Populations of galaxies which emit the bulk of their luminosity in the infrared were known to exist locally at the time of the discovery of the CIB. However, their exceptional rarity meant that, whilst they locally dominate the population of galaxies with bolometric luminosity $L_{bol} > 10^{11} L_{\odot}$ (Sanders and Mirabel, 1996), these galaxies only contribute about $\sim 6\%$ of the infrared emission in the local Universe (Soifer and Neugebauer, 1991). Much of what we infer about high redshift infrared bright galaxies is derived from observations and comparisons to these local galaxies, so here we briefly review their observed properties. Comprehensive reviews of the local luminous dusty galaxies are available in Sanders and Mirabel (1996) and Lonsdale et al. (2006).

Definitions

Here we define a few terms used throughout this thesis. We refer to galaxies that emit the bulk of their luminosity in the IR through dust reprocessed starlight as dusty star forming galaxies (DSFGs), whilst we refer specifically to the subset of DSFGs selected initially at $\sim 850\ \mu m$ as sub-millimeter galaxies (SMGs). Whilst all SMGs are DSFGs, the same cannot be said for the reverse, and here we generally refer to DSFGs when discussing the broader population. Furthermore, when referencing DSFGs, we are typically referring to the high-z $z >> 1$ population rather than the locally detected DSFGs unless otherwise stated. We define the infrared luminosity L_{IR} as the integrated rest frame luminosity of a galaxy between 8 and 1000 μm, whilst we define the far-infrared luminosity as the integrated rest frame luminosity between 42.5 and 122.5 μm. Using these definitions, we define a luminous infrared galaxy

could explain these results. However, source counts of extremely far-infrared luminous galaxies can already account for the majority of the CIB, and thus are likely the galaxies responsible (Lonsdale et al., 2006).

(LIRG) as any galaxy with $10^{11}L_{\odot} \leq L_{IR} < 10^{12}L_{\odot}$, an ultra-luminous infrared galaxy (ULIRG) as one with $10^{12}L_{\odot} \leq L_{IR} < 10^{13}L_{\odot}$, and a hyper-luminous infrared galaxy (HLIRG) as one with $L_{IR} \geq 10^{13}L_{\odot}$. We additionally define the far-infrared (FIR) wavelength range to cover $8-500$ μm, whilst the sub-mm generally refers to wavelengths between 500 μm and 1 mm. Whilst other definitions exist, these wavelength range definitions are primarily such that investigations by the Herschel satellite, used extensively in this work, can be entirely referred to as taking place in the FIR, whilst longer wavelength observations at 850 μm which formed the bulk of the early work on DSFGs can be referred to as taking place in the sub-mm.

The FIR luminosity - SFR conversion.

We also must briefly discuss the relationship between the star formation rate (SFR) and FIR luminosity of a galaxy; whilst DSFGs appear to be forming a large number of stars, there are numerous subtleties when converting from a FIR luminosity to a SFR. Regardless of method, when attempting to measure the SFR in a galaxy one looks for probes of the newly or recently formed young stellar population, whilst avoiding contamination from other phenomena (Calzetti and Daniela, 2013). Kennicutt (1998) define SFR indicators and calibrations for the UV, recombination lines, forbidden lines and the FIR continuum, and we naturally here focus on the latter.

The absorption cross-section of dust is strongly peaked in the UV (Draine, 2003). In the limiting case where the young stellar population dominates the intrinsic UV-visible emission (i.e before dust reprocessing), and the dust opacity is high everywhere, the FIR luminosity will perfectly trace the young stellar population. To convert to a SFR, one needs to further assume that the SFR remains reasonably constant over a specific timescale, and assume an initial mass function (IMF) for the stars (i.e. the distribution of stellar masses at birth). Kennicutt (1998) assumed the burst remained constant over 10 - 100 Myr timescales, and further assumed a Salpeter IMF (Salpeter, 1955), and found that

$$SFR(M_{\odot}\ yr^{-1}) \approx 1.72 \times 10^{-10}\ L_{8-1000\mu m}[L_{\odot}] \quad (Salpeter\ IMF), \tag{1.1}$$

where $L_{8-1000\mu m}$ refers to the infrared luminosity integrated over 8 - 1000 μm. Whilst Salpeter (1955) assumed a power law form for the stellar IMF, a more physical log-normal form was derived by Chabrier (2003), and this is more commonly used in the literature to convert from a FIR luminosity to a SFR. To convert from a power-law Salpeter IMF to the more physical log-normal Chabrier IMF, we simply multiply the Salpeter conversion by the constant value 0.63 (Madau and Dickinson, 2014), giving

$$SFR(M_\odot\ yr^{-1}) \approx 1.08 \times 10^{-10}\ L_{8-1000\mu m}[L_\odot] \quad (Chabrier\ IMF). \tag{1.2}$$

Indeed, whilst the Kennicutt (1998) value is still widely used within the literature, the most recent calibration on the infrared luminosity to SFR conversation factor (Kennicutt et al., 2009; Kennicutt and Evans, 2012) gives

$$SFR(M_\odot\ yr^{-1}) \approx 1.48 \times 10^{-10}\ L_{3-1100\mu m}[L_\odot] \quad (Kroupa\ IMF), \tag{1.3}$$

with the primary differences coming from the adoption of a Kroupa IMF which, like the Chabrier IMF, turns over at a mass of $\sim 0.1 - 1\ M_\odot$. In all cases, the infrared luminosity to SFR conversation factor is on the order $1 - 2 \times 10^{-10}\ M_\odot\ yr^{-1}\ L_\odot^{-1}$.

Using these definitions, a typical LIRG will have a dust reprocessed SFR on the order of tens of $M_\odot\ yr^{-1}$, a ULIRG on the order of hundreds, and a HLIRG on the order of thousands. This is of course an idealised case, and only really valid for starbursts with ages $< 100\ Myrs$ (Kennicutt, 1998); a lower dust opacity will mean the FIR luminosity underestimates the SFR, whilst heating from older stellar populations will mean the FIR luminosity overestimates the SFR. Additionally, dust heating from an AGN can also raise the FIR luminosity of a system without raising the SFR, so careful consideration of the AGN contribution to the FIR luminosity needs to be made. However, perhaps most uncertain is the assumed IMF within DSFGs. Early suggestions from galaxy formation models (Baugh et al., 2005) and more recent directly detected results (Zhang et al., 2018) suggest that within DSFGs, the IMF is significantly "top-heavy" (i.e. the ratio of massive to less massive stars in the IMF is much larger than in the Salpeter or Chabrier IMFs). Thus, the Salpeter or Chabrier IMFs could be overestimating the SFRs in these DSFG by a factor of 6 - 7 (Zhang et al., 2018). Throughout this thesis, however, we generally assume a Chabrier IMF when converting to a SFR, primarily to aid in the direct comparison to previously published results. The reader should be aware however of these recent results by Zhang et al. (2018), and that the quoted SFRs may be biased high.

Local DSFGs

Much of the early work on local DSFGs comes from the InfraRed Astronomy Satellite (IRAS, Neugebauer et al. (1984)), which surveyed $\sim$ 96% of the sky at completeness limits of $\sim$0.5 Jy at 12 μm, 25 μm, and 60 μm, and $\sim$1.5 Jy at 100 μm. The vast majority of previously catalogued optical/UV sources were only marginally bright infrared emitters, indicating that the IRAS selcted population was disjoint from the well studied optical/UV selected galaxies.

The bright galaxy survey (BGS, Soifer et al. (1989); Sanders et al. (1995), updated today to the revised bright galaxy survey, RBGS Sanders et al. (2003)), in particular studied the brightest infrared galaxies, specifically all extragalactic objects with total 60 μm flux density greater than 5.24 Jy, at galactic latitudes $|b| > 5^o$. The IRAS selected galaxies in the BGS had significantly higher bolometric luminosities than optically selected sources. All at $z < 0.1$, they have a median $L_{IR} = 10^{10.65} L_\odot$, with $\sim$ 33-50% of galaxies being classed as LIRGs, and around $\sim$ 2% as ULIRGs. The majority of these galaxies, both those with $L_{IR} < 10^{11} L_\odot$ (Sanders and Mirabel, 1996) and those with $L_{IR} > 10^{12} L_\odot$ (Genzel et al., 1998) appear to be powered by recent massive star formation as opposed to AGN activity, though there did additionally appear to be an increase in AGN activity with IR luminosity. This star formation appears to take place in a compact circumnuclear region, extended on scales of hundreds of pc (Miles et al., 1996). They are additionally extremely rich in molecular gas[4], with $M(H_2)$ mass estimates around 10^9 - 10^{10} $M_\odot$ (Sanders et al., 1991; Clements et al., 1996; Lonsdale et al., 2006). Furthermore, the fraction of BGS sources which show optical signatures of mergers increases with infrared luminosity, with $\sim$ 10% showing merger signs at $L_{IR} = 10^{10.5-11} L_\odot$ to $\sim$95% at $L_{IR} > 10^{12}$ (Sanders and Mirabel, 1996; Lonsdale et al., 2006). The typical spectral energy distribution

[4]Cool molecular hydrogen which can go on to collapse and form new stars

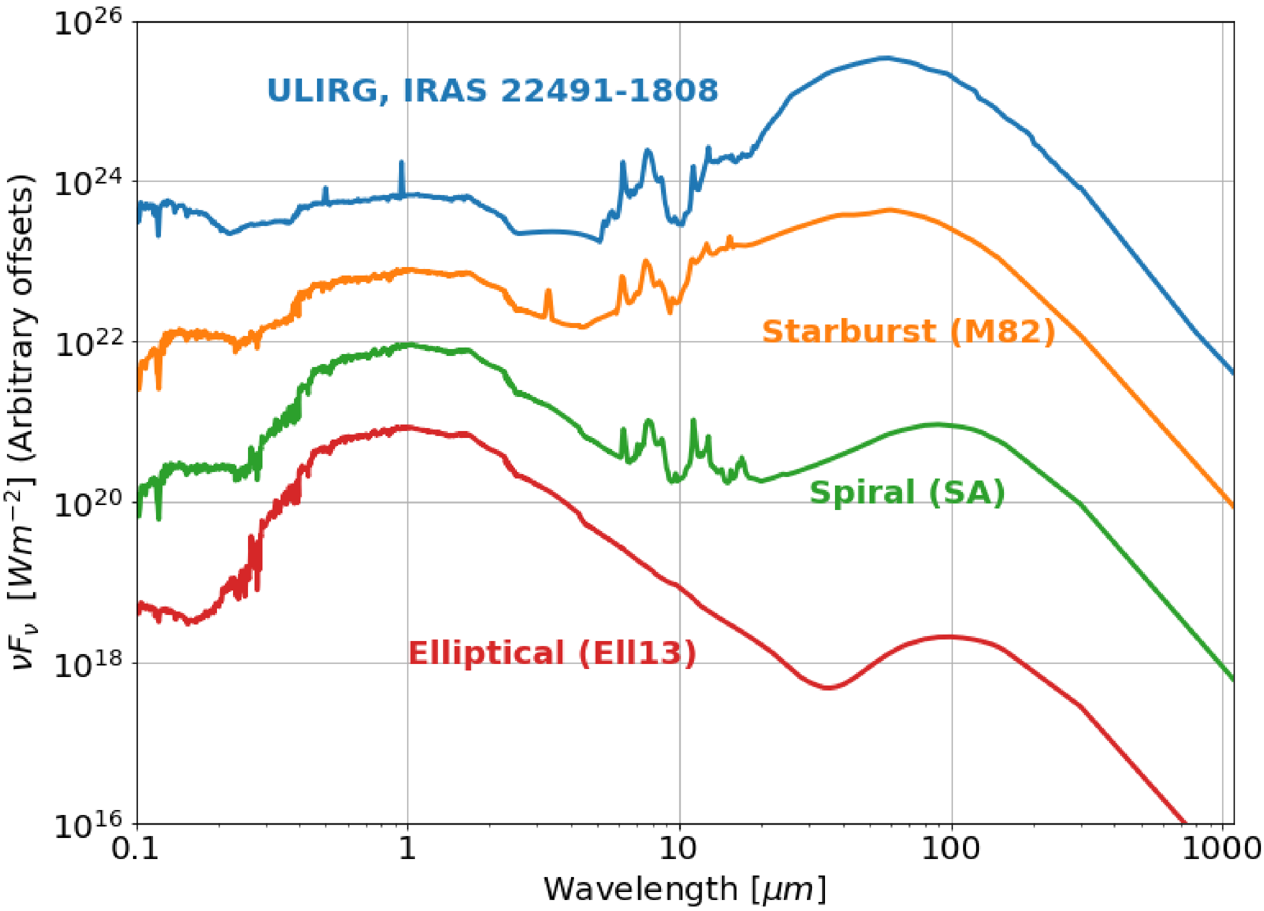

Figure 1.2: The SEDs of an elliptical, disk, starburst, and ultra-luminous infrared galaxy, all taken from the Polletta et al. (2007) set of templates. The name of each template is given next to each SED. The normalisation of each SED is offset, such that the relative power of different sections of the SED can be more easily understood. Whilst this work is original, it closely replicates Figure A.10 from Galliano (2004).

(SED) of a ULIRG is compared to other local populations in Figure 1.2.

The local (U)LIRGs thus appeared to be a series of FIR bright major mergers, powered by a burst of star-formation likely resulting from significant amounts of gas being driven towards the core of the galaxies during the merger process. Theoretical models suggest that this puts them on an evolutionary pathway towards the eventual formation of a elliptical galaxy (Hopkins et al., 2008; Casey et al., 2014). In this scenario, the major merger of two gas rich galaxies drives gas towards the centre of the merged galaxies, resulting in a burst of star formation. This burst results in the formation of significant amounts of dust, which absorb the short wavelength blue/UV light from young, massive, short lived stars and re-radiates it in the FIR, resulting in a short period where the galaxy would be expected to be FIR bright and detectable as a ULIRG. The coalescence of the two central super-massive black holes results in an AGN, fuelled by accretion from the in-falling material. Either the prolific star formation uses up all the available gas, or feedback from the AGN results in a cessation of the star formation ~ 100 $Myrs$ after it begins. The disturbed system, which is now both beginning to virialize and populated mostly by older stars, is now well on its way to forming a massive elliptical galaxy (Hopkins et al., 2008; Casey et al., 2014).

1.2 Infrared Astronomy

Before proceeding further into the evolution of DSFGs out to higher redshift, it is worth examining the observational benefits and challenges of FIR / sub-mm astronomy, as well as highlighting a few key missions and instruments that have been vital to the field and which feature prominently in this thesis.

1.2.1 Atmospheric Opacity

Whilst the atmosphere is almost entirely transparent to optical and near-UV light, in the infrared it is almost entirely opaque. The FIR and sub-mm especially suffer from an opaque sky due to molecular absorption, mostly rotational transitions of water. Though extremely dry sites are available (for example Mauna Kea, where JCMT and the SMA are based, the Atacama desert, where ALMA is based, and the South Pole, where the South Pole Telescope is based), these often only provide small atmospheric windows to space. In Figure 1.3, we plot the atmospheric transmission in the sub-mm and mm bands for a yearly averaged night on Mauna Kea, which corresponds to a precipitable water vapour of $\sim 2\ mm$, and a corresponding opacity at 225 GHz of $\tau_{225} \sim 0.1$[5].

As is immediately apparent, only the mm and 850 μm atmospheric window provide ready access to the sky all year round; exceptionally good weather (PWV < 0.8) is required for observations

[5]Obtained using the conversion by Dempsey et al. (2013) of $\tau_{225} = 0.04 \times PWV + 0.17$, with models calculated from Pardo et al. (2001).

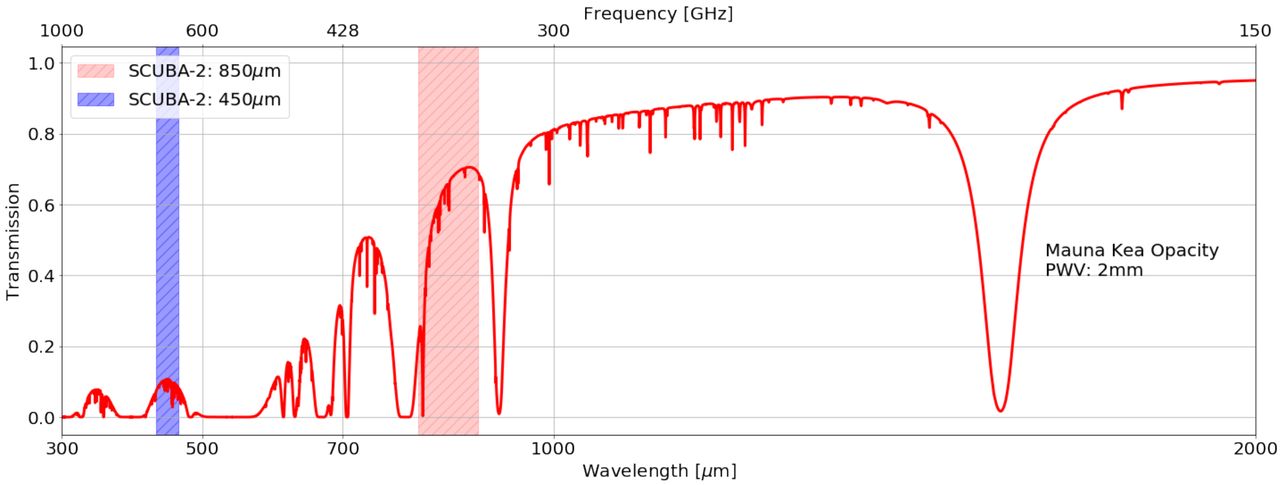

Figure 1.3: The atmospheric opacity in the FIR, sub-mm and mm bands on Mauna Kea. Model opacities taken from `http://www.submm.caltech.edu/cso/weather/atplot.shtml` and calculated from Pardo et al. (2001). The red line shows the transmission as a function of wavelength/frequency for a night with 2 mm PWV. The hashed regions show the observing bands for SCUBA-2 at 450 μm and at 850 μm.

in the SCUBA-2 450 μm band. The FIR is generally entirely opaque. Given that the peak of dust emission in a typical DSFG occurs around 100 μm, for redshifts from z = 0 - 8, this peak, which will be both the brightest part of the spectrum and strongly constrain the source redshift, will be unobservable from the ground. This constraint dominated the early years of DSFG study, before the launch of Spitzer and Herschel

1.2.2 Single Dish Observations

Whilst the first decades of FIR and sub-mm astronomy were dominated by problems associated with atmospheric opacity, the most recent has arguably been dominated by problems associated with single dish observations. For a circular aperture, to resolve two close sources requires a separation of at least $\theta = 1.22\lambda/D$, where θ is the angular separation in radians, λ is the observed wavelength and D is the diameter of the telescope. For a 2.5 m diameter optical dish working at 500 nm, its theoretical diffraction limited resolution is able to resolve 2 objects separated by $\sim$ 0.05 arcseconds. The same dish, operating at 500 μm rather than 500 nm, would have a diffraction limited resolution of $\sim$ 50 arcseconds.

There are two primary consequences of this resolution degrading, and both are apparent in

Figure 1.4, where we show the Hubble ultra deep field (HUDF, Beckwith et al. (2006)) in the optical, but with the effective resolution of five common FIR and sub-mm instruments. Firstly, the background variation in the FIR and sub-mm maps is dominated not by shot noise, but by fluctuations in the numbers of undetected sources clustered together on the scale of the beamsize. Determining the true flux density of a source requires this background component to be removed. As this variation is effectively stochastic, it is impossible to accurately determine the true background, and thus an additional component of noise from this confusion of faint background sources must be added to the instrumental noise. This "confusion noise" originates in real physical sources and therefore cannot be reduced with longer integrations. As such, for a given wavelength instrument installed on a given diameter telescope, this confusion noise sets a hard limit, below which it is impossible to detect individual sources, no matter how long the integration. Whilst no fixed definition is available, a survey is said to reach its flux density confusion limit when there are approximately 0.05 sources per instrumental beam (or equivalently, 20 beams per source). For example, SCUBA-2 at 850 μm and with a beamsize of 13.0 arcsec has a typical confusion limit of $\sim 1\ mJy$ (Geach et al., 2017), whilst the Herschel-SPIRE instrument at 250, 350 and 500 μm with beamsizes of 18 - 35 arcsec had typical confusion limits of 6 - 8 mJy[6].

Secondly, identifying the correct multiwavelength counterparts to FIR/sub-mm sources is often a difficult task, as many optical/NIR sources are contained within a typical single FIR/sub-mm beam. In Figure 1.4 we kept the wavelength fixed whilst degrading the resolution to show the effects of confusion, but sources bright in the FIR and sub-mm are not necessarily bright in the optical, and the two populations can be entirely disjoint from one another. For example, no optical counterpart of one of the first detected SMGs, HDF 850.1 (Hughes et al., 1998), is detected by Hubble, despite it lying in the centre of Hubble deep field. When crossmatching between the FIR and optical/NIR, not only is the resolution poor enough that tens of optically / NIR identified galaxies may be present within a single beam, but additionally it may be that many, one, or even none of those galaxies are actually responsible for the emission. Such a situation is made worse by the fact that whilst most optical sources can be assumed to be at

[6] The Spectral and Photometric Imaging Receiver (SPIRE) Handbook, version 2.5, March 24, 2014

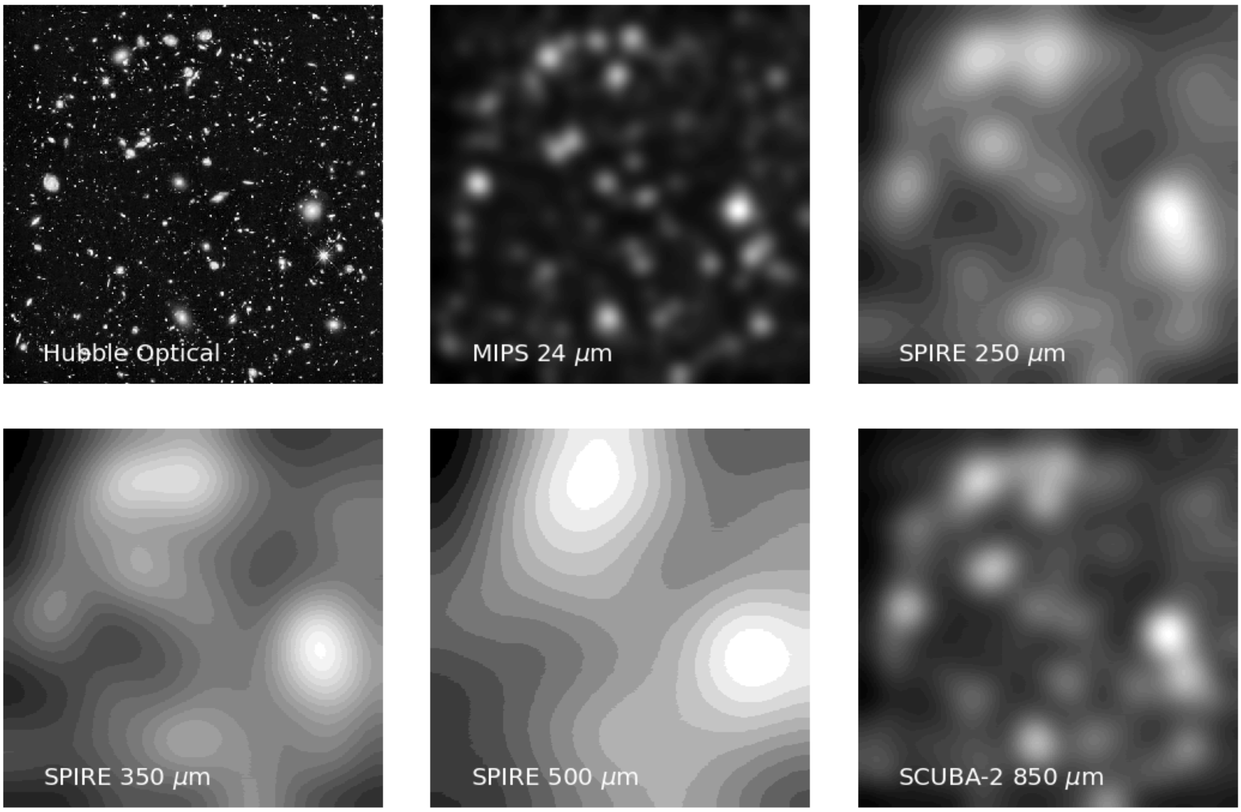

Figure 1.4: The effects of confusion on the 2.4 × 2.4 arcminute Hubble ultra deep field (HUDF Beckwith et al. (2006)). The 6 images show the HUDF as it would be seen in the optical, but with progressively poorer resolution, equivalent to the resolution of several common FIR and sub-mm instruments. From top left to bottom right, the resolution of the original Hubble optical image (with diffraction limited resolution of 0.05 arcsec), the resolution of the MIPS 24 μm instrument (6 arcsec), SPIRE 250 μm (17.6 arcsec), SPIRE 350 μm (23.9 arcsec), SPIRE 500 (35.2 arcsec) μm and SCUBA-2 850 μm (13.0 arcsec).

$z < 2$ due to decreased flux density with luminosity distance, the same cannot be said for the FIR / sub-mm detected sources (see Section 1.2.3). Given current ground based interferometers can only access the sub-mm atmospheric windows, understanding how the observed single dish FIR flux density is distributed between multiple counterparts is a challenge. Whilst the average multiplicity (how many sources are responsible for the single dish flux density of a given source) of single dish FIR / sub-mm sources is slowly becoming understood (Karim et al., 2013; Simpson et al., 2015; Oteo et al., 2017; Hill et al., 2018), it remains to this day a contentious topic in the DSFG community (Cowley et al., 2015; Rowan-Robinson et al., 2016; Béthermin et al., 2017; Oteo et al., 2017).

1.2.3 An Extremely Negative K-correction

Even without evidence from the CIB, sources detected in the sub-mm and mm were already thought to likely exist at high redshifts. This is because the observed flux density of DSFGs, in the sub-mm and mm bands, remains constant with increasing redshift, owing to an effect known as negative K-correction.

Two observations through the same filter on objects at different redshifts will generally sample different rest-frame portions of the spectral energy distribution. In order to compare the rest frame emission of the two objects in the same filter, a correction to the flux density, known as a K-correction, is applied (Hogg et al., 2002). This only depends on the intrinsic, and therefore often assumed, shape of the SED. For historical reasons this correction is generally referred to as “positive” if the observed spectral luminosity on a given SED decreases with redshift, and “negative” if it increases.

The FIR and sub-mm SEDs of DSFGs originate from the thermal emission of dust particles, and has been shown to be reasonably well represented by a single modified blackbody function (Blain, 2002; Bianchi, 2013; Casey et al., 2014). Assuming the emission is optically thin, this has the form $S_\nu \propto \nu^\beta B_\nu / D_L^2$, where ν is the frequency in Hz, S_ν gives the observed flux density, β is the dust spectral index and is usually found to be between 1 and 3 (Bianchi, 2013), D_L is the luminosity distance, and B_ν is the Planck function, given by

$$B_\nu(\nu, T) = \frac{2h\nu^3}{c^2} \frac{1}{exp(\frac{h\nu}{k_B T}) - 1}, \tag{1.4}$$

where h is the Planck constant, c is the speed of light, k_B is the Boltzmann constant, and T is the dust averaged temperature across the galaxy, typically found to be between 20 and 80 K for the FIR spectra of DSFGs and peaking at around 100 μm (Blain, 2002; Casey et al., 2014). In the long wavelength Rayleigh-Jeans approximation, applicable to the sub-mm, mm, and to a degree the FIR, this simplifies to $B_\nu \approx \frac{2\nu^2 k_B T}{c^2} \propto \nu^2$, and thus the flux density as a function of frequency is proportional to $S_\nu \propto \nu^\beta \nu^2 / D_L^2 = \nu^{2+\beta} / D_L^2$. Expressing this as a function of redshift in the observed frame, with $\nu_{obs} = \nu_{rest}/(1+z)$, we find $S_{\nu_{obs}} \propto \nu_{obs}^{2+\beta} / D_L^2 = (\nu_{rest}(1+z))^{2+\beta} / D_L^2$, and

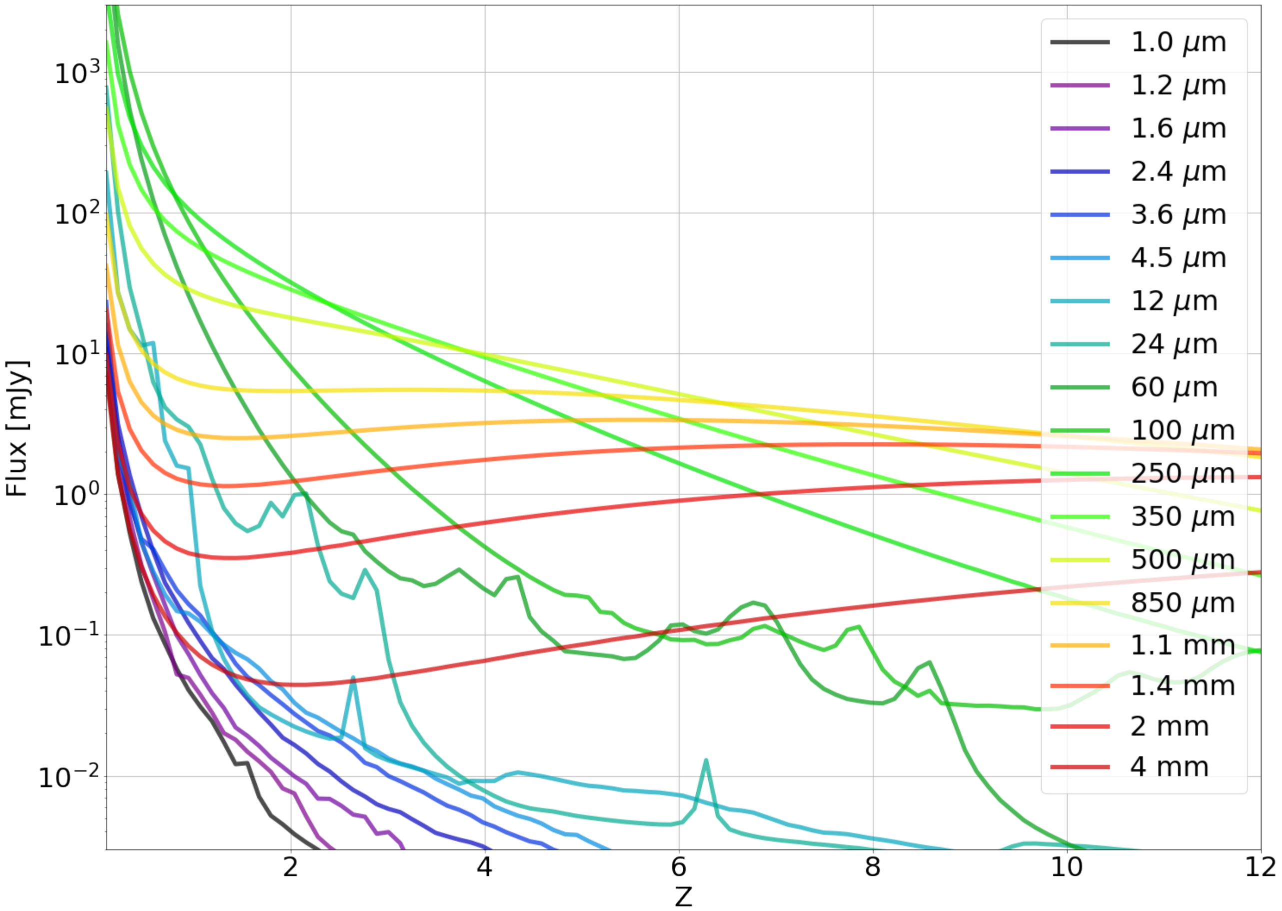

Figure 1.5: The observed flux density of the local ULIRG Arp 220 as a function of redshift, in a variety of near, mid and far infrared bands, as well as in the sub-mm and the mm. The total IR luminosity is normalised to $10^{12.5}$ $L_\odot$.

therefore $S_\nu \propto (1+z)^{2+\beta}/D_L^2$. Whilst it is not possible to analytically recast D_L in the form $(1+z)^N$, it can be shown numerically that $D_L \approx (1+z)^2$ between $z = 0.5$ - 3 (and $D_L \approx (1+z)^{1.5}$ between $z = 3$ - 8 (Casey et al., 2014)). In this case, the relationship between the flux density of a source and redshift becomes $S_\nu \propto (1+z)^{2+\beta}/(1+z)^4 = (1+z)^{\beta-2}$. For β values of 1 - 3, typical for what are found in SMGs (Magnelli et al., 2012; Greve et al., 2012; Roseboom et al., 2011; Bianchi, 2013), the observed sub-mm and mm flux densities of SMGs can therefore remain roughly constant out to $z \sim 8$ due to their extremely negative K-correction.

This is shown graphically in Figure 1.5, where we plot the observed flux density of the local ULIRG Arp 220 (Rangwala et al., 2011) as a function of redshift, and in a number of common FIR, sub-mm and mm bands. The total IR luminosity is normalised to $10^{12.5}$ $L_\odot$ and therefore corresponds to a SFR of ~ 300 $M_\odot$ yr^{-1}. Whilst the flux density in the near and mid-infrared bands rapidly fall off with redshift, the FIR, sub-mm and mm bands retain a relatively constant flux density over a wide range of redshifts, with some bands even becoming brighter at increasing redshifts.

1.2.4 Instrumentation

In this section, we detail several key missions and instruments that have been both vital to infrared astronomy and feature heavily in this thesis. For brevity, several instruments are not discussed in detail, but their contribution to sub-mm astronomy should not be discounted. These include AKARI (Murakami et al., 2007), WISE (Wright et al., 2010), LABOCA (Siringo et al., 2009), SPT (Carlstrom et al., 2011), AZTeC (Wilson et al., 2008), ALMA (Wootten and Thompson, 2009), and the original SCUBA (Holland et al., 1999).

Spitzer

The Spitzer space telescope was was launched in 2003 and primarily operated in the mid-infrared. It carried three scientific instruments, the Infrared Array Camera (IRAC), which observed simultaneously at 3.6, 4.5, 5.8 and 8.0 μm, the InfraRed Spectrograph (IRS), which was both a low and high resolution spectrometer operating between 10 and 40 μm, and the MultiBand Imaging Photometer (MIPS), which operated at 24, 70, and 160 μm. The primary mission lasted until 2009 when the cryogen supply for the telescope ran out. Since then, Spitzer has been operating in a limited capacity, with only its two shortest wavelength bands available.

MIPS in particular was used extensively in studies of mid-infrared bright DSFGs and was critical in constraining early results on DSFGs (Egami et al., 2004; Le-Floc'h et al., 2005).

Herschel

The Herschel Space Observatory (Pilbratt et al., 2010) was launched on 14th May 2009, and operated until the 29th of April 2013. Utilising a 3.5 m primary mirror, three instruments made up the science payload; The Photodetector Array Camera and Spectrometer (PACS, Poglitsch et al. (2010)), The Spectral and Photometric Imaging REceiver (SPIRE, Griffin et al. (2010)), and the Heterodyne Intstrument for the Far Infrared (HIFI, de Graauw et al. (2010)). PACS was both an imaging photometer and spectrometer, with the photometer offering simultaneous imagery in 70 or 100 μm and 160 μm, and the spectrometer operating between 50 - 210 μm. SPIRE contained both a 3 band photometer operating at 250, 350 and 500 μm, and a Fourier Transform Spectrometer (FTS) operating between 200 - 700 μm. HIFI meanwhile was a high resolution spectrometer operating between 157 - 212 μm and 240 - 625 μm. SPIRE and PACS both made use of a series of gridded bolometer arrays. A bolometer consists of a material which absorbs effectively at all wavelengths of light, attached by a thermal conductance to a heat sink with a stable temperature. A thermometer is additionally attached to the bolometer, to measure any changes in the temperature. A bias current is run through the thermometer, such that any change in the temperature, and therefore the resistance, will be detected as a voltage change. At FIR wavelengths, the noise in the instrument will be dominated by thermal emission from the telescope itself. As such, Herschel also had to be cryogenically cooled to operate at these wavelengths. It was switched off on the 17th of June 2013 at 12:25 GMT after its cryogen supply had run out.

Whilst PACS and HIFI feature little in this thesis, of extensive use are the data from the SPIRE instrument. The largest surveys with SPIRE included the Herschel Multi-tiered Extragalactic Survey (HerMES, Oliver et al. (2012)) and the Herschel-ATLAS (H-ATLAS, Eales et al. (2010)), which between them covered over 1,000 deg^2 of extragalactic sky to varying depths. SPIRE had beam full width half maxima of $\sim$ 17.6 arcsec, 23.9 arcsec, and 35.2 arcsec in the 250, 350 and 500 μm bands respectively[7].

SCUBA-2

The Submillimeter Common-User Bolometer Array 2 (SCUBA-2, (Holland et al., 2013)) is a sub-mm instrument currently installed on the 15 m diameter James Clerk Maxwell Telescope

[7] The Spectral and Photometric Imaging Receiver (SPIRE) Handbook, version 2.5, March 24, 2014

on Mauna Kea. It finished commissioning in 2011 and has operated there ever since, using a 10,000 pixel bolometer camera which operates simultaneously in the two atmospheric windows at 450 and 850 μm. It has a primary beam of 7.9 arcsec at 450 μm and 13.0 arcsec at 850 μm. It is able to map the sky 100 - 150 times faster than its predecessor, SCUBA (Holland et al., 2013).

Notable large extragalactic surveys with SCUBA-2 include the SCUBA-2 Cosmology Legacy Survey (S2CLS, Geach et al. (2017)), which mapped ~ 5 deg^2 to a 1σ 850 μm depth of ~ 1.2 mJy, the SCUBA-2 Ultra Deep Imaging EAO Survey (STUDIES, Wang et al. (2017)) which mapped 151 arcmin^2 at 450 μm down to 0.91 mJy, and S2COSMOS (Simpson et al. in prep), which mapped a contiguous 2 deg^2 of the COSMOS field to 1σ depths at 850 μm of 1.2 mJy.

The Sub-Millimeter Array

The Sub-Millimeter Array (SMA, Ho et al. (2004)) is a mm and sub-mm interferometer operating near the summit of Mauna Kea next to the JCMT, consisting of eight 6 meter diameter dishes, with baseline lengths that can range from 16 to 508 m. It operates from 180 to 420 GHz (700 μm - 1.6 mm)

Whilst today several sub-mm interferometers exist (ALMA, NOEMA), the SMA was the first instrument that imaged in the sub-mm with sub-arcsecond resolution (Beuther et al., 2004). It has been instrumental in the characterisation of a number of sources (Younger et al., 2008; Wang et al., 2011; Riechers et al., 2013), with Wang et al. (2011) in particular noting that $\sim$ 30% of single dish SMGs can resolve into multiple DSFGs at higher resolution that may or may not be physically associated (see Section 1.3.4).

1.3 Dusty Star Forming Galaxies

The local (U)LIRGs appear to be major merger induced starbursts, with the bulk of their energy being emitted in the FIR by thermal emission from cool (20 - 80 K) dust located in a compact, several hundred pc circumnuclear zone, and a gas depletion timescale (i.e. $\tau = M_{gas}/SFR$, where τ is the dynamical timescale and M_{gas} is the gas mas) of $\sim$ 100 Myrs. Whilst extreme, they alone cannot account for the total intensity or spectral shape of the CIB.

Around the same time as the detection of the CIB however, detections were also being made of numerous sub-mm bright ($> 1\ mJy$ at 850 μm) galaxies, many of which appeared to lack optical or NIR counterparts (Smail et al., 1997, 2002). Number counts and photometric redshift fitting suggested these sources not only likely lie at $z > 1$, but were 2 - 3 orders of magnitude more populous than the local LIRGs and ULIRGs. These redshift estimates suggested FIR luminosities of $> 10^{12}\ L_{\odot}$ and in some cases $> 10^{13}\ L_{\odot}$, implying SFRs of 100's to 1000's $M_{\odot}\ yr^{-1}$. As we go onto show, whilst apparently broadly similar to the local (U)LIRGs, they appear to be scaled-up, with higher luminosities, higher gas masses, more extended, and more numerous. Therefore, these $z \sim 2$ DSFGs likely dominated the cosmic SFR at their time, with $\sim 60\%$ of the CIB emission at 850 μm provided by such sources (Smail et al., 2002).

How similar are these high-z DSFGs to the local (U)LIRGs? Here we overview the properties of these high-z DSFGs, and set out some of the current problems and uncertainties the field faces with these sources. These include the redshift distribution, luminosity function evolution, physical characteristics, and environments of DSFGs. Finally, we discuss how DSFGs fit into models of galaxy formation and evolution, and highlight current problems and uncertainties in the field.

1.3.1 Redshift Distributions

Whilst numerous detections of DSFGs have been made since their discovery, their redshifts were initially poorly constrained owing to the problems set out in Section 1.2. The first well studied high-z DSFGs, and arguably still the best understood population, were the SMGs selected at $\sim$ 850 μm. The earliest spectroscopic redshift sample was gathered by Chapman et al. (2005), who obtained accurate positions for a sample of SCUBA sources by searching for 1.4 GHz radio counterparts to a parent sample of 150 SCUBA selected SMGs. They spectroscopically identify 73 sources, finding a median redshift of $z = 2.3$, and an interquartile range between $z = 1.7$ -

2.8, leading to a median FIR luminosity of $L_{FIR} = 5.6^{+2.1}_{-1.6} \times 10^{12}\ L_{\odot}$. Wardlow et al. (2011) meanwhile use a probabilistic argument to identify counterparts and fit photometric redshifts to a sample of 74 870 μm LABOCA sources, finding a median redshift of $z = 2.2 \pm 0.1$ and an interquartile range of $z = 1.8 - 2.7$, in excellent agreement with Chapman et al. (2005)[8]. More recently, Smith et al. (2017) use a novel method to estimate the redshift distribution of SCUBA-2 sources by searching for excess optical and NIR galaxies around the positions of the 850 μm sources, and associating those excess galaxies with the 850 μm source itself. They find a median redshift $z = 2.05 \pm 0.03$, with 68% of sources between $z = 1.06$ and $z = 3.06$. All three sets of authors suggest there exists a long tail in the redshift distribution, and all suggest that many of their undetected / unidentifiable sources likely will further populate this tail. This suggests that while the bulk of the SMG redshift distribution is now well understood, peaking at around $z = 2 - 3$, the $z > 4$ tail remains reasonably poorly understood. A plot of the redshift distribution of SMGs, reproduced from Simpson et al. (2014) is shown in Figure 1.6.

The redshift distribution of Herschel-SPIRE selected galaxies is far more uncertain, with only a handful of literature studies on generically selected 250, 350, or 500 μm sources. Amblard et al. (2010) use blackbody SED models with varying dust temperatures (10-60K), dust spectral indicies $\beta (\beta = 0 - 2)$ and redshift ($z = 0 - 5$) to fit PACS and SPIRE colours to 350 μm detected sources in the early science phase of H-ATLAS (Eales et al., 2010). They found a median redshift of $z = 2.2 \pm 0.6$, but without the high-z tail seen in the 850μm selected sources, with effectively no sources with $z > 3.5$. Casey et al. (2012) meanwhile use ancillary 24 μm and radio counterparts in order to locate and perform spectroscopy on generic SPIRE sources (i.e. detected in at least one SPIRE band). With a sample of 763 sources, they find their distribution peaks around $z = 0.85$, and even when specifically selecting 350 μm detected sources to compare to Amblard et al. (2010), find a statistically different sample. The cause of this disagreement is uncertain, but may be related to the assumptions in the blackbody models used by Amblard et al. (2010), or the requirement of a 24 μm or radio detection in Casey et al. (2012).

[8]These probabalistic counterparts were later confirmed with ALMA observations of the full sample (Simpson et al., 2014) and results were found to be consistent.

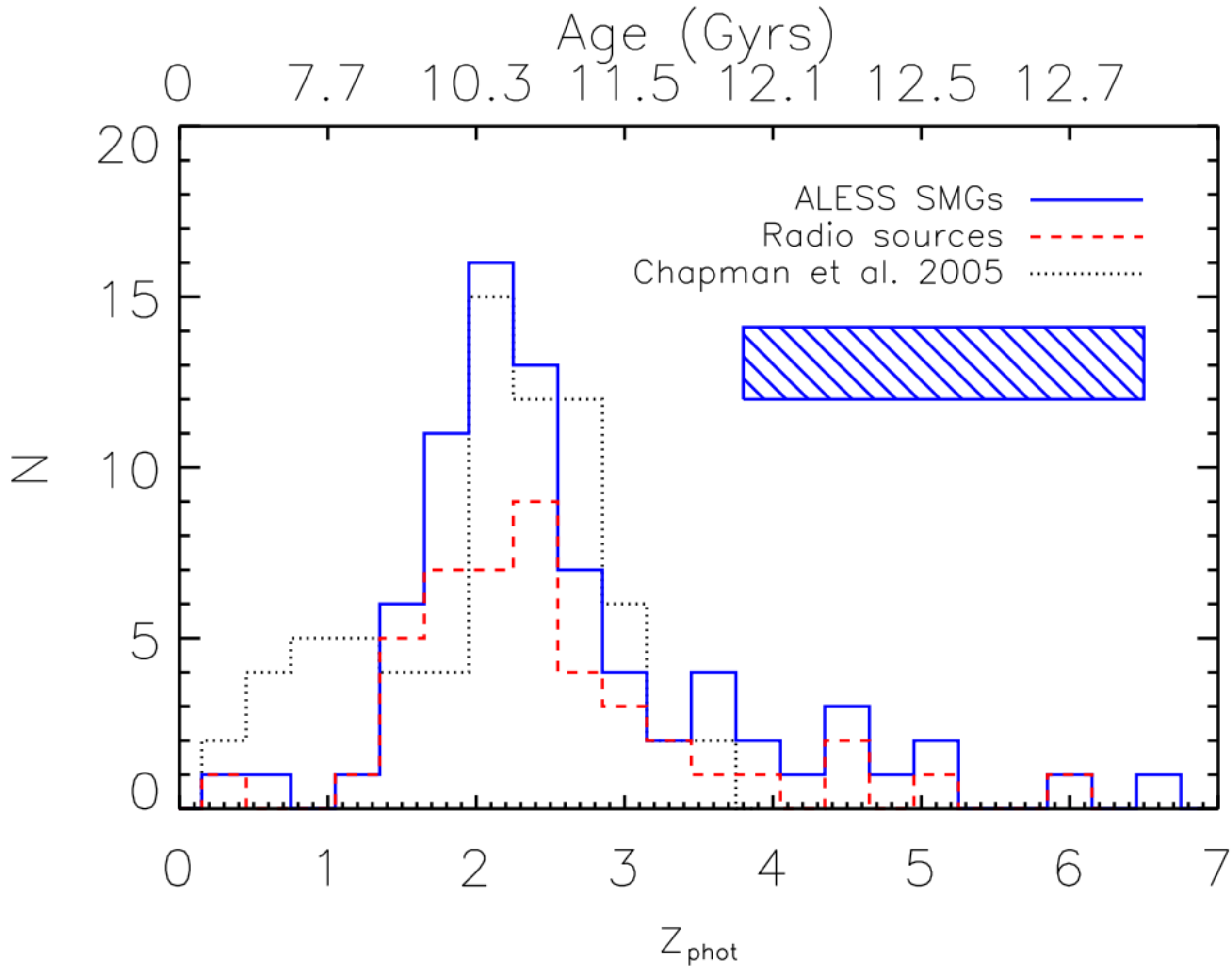

Figure 1.6: The photometric redshift distribution of SMGs reproduced with permission from Simpson et al. (2014). Also shown is the redshift distribution from Chapman et al. (2005). The red dashed line indicates the Simpson et al. (2014) sources with radio flux densities $S_{1.4\ GHz} > 40\mu Jy$, to compare with the radio selected Chapman et al. (2005) results. The shaded region indicates the area missing due to 19 sources without good photometric fits, which Simpson et al. (2014) find are likely at $z \gtrsim 3$.

Whilst generic samples of SPIRE selected galaxies have poorly constrained redshift distributions, specific subsamples are better studied. One of the better studied subsamples is the 500 μm riser population ($S_{500} > S_{350} > S_{250}$), which in theory should lie at $z \gtrsim 4$ as the peak of dust emission would have been redshifted into the 500 μm band. Dowell et al. (2014), using photometric redshifts from fitting modified blackbodies, find a peak in the redshift distribution for these red SPIRE sources at $z = 4.7$, with a 1σ range of 0.9, with spectroscopic confirmation of various 500 μm risers generally finding this distribution to be reasonable (Dowell et al., 2014; Asboth et al., 2016). Ivison et al. (2016) later found results slightly lower than Dowell et al. (2014) by using template fitting, with a median redshift for 500 μm risers of 3.66 and an interquartile range of 3.3 - 4.3, but still suggesting a high-redshift origin. Duivenvoorden et al. (2018) meanwhile use a sample of 188 500 μm risers with SCUBA-2 follow up, and find a median photometric redshift of $z = 3.6 \pm 0.4$, with 21 DSFGs likely at $z > 4$.

The redshift distributions confirmed both that these FIR and sub-mm selected galaxies primarily were at $z > 1$, with most studies of SMGs finding a peak around $z = 2 - 3$, and with typical $L_{IR} > 10^{12}$ $L_{\odot}$ (Chapman et al., 2005).

1.3.2 The Luminosity Evolution of Dusty Star Forming Galaxies

Whilst redshifts have been generally difficult to measure, and specific sub-groups show slightly different distributions, the bulk of the DSFG population appears to lie at $z \sim 2$, and given their flux densities are likely ULIRGs with FIR luminosities $> 10^{12}$ $L_{\odot}$. To examine their contribution to the stellar build up in the universe, here we examine the evolution in the luminosity function of DSFGs. The luminosity function encapsulates both the number density of DSFGs and their luminosities as a function of redshift. A luminosity function, $\phi(L)dL$, simply describes the number of galaxies with a given luminosity between L and $L + dL$ per unit volume, generally given as Mpc^{-3}. Typically this is done at a specific wavelength, i.e. 24 μm, but here we follow the literature and when we refer to the luminosity function we generally refer to the *integrated* infrared luminosity function between 8 and 1000 μm, so as to encompass the dust obscured star formation at a given redshift. The UV luminosity function meanwhile, will generally refer to

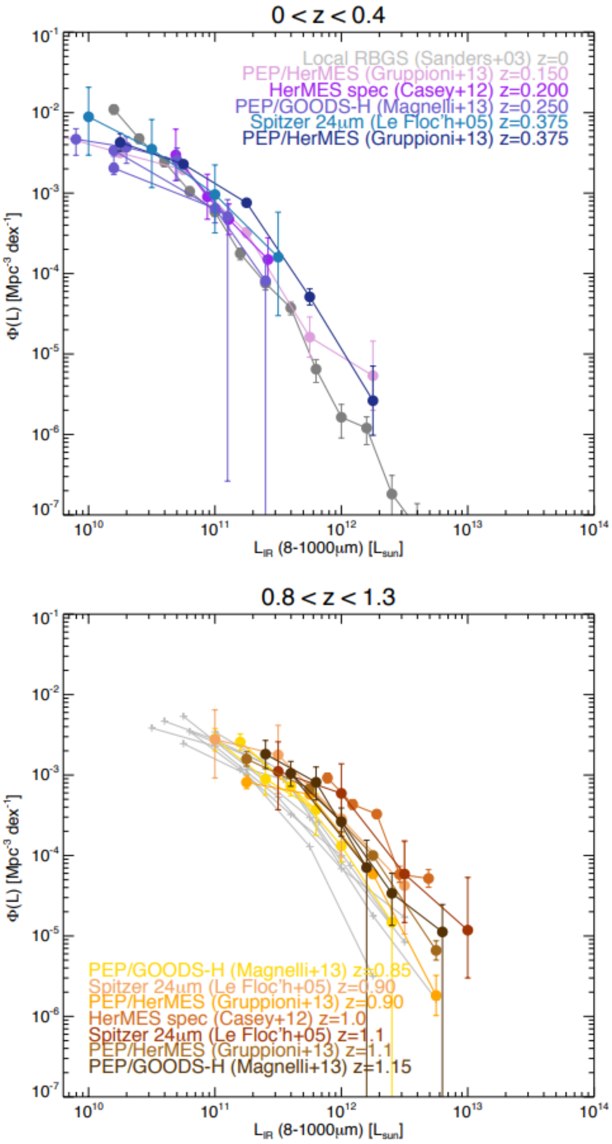

Figure 1.7: The evolution of the IR luminosity function, reproduced with permission from Casey et al. (2014). The different colours show the results from different surveys, referenced in the figures, and include Sanders et al. (2003); Le-Floc'h et al. (2005); Magnelli et al. (2011); Casey et al. (2012); Magnelli et al. (2013) and Gruppioni et al. (2013)

the luminosity function integrated across the UV and optical, and encompasses the unobscured star formation.

Even early results confirmed predictions from CIB measurements, that there was strong redshift evolution in the luminosity function of DSFGs (Kim, 1995; Smail et al., 1997). Le-Floc'h et al. (2005) used Spitzer observations at 24 μm to constrain the IR luminosity function out to $z \sim 1$, and confirmed that the evolution in the co-moving energy density in the infrared $\propto (1+z)^{3.9\pm0.4}$ between $z = 0 - 1$, compared to a UV evolution over the same redshift range of $\propto (1+z)^{\sim 2.5}$. Given these results, by z $\sim$ 0.7, LIRGs should dominate the star formation rate in the Universe, whilst ULIRGs contribute a larger, but still fractional, $\sim$ 10% at these redshifts. Daddi et al. (2005) observed near IR selected star forming galaxies[9] at $z \sim 1.4 - 2.5$ with Spitzer at 24 μm, and found that for massive galaxies ($> 10^{11}$ $M_\odot$), the typical IR luminosity was $L_{IR} > 10^{12}$ $L_\odot$, with associated SFRs of > 100 $M_\odot$ yr^{-1}. They place lower limits on the spatial density of ULIRGs at $z = 2$, and find they are 2 - 3 orders of magnitude higher than at $z \sim 0.1$.

Later studies with both Spitzer (Magnelli et al., 2011; Patel et al., 2013) and Herschel (Casey et al., 2012; Magnelli et al., 2013; Gruppioni et al., 2013; Koprowski et al., 2017) further supported these results; the IR luminosity function, and therefore obscured star formation rate density, strongly evolves out to $z \sim 1$, and then continues to evolve more moderately after that to at least $z = 2 - 3$, with LIRGs dominating the SFR density in the Universe at $z \sim 1$ and by both ULIRGs and LIRGs in roughly equal measure by $z \sim 2$ (Magnelli et al., 2013). Specifically, this dominance of the IR is due to both an increase in the number density *and* the luminosity out to $z \sim 2$ (Koprowski et al., 2017) (i.e. DSFGs become both more populous and more luminous with increasing redshift). A plot summarising how the IR luminosity function evolves with redshift up to $z \sim 3$ is reproduced from Casey et al. (2014) in Figure 1.7.

Because of various difficulties characterising DSFGs, including single dish observations, redshift confirmations, survey biases and small samples, the IR luminosity function remains highly uncertain above $z \sim 2{-}3$, with few constraints between $z = 2{-}5$ and no constraints above $z = 5$ (Figure 1 of Casey et al., 2018). Recently, several authors have attempted to quantify the $z > 4$

[9] Using a specific colour cut in the B, z, and K photometric bands (Daddi et al., 2004)

IR luminosity function, with some results suggesting that, unlike the UV luminosity function which appears to smoothly decay after peaking at $z = 2$ - 3 (Madau and Dickinson, 2014), the IR luminosity function may stay reasonably constant out to at least $z = 5$ (Rowan-Robinson et al., 2016; Novak et al., 2017). Others disagree, and find that whilst the IR luminosity of individual sources does continue to increase after $z \sim 3$, the number counts of DSFGs decrease at such a rate that the total IR luminosity function decreases, and that above $z \sim 4$ the UV (i.e. direct starlight) dominates the cosmic star formation rate density (star formation rate per comoving cubic megaparsec) (Koprowski et al., 2017; Michałowski et al., 2017). The results of Koprowski et al. (2017) are of particular note, as they use ALMA interferometric observations rather than the low resolution Herschel/SCUBA-2 observations used initially in Rowan-Robinson et al. (2016), and are therefore able to accurately identify blended sources. These blends can act to artificially raise the luminosity of a single-dish source, whereas in reality the emission comes from multiple sources, possibly not even physically associated.

Which of these results is correct remains unclear; both low resolution instruments and lack of samples at $z > 4$ make constraining the luminosity function difficult. These uncertainties are summarised neatly in Casey et al. (2018), where they model two "extreme" scenarios; one where DSFGs are too rare to contribute significantly above $z > 4$, and one where DSFGs dominate at $z > 4$ (contributing 90% of the total cosmic star formation in the first few billion years), and find that the current data cannot rule out either of these two models. Therefore, how the evolution of the IR luminosity function continues after $z = 3$ remains an important open question in infrared astronomy.

1.3.3 Scaled up Local (U)LIRGs

It's clear that more distant DSFGs are more FIR luminous that local DSFGs, at least out to $z = 3$ and with several examples of $L_{FIR} > 10^{13}\ L_{\odot}$ beyond this (Riechers et al., 2013; Strandet et al., 2017). Several studies have found that DSFGs, in particular SMGs, have extended sub-mm emission on the scale of ~ 5 *kpc*, which is large compared to the local ULIRGs, whose sub-mm emission typically only extends on hundreds of *pc* scales (Engel et al., 2010; Ivison et al., 2012; Hodge et al., 2016). This emission appears to be relatively smooth, suggesting that the star formation is taking place throughout a smooth disk rather than within specific clumps (Gullberg et al., 2018). Even though extended, it should further be noted that the sub-mm emission from DSFGs is still compact relative to the optical extent of local disk galaxies, which are extended on > 8 *kpc* scales (Casey et al., 2014). For a fixed IR luminosity, DSFGs at z $\sim$ 2 are additionally found to have both a much higher gas mass and a much higher gas to stellar mass ratio than local FIR bright galaxies, (Tacconi et al., 2008, 2010; Bothwell et al., 2013; Swinbank et al., 2014; Huynh et al., 2017). The larger physical extent of the FIR emitting region and larger gas to stellar mass fraction when compared to local ULIRGs led to the DFSG and particularly the SMG population being dubbed "scaled up" versions of this local population.

1.3.4 Multiplicity and Mergers

If the high-z DSFGs are analogous to the local ULIRGs, then they should display signs of recent or ongoing mergers. The low resolution of single dish telescopes and difficulty identifying counterparts at complimentary wavelengths has meant that only recently have large samples of DSFG been observed at a high enough resolution to identify such features.

Simpson et al. (2015) follow up 30 single dish SMGs with ALMA imaging, and detect 52 SMGs, and they suggest $61^{+19}_{-15}\%$ of single dish SMGs will resolve into multiple SMGs in the higher resolution maps. Later, Stach et al. (2018) follow up a larger sample of 606 single dish SMGs with ALMA, finding that $44^{+16}_{-14}\%$ of bright ($S_{850} > 9\ mJy$) SMGs are blends of two of more sources. These results are generally consistent with early results (Tacconi et al., 2006; Smolcic et al., 2012; Karim et al., 2013; Hodge et al., 2013); that whilst not all SMGs are clearly blends at higher resolution, a significant fraction of them are, though this should only really apply to the more often observed brighter $S_{850} \gtrsim 9\ mJy$ SMGs.

Are these blends physical associations however? Stach et al. (2018) and Chen et al. (2015) find through photometric redshifts that single dish sources which resolve into multiple sources generally are associated, whilst Simpson et al. (2015) finds the same by comparison to blank field counts. Tacconi et al. (2008) and Engel et al. (2010) use CO observations of a sample of 12 SMGs, and find that all 12 are either spatially separated but merging galaxies, have disturbed morphologies, or are compact dense galaxies which they interpret as a late stage merger, indicating that at the very least, most SMGs should be major mergers, similar to the local (U)LIRGs. Wiklind et al. (2014) meanwhile find only 3 of 10 SMGs observed with the Hubble Space Telescope show conclusive optical signs of a merger. However, they do find that all their SMGs show asymmetric morphologies compared to other galaxy types of a similar stellar mass and redshift, but stress this could simply be caused by a clumpy light distribution, and that precisely determining whether a source is a late stage merger is difficult. On the other hand, both statistical arguments (Scudder et al., 2016, 2018), and models (Hayward et al., 2013; Cowley et al., 2015) have suggested that while single dish sources may routinely resolve into multiple sources, these sources are unlikely to be associated, and may not be merger companions. Wardlow et al. (2018) searched for CO emission to confirm the redshifts of 6 single dish sources which resolve into multiple galaxies in ALMA observations to obtain redshifts. They found that whilst 61±18% of these blends are unlikely to be physically associated, 3 of their 6 sources have sub-millimeter faint CO emitting companions at a similar redshift to the source. There are furthermore a handful of examples where single dish sources with multiple resolved counterparts turn out to be at the same redshift and are physically associated (Oteo et al., 2018; Riechers et al., 2017), so it is clear that blends are not entirely unassociated sources.

Whilst a tentative picture of the multiplicity and merger rate of SMGs is beginning to emerge, a clear picture is still not apparent. In terms of multiplicity, most bright single dish SMGs appear to be blends of two or more sources[10], and there are clear cases where the multiple sources are both associated and not. The statistics of what fraction are associated remains poor. Some models in particular have recently suggested that high-z DSFGs form a very hetrogenous group, with both major mergers and isolated evolution being responsible for the starburst (Hayward et al., 2012; Cowley et al., 2015). Even so, most *detected* SMGs display some signs of a recent/ongoing merger, though the companion galaxy may not be sub-mm bright (Wardlow et al., 2018). For now, it seems that the merger induced starburst, similar to the local (U)LIRGs, continues to be the most likely *observed* physical explanation for DSFGs

[10]Though the brightest sources appear to be almost entirely lensed sources (Béthermin et al., 2017)

at high-z.

1.3.5 Environment

Much can be learned about the environment of DSFGs by studying their evolutionary descendents. Numerous results from the earliest studies of high-z DSFGs have suggested that their likely descendents are the massive elliptical galaxies that today inhabit the cores of massive galaxy clusters. Given the SFR and assumed $\sim$ 100 Myr length of the starburst, a typical $L_{FIR} = 10^{12.5}$ $L_{\odot}$ DSFG can build a stellar mass comparable to that of Milky Way ($\sim 6 \times 10^{10}$ $M_{\odot}$), in only a hundredth of the time (Licquia and Newman, 2014). CO measurements in particular find that most high-z DSFGs have both large dynamical masses and large gas masses, both on the order of 1 $\times 10^{10}$–1 $\times 10^{11}$ $M_{\odot}$ (Smail et al., 2002; Tacconi et al., 2008, 2010; Bothwell et al., 2013), and are some of the most massive galaxies at their given epoch. Furthermore Section 1.3.4 showed that the brightest high-z DSFGs all appear to be major mergers, suggestive of a reasonably dense environment, and measurements of the clustering length of DSFGs bear this out (Wilkinson et al., 2016). Meanwhile, studies of local elliptical galaxies show that their stellar population was likely formed in a single, rapid burst around $z = 2 - 3$ (Eisenhardt et al., 2008), matching the DSFG population. If DSFGs are the progenitors of massive ellipticals that exist in well formed galaxy clusters today, then it is reasonable to suggest that DSFGs may trace massive overdensities at $z = 2 - 3$. Indeed some have suggested that even a single 500 μm riser at $z > 4$ is enough to indicate the likely presence of a cluster in formation (Lewis et al., 2017).

This is a significant departure from local (U)LIRGs, which primarily exist in the field (Sanders and Mirabel, 1996). Indeed if DSFGs do trace the formation of massive ellipticals and therefore galaxy clusters themselves, it would mark a reversal of the local SFR-density relation (Elbaz et al., 2007), which finds that in the local Universe, denser environments host significantly less star formation than the field (Bamford et al., 2009). If DSFGs do trace massive overdensities at high-z however, this would also mark an easy way of detecting/studying galaxy clusters in formation. It is extremely difficult to detect the sites of cluster formation using traditional cluster detection methods such as searching for X-Rays from a hot intracluster medium, or searching for a red sequence of old passively evolving galaxies, as neither of these phenomena are likely to exist in the early stages of cluster formation. If DSFGs do trace the locations of galaxy clusters in formation, then their extreme luminosity and rarity provide excellent signposts for regions to be studied at other wavelengths.

While, several studies have found significant overdensities of galaxies around high-z DSFGs (Dannerbauer et al., 2014; Daddi et al., 2008, 2009; Capak et al., 2011; Walter et al., 2012; Ivison et al., 2013; Clements et al., 2014; Smail et al., 2014; Ma et al., 2015; Casey et al., 2015; Umehata et al., 2015; Clements et al., 2016; Flores-Cacho et al., 2016; Hung et al., 2016; Kato et al., 2016; Lewis et al., 2017; Oteo et al., 2018), others find that DSFGs actually make poor tracers of the underlying dark matter distribution and do not trace the most massive overdensities, both through observations (Chapman et al., 2009), and theory (Miller et al., 2015).

We leave an extensive discussion on galaxy clusters and DSFGs to the introduction to Chapter 2, where we search for examples of galaxy clusters in formation by searching for on-sky overdensities of DSFGs at $z \sim 2$, but note for now that the environment of DSFGs at high-z still remains unclear; it is clear that sometimes DSFGs are associated with massive overdensities at high-z, but whether this is true in general and whether they *always* trace the most massive overdensities at high-z remains uncertain.

1.3.6 Models of DSFGs

Since their initial discovery, DSFGs have proved problematic for models of galaxy formation and evolution. The problem doesn't lie purely in matching the SFRs, redshift distributions and luminosity function evolution of DSFGs and SMGs, but in doing so *whilst simultaneously* matching local $z = 0$ observations. Early models such as Baugh et al. (2005) adopted what were considered to be extreme assumptions in order to match observed number counts and redshift distributions, namely the assumption of both much higher gas masses, later shown to be true (e.g. Tacconi et al. (2010)), and the assumption of a flat IMF, which is still debated (Zhang et al., 2018). Today, such models are reasonably able to reproduce a wide range of observables (see, for example Lacey et al. (2016)), but it should be noted that such models have a number of variable parameters, and may be tuned to fit the data after the fact. Constraining the parameter space which these parameters can take is a key goal of FIR and sub-mm observations, and which can provide physical insight into the processes responsible for these DSFGs.

Significant discrepancies do remain however, particularly in the poorly studied $z > 4$ DSFGs. Recent models of galaxy formation and evolution from Béthermin et al. (2017) note that, whilst their model can reproduce the total cosmic star formation rate density at $z \sim 5$, they find that the UV luminosity function, after correcting for dust obscured star formation, can only account for ∼50% of the cosmic star formation rate density at $z \sim 4$, suggesting there is still room for a significant contribution from DSFGs at $z = 4$. This same model is further challenged by the apparent discovery of a significant number of red 500 μm risers (Dowell et al., 2014; Asboth et al., 2016; Ivison et al., 2016); observations found 1 - 2 orders of magnitude more red Herschel-SPIRE sources than predicted by models (See Table 6 of Dowell et al. (2014)). Whilst Béthermin et al. (2017) can explain the number of red Herschel-SPIRE sources, they need to invoke significant blending and clustering effects from single dish instruments. If such sources can be shown to be mostly single objects, it would demonstrate there is much we still do not understand about the high-z DSFG population.

Models that have attempted to include the effects of clustering in single dish instruments (Cowley et al., 2015; Béthermin et al., 2017), find that this clustering can have a significant impact on the observed number counts. Cowley et al. (2015) find that for a typical $S_{850} > 5\,mJy$ SMG, 3 - 6 physically unassociated galaxies are responsible for the observed flux density. Thus, once again the multiplicity of DSFGs and any physical associations arising from this multiplicity offer key constraints to models. Despite discussions in Section 1.3.4, several models are now finding that a significant number of DSFG could be formed *in situ*, by the collapse of an unstable disk rather than through a merger (Hayward et al., 2013), though this has never been conclusively observed. It is plausible to suggest that the disturbed disk morphologies, seen for instance in Wiklind et al. (2014), arise not from mergers but from collapsing disks of gas. Observations from future missions such as JWST which can probe the kinematics of the stellar population of these objects and compare these to the gas kinematics and morphologies may be key to determining whether mergers or direct disk collapse are responsible for the DSFGs.

1.3.7 Our Current Understanding of High-z DSFGs

Our understanding of DSFGs has made substantial progress over the last 20 years. We now know that they are the dominant sites of star formation above $z = 0.7$, are 2 - 3 orders of magnitude more populous at $z = 1 - 3$ than locally, and are significantly more luminous, extremely massive, with large gas masses, seem to mostly be major mergers and appear to be the evolutionary progenitors to today's massive elliptical galaxies.

Still, there is much we do not know about this population, with a particular lack of knowledge about the role DSFGs play above $z = 3 - 4$. The IR luminosity function is effectively unconstrained above $z = 4$, due to the difficulty in selecting large samples of $z > 4$ galaxies free from selection biases. Selection at 850 μm, whilst effective, offers no systematic way of selecting $z > 4$ galaxies. Selection using the Herschel-SPIRE bands can find likely $z > 4$ galaxies through 500 μm risers, but the large beamsizes introduce significant uncertainties. Given that only three DSFGs have been confirmed to exist above $z = 6$ (Riechers et al., 2013; Strandet et al., 2017; Zavala et al., 2017), and all three are extremely luminous with $L_{FIR} \sim 10^{13}\ L_{\odot}$, more samples are clearly needed to understand this population, especially at lower luminosities.

Moreover, the nature of $z > 4$ DSFGs continues to create difficulties for models of galaxy formation and evolution. Models *can* match the observed number counts, but only by invoking resolution and noise effects. There are practically no constraints on the number counts of $z > 6$ DSFGs, with only 3 samples spectroscopically confirmed. If $z > 4$ galaxies are more numerous than models predict, a conclusion reached by Dowell et al. (2014), Asboth et al. (2016) and Ivison et al. (2016), then it is possible that the $z > 6$ DSFGs may also be more numerous, and can provide new tests of our understanding.

The relationship between DSFGs and galaxy clusters, whilst developing, also remains poorly constrained. Recently, Wang et al. (2016) discovered a well formed galaxy cluster which contained a violently starbursting core known to host an overdensity of DSFGs. Comparison to models suggests that the stellar mass build up in this galaxy is a factor of 4 higher than predicted by any model, suggesting that there is still much we do not understand about massive galaxy cluster formation. There is a clear need for more samples, both of clusters in the early stages of formation and for more examples of systems like that found by Wang et al. (2016), of a collapsing starbursting core of galaxies.

1.4 This Thesis

This thesis sets out to target these uncertainties by searching for further examples of clusters in formation in the $z = 2 - 3$ Universe, characterise a number of 500 μm risers to look for evidence of mergers and multiplicity, and search for techniques and examples of further $z > 6$ galaxies. The results presented herein provide numerous targets for future follow up, in order to constrain the properties of all these different populations.

In Chapter 2, we detail the results of a search for a sample of uniformly selected DSFG rich galaxy clusters in formation, utilising both Planck and Herschel data. We discuss the statistics of this population, examine their likely redshifts and SFRs, and compare our results to models.

In Chapter 3, we detail the results of an interferometric survey of 34 candidate high-z DSFGs, all selected at 500 μm. The multiplicity of this population is studied and compared to similar studies in the literature, while several aspects of these high-z DSFGs are also examined, such as their SFRs.

In Chapter 4, we detail the follow up of a potential $z > 6$ galaxy serendipitously discovered during our initial follow up of results from Chapter 2. We target this source with a variety of FIR and sub-mm instruments, and detail the likely nature of this source, as well as the number counts of similar sources.

Finally, in Chapter 5, we summarise our conclusions from these three projects, briefly examine the start of the follow up work taking place on a number of these projects, and detail what the future goals of the field should be.

Throughout this thesis, we assume a concordance Λ Cold Dark Matter (Λ-CDM) cosmological model, with $H_0 = 67.74$ km s^{-1} Mpc^{-1}, $\Omega_\Lambda = 0.69$ and $\Omega_m = 0.31$. We also assume a Chabrier IMF unless otherwise stated, typical of what others have assumed in the literature.

"We may therefore say, that any experiment which leads us to investigate the truth of what was before admitted upon trust, may become of great utility to natural knowledge." - William Herschel, Phil. Trans. R. Soc. Lond. 1800 90, 255-283, published 1 January 1800.

Chapter 2

Protoclusters of DSFGs at z > 1

The bulk of this chapter has been published in Monthly Notices of the Royal Astronomical Society, Volume 476, Issue 3, 21 May 2018, Pages 3336-3359, *https://doi.org/10.1093/mnras/sty023*

2.1 Introduction and Motivation

Observations of the evolution of the large-scale structure of the Universe can place independent constraints not only on fundamental cosmological parameters (Harrison and Coles, 2011), but can also provide insight into and test theories of galaxy formation and evolution in the most extreme environments (Casey, 2016). Assuming light is a (biased) tracer of an underlying dark matter distribution, the underlying most massive dark matter density peaks should be traced by the most massive galaxy clusters and their progenitors at any given epoch. The formation and evolution of these massive clusters will therefore act as a proxy for tracing the evolution of large-scale structure in our Universe. Observations can then, for example, compare the most massive theoretical dark matter halo in a given cosmological paradigm at a given redshift to an observed halo mass at the same redshift (see Figure 1 of Harrison and Coles (2011)). Clusters also clearly play a strong role in shaping the properties of their constituent galaxies; at $z = 0$ there are significant differences in, for instance, the star formation rates (SFRs), colours, masses, and morphologies of galaxies in clusters compared to those in the field, (Dressler, 1980; Bamford et al., 2009; Casey, 2016). How these differences arose, and particularly at what time in the evolution of the cluster, remains uncertain and poorly constrained. As such, detecting and characterising galaxy clusters and their progenitors throughout cosmic history remains a key observational goal.

To place galaxy clusters and their progenitors in context, and to link their evolution to DSFGs, it is important to summarise the properties of a typical $z = 0$ galaxy cluster. For recent reviews, see Kravtsov and Borgani (2012); Bykov et al. (2015), and Overzier (2016). The total mass (stellar + gas + dark matter) of massive galaxy clusters ranges from $\sim 10^{13}$ - 10^{15} $M_{\odot}$. The three most massive components are dark matter (80-90%), a hot intracluster medium of gas ($\sim$ 10%), and a small contribution from stellar mass (1 - 10%) (Kravtsov and Borgani, 2012). The typical virial temperature of this gas is 10^{7} - 10^{8} K, so emission from this hot gas is dominated by X-rays from free-free bremsstrahlung. Locally, there is a strong correlation between density and morphology / colour / SFR, with early-type, red and dead[1] galaxies far more likely to be found in dense environments, and late-type, blue, star-forming galaxies in less dense environments (Dressler, 1980; Bamford et al., 2009). Galaxy clusters today therefore tend to primarily host early-type and lenticular galaxies, with little ongoing star formation and which are passively evolving.

Searches for galaxy clusters have typically looked for observational evidence of these signatures; X-ray emission, a red-sequence of passively evolving galaxies, and the Sunyaev-Zeldovich (SZ) effect (the inverse Compton scattering of CMB photons by highly energetic electrons in a cluster) have all been used to identify numerous $z < 1.5$ evolved galaxy clusters (Kravtsov and Borgani, 2012). However, beyond $z \sim 1$ - 1.5, these observational indicators become ineffective, both due to increasing distance and decreasing flux density, but also due to the evolutionary state of the cluster. A cluster which does not yet possess a well formed red sequence (i.e. the central cluster galaxies are still actively star forming), or where a hot intracluster medium has yet to be formed cannot be detected by searching for a red sequence, X-ray emission, or the SZ

[1] "red and dead" is typical nomenclature to describe red, passively evolving galaxies, with little ongoing star-formation

effect. Indeed, the only observational tracer to indicate a cluster at an earlier evolutionary stage is the detection of a physical overdensity of galaxies which is predicted to collapse down by $z = 0$. Observations to search for clusters that are still in formation, also known as protoclusters, are often time intensive, as both large areas due to their rarity, and deep integrations are needed to detect signs of an overdensity of more typically star-forming optical/NIR galaxies.

Due to this rarity, other rare galaxy phenomena such as high-z radio galaxies (HzRG), quasi-stellar objects (QSO), and SMGs have often been used as potential signposts indicative of a protocluster. The theory behind this idea is that the properties of a galaxy are generally related to some property of the dark matter halo/sub-halo in which they reside. Therefore, rare galaxy types may reside in the rarer (i.e. more massive) dark matter halos, and consequently indicate the presence of a density spike in the underlying dark matter distribution.

This signposting has proven remarkably successful, with numerous $z > 2$ protoclusters detected around HzRGs (Miley et al., 2006; Overzier et al., 2006; Rigby et al., 2013; Cooke et al., 2014), DSFGs (Daddi et al., 2008; Capak et al., 2011; Walter et al., 2012; Ivison et al., 2013; Smail et al., 2014; Dannerbauer et al., 2014; Umehata et al., 2015; Ma et al., 2015; Kato et al., 2016; Hung et al., 2016; Flores-Cacho et al., 2016; Oteo et al., 2018), and to a lesser degree QSOs (see Overzier (2016) and references therein).

From an evolutionary perspective, this also makes sense for the DSFGs; observations of $z \sim 1$ galaxy groups and clusters indicate that the star formation history of these sources favour a passively evolving model in which stars are formed in a 0.1 Gyr burst at $z \sim 3$ (Eisenhardt et al., 2008), similar to the starburst that accompanies high-z DSFGs. Furthermore, at $z > 2.5$, SMGs are found on average to occupy high-mass dark matter halos ($M_{halo} > 10^{13}\ M_{\odot}$), consistent with their evolution into massive quiescent galaxies at $z = 0$ (Wilkinson et al., 2016). Indeed, there is a growing bank of evidence that SMGs are the progenitors of todays massive ellipticals (Swinbank et al., 2006; Tacconi et al., 2008; Michałowski et al., 2010; Stevens et al., 2010; Hickox et al., 2012; Casey et al., 2014; Toft et al., 2014; Simpson et al., 2014; Dannerbauer et al., 2014). Here, we briefly review the growing body of observational evidence linking together SMGs and protoclusters.

Some of the earliest evidence that SMGs are highly clustered comes from Blain et al. (2004b) who, exploiting the FIR-radio correlation to first identify accurate positions, obtained Keck spectroscopy for a sample of 73 SMGs in several fields. They found a correlation length of (6.9 $\pm$ 2.1) h^{-1} Mpc for SMGs, in excess of what had already been found for the well studied Lyman break or UV selected galaxies at $z > 2$, and suggested the SMGs could trace the densest large scale structures in the Universe. At a similar time, Stevens et al. (2003) performed several sub-mm surveys around seven HzRGs, and found not only that the HzRGs had significant dust obscured star formation, but that several companion SMGs were present, but undetected at any other wavelengths.

Since then, several studies have found excess numbers of SMGs that are apparently clustered together on the sky, whether through the use of HzRGs (Dannerbauer et al., 2014), lensed or bright Herschel sources (Daddi et al., 2008, 2009; Walter et al., 2012; Ivison et al., 2013; Clements et al., 2016; Oteo et al., 2018), X-ray emission (Ma et al., 2015), overdensities of red sources selected in the optical/NIR (Smail et al., 2014; Umehata et al., 2015; Hung et al., 2016; Kato et al., 2016), direct searches for overdensities on sub-mm maps (Capak et al., 2011; Clements et al., 2014; Flores-Cacho et al., 2016; Lewis et al., 2017), or even serendipitously (Casey et al., 2015). Casey (2016) provides a useful review of the spectroscopically confirmed protoclusters containing significant numbers of DSFGs. The spatial extent of these discoveries range from a several arcsec (Oteo et al., 2018), to tens of arcmin (Casey et al., 2015). The total star formation rates of these objects is typically several thousand $M_{\odot}$ yr^{-1}, and is well in excess of the typical global star formation rate densities at these redshifts (Dannerbauer et al., 2014). These results hint towards a reversal of the SFR-density relation at $z > 1$ (Elbaz et al., 2007), whereby galaxies in the most overdense regions of the Universe host SFRs in excess of those in the field.

However, whether SMGs always trace the most massive overdensities at their epochs remains an open question. Chapman et al. (2009) find an excess of SMGs at $z = 1.99$, but subsequent UV observations reveal no excess in UV selected galaxies. In this case, the sub-mm observations suggest the structure should collapse by $z = 0$ whilst the UV measurements suggest that it will not, a discrepancy also seen in the Hung et al. (2016) cluster, though Hung et al. (2016) claim that the linear collapse model used by (Chapman et al., 2009) requires a number of assumptions and approximations, and that simulations by Chiang et al. (2013) suggest their structure should collapse down by $z = 0$. Miller et al. (2015), utilising simulations and mock catalogues, suggest that SMGs are in fact poor tracers of the underlying dark matter distribution, and that because they are so rare, their overdensities are in fact dominated by Poisson noise. Furthermore, Miller et al. (2015) also postulate that at $z < 2.5$, SMGs are extremely poor tracers of the most overdense regions of the Universe, as the highest density regions have already had their star formation quenched and would not be sub-mm bright.

A statistical sample large enough to confirm or refute the claims by Miller et al. (2015) has not yet been assembled, but this last point deserves further discussion. In several SMG hosting overdensities, the overdensity of SMGs and other galaxy types appears centred on the SMGs themselves, and in the densest part of the region (Umehata et al., 2015; Hung et al., 2016; Kato et al., 2016; Oteo et al., 2018), whilst in others, the SMGs primarily lie on the outskirts of the core (Dannerbauer et al., 2014; Smail et al., 2014; Casey et al., 2015; Kato et al., 2016). Furthermore, whilst the early type galaxies in the cores of a massive cluster at $z = 0$ appear to have formed at the same time, there is evidence to suggest that those early-type galaxies on the outskirts are slightly younger (Nelan et al., 2005; Smith et al., 2012). Figure 7 of Smail et al. (2014) in particular highlights that a passively evolving red and dead population of galaxies already exists in the cluster core, whilst the detected SMGs exist primarily in a medium density environment outside of this core.

Taking all of this together, a consistent picture emerges concerning the relationship between SMGs and cluster formation. Accepting that SMGs are likely to be the progenitors to the early type galaxies, at the highest redshifts, $z > 2.5$, SMGs will trace the sites of the formation of the cores of todays most massive galaxy clusters (Umehata et al., 2015; Hung et al., 2016; Kato et al., 2016; Oteo et al., 2018), a conclusion directly reached recently by Lewis et al. (2017), who find that the reddest, and therefore most likely at the highest redshift, DSFGs signpost massive protoclusters. At redshifts between $z \sim 1.5 - 2.5$, the most massive $z = 0$ clusters have already quenched the star formation in their cores, and a population of passively evolving early type galaxies (i.e. the creation of the red sequence) now inhabit the cores, likely continuing to grow their mass through dry mergers (Muldrew et al., 2018). In the less dense regions of the cluster meanwhile, SMGs exist / are triggered and enter their sub-mm bright phase, and will go on to form the outskirt early type galaxies of $z = 0$ clusters. Additionally, it is possible that other, less massive clusters will go through a sub-mm bright core phase around this redshift.

This picture is consistent with observations, but does raise several important questions; the radial evolution of the presence of SMGs seems to suggest that there is an environmental / density trigger for SMGs (i.e. there is some critical density above which SMGs in clusters are triggered as the cluster grows more dense over time), does this trigger exist and if so, what are its mechanisms? If it is not just the presence of SMGs but also their spatial distribution that indicates the evolutionary state of a cluster, how do we select a broad and unbiased population of evolving clusters to study (i.e. do the HzRGs, which imply black hole growth, bias us towards a particular evolutionary state of clusters)? How can we consistently explain this picture with overdensities such as those of Chapman et al. (2009) and Hung et al. (2016), which show overdensities of only SMGs, and not normal star forming galaxies?

These questions are not simple to answer, and require well characterised protoclusters in a variety of states of evolution to begin to answer. For starters, it is highly likely this picture of a radial evolution is too simplistic, as it's expected for a $z = 0$, $M_{z=0} > 10^{14}\ M_{\odot}$ cluster that at $z = 2$ the protocluster will be split into multiple dark matter halos, with a secondary halo hosting over 25% of the mass of the final cluster (Muldrew et al., 2015). Such secondary halos could also host SMG rich starbursting cores, which go on to merge with the main halo at a later date. However, we can make some progress by attempting to select a uniform sample of protoclusters. In particular, if we wish to obtain a sample of protoclusters with starbursting cores, we not only need to search for physical overdensities of SMGs, but for these overdensities to be confined to a region only a few arcmin across, with 1 arcmin at $z = 1$ - 3 corresponding to 0.4 - 0.5 Mpc. Such sources are expected to also be rare, and so large areas of sky are needed in order to build up a significant sample.

Negrello et al. (2005) demonstrated that a low resolution instrument may perceive several luminous sources clustered together on the sky as a single, bright source, whose flux density totals that of all the individual sources. The criteria for this to occur is that the clustering scale of the sources is similar to the beam-scale of instrument. Further observations with a higher resolution instrument at the same wavelength can then resolve this apparent single bright source into the individual sources, indicating the presence of an overdensity of sources. This overdensity may be due to a physical association, a purely line of sight effect, or even the presence of multiple, less populated, clusters along the line of sight (Flores-Cacho et al., 2016). The flux distribution of sources within the overdensity may be dominated by a single source, or evenly spread out amongst all the sources which make up the overdensity. In essence, this effect is the same effect as the SMG multiplicity problem discussed in Section 1.3.4, but rather than sources clustered together on arcsecond scales[2], Negrello et al. (2005) discuss applying effect to instruments with beam-sizes on the arcminute scale.

Both the Planck HFI (Planck HFI Team et al., 2010) and Herschel-SPIRE (Griffin et al., 2010) instruments operate at 350 μm / 857 GHz, with similar filter response curves, and at 500 μm and 545 GHz (550 μm), with filter response curves slightly offset from one another. These matching passbands and the approximately 10× difference in their beam-sizes, with 350 μm / 857 GHz beam-sizes of 24.2 arcseconds and 4.63 arcmin for Herschel and Planck respectively (and 35.2 arcseconds and 4.63 arcmin for the SPIRE 500 μm and Planck 545 GHz bands), make a Planck and Herschel cross-match ideal for searching for rare overdensities of DSFGs on the sky. Furthermore, at the expected epoch of cluster formation around $z = 2 - 3$, the rest-frame peak of dust emission at ∼100 μm will have become redshifted into the observed frame from 350 and 500 μm Herschel and Planck bands. The 857 GHz band is the highest frequency Planck band, so no matching passband is available for the SPIRE 250 μm band.

Clements et al. (2014) searched for protoclusters in $\sim 100\ deg^2$ of Herschel data with an early release of point sources detected on the Planck maps. They found 4 candidate protoclusters, which all show enhanced star formation rates and likely lie around $z \sim 1 - 2.3$. Here, we extend the work begun in Clements et al. (2014) to include the full data release of Planck, which includes 2 further releases of Planck point like sources, and increase the Herschel area

[2] Indeed, it is entirely possible that what Herschel views as an individual source within an overdensity is furthermore actually made up of 2+ sources when observed at even higher resolution, see (Oteo et al., 2018) for instance.

surveyed to over 800 deg^2, combining several large extragalactic Hershcel surveys together. Our work not only touches on the nature of DSFG rich protoclusters, but also on the nature of the point-like sources detected by Planck, and how choices of filters and detection methods affect selection of object types.

In Section 2.2, we discuss the various Planck and Herschel maps and catalogues used in this work, detailing their selection methods and flux density limits. In Section 2.3, we detail our selection of candidate protoclusters, and include identifications of all the Planck sources located in Herschel fields. In Sections 2.4 and 2.5 we examine the photometry and colours of the Planck sources, including the protoclusters. Section 2.6 specifically looks at the properties of the candidate protoclusters and compares them to simulations. We discuss all our results in Section 2.7, and summarise our key conclusions in Section 2.8.

We routinely refer to "protoclusters" throughout this chapter. The definition of a protocluster varies between author, and generally has referred to structures which, by $z = 0$ will have virialized into a $> 10^{14}\ M_\odot$ cluster (Overzier, 2016). Here however, we define a "protocluster" as a source where we *explicitly assume* that the overdensity is physically clustered, as well as going on to collapse down to a $> 10^{14}\ M_\odot$ structure at $z = 0$. We stress here that this may not be the case, and that only future observations will be able to determine if these assumptions are valid.

2.2 The Data

All the Planck catalogues and maps detailed in the section are publicly available, and can be downloaded at the Planck Legacy Archive: `http://pla.esac.esa.int/pla/`*. The H-ATLAS maps and catalogues are avaliable at* `http://www.h-atlas.org/public-data/download`*, the HerMES maps and catalogues at* `https://hedam.lam.fr/` *and the HerS data at* `http://www.astro.caltech.edu/hers/HerS_Home.html`

In this section, we detail all of the maps and catalogues used in this chapter, as well as the filtering and extraction methods used.

2.2.1 The Planck Catalogues of Compact Sources

Planck produced three catalogues of compact, point-like sources across the whole sky, each using slightly different reduction techniques and detection criteria. Each catalogue contains nine separate sub-catalogues, one for each of the bands on both the low frequency instrument (LFI) and high frequency instrument (HFI, Planck HFI Team et al. (2010)) on board Planck. In this chapter, we solely use data from the HFI. A target of 80% reliability was required for the catalogues, such that 80% of the sources within the catalogue are real.

The first catalogue released was the Early Release Compact Source Catalogue (ERCSC, Planck Collaboration et al. (2011)), which was reduced and released after the Planck satellite completed 1.6 full surveys of the sky. For the 217, 353, 545 and 857 GHz bands (i.e. the HFI bands), the ERCSC used SExtractor (Bertin and Arnouts, 1996) to extract point like sources. The Planck maps are first divided up into several smaller patches and convolved with a Gaussian kernel, the full width half maximum (FWHM) of which is the same size as the Planck beam at each frequency. SExtractor then extracts objects by selecting isolated groups of connected pixels that are above a chosen σ threshold. Several flux density estimates are made for each extracted source, including Gaussian fits, PSF fits and aperture photometry. Reliability cuts were made to ensure that 90% of sources have flux densities accurate to within ±30%. Secondary cuts, including those to account for artefacts left by transits, extended Galactic cirrus, and sources with negative flux density (see Section 2.3 of Planck Collaboration et al. (2011)) were further made. In the 857 GHz band, the final catalogue contains $8,988$ sources, $4,513$ of which lie at galactic latitudes $|b| > 30^o$. The ERCSC does not provide completeness limits or flux density limits, but the faintest source at $|b| > 30^o$ is 655 ± 89 mJy, with a measured flux density of the faintest 10σ detected source of 813 ± 109 mJy[3], which provide a rough idea of the flux limits of the catalogue, as there is no fixed flux limit. The beam FWHM of each band changes between catalogues owing to improvements in calibration, and in the 545 and 857 GHz bands

[3] The quantity flux / flux error here is $< 10\sigma$, as the detection strength is determined by several factors, see Section 2.2 and 2.3 of Planck Collaboration et al. (2011) for more details.

of the ERCSC was 4.47 and 4.23 arcmin respectively. The 545 GHz band on the other hand, contains $7,223$ sources, $2,535$ of which lie at $|b| > 30^o$. Its faintest measured source flux density is 381 ± 51 mJy, with the faintest 10σ source flux density 471 ± 46 mJy, and a beam FWHM of 4.47 arcmin.

The second catalogue released was the Planck Catalogue of Compact Sources (PCCS1, Planck Collaboration et al. (2014)), after 2.6 all sky surveys. The PCCS1 differed in its source detection routine to the ERCSC. Like the ERCSC, the PCCS1 first divided the Planck map into multiple patches using a gnomic projection. The size of the patches was large enough that a fair sample of the noise was obtained, but small enough that the characteristics of this noise / foregrounds were reasonably uniform across the patch. Patches were also made to overlap to minimise edge effects. These patches were then convolved with a 2d second order Mexican-hat wavelet filter. The Mexican-hat wavelet contains only one free parameter, the scale R, and can be represented in Fourier space by

$$\hat{\psi}(kR) \propto (kR)^n \tau(kR), \tag{2.1}$$

where n is the nth order wavelet, R is the scale parameter, k is the wave number, $\tau(kR)$ approximates the Planck PSF in Fourier space, which approximates a Gaussian, and $\hat{\psi}(kR)$ is the representation of the wavelet in Fourier space. The family of Mexican-hat wavelets can be intuitively understood as applying the Laplacian operator to a Gaussian n times to get the nth order Mexican hat wavelet. The wavelet was normalised such that the amplitude of the source was preserved, i.e. $\int\int_{-\infty}^{\infty} \psi(x,y)dxdy = 1$, and Figure 2.1 shows the zeroth, first, and second order Mexican-hat wavelets for comparison. As can be seen, the first and second orders become negative after the initial peak, such that emission at these scales will contribute *negatively* to a source in the filtered maps. This contrasts with the ERCSC, which effectively used a Gaussian (blue line in Figure 2.1). This negative contribution was deliberately included to reduce contamination in the catalogues from extended rather than point sources, i.e. Galactic cirrus. The parameter R was optimised on each patch to maximise the signal to noise of detected sources. Sources were then extracted based on a signal to noise ratio (S/N ratio) that depended on both band and whether the source was within the galactic plane or not. These

S/N values were 4.7 and 4.9 for the 545 GHz and 857 GHz bands respectively and in the area of sky under consideration here. For the HFI bands, the patches were not only convolved with the filter at the optimised scale, but at four additional scales which bracket the optimal scale. The behaviour of the candidate detection was then compared to the expected behaviour of a point source at all 4 scales, and the χ^2 of the observed against predicted values were minimised to provide an alternative measurement of the amplitude. The S/N detection ratio, the minimum χ^2, and the ratio of these numbers were then used to determine if a source was accepted or rejected. Finally, to reject narrow structures, the expected number of connected bright pixels for a point source was compared to the actual number of connected pixels, rejecting the source if this threshold was not met. We note in detail the specifics of the source detection and acceptance here, because as we show later there appear to be significant differences between the types of sources detected between the three catalogues, especially for sources which may not typically be point-like (i.e. multiple point-like sources which make up a protocluster). In total, the PCCS1 contains $24,381$ detected sources at 857 GHz, and $16,933$ at 545 GHz, with $7,536$ and $3,738$ sources at $|b| > 30^o$ in the two bands respectively. The 90% completeness limits are 680 and 570 mJy for the 857 GHz and 545 GHz bands respectively, with the minimum measured flux density of sources detected at $|b| > 30^o$ after excluding the faintest 10% of sources of 658 and 457 mJy respectively.

The third catalogue released was The Second Planck Catalogue of Compact Sources (PCCS2, Planck Collaboration et al. (2015a)), produced after 8 full sky surveys for the LFI and 5 full sky surveys for the HFI. Like the PCCS1, it also used a detection pipeline based on the second order Mexican-hat wavelet, but further divided up the sources into those where the reliability could be quantified (PCCS2) from those that couldn't (PCCS2E). This was primarily a function of position on the sky, and especially due to crowded fields from Galactic cirrus, with sources generally in the PCCS2E at $|b| < 30^o$, and those in the PCCS2 generally at $|b| > 30^o$. The effective beam FWHM was 4.83 and 4.64 arcmin in the 545 and 857 GHz channels respectively, and the PCCS2 contains $1,694$ and $4,891$ sources in the two bands respectively at $|b| > 30^o$. The 90% completeness limits are given as 555 and 791 mJy in the 545 and 857 GHz sub-catalogues respectively for the PCCS2, with a minimum measured flux density recorded after excluding the

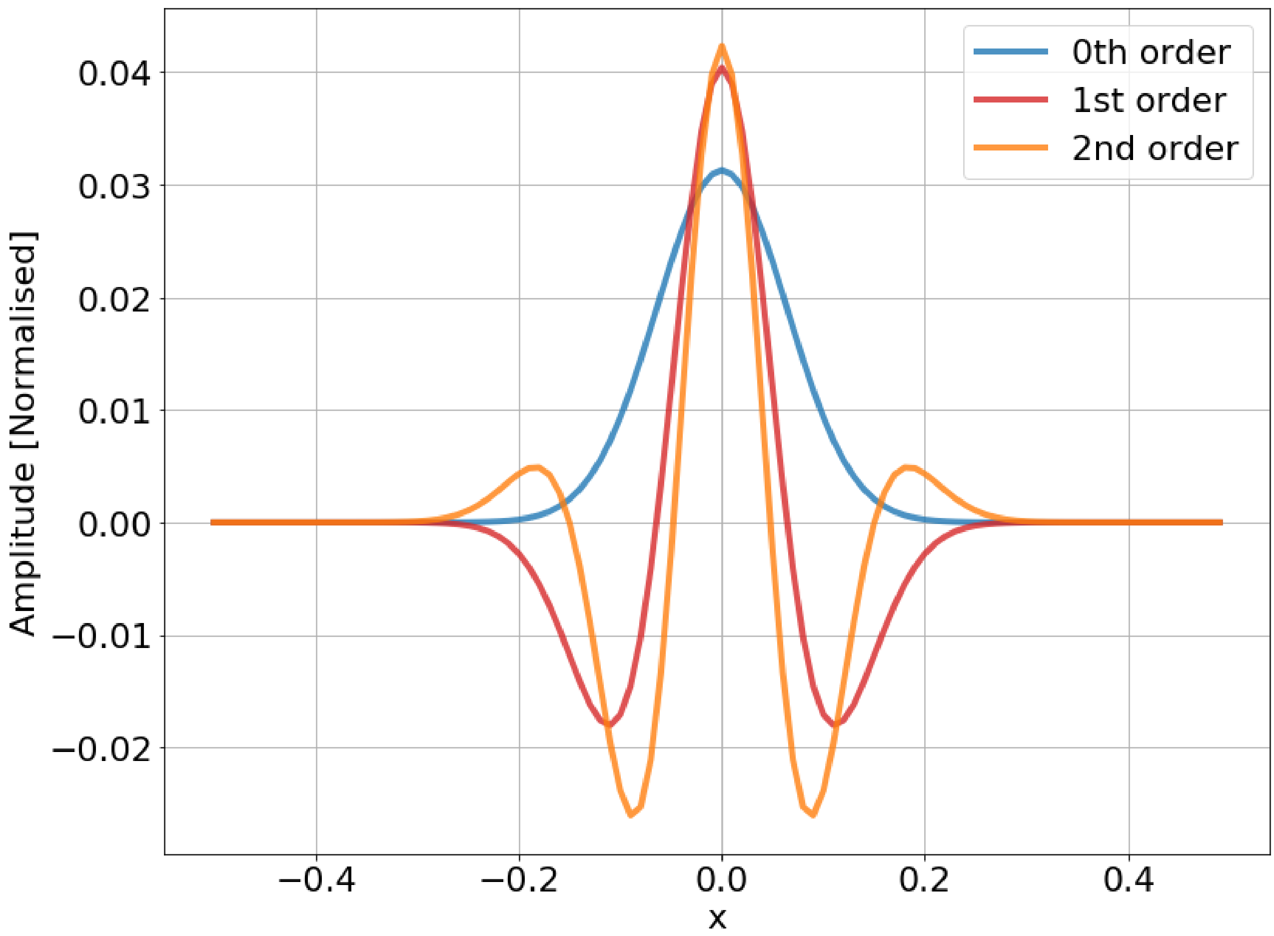

Figure 2.1: The first three Mexican-hat wavelets, generated using Equation 2.1. The zeroth order (blue) is a Gaussian, with the first order (red) and second order (orange) showing the characteristic dip outside of the central peak. All three have been normalised such that the total area under each is unity.

faintest 10% of sources being 535 and 720 mJy for the two bands respectively. This is actually higher than for the PCCS1, and is detailed in Section 3.2.3 of Planck Collaboration et al. (2015a), but briefly this is due to improvements in the physical modelling of the simulations used to asses the reliability of the catalogues, which resulted in lower reliability estimates at a given S/N. The S/N threshold for inclusion in the catalogue therefore was shifted to higher S/N, resulting in fewer sources than the PCCS1.

All three catalogues provide positional information, four separate flux measurements based on the detection flux, aperture flux, PSF flux and a flux from a Gaussian fit[4], and in the case of the 857 GHz sub-catalogue, the aperture flux densities at those positions for the 217, 353 and 545 GHz maps. Here, we choose to use the flux density measurement based on aperture photometry, as it is easiest to replicate, can be compared across catalogues with few assumptions, and is likely to capture emission from extended structures such as protoclusters. In general, this method measured the flux density from a source using an aperture of radius equal to the Planck beam FWHM, and measured the sky background in an annulus of inner radius 1 $\times$ the Planck beam FWHM and outer radius 2 $\times$ the Planck beam FWHM in each band. All future references to the Planck flux density of an object in this chapter will refer to this unless otherwise stated.

2.2.2 The Herschel Extragalactic Legacy Surveys

Herschel performed several large extragalactic surveys. The largest of these surveys included the Herschel Astrophysical Terahertz Large Area Survey (H-ATLAS, Eales et al. (2010), the Herschel Multi-tiered Extragalactic Survey (HerMES, Oliver et al. (2012)), and the Herschel Stripe 82 Survey (HerS, Viero et al. (2014)). Here, we briefly describe these surveys, the maps, and the catalogues used to search for protoclusters of galaxies. Table 2.1 identifies all the fields used during the search for protoclusters, their area, and the number of Planck compact sources they contain in both the 857 and 545 GHz bands.

[4]See appendices A.1, A.2 and A.3 in Planck Collaboration et al. (2014) for further details

H-ATLAS

The Herschel-ATLAS (H-ATLAS, Eales et al. (2010)) was the largest open-time survey on Herschel. It comprised five survey fields, chosen to both maximise legacy value and minimise contaminating emission from dust within the Milky Way: one close to the North Galactic Pole (NGP) with a total area around 170 deg^2, one close to the Southern Galactic Pole (SGP) with total area 285 deg^2, and three along the celestial equator at RA's of approximately 9, 12 and 15 hours (GAMA09, GAMA12, GAMA15), each with an area around 54 deg^2 and designed to overlap the fields surveyed by the Galaxy and Mass Assembly redshift survey (GAMA, Driver et al. (2011)).

After correcting and masking the raw SPIRE data (see Valiante et al. (2016) for the GAMA fields and Smith et al. (2017) for the NGP and SGP for more details, but these corrections generally included astrometric calibration, sudden changes in receiver voltage, and long term drifts in the bolometer signals due to temperature changes), maps were produced using a customised pipeline within The Herschel Interactive Processing Environment (HIPE, Ott et al. (2010)), with pixel sizes of 6, 8 and 12 arcseconds for the 250, 350 and 500 μm bands respectively. This is approximately 1/3 the FWHM of the PSF of the SPIRE beam, measured as 17.8, 24.0, and 35.2 arcsec for the 250, 350 and 500 μm bands respectively (Valiante et al., 2016).

Instrumental noise was estimated from a jackknife map by subtracting one half of the total data from the other, removing any real astronomical structure and leaving a map that should only comprise instrumental noise. The confusion noise was estimated by first producing histograms of all the pixels on the final maps, then fitting a Gaussian to the negative on the maps. This gave an estimate of the total noise, and the confusion noise can then be estimated from $\sigma^2_{total} = \sigma^2_{confusion} + \sigma^2_{instrumental}$. The noise varies slightly between maps, but is generally around 5.5, 6.5, and 7.5 mJy for the 250, 350 and 500 μm maps, after the maps had been background subtracted and convolved with the SPIRE beam PSF.

Sources were extracted using the Multi-band Algorithm for source Detection and eXtraction (MADX, Maddox et al. (2017)). First, large scale emission from Galactic cirrus is removed from all three bands. The maps are then convolved with a "matched filter" (Chapin et al., 2011, Appendix 1), which maximises the S/N ratio for unresolved sources in the presence of both confusion noise and instrumental noise. Peaks above 2.5σ in the resulting 250 μm map are considered as potential sources. Starting with the brightest potential source, and using the position from the highest resolution 250 μm map, an improved estimate of the flux density of the source is made in all three bands. This is then convolved with the PSF at all three wavelengths, and is then removed from the maps at the position of the 250 μm source. In this way, if the bright source overlaps with a nearby fainter source, any contamination should be removed by the convolved PSF. The process continues with the next brightest source, until all sources have been fit. Some small further corrections are made due to astrometric uncertainties. Catalogues of sources can then be produced by choosing a σ cut on this master catalogue. Estimates of the completeness and positional accuracy for different choices of σ cuts are given in Valiante et al. (2016), but here all those sources which have a $> 4\sigma$ detection in at least 1 SPIRE band are kept. This extraction effectively selects objects at 250 μm, requiring at least a 2.5σ detection in this map. The effect this might have on fainter, redder, and possibly higher redshift objects which are faint at 250 μm but brighter at 350 and 500 μm is discussed in Section 2.7.

HerMES

HerMES (Oliver et al., 2012) was a Herschel legacy survey, designed to map several well studied nested extragalactic fields which should cover a broad range of cosmic environments, including filaments, cores, and voids. Field sizes varied from 0.01 to 20 deg^2, with an additional large 270 deg^2 field, the HerMES Large Mode Survey (HeLMS). The fields which reached high sensitivity over a small area, generally identified in HerMES as level 1 - 4 fields, were designed to search for low-luminosity objects, whereas the wide shallow fields, levels 5 - 6, were designed to search for the rare but higher luminosity objects. We nearly exclusively used the wide shallow fields to search for protoclusters, as the smaller fields are not large enough to contain any Planck compact sources.

Maps were produced using the SPIRE-HerMES Iterative mapper (Levenson et al., 2010), with pixel sizes of 6.0, 8.3 and 12.0 arcseconds in the three bands respectively. The instrumental noise varies between fields, and the confusion noise was only measured on a few fields from the HerMES Science Demonstration Phase (SDP). In these fields, the 1σ SPIRE confusion noise was found to be roughly between 6 - 8 mJy per SPIRE beam (Nguyen et al., 2010), similar to what was found in H-ATLAS. Under the assumption that this confusion noise is similar to other fields, we add it in quadrature to the instrumental noise for the large fields. This gives total 1σ noise levels of 6.2 - 6.8, 7.1 - 7.5 and 8.2 - 8.9 mJy for the 250, 350 and 500 μm bands respectively for the level 5 fields, noise levels of 7.9, 8.2 and 10.1 mJy respectively for the level 6 fields, and 1σ noise levels of 14.1, 12.7, and 16.8 mJy for the single level 7 field, HeLMS.

Multiple catalogues were made for the HerMES maps, each using slightly different extraction algorithms. To search for protoclusters, and so that catalogues similar to those from H-ATLAS are used, we used the data release 4 XID250 catalogues. Full details are available in Hurley et al. (2016), but briefly, sources are first blind extracted on the 250 μm maps (Roseboom et al., 2010; Smith et al., 2012), the positions of which are then given to XID. XID is a probabilistic deblender for confusion dominated maps, which uses positional priors and the PSF of the SPIRE beam to simultaneously fit all the sources to the 250, 350, and 500 μm maps, providing accurate flux densities and uncertainties.

Herschel Stripe 82 Survey

The Herschel Stripe 82 Survey (HerS, Viero et al. (2014)), was a 79 deg^2 survey motivated by an attempt to understand the CIB by characterising the properties of the galaxies that contribute to it from a multi-wavelength perspective. It was designed to cover a region of the sky that overlaps with both existing and future galaxy surveys in the Sloan Digital Sky Survey's (SDSS, Abolfathi et al. (2017), and references within) "Stripe 82" field.

Maps were produced using the Signal and Noise Estimation Procedure Including Correlations (*SANEPIC*, (Patanchon et al., 2008)), with pixel sizes of 6, 8.33 and 12 arcseconds for the 250, 350 and 500 μm bands respectively. The total noise levels (confusion + instrumental) are found to be 8.3, 8.6 and 9.7 mJy beam^{-1} in the 250, 350, and 500 μm maps respectively.

After filtering the map to remove large scale fluctuations from Galactic cirrus, sources were extracted using the IDL software package *STARFINDER* (Diolaiti et al., 2000), requiring a S/N > 3 for a detection. At 250 μm, these sources are then used as priors that are fed into *DESPHOT* (Roseboom et al., 2010, 2011; Wang et al., 2013), the precursor to XID (Hurley et al., 2016).

2.3 Selection and Identification of Sources

In this section, we detail how we combined the Planck catalogues with the Herschel maps and catalogues in order to identify a number of candidate protoclusters, as well as the nature of all the Herschel detected Planck sources.

At both 857 and 545 GHz, the Planck beam of 4 - 5 arcmin corresponds to a physical size of a few hundred kpc at $z = 0.1$ to a maximum of around 2.5 Mpc at $z = 1 - 3$. On the other hand, the beamsize of Herschel-SPIRE is around $17 - 35$ arcseconds, and corresponds to a physical size of 30 - 65 kpc at $z = 0.1$, and 150 - 300 kpc at $z = 1$ - 3. The Planck beam is therefore on the same scale as several of the confirmed SMG rich protocluster and protocluster cores detailed in Section 2.1, whilst the Herschel beam can resolve out the individual sources associated with this protocluster.

Therefore, by visually inspecting the Planck point sources with the higher resolution Herschel maps, we can determine the nature of these point sources. Bright individual sources, such as gravitational lenses or blazars, will remain point-like in the Herschel maps, very local galaxies will be resolved and can easily be identified through cross-matching with known galaxy catalogues, whilst clusters / protoclusters of distant DSFGs will resolve into multiple point sources on the Herschel maps, clustered on the scale of the Planck beam.

As detailed in Section 2.2, each subsequently released Planck catalogue contained deeper integrations, but also changed the detection algorithm between releases. As these different detection pipelines could be sensitive to different source populations, we include all three catalogues in our analysis.

2.3.1 Source Selection

We took each of the Planck compact source catalogues in turn, and cross-matched them with each of the Herschel catalogues described in Section 2.2. We used a search radius equal to the Planck FWHM at 857 GHz in the PCCS2, 4.63 arcmin, as this used the most up to date calibration and beam information. The Herschel source density is high enough that, as long as a Planck compact source is located in one of the Herschel fields, there are always multiple Herschel sources located within the Planck beam, and typically > 10. As the published Planck beam varies both with channel and catalogue release, we varied this value between 4.0 and 5.0 arcmin, but found that the number of successful Planck-Herschel matches did not change, though we did find small variations in the number of Herschel sources we associated with each Planck source.

For the 857 GHz sub-catalogues of the Planck Catalogues of compact sources, we found a total of 160 ERCSC sources that lie in a Herschel field, 229 for the PCCS1 and 168 from the PCCS2. For the 545 GHz channel, we found 50 ERCSC sources, 99 PCCS1 sources and 60 PCCS2 sources. Cross matching the three Planck catalogues with one another to remove common sources, we found 313 unique Planck sources for the 857 GHz channel and 118 unique Planck sources for the 545 GHz channel. Cross-matching these two catalogues together, we find there are 354 unique Planck compact sources in either the 857 or 545 GHz sub-catalogues which are located within the 808.4 deg^2 from H-ATLAS, HerMES or HerS. Table 2.1 lists the 17 fields where we detected at least one Planck source in either the 857 or 545 GHz subcatalogues. Due to the lack of a publicly available and verified catalogue, we do not include the HeLMS field in our primary analysis, but do discuss the Planck sources that fall within it in Section 2.7. The 354 unique Planck sources are those which do not lie in the HeLMS field.

To quantify any overdensities, we further created a catalogue of all the Herschel sources that fall within 4.63 arcmin of each Planck source, linking each Herschel source to the Planck source it is associated with. The Herschel catalogues produced by different groups are inhomogenous, and we therefore artificially imposed a minimum flux density cut, requiring a measured Herschel flux density of 25.4 mJy in at least one of the three SPIRE bands. This limit of 25.4 mJy

Table 2.1: The 17 Herschel fields that contained at least 1 Planck compact source in either the ERCSC, PCCS1 or PCCS2, excluding HeLMS.

		Planck source count	
Field	Area [deg^2]	857GHz	545GHz
NGP	170.0	82	21
SGP	285.0	91	35
GAMA09	53.4	26	13
GAMA12	53.6	15	5
GAMA15	54.6	16	13
ADFS	7.5	3	3
BOOTES	11.3	11	2
CDFS-SWIRE	10.9	5	1
COSMOS HerMES	4.4	2	1
EGS HerMES	2.7	1	0
ELAIS N1 SWIRE	12.3	6	2
ELAIS S1 SWIRE	7.9	2	0
FLS	6.7	5	3
GOODS-North	13.5	0	0
LOCKMAN-SWIRE	16.1	6	3
XMM-LSS-SWIRE	18.9	4	2
HERS	79.0	38	14
Total	808.4	313	118

was chosen as a compromise between ensuring a sufficient number of Herschel sources were included per Planck source, requiring a flux density limit reasonably above that of any of the catalogues such that we are not biased against a particular field / catalogue, and a flux density value where reliable number count estimates are available in order to estimate the level of the overdensities. After cross-matching, the Herschel source catalogue associated with the 857 GHz selected Planck sources contains 3,709 sources that are within 4.63 arcmin of a Planck source, whilst the 545 GHz μm Herschel matched catalogue contains 709 sources within 4.63 arcmin of a Planck source.

We further checked for any cross-matches between our Planck compact sources and the Planck Sunyaev-Zel'dovich Galaxy Cluster Catalogue (PSZ, Planck Collaboration et al. (2015b)), the Planck Galactic cold clump catalogue (Planck Collaboration et al., 2015c), and the Planck high-Z catalogue (PHZ, Planck Collaboration et al. (2016)). We found no matches between our Planck sources and the SZ catalogue, a single match with the Galactic cold cores catalogue, PLCKERC857 G339.76-85.56, and four matches in the PHZ, PCCS1 545 G160.59-56.75, PCCS1 545 G084.81+46.34, PLCKERC545 G007.56- 64.14 and PCCS1 545 G012.89-66.24. After attempting to identify all our Planck sources (see next section), we found we cannot associate the Galactic cold clump source, and three of the PHZ sources, with any known source. The final PHZ source we initially associate with the $z = 0.2020$ galaxy 2MASX J02094125+0015587. Also known as SDSS J020941.27+001558.5, both Harrington et al. (2016) and Geach et al. (2015) predicted this was likely a lensed candidate, and both identified a background $z = 2.553$ DSFG, also known as “9io9”(Geach et al., 2015), being lensed by 2MASX J02094125+0015587. We note that we do not specifically identify any cross-matched source with any known cluster or protocluster, despite both the PHZ and PSZ likely tracing young and evolved clusters themselves respectively.

2.3.2 Source Identification

To identify each of the Planck sources, we visually inspected each source in the Herschel maps at the position of the Planck source. A summary table of our results is available in Table

Table 2.2: Identifications of all the Planck objects that fall within one of the Herschel survey fields under consideration here.

Type	857 GHz	545 GHz	Unique
Local galaxies	187	54	192
Galactic cirrus	37	18	43
protocluster candidates	21	10	27
Lensed sources	12	2	12
Stars	3	2	3
QSOs	2	1	2
Off Map	13	3	14
No Assignment Given	38	28	61
Total	313	118	354

2.2, and a full table for all 313 857 GHz and all 188 545 GHz Planck sources is available in Appendix A.

All 354 sources were visually inspected, and the positions of the Planck source and any Herschel sources within the Planck source were cross-matched with the NASA Extragalactic Database (NED), with which we identified 192 local galaxies, two QSOs, and eight lens candidates that have known H-ATLAS identifications. Fourteen sources lie on the edge or just off the Herschel map, and these are not considered further. On four occasions, we found the Planck source resolved in the Herschel maps to a single bright source with $S_{350} > 50\ mJy$, but which had no optical or other known counterparts in NED or elsewhere. We assign these sources as lens candidates, though it is also possible that these could be examples of H/ULIRGs, and are intrinsically highly luminous ($L_{FIR} > 10^{13}\ L_{\odot}$). Furthermore, all sources were also cross-matched with the Set of Identifications, Measurements and Bibliography for Astronomical Data (SIMBAD, Wenger et al. (2000)), and three stars, Fomalhaut, Mira, and R Sculptoris, were identified in this way.

We then examined the 100 μm maps from the Improved Reprocessing of the IRAS Surveys (IRIS, Miville Deschenes and Lagache (2005)) at the positions of the 131 Planck sources which remain unidentified. We expect the peak of dust emission for $z > 1$ DSFGs to occur at wavelengths $> 200\ \mu m$ in the observed frame, and the steep Wien tail of the blackbody emission will mean such sources are reasonably faint in the IRIS 100 μm maps. Galactic cirrus, on the

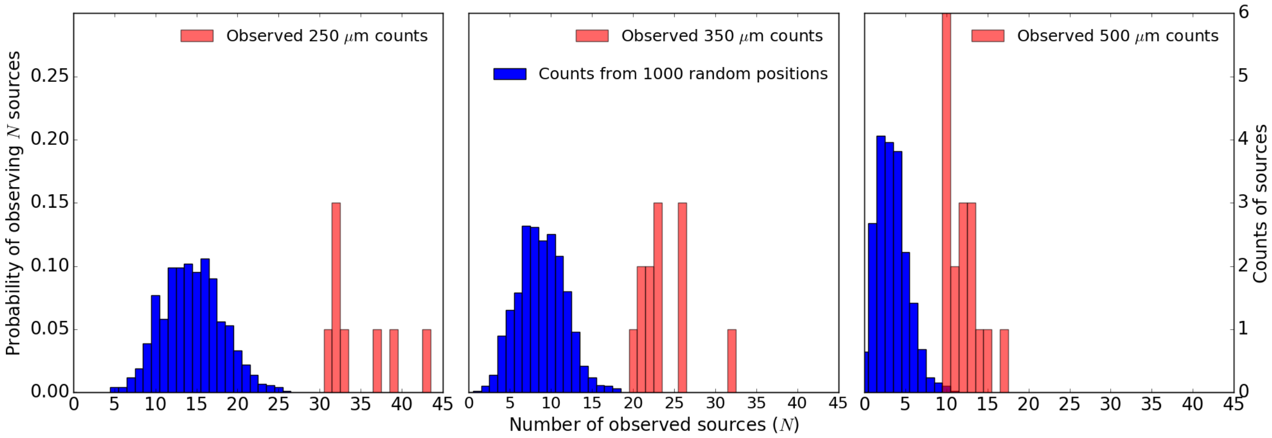

Figure 2.2: Histograms of the counts of Herschel sources with flux densities > 25.4 mJy in the three SPIRE bands. Blue shows counts from 1,000 random positions on the Herschel maps, whilst red shows the Herschel counts of our candidate protoclusters.

other hand, will likely have its emission peak around 100 μm in the observed frame, and so will be comparatively bright in the IRIS 100 μm maps. Furthermore, it is likely the Galactic cirrus will be of a filamentary nature, and generally extended in the Herschel maps, whereas on-sky overdensities of DSFGs are likely to appear as several point sources. A combination of examining the Herschel maps, the IRIS maps, and looking for filamentary structure identifies 43 of the remaining 131 sources as Galactic cirrus. We have generally been conservative in this identification, with any sign of filamentary structure of emission at 100 μm leading to a Galactic cirrus classification, as our goal is to be confident in our protocluster identification.

For the remaining 88 sources, we count the number of Herschel sources with 250, 350 or 500 μm flux densities > 25.4 mJy that lie within 4.63 arcmin of each Planck position. Taking number counts from Clements et al. (2010) and Valiante et al. (2016) and assuming our sources are distributed in a Poisson manner, we expect to detect, on average, 16.5 ± 4.1, 9.1 ± 3.0 and 2.7 ± 1.7 250, 350 and 500 μm Herschel sources per Planck beam. If the sources are distributed in a Poisson manner, a 3σ overdensity corresponds to detecting more than 31, 19 or 9 sources in either of the 250, 350 or 500 μm bands respectively. Applying this limit to each of the remaining 88 Planck sources, we find 27 sources are at least this dense in Herschel sources.

These could be overdensities of sources, but it is also possible that the Poisson distribution is not an adequate description of the complex distribution of galaxies. To assess this assumption, we sampled the distribution of the number of Herschel sources per Planck beam by placing 10,000 Planck beams randomly on the NGP field. We modelled the Planck beam as a circle of radius 4.63 arcmin, and on each sample we counted the number of 250, 350 and 500 μm sources with flux densities $> 25.4\ mJy$ that fell within this beam. We furthermore ensured that any randomly placed beam occurred away from the edge of the map. We further found that 10,000 beams effectively saturated the map such that we were re-sampling positions previously sampled, so we additionally used the SGP field, as well as several smaller fields. A subset of this, with only 1,000 positions, is plotted in Figure 2.2 for all three SPIRE bands, showing both the 1,000 random positions and the overdensities we have discovered to be associated with our Planck sources. For the NGP, we found only 16 of our 10,000 random positions contain at least 19 350 μm sources with $S_{350} > 25.4$. Interpreting 16 / 10,000 as a probability, and converting this to an equivalent σ value in the Normal distribution, this corresponds to 2.94σ. Similar results are found for the 250 and 500 μm bands. This is in excellent agreement with our assumption that we can model the distribution of galaxies, at least for searching for overdensities, as Poisson. We have therefore clearly demonstrated that these 27 Planck compact sources are over-dense to $\gtrsim 3\sigma$ in Herschel sources, and we classify them as candidate protoclusters, though we retain the possibility that these sources are in fact only line of sight effects or indicate where multiple clusters of DSFGs lie along the line of sight.

There still remain 61 Planck compact sources where we have ruled out local galaxies, Galactic cirrus, distant lensed / intrinsically luminous DSFGs or on-sky overdensities of DSFGs as an origin for their emission. Rather than attempting to determine the nature of these sources, we here simply do not assign them any classification, and an extended discussion on their nature after determining their flux densities and colours can be found in Section 2.7.

We therefore have 279 unique Planck sources for which we have secured a reasonable identification, including lens candidates, local galaxies, Galactic cirrus and candidate protoclusters of galaxies, and a further 61 sources which we were unable to identify, for a total of 340 Planck compact sources.

2.3.3 Diffuse and Dominated Sources

In our selection of candidate protoclusters, we used only the number of Herschel-SPIRE sources with flux densities $> 25.4\, mJy$, and did not examine in detail how the flux is actually distributed amongst sources.

To examine this in more detail, we took all the Herschel sources associated with a Planck 857 GHz object, and calculated the standard deviation of their Herschel 350 μm flux densities, σ_{350}. This was repeated for each individual Planck source. A large value of σ_{350} implies there is a large spread between the 350 μm flux density of the Herschel sources that comprise the Planck sources, or in other-words there are likely one or two individually bright sources which dominate the Planck flux density, and several fainter sources which are sub-dominant. On the other hand, a small value of σ_{350} implies that the 350 μm flux densities of all the sources are similar to each other, and the total Planck flux is the sum total of these equally contributing sources. We do not include Planck sources where there is only one detected Herschel source, and we find only 28 sources with only 2, 3 or 4 associated Herschel sources, so the vast majority have reasonable samples with which to calculate σ_{350}. We repeat this process for the Planck 545 GHz and Herschel-SPIRE 500 μm sources. At this stage, we make no reference to the particular type of object each Planck source is associated with.

In Figure 2.3 we show the results of this for both the 857 GHz sources and the 545 GHz sources. Additionally, we show the result when we calculate σ_{350} for 1,000 random positions in the NGP field. Both the 857 and 545 GHz sources clearly break up into two distant regions, which we label as diffuse and dominated. This contrasts strongly with the 1,000 random positions, which all appear to comprise sources with similar flux densities. The diffuse region contains Planck sources where the bulk of the Planck flux comes from multiple, roughly equal flux density sources, whilst the dominated sources tend to be dominated by a single bright Herschel source. A division by eye around $\sigma_{350} \sim 45\ mJy$ allows us to split our sources into diffuse and dominated sources.

Comparing these to our source identifications for the 857 GHz Planck sources, 155 are identified

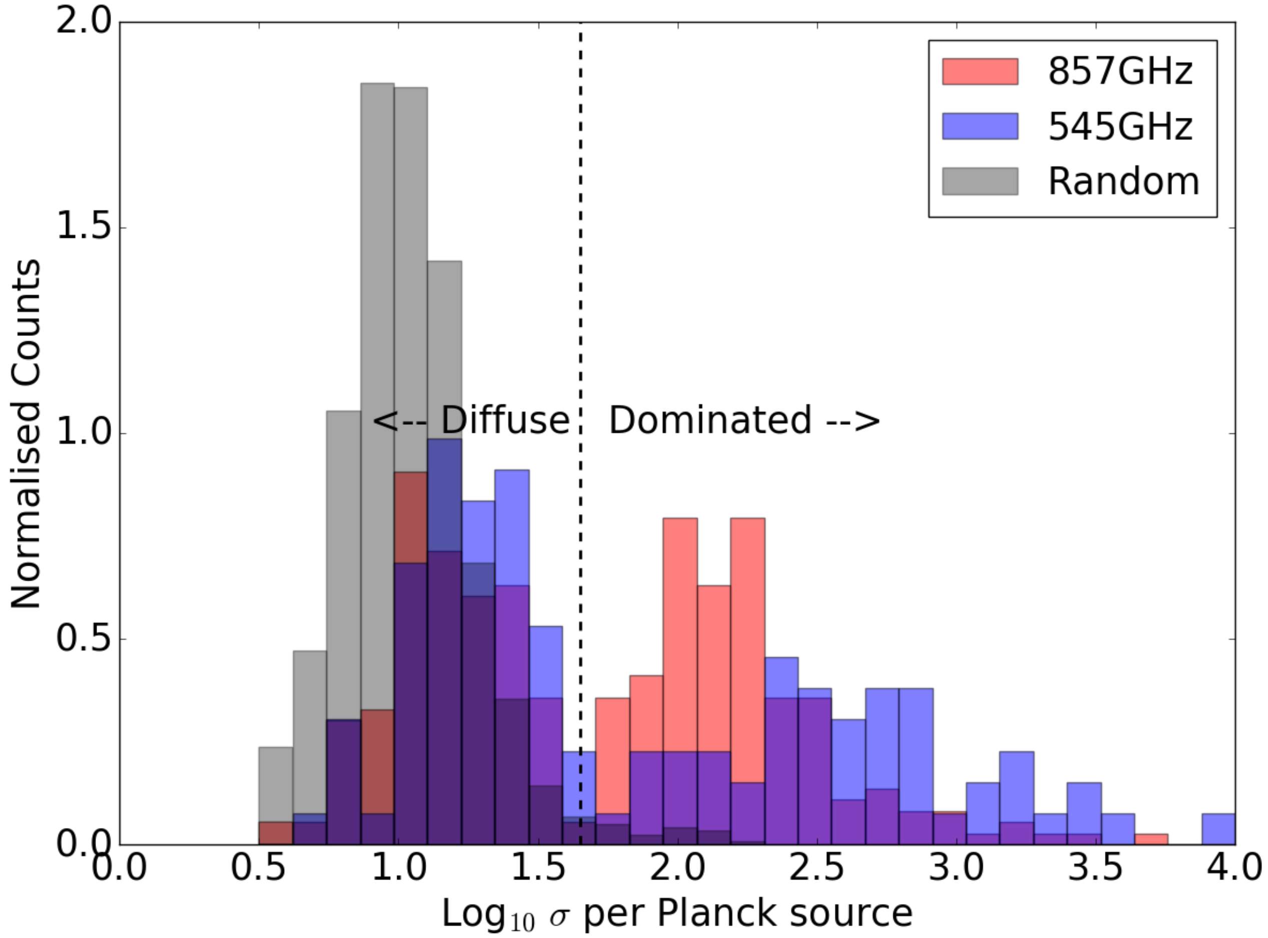

Figure 2.3: The $log_{10}(\sigma_{350})$ of all the Herschel sources associated with each Planck source. In red are those Planck sources identified at 857 GHz, in blue are those identified at 545 GHz, and in gray are those associated with 1,000 random positions. The black dashed vertical line indicates the apparent break between the bimodal distributions.

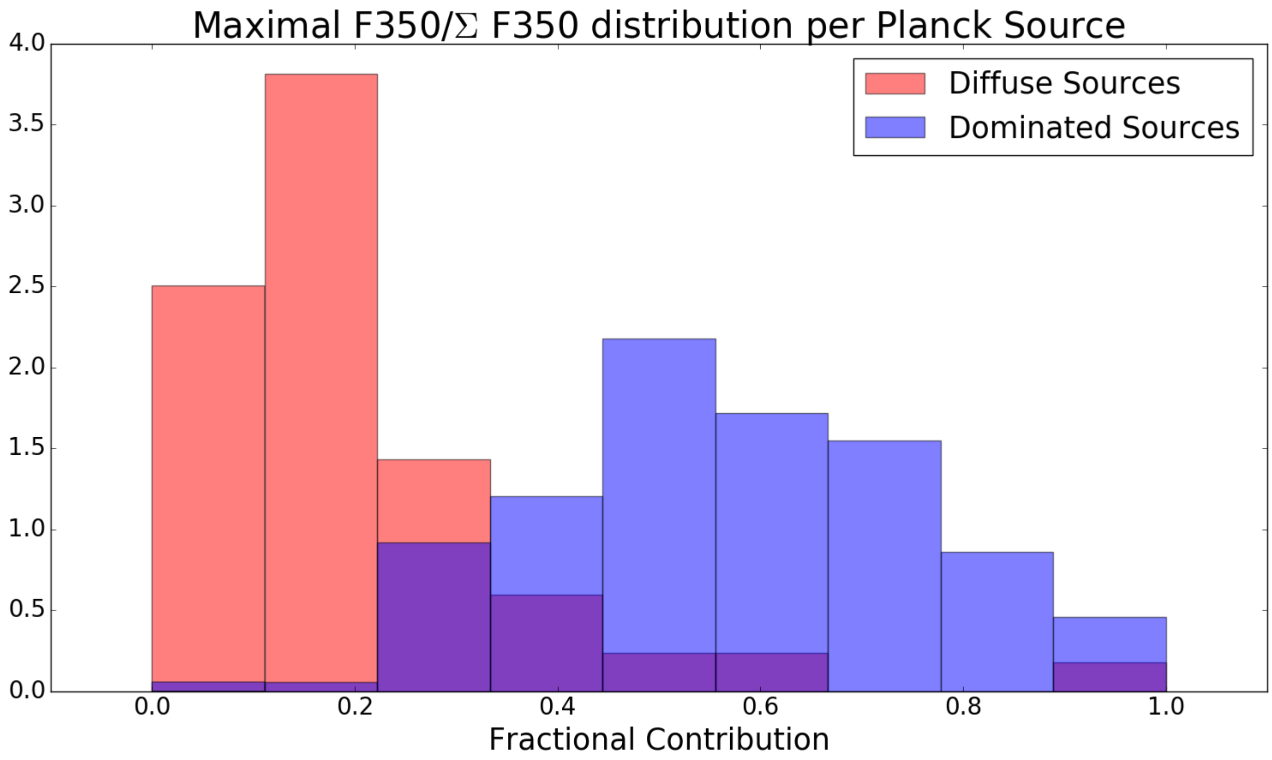

Figure 2.4: The fractional contribution of the brightest Herschel source to the sum of all the Herschel sources associated with each Planck source. In red are those source identified as diffuse, and in blue are those identified as being dominated by a single source.

as dominated and 144 as diffuse[5]. For the 545 GHz Planck sources, 44 are dominated and 55 are diffuse. Overall, there are 159 unique dominated sources and 186 unique diffuse sources. All the sources identified with Galactic cirrus, protocluster candidates and all but one of the not assigned sources are diffuse in nature, whilst the dominated sources are all identified with local galaxies, QSOs, lens candidates and stars. Of the 186 diffuse sources, 41 are associated with local galaxies, usually due to extended emission or where a source has several bright neighbours. Furthermore, four of the lensed sources are diffuse, though they lie near the border between diffuse and dominated.

Another way to examine how each Herschel source contributes to the Planck flux is to simply look at the fractional contribution each Herschel source makes to the sum of all the Herschel sources associated with a given Planck source (i.e. source A contributes 10% to the total flux density, source B 30%, and source C 60%). In Figure 2.4 we plot the fractional contribution

[5]This is slightly less than the 313 identified sources as some sources are off the map and some have only one associated Herschel source

Table 2.3: Source identification as a function of Planck catalogue

Source Type	ERCSC [%]	PCCS1[%]	PCCS2[%]
Local Galaxies	56.0	61.0	80.0
Galactic Cirrus	16.7	8.8	5.0
Cluster Candidates	9.5	4.6	1.1
No Assignment Given	11.9	16.1	5.6
Lenses	1.2	3.8	3.3
QSO	0.0	0.8	0.5
Stars	0.6	1.1	1.7

of the brightest Herschel source to each Planck 857 GHz source, and divide this into diffuse and dominated sources. Once again, we see a clear divide between the diffuse and dominated sources, affirming that the Planck flux density from the diffuse sources truly come from ~ 5 or more equally bright sources, whilst the dominated sources usually do dominate the source.

According to this analysis, roughly half of the Planck compact sources are actually extended on scales somewhat smaller than the Planck beam. This demonstrates that the assumption that the Planck compact sources are generally point-like is not necessarily valid. Given this assumption was used in the simulation which led to the selection of the detection and extraction methodology in the PCCS1 and PCCS2 (López-Caniego et al., 2006), and given our protocluster candidates are entirely diffuse sources, it is worth briefly examining how the detected fraction of each source type (i.e. local galaxies, protocluster candidates or Galactic cirrus) varies with the three released Planck catalogues.

2.3.4 Variations between the ERCSC, PCCS1 and PCCS2

In Table 2.3 we show the fractional make up each source type (i.e. local galaxies, protocluster candidates, Galactic cirrus) contributes to each catalogue. There is clearly a strong evolution between the ERCSC and PCCS2, especially with regard to local galaxies, Galactic cirrus and protocluster candidates. The 25% increase in local galaxies, and the $\sim 10\%$ decrease in both protocluster candidates and Galactic cirrus indicate a shift away from sources we have identified as diffuse in nature and towards those we have identified as dominated.

Partially, this shift can be explained in the different methodology used in the creation of all three catalogues; ERCSC first convolved the maps with a Gaussian, whilst the PCCS1 and PCCS2 convolved the map with a second order Mexican-hat wavelet. This latter design choice was to minimise contamination from Galactic cirrus. Furthermore, simulations on the reliability of the catalogues were all performed by injecting *point-sources* into fake maps, and attempting to recover them, with special care taken to specifically not inject multiple sources at roughly the same position (López-Caniego et al., 2006). To achieve the 80% reliability, simulations were run on these fake maps with only point-sources injected, so it is not surprising to see that in the PCCS2, we have 80% of sources being identified with the point like local galaxies. In this way, the PCCS2 is a catalogue with 80% of sources both real *and point-like*. However, it is clear that Planck is detecting other phenomena that are not point like; in the ERCSC, only 56% of sources are local galaxies, and though roughly 15% of sources are identified with Galactic cirrus, we find no evidence for cirrus contamination for a further 20% of sources. There is also strong evidence that these diffuse or extended structures are real (Herranz et al., 2013; Clements et al., 2014, 2016; Planck Collaboration et al., 2016). The inclusion of the Mexican-hat wavelet for detection, and reliability tests only using point sources clearly biases the catalogues away from these kinds of sources. Given the exposure time in the PCCS2 is roughly $3\times$ that of the ERCSC, with a corresponding depth $\sim\sqrt{3}$ better, it would be of great interest to reduce the final Planck maps using the same methodology as the ERCSC, examine these maps again in the same Herschel fields, and determine any differences between that and the PCCS1 and PCCS2.

2.4 Photometry

Several Planck works have verified that the photometry between Planck and Herschel-SPIRE is consistent (Herranz et al., 2013; Bertincourt et al., 2016). These are typically performed by integrating the flux density over a Planck beam at a given position on the Herschel maps and comparing the measured flux density to that of Planck. Here however we specifically have a catalogue of detected Herschel sources, and it is uncertain whether these detected sources alone are enough to account for the Planck flux, or if there is a significant contribution from background/faint sources. Furthermore, here we have identified the nature of the Planck sources, and so can differentiate between the photometry from, for instance, local galaxies and proto-cluster candidates. Therefore, in this section we first set out to reaffirm that integrating over a Planck beam on the Herschel maps successfully reproduces the measured Planck flux density, and then later assess whether the bright detected Herschel sources alone can account for the Planck flux density.

2.4.1 Are the Planck and Herschel Photometry Consistent?

The Planck 857 GHz band and SPIRE 350 μm band are well matched, both in central frequency and passband, and can be directly compared with few assumptions. The Planck 545 GHz and SPIRE 500 μm bands however differ slightly in their central wavelength and passbands. We therefore restrict ourselves to comparing the 857 GHz and 350 μm bands here. Our procedure generally follows that set out in Appendix 1 of Aghanim et al. (2015) for estimating the aperture photometry of a Planck source, except here we use the Herschel maps instead of the Planck maps. We took the background subtracted and matched-filtered maps of all of the Herschel fields and integrated the SPIRE 350 μm flux density over a Planck 857 GHz beam of 4.63 arcmin. All pixels on the Herschel 350 μm map that fell within this radius of the nominal Planck position were summed to give a flux density estimate. Once again, as estimates of the Planck beam vary between catalogues, we varied the radius between 4.0 and 5.0 arcmin, and found consistent results. We further repeated our photometry estimates using a Gaussian with a FWHM of 4.63 arcmin instead of assuming a circular beam, but found minimal difference to our original results. A background annulus of inner radii 1 $\times$ FWHM and outer radii 2 $\times$ FWHM was used to estimate the median background flux, and this was removed from the aperture flux estimate. Any sources that contained null pixels in either the primary or background aperture had aperture flux densities assigned to them of 0.0 to prevent edge effects. Errors were estimated from a combination of SPIRE instrumental noise from the Herschel map, a SPIRE calibration error of 5.5% [6] and a constant confusion noise estimate of 7 mJy per SPIRE

[6]The SPIRE handbook, `http://herschel.esac.esa.int/Docs/SPIRE/html/spire_om.html`, version 2.5, March 24, 2014

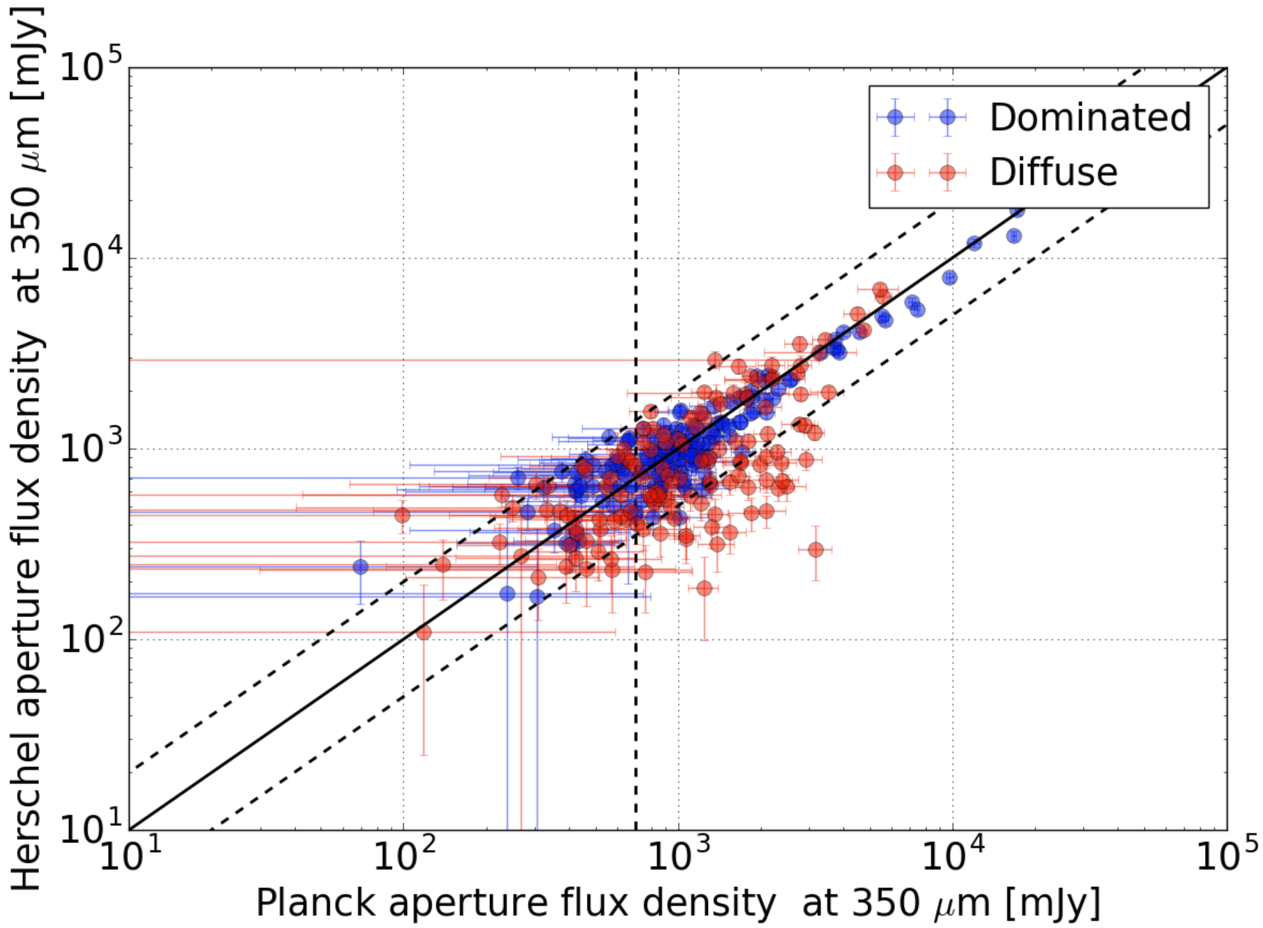

Figure 2.5: Comparison between the *Planck* aperture flux density and the *Herschel* aperture flux density, as calculated in the text. The red points are the those sources considered to be diffuse, and the blue those considered dominated by a single source. The solid black line shows the 1:1 ratio. The diagonal dashed lines show the limits where the *Herschel* flux is half/double that of the *Planck* flux, and the vertical dashed line shows the PCCS 90% completeness limit.

beam(Valiante et al., 2016), all added in quadrature.

Our results are plotted in Figure 2.5. Overall, there appears to be good agreement between Planck and Herschel aperture photometry. Following Herranz et al. (2013), we calculate the absolute relative flux density difference between Herschel and Planck for each of our sources,

$$\eta = 100 \times \left| \frac{S_{SPIRE} - S_{Planck}}{S_{SPIRE}} \right|, \tag{2.2}$$

where η gives the absolute relative flux density difference for a single source, S_{SPIRE} is the Herschel aperture flux density and S_{Planck} is the Planck aperture flux density. We then take the weighted average of these values, and find an absolute relative flux density difference between Planck and Herschel of only 4.9%, comparable to the 1 - 5% uncertainty found in Bertincourt et al. (2016).

However, a number of diffuse sources appear to have Herschel aperture flux densities less than half that of Planck. Indeed, calculating the absolute relative flux density difference for the diffuse and dominated sources separately, we find a difference of only 1.8% for the dominated sources, but a difference of 11.4% for the diffuse sources.

For consistency, we have been using the background subtracted maps from H-ATLAS, HerMES and HeRS, as the background subtracted maps are available for all three surveys. H-ATLAS further provide raw maps, which have had no background subtraction applied to them, and could contain the missing flux for the diffuse sources. Repeating our analysis for the H-ATLAS raw maps and fields only, we find absolute relative flux density differences of only 4.8% and 3.8% for the dominated and diffuse sources respectively, demonstrating that this missing flux is likely being removed during the background removal process, and that for this subset of sources, this diffuse background can significantly contribute to the total flux density.

2.4.2 Are the Detected Herschel Sources Enough to Match the Planck Flux Density?

Given that around 40% of all Planck sources appear to be diffuse in nature, and consist of discrete sources with comparable flux densities, we here consider whether we can match the Planck photometry by summing over the detected Herschel sources. To do this, we simply add up the fluxes of any detected Herschel sources with a flux density $> 25.4\ mJy$. Once again, we use only the 857 GHz and 350 μm bands. If the measured flux in Planck and Herschel are similar, it implies that we are capturing most of the flux from these sources, and that the detected sources are by far the dominant components of the source. On the other-hand, if there is a significant flux difference between the Herschel and Planck measurements, it implies that there are large numbers of faint sources which are going undetected, but which significantly contribute to the flux density.

In Figure 2.6, we plot our results, separating our sources into their respective classifications. Two things are immediately apparent. First, for most sources there continues to be a good match between Planck and Herschel, implying that the detected sources are responsible for the bulk of the Planck flux. Second, the Galactic cirrus and protocluster candidates, whilst both diffuse in nature, occupy different regions of the plot, with protocluster candidates generally able to reproduce the Planck flux densities using only detected sources and cirrus unable to do so. This suggests that estimates of the physical properties of these protocluster candidates can be derived reasonably from the Planck flux alone, as it generally represents the summed total of all the individual Herschel sources responsible for the emission. Specifically, for sources not associated with Galactic cirrus and using equation 2.1, we find a relative absolute flux density difference of 5%, whereas for sources associated with Galactic cirrus this value is 76%.

The protocluster candidates all lie near the detection limits of the Planck catalogues, with a median Planck aperture 857 GHz flux density of 886 mJy. Only eight of the 21 protocluster candidates detected at 857 GHz have flux densities > 1 Jy. For the sources where we did not assign an identification, only 14 of 63 have Planck 857 GHz flux densities > 1 Jy, and often the Herschel and Planck fluxes for these bright unassigned sources are in disagreement, with Herschel aperture flux densities > 1 Jy only found for two of the unassigned sources, and none of the unassigned sources have > 1 Jy measured flux densities when summing up the Herschel sources . Given that we see few protocluster sources with 857 GHz flux densities > 1 Jy, we are likely only sampling the bright-end tail of the protocluster flux density distribution. Therefore, protoclusters detected in Planck as point-like objects, which host $> 3\sigma$ overdensities of Herschel sources and which have integrated fluxes at 350 $\mu m > 1$ Jy are rare. To put this another way, there are likely few protoclusters with numerous DSFG distributed over a 4.63 arcminute diameter circular region that are brighter than 1 Jy at 350 μm.

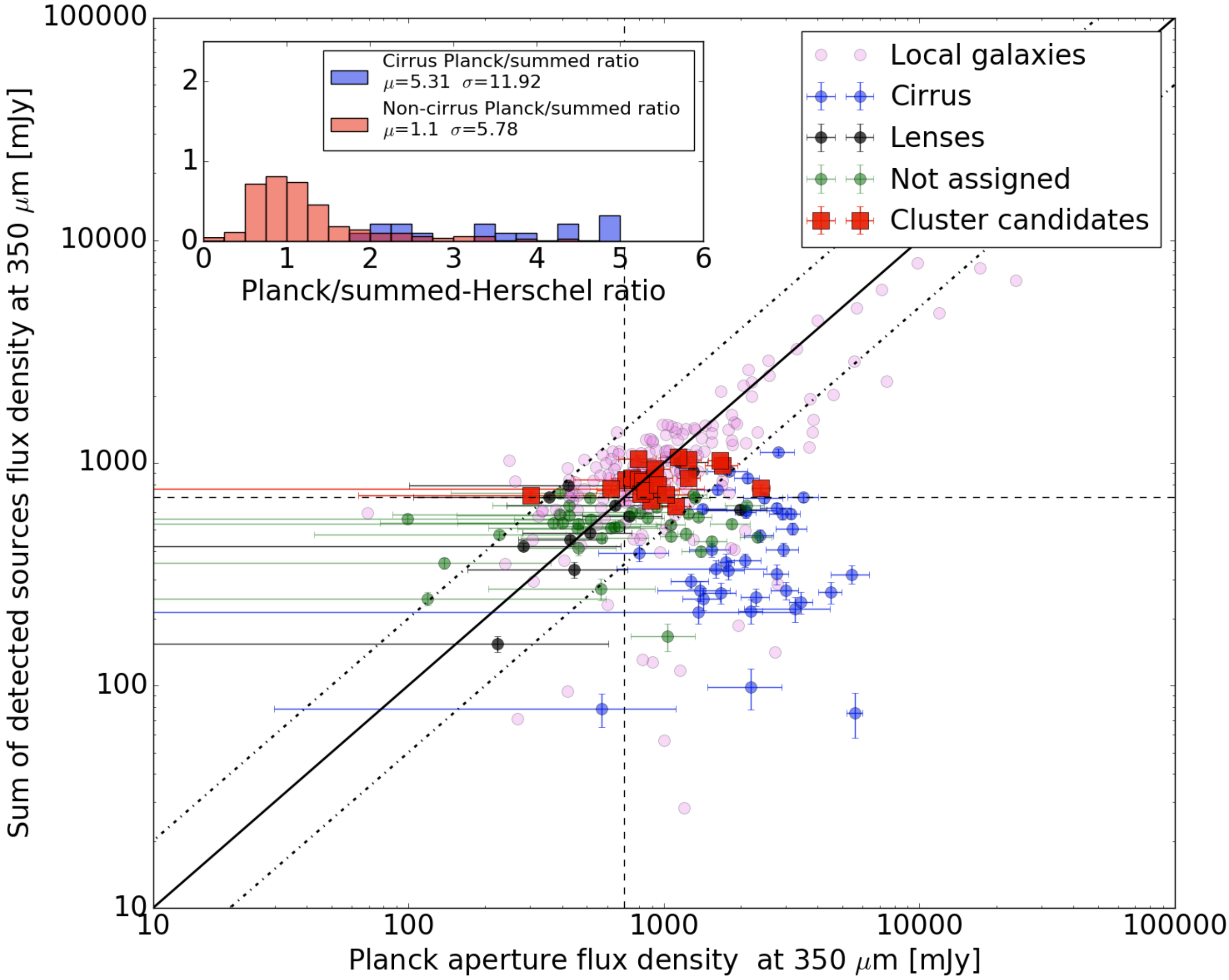

Figure 2.6: Comparison between the *Planck* aperture flux density and summing up the 350 μm flux density from the detected *Herschel* sources. The light pink points are local galaxies, the blue are cirrus, the red are proto-cluster candidates, the black are lens candidates and the green are those points not assigned an identification. The solid black line shows the 1:1 ratio, whereas the dot-dashed lines show where the *Planck* aperture flux is double or half the summed detected sources. The vertical and horizontal dashed lines show the nominal *Planck* 90% completeness levels from the PCCS1. Error-bars are not shown for the local galaxies to aid in clarity, but are comparable to other sources at all fluxes. The histogram in the top left corner shows the *Herschel Planck* ratio, with cirrus sources indicated in blue, and non-cirrus sources indicated in red, as well as the mean and standard deviation. The histogram has been truncated to a maximum ratio of 6 for clarity, with 19 cirrus sources with ratios beyond this.

2.5 Colours

The sub-mm colours of Herschel sources have often been used as a useful proxy for their redshift (Clements et al., 2014; Dowell et al., 2014; Dannerbauer et al., 2014; Asboth et al., 2016; Rowan-Robinson et al., 2016; Ivison et al., 2016). At the same time, the photometric redshifts from sub-mm colours often have large intrinsic uncertainties; even in the simplistic case that the dust emission can be perfectly described by a blackbody, combining Wien's displacement law and the 20 - 60K approximate range of DSFG dust temperatures (Sanders and Mirabel, 1996) suggests an observed wavelength peak between 86 and 258 μm for the blackbody. If a DSFG of unknown redshift is observed to have a dust SED which peaks around 350 μm, the inferred redshift through photometric fitting can vary between $z_{phot} = 0.36$ and $z_{phot} = 3.07$, assuming the rest frame peak in dust emission lies between 86 and 258 μm. Bearing these uncertainties in mind, in this section we look at both the Planck and Herschel colours of our sources, in particular the protocluster candidates, and compare our assessments to those of the PHZ, which used a colour cut to select candidate high-z sources as opposed to the overdensity method used here.

2.5.1 Planck Colours

The 857 GHz sub-catalogues of the Planck compact source catalogues provide aperture photometry measurements at 857 GHz, as well as at 545 GHz, 353 GHz and 217 GHz, all at the position of the 857 GHz detected source. As the 545 GHz sub-catalogues do not do this, throughout this section we only use the 857 GHz sources to investigate the Planck colours of our sources. Given we are uncertain about the redshift of these sources, we do not make attempts to constrain their dust temperature. We do however note that by requiring a detection at 857 GHz (350 μm), sources which are faint at 350 μm but which are bright and detected at 545 GHz (550 μm) could therefore be missed by such a selection.

In Figure 2.7 we plot the Planck 857/545 GHz (350/550 μm) and 545/353 GHz (550/850 μm) colours for the four major populations we identified in Section 2.3.2, local galaxies, protocluster

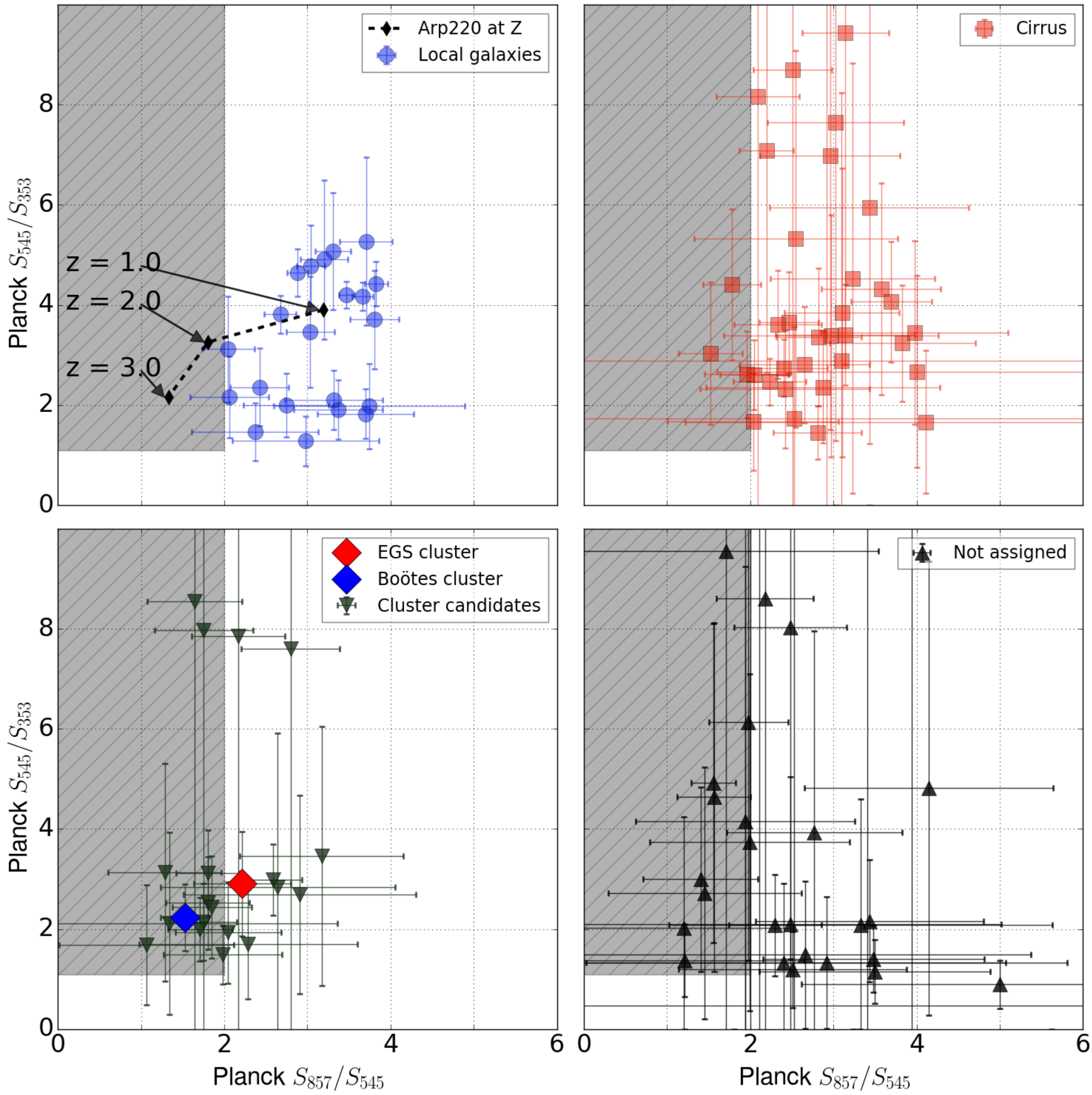

Figure 2.7: Planck 857/545 GHz and 545/353 GHz colours for the categories of source we identify as local galaxies (top left), cirrus sources (top right), cluster candidates (bottom left) and unassigned sources (bottom right) . The grey shaded region represents the selection criteria used in Planck Collaboration et al. (2016) for their selection of high redshift source candidates. The black line in the top left plot shows the Planck colours of Arp 220 as it would appear at z=1,2 and 3, and the blue and red diamonds in the proto-cluster candidates plot show, respectively, the Bootes and EGS proto-cluster candidates identified in Clements et al. (2014).

candidates, Galactic cirrus and sources we did not assign an identification. The PHZ team, in their selection of likely high-z candidates, searched directly on the maps and required Planck colours of 857/545 $GHz < 2$ and 545/353 $GHz > 1$ to search for high-z DSFGs and clusters of DSFGs. The 857/545 $GHz < 2$ requirement selects "red" sources which are likely to be very cold or at high-z, whilst the 545/353 GHz criterion ensures that the sample is unlikely to be contaminated by QSOs. Their selection criteria are marked on Figure 2.7 as the grey hashed region. Furthermore, to ensure clarity of the plot, we only plot the local galaxies which are detected to a 3σ level in all three of the 857, 545 and 353 GHz Planck bands. We additionally highlight two of the protocluster candidates detected by Clements et al. 2014, who used the same method of cluster identification as we do here, and their sources are in fact also detected by us.

Of the 21 candidate protoclusters that appear in the 857 GHz sub-catalogue, only twelve lie in the PHZ selection region, with an overall mean S_{857}/S_{545} ratio of 2.0 ± 0.5. Contrasting the protocluster candidates to other source types, the local galaxies and Galactic cirrus have mean 857/545 GHz ratios of 3.0 ± 1.0 and 2.8 ± 0.7 respectively, whilst the unassigned sources have a mean ratio of 2.5 ± 1.0. Of these unassigned sources, nine would be selected by the PHZ as potentially high redshift. The lens candidates have a mean 857/545 GHz ratio of 1.8 ± 0.5, the stars a mean ratio of 3.0 ± 0.4, and the single QSO, at a redshift of 2.099, has a 857/545 GHz ratio of 0.8 ± 0.4. It is interesting to note that in general, the larger 857/545 GHz ratios correspond to local phenomena (stars, local galaxies, Galactic cirrus), whilst the lower ratios correspond to likely more distant objects (protocluster candidates, QSOs, lens candidates). The unassigned sources sit in between these two regimes, but the inclusion of several of them as having very red colours is potentially indicative of the location of yet more protocluster candidates, but with individual Herschel sources with either fluxes below that of the cut-off chosen here, extensions beyond the 4.63 arcmin Planck beam, or a combination of the two. Furthermore, nine of our protocluster candidates have colours that would not be chosen by the PHZ team as high-z, indicating our selection might include populations of lower-redshift / warmer protoclusters than those in the PHZ.

However, there are alternative explanations to the warmer / lower-z protocluster candidates. As the Planck beam is so large in comparison to the typical source size, its Planck colours are likely to be a combination of both the intrinsic colour of the source plus an additional component coming from other background / foreground sources. In the case of the warm protocluster candidates, it is possible that a significant foreground contamination from sources unassociated with the protocluster candidate is boosting the 857/545 GHz ratio outside of the PHZ selection criteria. Given that both observationaly (Flores-Cacho et al., 2016), and theoretically (Negrello et al., 2017), these overdensities have been claimed to be purely line of sight effects, we set out to investigate how foreground and background sources affect the apparent colour of a protocluster. We created a simple simulation where we simulate a number of sources that are at the same redshift, indicating a cluster, and a number of foreground / background sources that were not members of this cluster. On average, we have chosen our simulated protoclusters to have 11 members which would be selected by our flux cut-off at 350 μm of $S_{350} > 25.4$ mJy. The foreground / background sources on the other hand, have on average 9 sources which would be selected by our cutoff. The total number of detected sources would then be, on average, equal to 20, which is just high enough to be selected as a candidate protocluster for our sample. FIR SEDs were drawn from a single temperature modified blackbody function

$$S_\nu \propto \nu^\beta B_\nu(T), \tag{2.3}$$

where S_ν is the flux density at frequency ν, and ν^β models the emissivity function of the dust and $B_\nu(T)$ is the Planck function at temperature T. The SEDs of each source were then normalised to a 350 μm flux density, which is drawn from an exponential distribution that roughly matches the distribution of fluxes we see in our catalogues of 350 μm detected Herschel sources. The temperature T was fixed at 29K and β was fixed at 2, so that the background sources have an average S_{850}/S_{545} flux density ratio that matches those seen in the Herschel maps. Four separate protoclusters, at redshifts of 1, 2, 3 and 4, were simulated 100 times, using the method detailed above, for a total of 400 protocluster simulations. Foreground sources were randomly distributed between z = 1 and 3, similar to the distribution of Herschel sources selected at 350 μm (Casey et al., 2014). We determine the total colour of the foreground + protocluster by summing the total 857 GHz flux density of all the individual sources and dividing by the

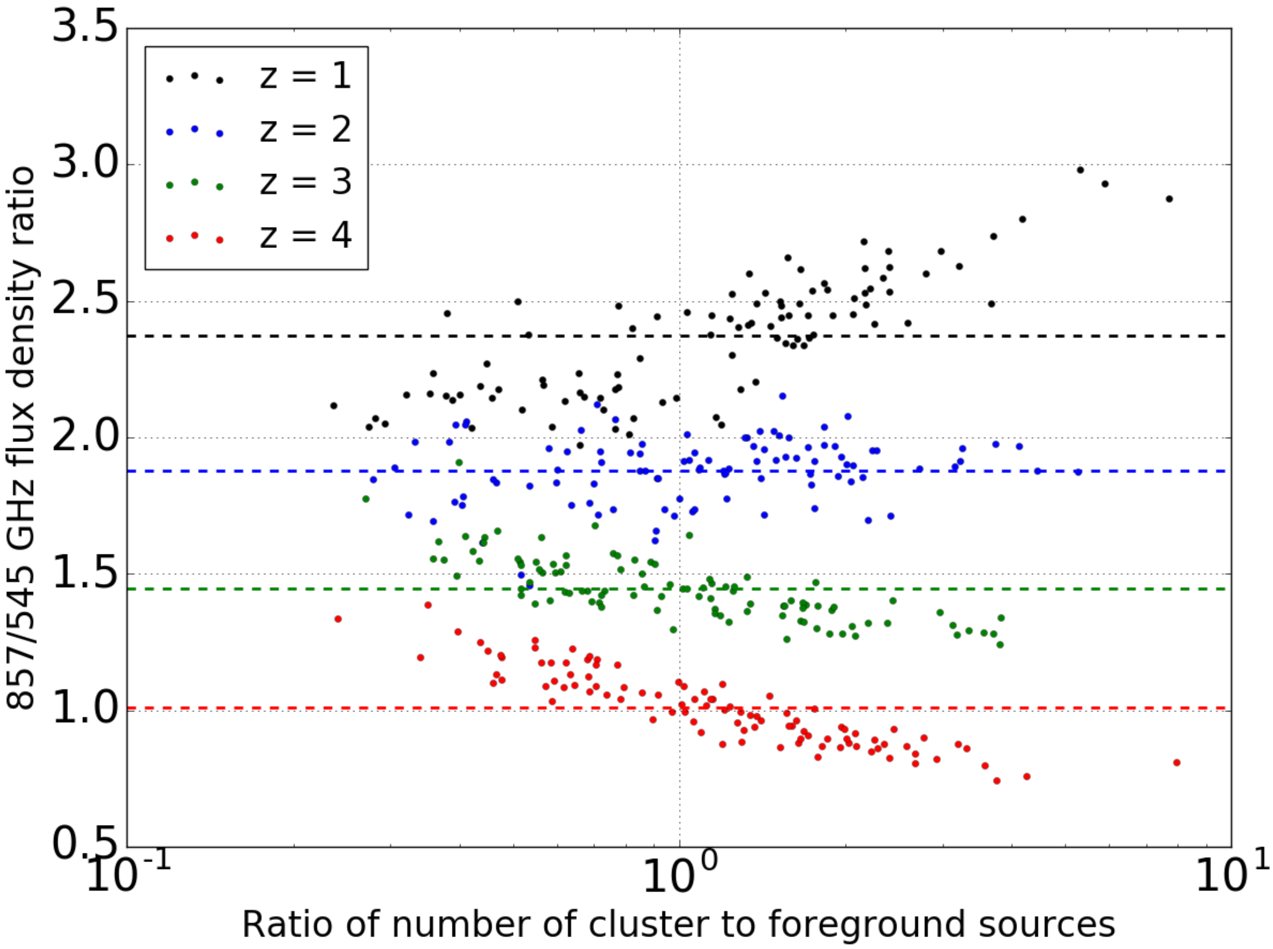

Figure 2.8: Estimated Planck 857/545 GHz flux density ratio of 400 proto-clusters, as a ratio of the number of proto-cluster to background/foreground sources. Points in black are proto-clusters at a redshift of one, in blue at a redshift of two, in green at a redshift of three and in red at a redshift of four. The dashed lines show the average colour of the 100 proto-clusters at each redshift. Large symbols show proto-clusters which would be selected by our 3σ overdensity requirement, with small labels showing proto-clusters that would not be.

total 545 GHz flux density. The results of this process are shown in Figure 2.8, with the four different colours indicating the four different redshift bins we used for the protoclusters.

As expected, if the foreground sources dominate over the protocluster sources, the colours tend to the average colours of the foreground sources, in this case $S_{857}/S_{545} = 1.87$. Only once there are roughly equal numbers of protocluster and foreground sources does the protocluster start to dominate the source, and we find that at this point the colour is mostly determined by the redshift of the protocluster. At redshifts 1 and 2, where we generally expect our protoclusters to lie, the protocluster is in effect indistinguishable from the foreground sources, with the redshift one cluster in fact increasing the S_{857}/S_{545} flux density ratio and the redshift two cluster having a mean S_{857}/S_{545} flux density ratio similar to the foreground sources. Even for higher redshift protoclusters at $z > 3$, we would still require the sources that are physically associated with the protocluster to dominate over the foreground source in order to make a colour selection.

This simulation is over-simplified, but illustrates that lower redshift clusters can feasibly have higher S_{857}/S_{545} flux density ratios than those selected by the PHZ. We further note that our results are highly sensitive to our assumption that the temperature is fixed; If we allow the temperature of our galaxies to vary even by ±5K, the standard deviation on the S_{857}/S_{545} flux density ratio for a protocluster can double from 0.1 to 0.2 for a protocluster at $z = 2$. These uncertainties make any photometric attempt to select protoclusters difficult at best, and highlight the importance of follow up work to accurately characterise the nature of any candidate protocluster.

2.5.2 Herschel Colours

Despite often being used (Herranz et al., 2013; Noble et al., 2013; Clements et al., 2014; Ivison et al., 2016; Negrello et al., 2017), the precise interpretation of Herschel-SPIRE colour-colour diagrams remains uncertain. Typically, sources whose SEDs peaks at longer wavelengths tend to lie at higher redshifts (Casey et al., 2014; Dowell et al., 2014; Asboth et al., 2016; Ivison et al., 2016), and therefore sources whose SED peak at 250, 350 and 500 μm likely indicate progressively higher redshifts. However, intrinsic variation in DSFG SEDs and the assumptions about the dust properties and temperature of a source can all act to boost sources into and out of these peak regions, so caution should be used.

In Figure 2.9 we simulate the Herschel colours, once again drawing samples from a single modified blackbody with the same parameters as above, but this time varying the temperature values between 20 and 60K, and the β values between 1 and 2.5, both of which are typical ranges used and found in similar studies (see Bianchi 2013; Casey et al. 2014 and references therein). We further fix the redshifts at 0, 2 and 4, to investigate the role redshift plays, and choose these values as they are the values, all other things being equal, where we typically would expect the flux density of a DSFG to peak progressively in the three SPIRE bands. The

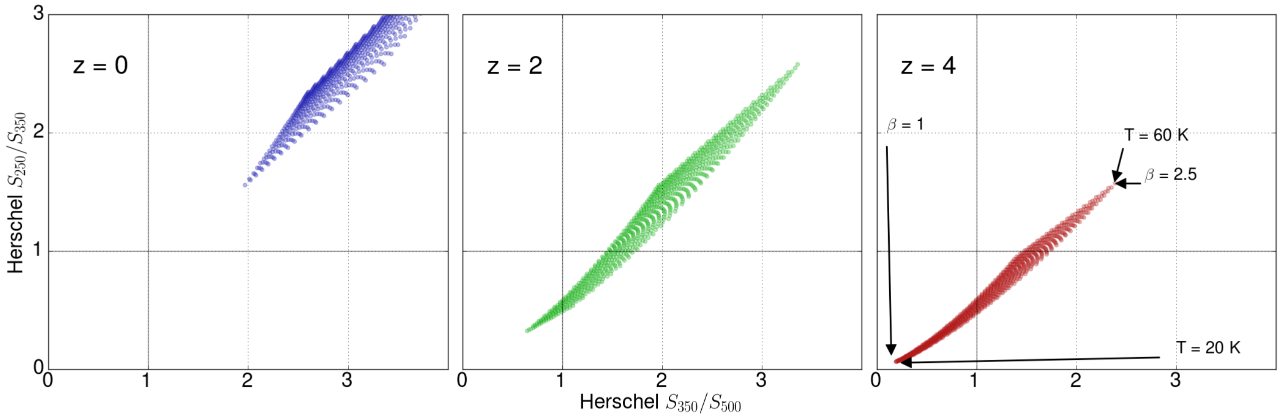

Figure 2.9: Simulated Herschel-SPIRE colours for sources with varying temperature, β values and redshift. The left plot shows sources at $z = 1$, the middle for sources at $z = 2$ and the right hand plot for sources at $z = 4$, which correspond roughly to the redshifts where the flux density of sources would peak in the three SPIRE bands at 250, 350 and 500 μm. Temperature and β values vary, with the general trend of low T and β occurring at the bottom left point, and high T and β in the top right.

three plots generally show that, under the reasonable assumption in parameter variation, the SPIRE colours of a source can act as a proxy to the redshift of the source, but that also large variation is possible even at fixed redshift.

In Figure 2.10 we plot the observed Herschel-SPIRE colours for all the Herschel sources associated with each of our Planck sources, highlighting the Herschel sources associated with local galaxies and protocluster candidates. Any local galaxy extended on arcminute scales, or where extraction on the Herschel map has clearly divided the single local galaxy into multiple Herschel sources were removed. We found mean S_{250}/S_{350} μm and S_{350}/S_{500} μm flux density ratios of 2.05 ± 0.43 and 2.60 ± 0.74 for the local galaxies, wheras for the protocluster candidates these values are 1.13 ± 0.47 and 1.57 ± 0.49.

Figure 2.10 neatly divides into roughly two sections, one associated with low redshift sources such as the local galaxies, and one at higher redshifts, and primarily associated with the protocluster candidates. Directly comparing these regions to the Arp 220 colour track suggests that the protocluster candidates all lie around redshift $z = 2 - 3$, well beyond what is typically possible to select with traditional cluster selection methods. However, as has been discussed, estimating the precise redshift of sources from their Herschel colours alone can be difficult, and with the large uncertainties given here, alongside the variation seen in Figure 2.9, we can

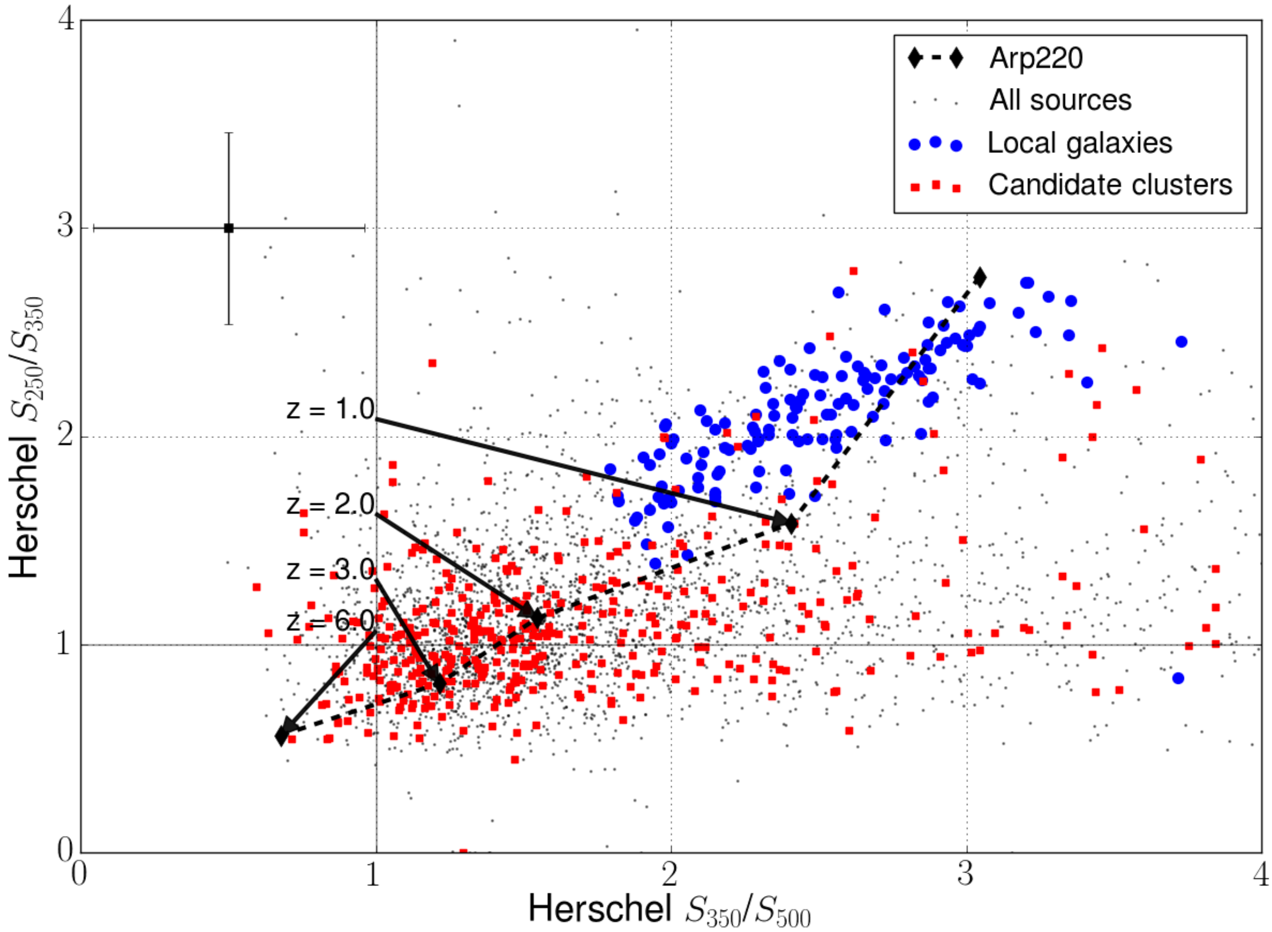

Figure 2.10: The Herschel-SPIRE colours of all the Herschel sources associated with a Planck compact source. In black are plotted all the Herschel sources, the local galaxies are plotted in blue, and the Herschel sources associated with candidates protoclusters are plotted in red. The dashed line marks the colours of ARP 220, as it would be seen at $z = 0, 1, 2, 3$ and 6. Typical error bars are given by the black point in the top left.

reasonably say these protocluster candidates are likely to be at $z > 1$, but little more until future follow up work can constrain these sources further.

2.6 The Candidate Protoclusters

Of the 354 unique Planck compact sources that lie in one of the Herschel fields under consideration here, 27 appear to be $> 3\sigma$ overdensities of Herschel sources, whose Planck flux comes from a number of discrete individual Herschel sources, the colours of which indicate they generally all lie at $z > 1$. It remains unclear whether these are chance line of sight effects, physical clusters of Herschel sources, or multiple weak clusters, aligned along the line of sight. In this section, we attempt to quantify these protocluster candidates further, and examine the likelyhood that these are physical clusters, and if we further assume that they are, whether their properties match up with what others have found in the literature both through simulations and observations.

2.6.1 Line of Sight Effects

Under the assumption that the overdensities of Herschel sources are simply line of sight effects, we should be able to describe the global distribution of Herschel sources using Poisson statistics, with these overdensities sitting in the tail of the distribution. We use the distribution of sources calculated from 10,000 random positions, as shown in Figure 2.2, and under the assumption that the cluster sources are rare (See Section 2.7).

Given we here examine roughly 800 deg^2 of sky, and given our flux density limits and assuming our sources are distributed in a Poisson manner, we may expect to find around 89 patches where there are 26 or more 250 μm sources, 33 regions where there are 10.2 or more 350 μm sources, and 1.3 regions where there are 11 or more 500 μm sources purely from statistical variation. If all our protoclusters were only this over-dense, this might explain our results, however, many of our protoclusters host far stronger overdensities, with 14 of our 27 protocluster candidates containing either ≥ 36 sources detected at 250 μm, ≥ 23 sources detected at 350 μm, or ≥ 12 sources detected at 500 μm respectively. Over the area we searched, we would only expect to see only 0.5, 1.5 and 0.3 patches this dense in each band. We in fact see 4 patches at least this over-dense in the 250 μm band, 8 at least this over-dense in the 350 μm band, and 10 at least this over-dense in the 500 μm band. Our most overdense protocluster candidates host 43, 32 and 17 sources for the three bands respectively. This variation cannot be explained solely by the large area surveyed in this paper. Given that we previously demonstrated that the source distribution can be well modelled as a Poisson distribution, we can reasonably rule out that a purely line of sight effect explains the overdensities we are observing, and that it is more likely that these overdensities represent either physical clusters or multiple clusters along the line of sight.

At the same time, even if the protocluster candidates are physical clusters, we would expect some level of contamination from foreground and background sources unassociated with the cluster itself. Given that these foreground and background sources can be well described by a Poisson distribution (see Figure 2.2), the total number of sources we detect will be a combination of both field and cluster sources,

$$M = N_{field} + N_{cluster} \tag{2.4}$$

where M is the total number of sources, N_{field} is the total number of field, or foreground / background, sources, and $N_{cluster}$ is the total number of sources physically associated with the cluster itself. Our field galaxies can be roughly described as Poisson distributed, so the probability of observing N_{field} galaxies is

$$P(N_{field}|\mu) = \frac{\mu^{N_{field}}}{N_{field}!} exp(-\mu), \tag{2.5}$$

where μ is the expected number of Herschel sources per Planck beam, and depends on the chosen SPIRE band. However, the number of field galaxies is simply the total number of observed galaxies minus the galaxies associated with the cluster, so

$$P(N_{field}|\mu, M) \propto \frac{\mu^{M-N_{cluster}}}{(M-N_{cluster})!} exp(-\mu). \tag{2.6}$$

Renormalising this, as the total possible number of field galaxies is now M, not ∞, by summing over and dividing by all possibilities gives

$$P(N_{field}|\mu, M) = \frac{\left[\frac{\mu^{M-N_{cluster}}}{(M-N_{cluster})!}\right]}{\Sigma_{i=0}^{M}\left[\frac{\mu^{i}}{i!}\right]}. \tag{2.7}$$

For instance, for our mean of 20.6 350 μm Herschel sources associated with each cluster, this suggests that 50% of the time, 11 or more of the Herschel sources would be likely to be associated with the protocluster, with only a 0.7% chance of having 3 or fewer protocluster members.

Overall, from a statistical perspective it is difficult to understand these sources if they are merely line of sight effects. We therefore find it more likely that these are physical clusters of DSFGs or multiple clusters along the line of sight, but without further information it is difficult to distinguish between these two possibilities.

2.6.2 Properties of the Protocluster Candidates

Throughout this section, we assume all 27 of the candidate protocluster candidates are physical associations of sources, rather than chance line of sight effects or multiple clusters along the line of sight.

Surface Density

For protoclusters detected by either the ERCSC, PCCS1 or PCCS2, we find a surface density of protocluster candidates of $(3.3 \pm 0.7) \times 10^{-2}$ sources deg^{-2}, with flux density limits of roughly 700 mJy, roughly equal to the Planck point source flux density limits. This surface density is in reasonably good agreement with Clements et al. 2014, who find a surface density of

$(4.4 \pm 2.2) \times 10^{-2}$ sources deg^{-2}. The PHZ (Planck Collaboration et al., 2016) searching directly on the Planck maps, discover 2,151 candidate high-z sources across approximately 10,000 deg^2 of the cleanest section of the sky. Initial follow up suggests around 94% of these are overdensities of Herschel sources, and like our candidates, may be physical clusters of DSFGs (Planck Collaboration et al., 2015d). Given the differences in our approaches, it is difficult to make a direct comparison between Planck Collaboration et al. 2016 and our work here, but their detection of around 2,000 sources corresponds to a rough surface density of 0.18 ± 0.01 sources deg^{-2}, 5 times larger than the surface density we found here. Attempting to address this discrepancy, if we include the sources we did not assign a classification, some of which lie in the PHZ selection region (see Figure 2.7), our estimated surface density rises to 0.11 ± 0.02 sources deg^{-2}, closer to but still lower than the surface density estimated by the PHZ. Though it is possible that this discrepancy represents some sort of physical difference between the cluster candidates selected here and by the PHZ, it is more likely that observational differences are the source of the disagreement. There are several areas of discrepancy: our work here relies on the Planck catalogues of compact sources whereas the PHZ works with the maps directly, the selection used by the PHZ is sensitive to a larger range of scales whilst our work requires clusters compact on the scale of the Planck beam, and the PHZ cannot be fully confident that all of their sources are on-sky overdensities of Herschel sources whilst we can be with our work. Indeed, further to this last point, of the four cross-matches between our catalogue and the PHZ, three sources are not assigned any classification and one is a single bright gravitational lens (Geach et al., 2015; Harrington et al., 2016). Only the gravitational lens is detected at 857 GHz, whilst all four are detected at 545 GHz, and so only the aperture fluxes for the gravitational lens is available at 545 and 353 GHz. Even so, this source is red enough in the compact source catalogues to be classed as a red candidate for the PHZ (See Figure 2.7). Additionally, Negrello et al. (2017) also find the surface density reported by the PHZ of protoclusters to be significantly higher than expected from dark matter halo assembly. They attribute this higher surface density to detecting multiple protoclusters along the line of sight, but both the PHZ and our work here should be sensitive to this effect. Therefore, the tension between the protocluster surface densities found between the PHZ and this work remains.

Field-to-Field Variation

Using our inferred surface density of protocluster candidates, the number of protocluster candidates we detect in each of our 17 fields is in mostly good agreement. We detect ten out of an expected eleven in the SGP, seven out of six for the NGP, and roughly one in each of the smaller HerMES fields. No protocluster candidate is detected in either HERS, where we expected four, or any of the three GAMA fields, where we expect to detect five overall. We ascribe this to the large amount of Galactic cirrus present in these fields. This is especially prevalent in GAMA09 and HeRS, where we identify 18 of the 26 and 17 of the 38 detected sources with Galactic Cirrus in each field respectively. These two fields alone account for 81% of all the sources we classify as Galactic cirrus, and highlight the difficulty of extending this kind of Planck-selected protocluster analysis outside of the sections of the sky cleanest of Galactic cirrus. However, GAMA12 and GAMA15 are reasonably free of Galactic cirrus, yet we do not see any protocluster candidates despite expecting 3.3. The number counts are low, so it may just be a statitisical fluctuation, but we do note we do detect the well studied galaxy protocluster containing the lensed source H12-00 (Herranz et al., 2013; Clements et al., 2016) in GAMA12, but identify it only as a lensed source.

Flux Distributions

For the protocluster candidates detected at 857 GHz, the median 857 GHz Planck aperture flux density of the cluster candidates, without correcting for any foreground contamination, is 912 ± 447 mJy, with minimum and maximum values of 302 and 2403 mJy, indicating the presence of a large tail in the distribution. The median 545 GHz flux density on the other hand, is 410 ± 204 mJy, with minimum and maximum values of 182 and 872 mJy. For those protoclusters detected at 545 GHz, the median 545 GHz Planck aperture flux density of the protocluster candidates is 447 ± 204 mJy, with minimum and maximum values of 182 and 872 mJy respectively. Flux distributions of these sources can be viewed in Figure 2.11

In Section 2.4.2, we demonstrated that in general, the Planck flux density of a source can

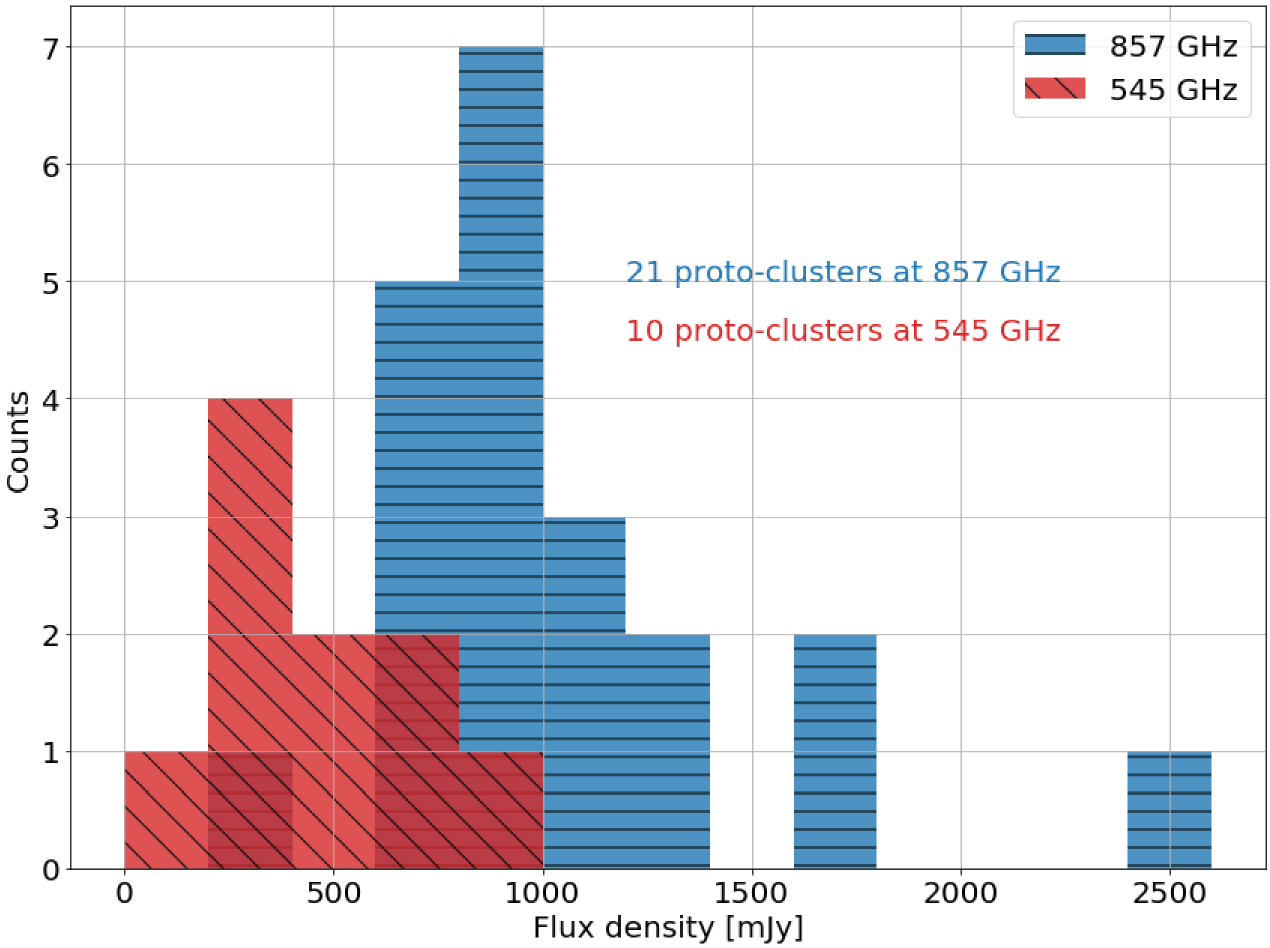

Figure 2.11: The 857 GHz and 545 GHz flux distributions of all 27 of our protocluster candidates, in blue horizontal hashed and red diagonal hashed respectively.

be reproduced by summing up detected Herschel sources, with Herschel flux densities above 25.4 mJy at 350 μm. How is the flux distributed amoungst these sources however? For our protocluster candidates detected at 857 GHz, we find 50% of the Planck flux is contributed by 36 ± 7% of sources, indicating that on average, the flux is evenly spread between our sources, reflecting our results in Section 2.3.3. These numbers are similar for the 545 GHz detected clusters, with 34 ± 10% of sources contributing 50% of the total flux density at 545 GHz. For the individual Herschel sources, the mean 350 μm flux of our 857 GHz selected clusters is 40.6 ± 15.8 mJy, whilst the median is value is 35.81 mJy, indicating the distribution is slightly skewed towards a long tail at higher flux densities. For the 545 GHz clusters, the mean 500 μm flux density of individual Herschel sources is 38.8 ± 13.4 mJy, with a median value of 33.0 mJy.

Photometric Redshifts, Luminosities and SFRs

There is currently a large scale follow up program in place to identify the redshifts of the Herschel sources detected in the candidate protoclusters. With spectroscopic redshifts, not only can we confirm whether the candidates are physical clusters or line of sight effects, but we can also infer other physical properties such as the star formation rate, luminosity, and average dust temperatures of our sources. With some assumptions, we can make some rough estimates of these physical properties already, and in this section this is what we attempt. However, we note there is much uncertainty in these calculations, and these results should be treated with skepticism, though they should be broadly accurate to roughly within an order of magnitude. Because of this, these results were not included in the published paper, but are included here to discuss the nature of the Planck-selected Herschel protoclusters.

To estimate redshifts for the Herschel sources associated with the candidate protoclusters, we fit the data, in this case the measured 250, 350 and 500 μm flux densities of each Herschel source, to eight template SEDs, which have been chosen to span a wide range of well studied DSFGs with a wide range of properties. In each case, the redshift and normalisation are varied, and the reduced χ^2 between the data and model are minimized. This provides eight estimates of the redshift of our source. Owing to differing dust properties in different galaxies, leading to phenomena such as the redshift-temperature degeneracy, individual template fits do not capture the true uncertainty in the redshift of a source. The eight estimates can however provide a rough upper and lower bound on the likely redshift of the source.

Using these upper and lower bounds, we estimate both FIR luminoisities and SFRs of these sources. To estimate FIR luminosities, we fit a single modified blackbody by minimizing the χ^2 between our data and a single modified blackbody. We fix $\beta = 2$, typical of other well studied DSFGs (Casey et al., 2014; Bianchi, 2013), and the redshift to the upper and lower bounds from above, and allow both the temperature and normalisation amplitude to vary. We then convert from a model flux to a model luminosity, and integrate under the rest frame 42.5 - 122.5 μm to obtain our FIR luminosity estimates. Finally, this is converted to a SFR, following Riechers et al. (2013), by adopting a top heavy Chabrier IMF, and using the Kennicutt (1998) conversion, which leads to $SFR = 1 \times 10^{-10} L_{FIR}[L_{\odot}]$.

Individually, the Herschel sources have an average FIR luminosity of $log_{10}(L_{fir}/L_{\odot}) = 12.9\pm0.3$, with an associated SFR of 900 ± 600 $M_{\odot}yr^{-1}$. There is significant uncertainty in these numbers; the uncertainties from the lower and upper redshift bounds alone lead to a difference of 30 - 50% in the L_{fir} or SFR estimates. Even with this uncertainty, it is clear that as an order of magnitude estimate, many of these sources appear to have L_{fir} values on the order of 10^{12} - 10^{13} $L_{\odot}$, and associated SFRs between a few hundred to a few thousand $M_{\odot}$, consistent with and typical of other bright ($\lambda \sim 350$ μm, $F_{\nu} > 25$ mJy) $z > 1$ FIR selected galaxies (Kovacs et al., 2006; Chapin et al., 2011; Geach et al., 2013; Swinbank et al., 2014; Casey et al., 2014).

To investigate the cluster luminosity and SFR, for each individual Herschel source we either assign it as a foreground or protocluster source. To do this, we simply check if the upper and lower bounds on the redshift of the Herschel source are consistent with the mean redshift of all the Herschel sources associated with the area around the protocluster. On average, we find 10.2 ± 2.4 Herschel galaxies appear to be associated with the protocluster itself, in excellent agreement with our predictions in Section 2.6.1. Still, like the redshift estimation, this procedure and which galaxies are actually physically associated with the protocluster is inherently uncertain without spectroscopic redshifts, and only rough order of magnitude conclusions should be drawn from it.

Summing the FIR luminosities and SFRs from these sources associated with the protocluster, we find mean $L_{fir} = 9.9 \pm 3.3 \times 10^{13}$ $L_{\odot}$, and corresponding mean SFRs $SFR = 9900 \pm 3300$ $M_{\odot}$ yr^{-1}. In Figure 2.12, we plot the estimated redshift and estimated SFRs of the protocluster candidates. Errors on both the redshift and SFRs are estimated by taking the mean minimum redshift/SFR from template fitting on all the sources associated with the protocluster to the mean maximum. Taking into account our uncertainties, we conclude that the typical cluster FIR luminosity is of the order of 10^{13} - 10^{14} $L_{\odot}$, with SFRs of several thousand to a few tens of thousand $M_{\odot}$ yr^{-1}. This is in excellent agreement, not only with estimates from the PHZ (Planck Collaboration et al., 2016), but also with the few spectroscopically confirmed DSFGs in protoclusters in the literature (Blain et al., 2004a; Chapman et al., 2009; Yuan et al., 2014; Dannerbauer et al., 2014; Casey et al., 2015; Tamura et al., 2009; Daddi et al., 2008; Walter et al., 2012; Capak et al., 2011). These studies have generally found, for DSFGs spectroscopically confirmed to lie within the protoclusters, aggregate SFRs on the order of several thousand $M_{\odot}\ yr^{-1}$ (see Table 1 of Casey 2016).

Pillepich et al. (2018) estimate that for a cluster with halo mass $\sim 10^{14}\ M_{\odot}$, the total stellar mass of the cluster should be around $2 \times 10^{12}\ M_{\odot}$, roughly equally split between central galaxies and satellite galaxies. For the most massive $10^{15}\ M_{\odot}$ galaxy halos, the stellar mass values are expected to be around $10^{13}\ M_{\odot}$, again equally split between the satellites and central galaxies. Taking our rough order of magnitude estimates of a cluster SFR between 1,000 and 10,000 $M_{\odot}\ yr^{-1}$, and the expected 100 Myr lifetime of DSFGs, we find we can form a stellar mass of between 10^{11} and $10^{12}\ M_{\odot}$ in 100 Myrs, a significant fraction of the estimated total stellar mass of the cluster. This suggests that much of the stellar mass present in a $z = 0$, M $> 10^{14}$ $M_{\odot}$ cluster can be formed during the early stages of the cluster formation, and possibly before the core has virialized.

Our numbers here are uncertain, and we should not draw strong conclusions from them. However, it is interesting to note that our SFR estimates are not only in reasonable agreement both with what others are finding in the literature, but also with the final stellar mass of $z = 0$ massive galaxy clusters, particularly those central to the clusters. There are several caveats to this; we have not confirmed the redshift of our sources and they may not be associated with one-another, the lifetime of a DSFG may be much longer or much shorter leading to significantly different stellar mass build up estimates, with only three photometric bands our fitting procedure may be poor. Nevertheless, how obscured star formation contributes to the formation of stellar mass in protoclusters is not well understood. Samples of DSFGs in protoclusters are sparse, but our order of magnitude estimates indicate they could be the sites of significant stellar mass build up, which may then go on to merge and collapse down into the central cores of todays most massive galaxy clusters.

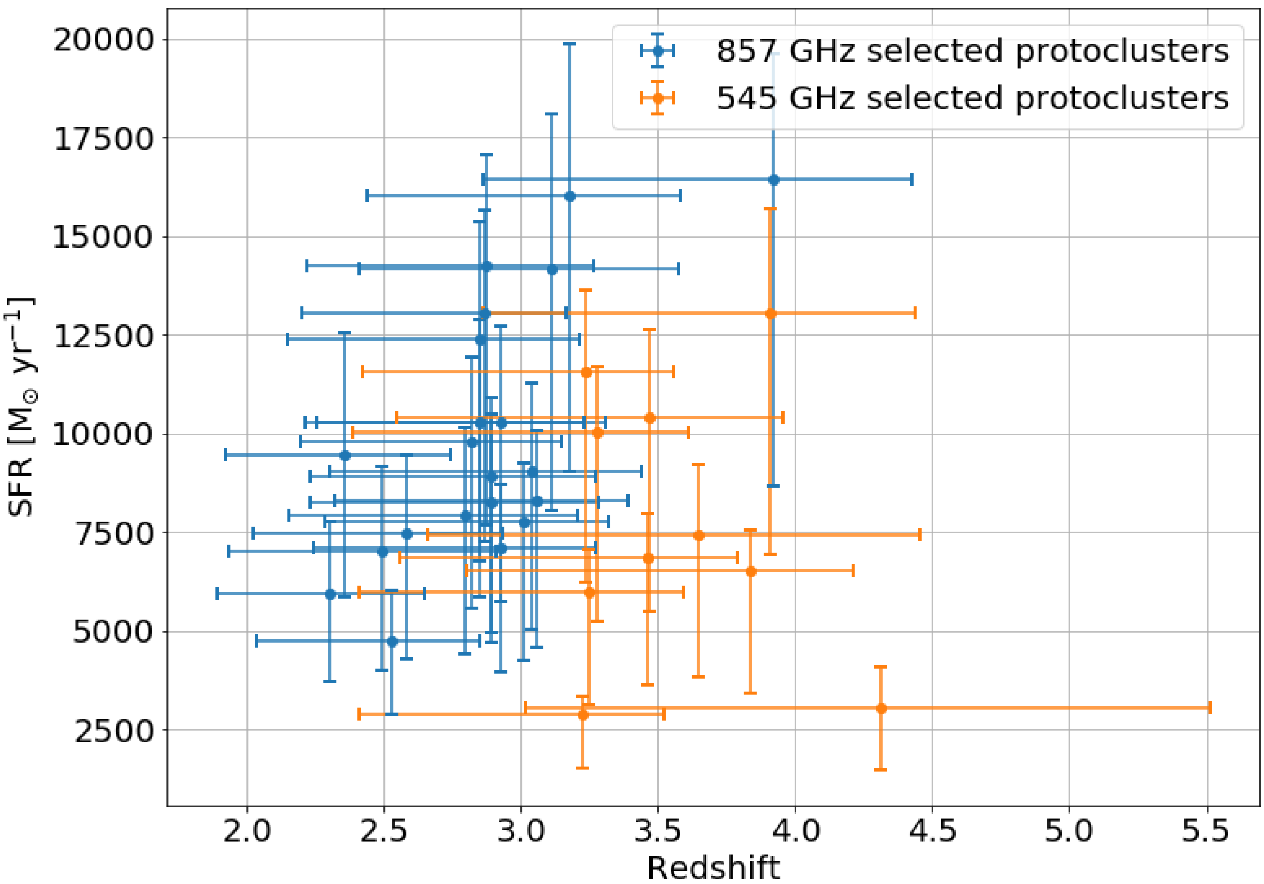

Figure 2.12: The estimated redshift and SFRs of protocluster candidates selected at 857 GHz (blue points) and 545 GHz (orange points). See text for details.

Density Contrasts

Spectroscopically confirmed protoclusters have been found to be extended on scales of tens of arcmin (Casey 2016 and references therein). Given we have detected overdensities on the scale of the 4.63 arcminute FWHM Planck beam, it implies we are detecting systems that are highly compact with respect to these larger tens of arcminute scale systems. Using the redshift distribution of Herschel sources from Pearson et al. (2013), we can utilise the redshift estimates discussed in the previous section to estimate the density contrast of our detected systems.

Once again, we select the median redshift of all the Herschel sources for each protocluster candidate as the likely protocluster redshift. We then select a redshift range corresponding to the minimum and maximum redshift estimates of all Herschel sources whose redshift estimates are consistent with the protocluster redshift estimate. These are often broad, with $\Delta z > 1.0$. To calculate the density contrast, we use the definition from Chiang et al. 2013, which defines:

$$\delta_{gal}(\mathbf{x}) = \frac{n_{gal}(\mathbf{x}) - < n_{gal} >}{< n_{gal} >}, \tag{2.8}$$

where δ_{gal} gives the density contrast, $n_{gal}(\mathbf{x})$ gives the number of actually observed galaxies within the redshift range, and $< n_{gal} >$ gives the expected number of galaxies observed in that redshift range. Selecting our 857 GHz Planck detected protoclusters, and applying a flux cut of $F_{350} \geq 36.0\ mJy$ to conform with the selection made by Pearson et al. 2013, we find a mean density contrast of 3.8 ± 2.2, with a median value of 3.2, and minimum and maximum values of 0 and 10.1 respectively.

At the time of writing, there is no clear consensus on the interpretation of these values, short of a larger $\delta_{gal}(\mathbf{x})$ generally implying a stronger overdensity (See Overzier 2016 for a recent review, with Section 3.1 and Figure 6 of particular relevance to the discussion here). A broad range of values of galaxy overdensity have been found for protoclusters and galaxy clusters above $z = 1$, but this may be due to the broad definition typically ascribed to protoclusters, and the difficulty in selecting a sample at a particular evolutionary state.

However, if in a given cluster, the Herschel sources are largely at the same redshift, the density contrast will not be spread out over $\Delta z = 1.0$, but over $\Delta z < 0.1$. This leads to mean, median, min and max values of $\delta_{gal}(\mathbf{x})$ of 37.3 ± 40.7, 26.7, 0.0 and 200.0 respectively, around $10 \times$ higher and indicative of a significant contrast with the blank field redshift distribution estimates from Pearson et al. 2013. Such a conclusion should only be reached after spectroscopic redshift confirmation, as the current redshift uncertainties are too large to draw many conclusions from. If true however, then such density contrasts are not consistent with these sources being merely protoclusters which will collapse at some later date, but imply that these are systems well on their way to collapse.

Physical Size

At $z = 1 - 2$ the Planck beam of 4.63 arcmin corresponds approximately to a physical size of 2.3 Mpc. Given we use this beamsize as a radius, the physical size of the structures we are detecting are on the order of 4.6 Mpc in one of the dimensions.

Generally, protoclusters are expected to extend on scales from several to several tens of arcmin (Overzier, 2016). We can get some idea of the spatial distribution of our sources by looking at those members we have identified as likely being cluster members by their photometric redshifts.

For each of our 27 protoclusters, we take all the sources we have identified as likely being part of the protocluster, calculate their median RA and DEC, then count the number of Herschel sources as a function of radial on-sky distance, using a bin size of 0.5 arcmin, and limiting ourselves to sources with $S_{350} > 25.4$ mJy in order to compare number counts. In Figure 2.13, we plot the number of Herschel sources as a function of radial on-sky distance for all 27 clusters. Additionally, we also plot the median number of sources detected as a function of radial distance for all 27 clusters, and further plot the expected number of Herschel sources as a function of radius using number counts from Valiante et al. (2016).

Overdensities as compared the Poisson distribution are seen at all scales, somewhat as expected given our sources are selected as overdensities of Herschel sources. However, Figure 2.13 shows

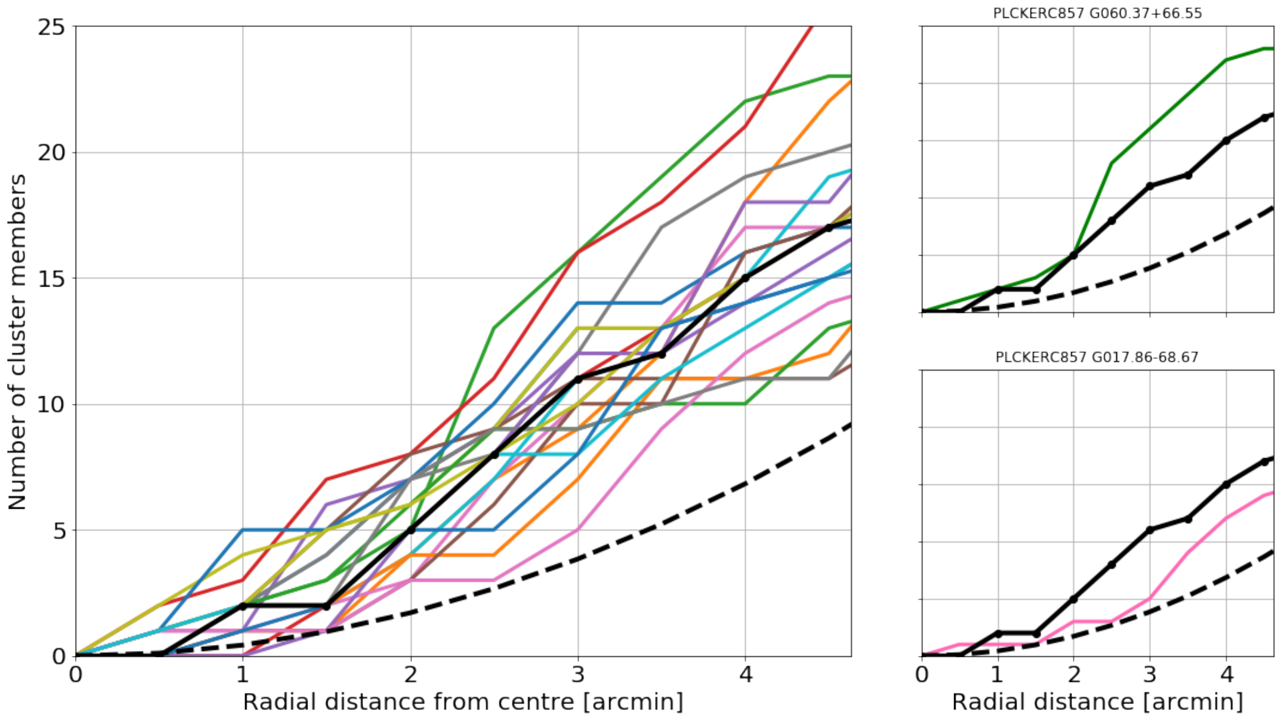

Figure 2.13: *(Left)* The number of Herschel sources with $S_{350} > 25.4 mJy$ as a function of radial distance from the mean centre of all the Herschel sources associated with each Planck protocluster. The different coloured lines represent different clusters, whilst the thick black line represents the median value for all the clusters. The dashed black line represents the expected number of sources for a Poisson-distributed sample, using number counts from Valiante et al. (2016). *(Right)* A clearer view of two individual clusters, PLCKERC857 G060.37+66.55 and PLCKERC857 G017.86−68.67, showing two different radii (2 and 3 arcmin for the top and bottom protocluster candidate respectively) where a spike in the number of detected DSFGs is seen, as compared to what may be expected from the Poisson distribution.

a distinct marked rise in the number of detected sources as compared to Poisson at around 1.5 arcminutes, such that at ∼2.0 arcminutes the median number of detected Herschel sources is 3× higher than that expected from the Poisson distribution alone, and this level is maintained out to 3 arcminutes. At 1.5 arcminutes itself, the median value is only 2× higher than Poisson. At the largest radii of 4.63 arcminutes, there is some tentative evidence that the overdensity appears to be falling away, with the median value once again $\lesssim 2\times$ the value expected from Poisson. As such, it appears that for these Planck selected protocluster candidates, there is a marked increase in the number of sources at radial distances of 2 - 3 arcminutes, corresponding to physical distances of $\sim 1\ Mpc$, possibly suggesting a ring like structure of violently starbursting DSFGs. However, without accurate redshift information or an understanding of the non-starbursting population within these structures, such a conclusion remains highly speculative, and further observations are needed to understand the spatial arrangement of these sources.

Turning now to the cumulative fraction of sources as a function of radius, significant numbers of sources appear clustered on arcmin scales with, on average, 53% of protocluster members lying within 3 arcmin of the protocluster centre, and 21% within 1.5 arcmin. These radii corresponds to 1.5 Mpc and 750 kpc respectively. There is little evidence to suggest clustering at scales below 1 arcmin, but this can partially be explained by the beamsize of SPIRE. With FWHM of 17.9 arcsec at 250 μm, even a few sources are likely to begin to blend at sub-arcmin scales, and are likely to resolve into multiple components at higher resolution (see Oteo et al. (2018) for an example of > 10 DSFGs blended into a single Herschel source). In any case, it is clear that if these sources are physically clustered, they are doing so on or near arcminute scales.

Associated Sources

Three of our candidate protoclusters appear to be associated with known galaxy clusters. PCCS1 545 G058.72+82.59 (PCCS1 857 G058.53+82.57) lies only 4.3 arcmin away from the core of the galaxy cluster GHO 1319+3023 (Gunn et al., 1986), at a redshift of 0.4, PCCS1 545 G027.38+84.85 (PLCKERC857 G027.36+84.83) is associated with the redshift 0.43 galaxy cluster GMBCG J198.59994+26.5688 (Hao et al., 2010), and PCCS1 545 G084.40+81.05 is associated with the estimated redshift 0.43 galaxy cluster NSCS J131812+335831 (Lopes et al., 2004). The redshifts of these clusters appear to be at odds with our results in Section 2.5, where we predicted redshifts of between $z = 1 - 2$. Furthermore, if the Herschel sources are associated with these z = 0.4 clusters, then the physical extent of the overdensity of Herschel sources is only 1.5 Mpc. The other alternative is that these $z = 0.4$ clusters may be lensing a background cluster at $z = 1 - 2$, which actually contains the Herschel bright sources.

Additionally, three of our protoclusters, PLCKERC 857G017.86-68.67, PLCKERC857 G149.81+50.11 and PLCKERC857 G095.44+58.94 are co-incident with QSOs. Whether these QSOs are physically associated with the protocluster candidates or not is uncertain, but the QSOs generally lie between $z = 1 - 2$, and could be signposting the true redshift of the protocluster.

Given we expect our protocluster candidates to generally lie at z > 1, it is perhaps surprising to find three of them along the same line of sight as known, z < 0.5, galaxy clusters. Differences in the selection and methodology of these associated known galaxy clusters vary substantially, such that the estimated surface density varies between ~ 3.7, ~ 6.9 and ~ 11 galaxy clusters per square degree at redshifts between 0 and 0.5 (Lopes et al. (2004); Hao et al. (2010) and Gunn et al. (1986) respectively).

If we define an associated low-z galaxy cluster to be any galaxy cluster that lies within 5 arcminutes of one of our protoclusters, then we can calculate the expected number of low-z galaxy clusters that appear to be associated to our protocluster candidates. For a 5 arcminute radius and for 27 protoclusters, we cover an area of $27 \times \pi(5/60)^2 = 0.59\ deg^2$. Given the above estimate of the surface density of low-z galaxy clusters, we may then expect anywhere between 2.2 and 6.5 low-z galaxy clusters to be associated to our sources, in perfect agreement with the three we do detect. There is therefore no reason yet to suspect that these DSFGs are associated with this low-z source, but once again caution should be maintained until spectroscopic redshifts can be confirmed for large numbers of the Herschel sources associated with these protocluster candidates.

2.6.3 Simulations of DSFGs in Clusters

Whilst cluster and protocluster numerical simulation has a rich history (see, for instance, Granato et al. 2015; Muldrew et al. 2015, 2018 and references therein), studies which have investigated the FIR and sub-mm properties of these clusters are less forthcoming. Partially, this comes down to the added complexity that dust brings; dust reprocessing requires a full radiative transfer code, and assumptions such as a dust geometry that is spherical and symmetricly distributed throughout a galaxy may be too simplistic to correctly reproduce the FIR/sub-mm emission.

Granato et al. (2015) study the infrared and sub-mm properties of a selection of 24 simulated clusters at $z > 1$ by combining a set of hydrodynamical zoom in simulations with a radiative transfer code, GRASIL-3D, that can account for dust reprocessing in arbitrary geometries. The selected galaxy clusters all have a virial mass between $1-3 \times 10^{15}\ h^{-1}\ M_{\odot}$ at $z = 0$. Details of the simulations can be found in Granato et al. (2015), but features included gas cooling, star formation, supernova and AGN feedback, and assumed a Chabrier IMF (Chabrier, 2003).

Granato et al. (2015) simulate the expected 350, 550 and 850 μm flux densities of their clusters / protoclusters as they would appear at $z = 1, 2$ and 3. We can compare these results to the measured 350 μm flux densities of our protocluster candidates. We first attempt to remove any foreground contribution to our protoclusters by first placing 1,000 randomly positioned Planck beams down on each of the Herschel map and measuring the aperture photometry in each to get an idea of the typical median foreground/background contribution to any position on the sky. This value, typically around 100 to 300 mJy and depending on the map, is then removed from the Herschel aperture flux densities for each of the protoclusters. Furthermore, to be conservative, we compare our results to the redshift bin from Granato et al. (2015) where the flux densities are brightest, the $z = 1$ bin. In effect, we are therefore conservatively assuming that all our clusters are at $z = 1$, and that all have a foreground contribution of between 100 - 300 mJy. Taking Figure 7 from Granato et al. (2015), we overplot our results in Figure 2.14.

It is immediately apparent that our detected protoclusters have flux densities significantly

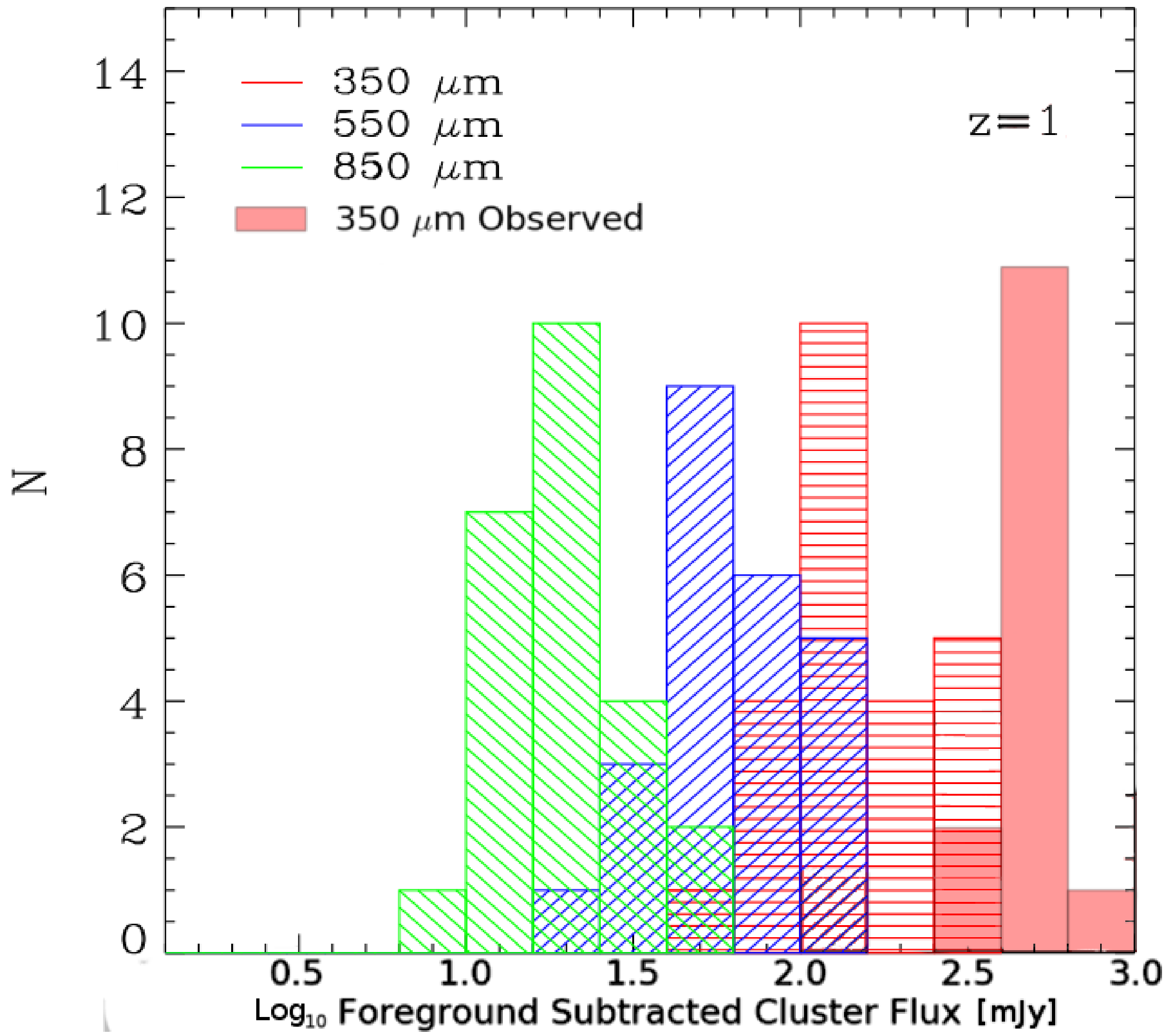

Figure 2.14: (Hashed histograms) predictions of the sub-mm flux density of a protocluster predicted by Granato et al. (2015) at $z = 1$. (Solid histogram) foreground subtracted flux density of our observed candidate protoclusters at 350 μm.

brighter than the simulated clusters, with a median flux density of 131 mJy at 350 μm for the simulated clusters, but a median flux density of 500 mJy for our observed protoclusters. Not only this, but these results represent the best case scenario; at redshift 2, where we estimate many of our protoclusters lie, the median simulated 350 μm flux density is 85 mJy. The estimated SFRs of the simulated clusters within a Planck beam, measured directly from the simulations, varied between 316 and 1600 $M_{\odot}\ yr^{-1}$, again approximately 5× less than what we have measured for our candidate protoclusters.

How do we account for this difference? It is not possible to simply increase the SFR of these systems at $z = 1 - 2$, as these same simulations currently may over-predict the stellar mass in the brightest cluster galaxies at $z = 0$ (Ragone-Figueroa et al., 2013), especially if features such as AGN feedback are switched off or minimized in order to increase the FIR/sub-mm flux density of the source. Indeed, we have already shown that the infered SFRs of our protocluster could reproduce the observed stellar mass in $z = 0$, $10^{14} - 10^{15}\ M_{\odot}$ clusters in only 100 Myrs, assuming the rate is maintained over those 100 Myrs. Another way to increase the apparent SFR / flux density of the simulated clusters is to adopt a top-heavy IMF. A top-heavy IMF has been suggested as a possible explanation to the number counts of DSFGs since Baugh et al. (2005), who originally suggest a flat IMF for starbursting galaxies. Granato et al. (2015) also find that the IMF would need to be near flat to match the simulations to observations[7]. For now, it is clear that simulations are failing to re-produce the observed FIR/sub-mm flux densities of clusters / protoclusters. Exactly where the corrections lie, whether in observations, theory, or simulation limitations, remains an open question.

2.7 Discussion

In this section, we summarise the key results of the analysis on the nature of the Planck compact sources, and compare them to what others have found in the literature. In addition to what was published in Greenslade et al. (2018), we also here include a section on the future direction

[7]For a more detailed discussion on IMF variations, and its effects on numerical models of galaxy formation and evolution, see Section 10.2.1 of Casey et al. 2014

of this research, including our current multi-wavelength follow up programs for these sources, and what the next steps should be in order to fully understand this population.

2.7.1 The HeLMS Field

The HerMES Large Mode Survey (HeLMS, P.I. Marco Viero) was a 280 deg^2 shallow wide survey with Herschel-SPIRE. It is the largest of the HerMES fields, but was not included in our main analysis for two reasons. Firstly, no publicly available and verified catalogues have yet been produced for the HeLMS field. This is partially due to the second reason, which is that HeLMS is severely cirrus contaminated compared to any of the other H-ATLAS, HerMES fields, or HerS. For completeness, we repeat the selection and identification process for HeLMS using a private catalogue (Marco Viero, private communication) and provide the results here, but do not include them in the rest of our analysis.

We find 130 857 GHz and 40 545 GHz Planck compact sources in this field, and 137 unique sources. Of these, we identify 64 (46%) regions of Galactic cirrus, 61 (45%) local galaxies, 2 QSOs (LBQS 0106+0119 and CRATES J2323-0316), 1 candidate protocluster, and 9 sources with no clear identification. To highlight the cirrus contamination, even in the PCCS2 where we found that only 2.5% of sources were associated with Galactic cirrus in our previous analysis, we find 27% of PCCS2 sources in the HeLMS field are associated with Galactic cirrus.

2.7.2 The Nature of the Planck Sources

It is clear that the Planck catalogues of compact sources select a wide range of physical phenomena, not only those that are point like on smaller, sub-arcmin scales, but also those that are reasonably extended on arcminute scales. We have shown in Figure 2.3 that almost half of the Planck sources are resolved by Herschel on scales of a few tens of arcseconds. As expected, some of these extended sources are Galactic cirrus, around 10% in the extragalactic fields. A similar number of sources however appear to be overdensities of Herschel sources, clustered together on the scale of the Planck beam. The Mexican-hat wavelet filters used in the creation of the

PCCS and PCCS2 were designed to down-weight emission from the wings of the Planck beam, in order to decrease the fraction of Galactic cirrus within the Planck catalogues. However, this filter could have the same effect on Herschel overdensities, decreasing their likelihood of being included in the catalogue. Examining the fractional make up of source types in each of the ERCSC, PCCS and PCCS2 (see Table 2.3), this appears to be be the case, with the PCCS and PCCS2 hosting significantly fewer cluster candidates than the ERCSC, which convolved with a Gaussian rather than the Mexican-hat wavelet.

Addressing the candidate protoclusters specifically in Section 2.7.3, here we briefly discuss the other source types we have identified during this work.

Stars

Three stars are present in the Planck catalogues of compact sources; Mira, R Sculptoris, and Fomalhaut. Two of these, Mira and R Sculptoris, are both asymptotic giant branch stars, known to produce large amounts of dust (Mayer et al., 2011; Maercker et al., 2015). Fomalhaut meanwhile, is known to host a dusty debris disc (Acke et al., 2012). No systematic published study of Planck selected / detected stars has yet been produced, but if these three stars are representative of the broader population of Planck selected / detected stars, then Planck could be useful for homogenously selecting a population of stars which host large amounts of dust. Given also the Planck flux density limits, such sources are likely to be bright in the sub-mm, and could easily be confirmed with higher resolution ground based instruments in a short amount of time, enabling a rapid characterisation of the FIR/sub-mm and mm spectra of these dusty stars using the Planck bands.

Lensed Sources

One of our lens candidates, PLCKERC857 G047.32+82.53 (H-ATLAS J132426.9+284452, Negrello et al. (2017)), has a 3.1σ overdensity of 500 μm sources. The lensed source itself has been identified to lie at $z = 1.676 \pm 0.001$ (George et al., 2013; Bussmann et al., 2013), and could indicate the true redshift of the cluster.

We also note that PCCS2 857 G270.56+58.54 (H12-00, (Fu et al., 2012; Herranz et al., 2013; Clements et al., 2016) hosts a 2.8σ overdensity of 350 μm sources, and Clements et al. (2016) in particular find an overdensity of SCUBA-2 850 μm sources around this source. This source merits further discussion, as how the strength of the overdensity varies has relevance for the nature of those sources we did not find to be overdense on the scale of the Planck beam, but could not assign any other identification. In Clements et al. (2016), we restricted ourselves to sources detected to $> 5\sigma$ in the 350 μm band, and counted the number of detected sources within a 2, 2.5, 3, 4, 5 and 10 arcmin radius of the lensed source H12-00. We compared the source density around H12-00 to the source density around 10,000 randomly selected positions in the GAMA12 field for all 6 of our radii. We further interpreted the number of comparably dense regions as a probability (i.e. if 5 out of our 10,000 regions are at least as overdense as around H12-00, we interpret this as a probability of observing a region at least this overdense as 5×10^{-4}). Performing this calculation for radii of 2, 2.5, 3, 4, 5 and 10 arcmin, we find overdensities of 350 μm SPIRE sources of 7×10^{-3}, $< 1 \times 10^{-4}$, $< 1 \times 10^{-4}$, 8×10^{-4}, $< 3 \times 10^{-4}$ and $< 3 \times 10^{-4}$ respectively. Converting these to their equivalent σ values for a normal distribution, this corresponds to 2.5σ, $> 3.7\sigma$, $> 3.7\sigma$, 3.1σ, 3.4σ, and 3.4σ overdensities at 2, 2.5, 3, 4, 5 and 10 arcmin respectively. At the redshift of the $z = 3.26$ lensed source, a 10 arcmin radius corresponds to 5 Mpc, or 10 Mpc diameter, and the presence of an overdensity suggests a structure on this kind of scale. The 10 Mpc physical size of this structure, if real, would be large, but comparable to a number of known DSFG hosting protoclusters (Noble et al., 2013; Casey et al., 2015; Casey, 2016). Of note is that such a structure would extend beyond the Planck beam, and hints towards structures of DSFGs extended beyond the Planck 4.63 arcmin beam, as can also be seen in Figure 2.13, especially for those sources only reaching $\sim 60\%$ cumulative fraction at ~ 5 arcmin.

Unassigned Sources

The 61 Planck compact sources that we were unable to provide a reliable identification for constitute almost 20% of all the Planck sources. If this extends to the full Planck catalogues, instead of just the 808.4 deg^2 under consideration here, there could be several thousand sources amongst the ERCSC, PCCS1 and PCCS2 that could share there properties, and they are worth examining further.

The 61 Planck sources could simply be false detections; indeed the Planck compact source catalogues stated goal of an 80% reliability catalogue matches up well if these 20% of sources are not real. However, there is some suggestion that at least a subset of these sources are real. Ten of the sources are detected in multiple catalogues (i.e. in both the ERCSC and PCCS1), and of these ten, six are detected in both the ERCSC and PCCS1 or PCCS2, which used different extraction and detection methodology. The median detection level of the unassigned sources in the PCCS1 and PCCS2 is $5.4 \pm 0.5\sigma$, similar to that of the candidate protoclusters at $5.4 \pm 0.3\sigma$. In fact, whilst varying the search radius in Section 2.3 to check for consistency, we found several of the unassigned sources became classed as candidate protoclusters as the radius changed, and vice versa. In all cases, around 30 candidate protoclusters were identified, with the exact number depending on both search radius and flux density cut. Furthermore, of the four Planck compact sources that also appear in the PHZ, three are not assigned a classification here. Given the other PHZ source is a lensed $z = 2.5$ DSFG, it is likely at least some of these 61 unassigned sources are real, and indeed possible that some are overdensities of red sources, but which are too faint or slightly not numerous enough to be classed as such here.

At the same time, this should not be interpreted that all of the 61 unassigned sources are real but too faint. In the preliminary versions of the ERCSC, PCCS1 and PCCS2, significant variation in which sources were included around the detection threshold was seen (D. Harrison, private communication). Keeping the parameters for the Planck catalogue creation the same, sources near this detection threshold would appear / disappear, depending on the preliminary version of the map used in the creation of the catalogues. For high S/N sources, this was rarely a problem, but for sources near the detection limit this was more common.

The bright lensed source H12-00 means that we identified the associated Planck source as a lens candidate in our work. Removing this source, we would likely have been unable to assign this source a classification, as it does not show a $> 3\sigma$ overdensity in any of the three SPIRE bands, despite the evidence suggesting a cluster presented in Clements et al. (2016). Turning to the other 61 sources for which we were unable to assign a classification, we find 28 (45%) of them host overdensities between $2-3\sigma$ in either the 250, 350 or 500 μm SPIRE bands. Furthermore, Figure 2.7 indicates that several of our unassigned sources have very red colours, indicative of a high-redshift solution. Given they are not assigned as protocluster candidates by us, this could be due to a number of fainter (SPIRE flux-densities < 25.4 mJy) Herschel sources. Our selection of which Herschel catalogues to use was motivated by a desire for a consistent analysis across heterogeneous data sets, and so all catalogues are effectively selected at 250 μm (see Section 2.2. If an overdensity of sources which are faint at 250, but bright at 350 or 500 μm exists, it may not be selected by these catalogues and would therefore not be assigned as a protocluster candidate in this work, but would be detected by the work in the PHZ. We find it is therefore likely that many of the unassigned sources could also be physical associations / protoclusters containing a large number of DSFGs, but that the specific flux and overdensity cut used here mean that they are not selected as such. However, there are alternative explanations. As previously noted, significant variation was seen in preliminary versions of the catalogue for sources near the detection threshold, and many of these unassigned sources could be simply noise fluctuations near the detection threshold. Additionally, clustering of CMB fluctuations are known to posses a strong S/N tail, and can appear as high S/N sources (see Figure 10 of De Zotti et al. 2015). Figure 2.6 however does show that many of the unassigned sources can have their aperture flux density entirely accounted for by discrete, detected Herschel sources, giving credence to the idea that many of these sources are larger structures, or high-density regions which do not pass the previously set out criteria.

2.7.3 The Nature of the Candidate Protoclusters

Sites containing multiple DSFG have now been found over a wide range of cluster environments, from scales which range to > 10 arcmin (Noble et al., 2013; Dannerbauer et al., 2014; Casey et al., 2015; Casey, 2016), to scales comparable to the Planck beam (Herranz et al., 2013; Clements et al., 2014; Planck Collaboration et al., 2016; Clements et al., 2016; Greenslade et al., 2018) to scales of only a few tens of arcsec (Oteo et al., 2018). These observations are surprising; most simulations predict that these sources are likely unassociated, and are simply line-of-sight effects (Hayward et al., 2013; Cowley et al., 2014). Indeed, without either a longer duty cycle, or a large scale environmental starburst triggering event (Emonts et al., 2016; Dannerbauer et al., 2017; Oteo et al., 2016b), then physical associations of multiple DSFGs are expected to be exceedingly rare (Casey, 2016). However, observations have now shown that many overdensities of DSFGs are indeed physical associations (Daddi et al., 2008, 2009; Capak et al., 2011; Walter et al., 2012; Ivison et al., 2013; Dannerbauer et al., 2014; Smail et al., 2014; Ma et al., 2015; Umehata et al., 2015; Casey et al., 2015; Hung et al., 2016; Kato et al., 2016; Flores-Cacho et al., 2016; Oteo et al., 2018). The SFRs of these detected clusters is often on the order of several thousand $M_{\odot}\ yr^{-1}$, and these sources are often found at $z >> 1$. Meanwhile at $z < 1$, SFR is efficiently quenched in cluster environments, particularly in the cluster cores (Dressler, 1980; Scoville et al., 2013; Darvish et al., 2016). In this chapter we have found similar sources, with sizes of ~ 5 arcmin, SFRs on the order of several thousand $M_{\odot}\ yr^{-1}$, and redshifts between $z = 1-3$. Assuming they are physical associations, what could these systems represent? and what epoch of cluster formation are we witnessing?

It is possible these systems are currently in the process of virialisation, and that we are seeing the initial formation of the cluster core. Several lines of evidence point towards this. Observations of local galaxy clusters suggest a significant fraction of the stellar mass in cluster cores was built up rapidly (< 1 Gyrs), and at $z = 2 - 3$. The high SFRs and short duty cycles seen in DSFG hosting clusters/protoclusters could be responsible for this build up. Meanwhile, the overdensity of our candidate protoclusters with respect to the background suggests a system that is well on its way to collapse, and with density contrasts $\delta > 10$, are more similar to clusters than protoclusters (Chiang et al., 2013; Overzier, 2016). The spatial distribution of our clusters in Figure 2.13 suggest that $\sim 50\%$ of the sub-mm emission comes from a region only 1.5 - 3 Mpc across. However, few of the galaxy clusters / protoclusters containing significant numbers of DSFGs are confirmed to have been virialised or host a strong intra-cluster medium, suggesting they are yet to collapse or are about to. Additionally, since these DSFGs are expected to evolve into massive elliptical galaxies, we simultaneously would expect to see the build up of a red sequence in these systems, with our detected DSFGs going on to form the most massive ellipticals in the cluster core.

Such a hypothesis is speculative, and no strong conclusions should be taken prior to spectroscopic confirmation, alongside observations at optical/NIR wavelengths to confirm the presence of an overdensity of sources. In Section 2.1, we discussed the possibility that DSFG rich protoclusters represent a stage of cluster formation hitherto missed in typical galaxy cluster formation surveys. Assuming that at least some of our sample represent true protoclusters, the small overlap between our sample and known galaxy clusters / protoclusters in the literature supports this. However, significant work should be undertaken in order to understand precisely what our sample of protocluster candidates represent.

2.7.4 Future Work

The confirmation of the evolutionary state of these DSFG hosting protoclusters / clusters (i.e. are they virialised? does the cluster possess a significant red sequence or hot intracluster medium?) should be a key goal to answer the question of what these DSFG hosting protoclusters represent, as should exactly what processes must take place at $z > 1$ to turn galaxy clusters / protoclusters from sites of significant star-formation to sites of efficient quenching of star formation.

Here we have presented a homogeneously selected sample of the most DSFG overdense and compact protocluster candidates, ideal for such a program. This program is ongoing, and new observations are currently being taken both to confirm an optical/NIR presence of an overdensity, and also to confirm the physical association of the DSFGs. Additionally our work offers a complementary selection to the PHZ; while the PHZ generally selected the reddest and brightest candidates, our work is able to select fainter and warmer candidates.

However, we also note that we have concluded that the methodology used in the creation of the PCCS and PCCS2 is biased against extended emission by design. Given this, and the fact that the PCCS2 is based on 5 all sky observations compared to the ERCSCs 1.6, it would be worthwhile to re-create a fourth Planck catalogue of compact sources, using all 5 full sky observations and a filter which does not down-weight extended emission. As Herschel data is only available for around 1000 deg^2 of extragalactic sky, it is likely each individually detected source can be manually examined to search for evidence of cirrus emission. The Planck team have already produced a catalogue of what are likely overdensities of Herschel sources at $z \sim 2$ in the PHZ (Planck Collaboration et al., 2016). We however have seen in both Figure 2.7 and in the cross-match between our protocluster candidates and the PHZ that we are likely not selecting the same candidates A selection similar to ours which selects only based on overdensities of Herschel sources can identify bluer / cooler protocluster candidates.

2.8 Conclusions

By cross-matching the Planck catalogues of compact sources with 808.4 deg^2 of Herschel extragalactic fields, we have identified 27 candidate protoclusters of DSFGs that are at least 3σ overdense in either 250, 350 or 500 μm sources. We have further identified 192 local galaxies, 43 regions of Galactic cirrus, 12 candidate lensed sources, three stars, and two QSOs from the Planck catalogues of compact sources. For a further 61 sources we have been unable to assign a classification, but many have red colours and are at least 2σ overdense in Herschel sources, and it is possible that some may represent candidate protoclusters, but at a lower density contrast.

We found significant differences between the three catalogues of Planck compact sources, with different versions hosting significantly different fractional types of sources. We ascribe this difference to the different filters used in the creation of the catalogues, with the PCCS and PCCS2 Mexican-hat wavelet filter likely suppressing the inclusion of both Galactic cirrus, and candidate protoclusters.

We verified that there is good agreement between the aperture photometry of both Planck and Herschel, and further showed that the 857 and 545 GHz aperture photometries can be completely accounted for by summing up the discrete detected sources with flux densities > 25.4 mJy at 350 and 500 μm.

The colours of our protoclusters are generally redder than other source types, but we note that the selection used by the PHZ of $S_{857}/S_{545} < 2$ can miss some candidates, which may represent warmer or lower-z protocluster candidates. Both the Planck and Herschel colours indicate that our sources generally lie at $z > 1$, with specific photo-z fits to the FIR photometry of sources favouring $z = 2 - 3$, though the uncertainties in these fits are of the order $\Delta z = \pm 1$.

We find a surface density of protocluster candidates of $(3.3 \pm 0.7) \times 10^{-2}$ sources deg^{-2}, in good agreement with other results. Crossmatching our catalogue to the PHZ, we find only four matches, none of which we classify as a candidate protocluster (three we do not assign a classification, and one we find is gravitationaly lensed).

Comparing our results to simulations from Granato et al. (2015), we find the FIR flux density of our clusters is $\sim 5\ \times$ greater than that of the simulations, even in our most conservative estimates.

Without redshift confirmation, there remains the possibility that some of these objects are not physical clusters/protoclusters. However, given the number we have found alongside other groups, if they are clusters/protoclusters it is a challenge to explain how groups of > 20 associated DSFGs exist, given their expected lifetimes of ~100 Myr. Such protoclusters of DSFGs are being found from arcminute to arcsecond scales, yet we do not see such objects in the local Universe, indicating that star formation is quenched in clusters at low redshifts, but takes place in clusters/protoclusters at higher redshifts. Since we do not know if these sources are virialized, further characterization, particularly of the environment and state of virialization, should be a key focus for follow-up observations. Given also that we expect DSFGs such as these to evolve into the brightest cluster members at the cores of galaxy clusters, they likely play a vital role in the earliest stages of cluster formation and evolution.

Chapter 3

Multiplicities of 500 Micron Risers

3.1 Introduction and Motivation

At z $\geq$ 4, only a handful of DSFGs have been spectroscopically identified (Capak et al., 2008; Coppin et al., 2009; Daddi et al., 2008; Riechers et al., 2010; Cox et al., 2011; Capak et al., 2011; Combes et al., 2012; Walter et al., 2012; Riechers et al., 2013; Dowell et al., 2014; Yun et al., 2015; Ivison et al., 2016; Oteo et al., 2016c; Asboth et al., 2016; Riechers et al., 2017; Zavala et al., 2017; Strandet et al., 2017; Fudamoto et al., 2017; Oteo et al., 2016b; Marrone et al., 2017). As such, the statistics of this population remain poorly constrained. There is disagreement over whether DSFGs significantly contribute to the cosmic SFR-density above $z > 4$ (Rowan-Robinson et al., 2016; Liu et al., 2017; Novak et al., 2017) or not (Michałowski et al., 2017; Koprowski et al., 2017). So few samples exist in fact, that neither a model where they dominate or one where they barely contribute can be ruled out (Casey et al., 2018). Futhermore, galaxy formation and evolution models have consistently been unable to reproduce the observed number counts of the red SPIRE selected 500 μm risers, i.e. selecting sources with SEDs that appear to peak at wavelengths > 500 μm ($S_{250} < S_{350} < S_{500}$), which photometric and spectroscopic redshifts suggest lie at $z > 4$ (Dowell et al., 2014; Asboth et al., 2016; Ivison et al., 2016). Whether this mismatch between models and observations is due to observational issues such as blending or lensing (Karim et al., 2013; Scudder et al., 2016; Béthermin et al., 2017; Negrello et al., 2017; Donevski et al., 2017; Scudder et al., 2018), or due to the assumptions that have gone into the numerical models (Baugh et al., 2005; Valiante et al., 2009; Borgne et al., 2009; Béthermin et al., 2011, 2012, 2017) remains unclear.

Until the launch of Herschel (Pilbratt et al., 2010), a uniform sample selection of candidate high-z DSFGs was difficult to achieve; only observations using the small atmospheric windows at 850 μm and in the mm bands were possible, all well beyond the typical peak of dust emission (rest frame $\sim$ 100 μm, Blain (2002); Casey et al. (2014)), even at $z \sim 4 - 5$. As such, observations could only probe the Rayleigh-Jeans tail of emission, effectively a straight line in log space, and offered little in the way of redshift features to select on. With the launch of Herschel, and particularly the Herschel-SPIRE instrument (Griffin et al., 2010), it was possible to perform sub-mm and FIR colour selections. Under the reasonable assumption that the dust temperatures of DSFGs does not evolve with redshift[1], a typical DSFG whose dust emission peaks at 100 μm in the rest frame will appear to peak in the observed frame 250, 350 and 500 μm bands at $z \sim$ 1.5, 2.5, and 4, offering a new way to select DSFGs at different redshifts.

One of the first to apply the now well known high-z 500 μm riser selection, was Cox et al. (2011), who discovered and confirmed the presence of a $z = 4.2$ lensed DSFG in the GAMA-15 field of the H-ATLAS (Eales et al., 2010) survey. Since then, numerous other $z > 4$ DSFGs have been selected and spectroscopically confirmed using these criteria (Combes et al., 2012; Riechers et al., 2013; Dowell et al., 2014; Yun et al., 2015; Asboth et al., 2016; Ivison et al., 2016; Fudamoto et al., 2017). This selection was also used to identify some of the highest redshift DSFGs found to date at $z > 6$ (Riechers et al., 2013; Zavala et al., 2017). Both Dowell et al. (2014) and Asboth et al. (2016) selected 500 μm risers from the Herschel Multi-tiered Extragalactic Survey (Oliver et al., 2012, HerMES), in order to understand the statistics of the 500 μm riser population. Dowell et al. (2014) found that the number of bright ($S_{500} > 30\ mJy$) 500 μm risers was 1 - 2 orders of magnitude greater than predicted from galaxy evolution and formation models (Béthermin et al., 2011, 2012, 2017). Results from Asboth et al. (2016), using different flux limits, were generally in agreement, and reaffirmed that the 500 μm riser

[1]This result is not necessarily valid; for instance Ivison et al. (2016) find the typical dust temperature of DSFGs changes by ΔT = 9.4 between z = 2 and 6. However the colour selection technique appears to still be reasonably successful.

population likely represented the z > 4 DSFG population and was in excess of that predicted from models. Ivison et al. (2016) meanwhile, use a similar selection to probe the space density of DSFGs at $z > 4$ in H-ATLAS, using a colour cut of $S_{500}/S_{250} > 1.5$ and $S_{500}/S_{350} > 0.85$. They find that the photometric redshift distribution of their sample is shifted redwards by $\Delta z \sim 1$ compared with models using the same colour cut. All three studies find that the typical median luminosities of the 500 μm riser population are $> 1 \times 10^{13}\ L_{\odot}$, and that most 500 μm risers detected in single dish observations appear to be HLIRGs.

Several recent studies have attempted to explain the discrepancy between models and observations. Simulations by Béthermin et al. (2017) find at 500 μm the brightest galaxy only contributes on average 60% to the total Herschel 500 μm flux density (though this is also a function of 500 μm flux, and above $S_{500} = 60\ mJy$ they find almost all sources should be single galaxies, see Figure 6 of Béthermin et al. (2017)). They go on to show that by invoking multiple sources within the 500 μm SPIRE beam, they can account for the excess of red galaxies. Donevski et al. (2018) meanwhile select 133 500 μm risers over 55 deg^2 from the Herschel Virgo Cluster Survey (Davies et al., 2010, 2012), finding a median redshift and FIR luminosity of $\bar{z} = 4.28$ and $\bar{L}_{FIR} = 1.98 \times 10^{13} L_{\odot}$. They find good agreement with models from (Béthermin et al., 2017), and additionally find that the inclusion of both confusion and instrumental noise can increase the fraction of observed 500 μm risers by a factor of 3, though they note this increase comes primarily from both true 500 μm risers just below the flux limit and from sources with $S_{250} < S_{350}$ and $S_{350} \approx S_{500}$). By simulating SPIRE maps using the models of Béthermin et al. (2017), they go on to show that the brightest source only contributes, on average, 75% and 64% of the 250 and 500 μm flux respectively.

Both Béthermin et al. (2017) and Donevski et al. (2018) propose that a combination of resolution effects and noise can explain the discrepancy between models and observations of the number of 500 μm risers. As such, one might expect that a significant fraction of 500 μm risers are composed of multiple galaxies. Whilst numerous inteferometric studies of Herschel sources have been performed (Karim et al., 2013; Hodge et al., 2013; Swinbank et al., 2014; Simpson et al., 2015; Oteo et al., 2017; Hill et al., 2018), most of these statistical studies have sampled from SMGs selected at 850 μm and not from Herschel selected sources. Oteo et al. (2017) however perform ALMA observations on 500 μm risers selected from (Ivison et al., 2016). They find that 27 of their sample of 44 single dish sources (61%) are single sources, whereas the remaining 16 sources (39%) split into multiple galaxies. Additionally, they find several sources with multiplicities > 3, and one source where a single Herschel source resolves into 5 galaxies in the ALMA maps. This may not be too surprising; given both our results in Chapter 2 and studies which suggest 500 μm risers are likely associated with high-z overdensities / protoclusters (Lewis et al., 2017), some of these sources may represent clusters of DSFGs, clustered on the scale of the Herschel beam (De Breuck et al., 2017; Oteo et al., 2018). Though the number of 500 μm risers are in excess of models, they find their observations at 850 μm are in agreement with models of number counts at 850 μm. They ascribe the simultaneous poor agreement at 500 μm with the good agreement at 850 μm to a combination of flux boosting in the SPIRE maps, and clustering of multiple sources within the SPIRE beam.

Given all of this, the high resolution study of 500 μm risers can provide constraints on models, particularly the multiplicity of such sources and the relative contribution of multiple sources to the single dish flux observed flux density. Furthermore, there are strong predictions from these models about the multiplicity of Herschel-SPIRE sources, in particular that for sources with $S_{500} > 60\ mJy$, they should almost entirely be lensed single galaxies, a prediction not borne out by the results of Oteo et al. (2017). This chapter details the results of an interferometer follow up of 34 500 μm risers using the Sub-Millimeter Array (SMA, Ho et al. (2004)). Several of these sources have been presented elsewhere (Riechers et al., 2013; Dowell et al., 2014), but this Chapter represents the first uniform reduction of the data to examine the statistical properties of this population at resolutions of ~ 2 arcsec.

3.2 Target Selection

All 34 500 μm risers had been selected from the HerMES survey (Oliver et al., 2012), and from both preliminary and published maps and catalogues. As such, their selection is hetrogenous in the sense that no clear or consistent flux density or colour cut was used to select sources

Map	RA	DEC	Date	Freq [GHz]	Config	Project Code
HFLS1	17:08:17.67	58:28:45.11	05/19/10	270	Compact	2010A-S035
			03/14/11	265	SubCompact	2010B-S042
			03/23/11	265	SubCompact	2010B-S042
			08/02/11	265	Extended	2011A-S053
HFLS3	17:06:47.69	58:46:23.88	05/12/10	270	Compact	2010A-S035
			03/14/11	265	SubCompact	2010B-S042
			03/23/11	265	SubCompact	2010B-S042
			08/02/11	265	Extended	2011A-S053
			08/03/11	345	Extended	2011A-S053
			07/06/11	336	SubCompact	2011A-S053
			09/06/11	336	Very Extended	2011A-S053
Lock2	10:53:10.92	56:42:06.84	05/12/10	270	Compact	2010A-S035
			03/14/11	265	SubCompact	2010B-S042
			03/23/11	265	SubCompact	2010B-S042
			02/14/12	345	Extended	2011B-S020
HFLS5	17:20:49.49	59:46:27.12	05/19/10	270	Compact	2010A-S035
			03/14/11	265	SubCompact	2010B-S042
			03/23/11	265	SubCompact	2010B-S042
			08/02/11	265	Extended	2011A-S053
Lock5	10:51:32.09	56:36:17.64	05/19/10	270	Compact	2010A-S035
			03/14/11	265	SubCompact	2010B-S042
			03/23/11	265	SubCompact	2010B-S042
			02/14/12	345	Extended	2011B-S020
XMM_M2	02:25:15.10	-02:47:09.20	12/08/11	345	Compact	2011B-S038
XMM_R7	02:29:29.32	-04:42:17.00	12/08/11	345	Compact	2011B-S038
XMM_M7	02:26:44.76	-03:25:05.50	12/08/11	345	Compact	2011B-S038
XMM_M5	02:18:56.74	-04:35:44.90	12/09/11	345	Compact	2011B-S038
XMM_R3	02:26:05.19	-03:18:28.10	12/09/11	345	Compact	2011B-S038
XMM_R2	02:17:43.86	-03:09:11.20	12/09/11	345	Compact	2011B-S038
XMM_26	02:25:45.31	-02:59:16.10	11/27/12	265	Compact	2012B-S018
XMM_81	02:21:57.82	-04:12:25.60	11/27/12	265	Compact	2012B-S018
XMM_65	02:18:57.91	-03:35:05.60	11/27/12	265	Compact	2012B-S018
LSW_28	11:01:27.29	56:19:31.40	11/27/12	265	Compact	2012B-S018
LSW_73	10:56:19.61	56:53:50.60	11/27/12	265	Compact	2012B-S018
LWS_52	10:55:48.89	57:33:57.24	11/27/12	265	Compact	2012B-S018
Bootes_27	14:38:45.14	33:22:31.80	03/19/13	265	Compact	2012B-S018
Bootes_33	14:31:32.11	34:21:16.60	03/19/13	265	Compact	2012B-S018
Bootes_13	14:35:43.51	34:47:42.70	03/19/13	265	Compact	2012B-S018

Table 3.1: The positions, dates, frequencies, array configurations, and project codes for the 34 SMA observations of HerMES selected 500 μm risers, ordered roughly by the date of observation. A list of the SPIRE fluxes at the positions of these sources in given in Table 3.2.

Map	RA	DEC	Date	Freq $[GHz]$	Configuration	Code
Lock_102*	10:40:50.64	56:06:53.84	03/02/13	302	Compact	2012B-S078
			01/19/13	302	Extended	2012B-S078
			02/03/13	302	Very Extended	2012B-S078
HeLMS_28	00:44:09.94	01:18:28.40	07/02/13	265	Compact	2013A-S005
HeLMS_12	00:52:58.52	06:13:18.80	07/02/13	265	Compact	2013A-S005
HeLMS_34	00:22:21.16	-01:55:21.70	07/02/13	265	Compact	2013A-S005
HeLMS_493	23:54:11.79	-08:29:12.00	07/15/13	265	Compact	2013A-S005
HeLMS_45	00:03:04.39	02:40:49.80	07/15/13	265	Compact	2013A-S005
HeLMS_62	00:55:17.18	02:04:01.20	07/15/13	265	Compact	2013A-S005
HeLMS_32	23:24:35.09	-05:24:51.80	07/09/13	265	Compact	2013A-S005
HeLMS_783	00:41:29.86	-02:47:48.10	07/09/13	265	Compact	2013A-S005
HeLMS_11	00:29:36.26	02:07:09.80	07/09/13	265	Compact	2013A-S005
Bootes_15	14:40:09.66	34:37:55.70	06/30/14	346	Compact	2014A-S092
Bootes_24	14:36:21.30	33:02:29.00	06/30/14	346	Compact	2014A-S092
Cosmos_9	10:02:49.11	02:32:57.40	11/28/14	231	Compact	2014A-S092
HeLMS_35	00:21:15.55	01:32:58.60	05/07/15	345	Compact	2014A-S092

Table 3.1: Continued

for follow up. They were however all selected on the basis of their very red SPIRE colours at the time. They have 500 μm flux densities that range from 27 to 160 mJy, with an average of 67 ± 29 mJy. Our sources were observed over a number of years, from 2010 to 2015, mostly in compact configuration, and sources were mostly observed either at 270 GHz (1.1 mm) or 345 GHz (870 μm) A full list of our targets, the frequency at which they were observed, the array configuration, and dates, are available in Table 3.1. As can be seen, the precise observed frequencies vary, and for consistency we will generally refer to them as 270 GHz or 345 GHz observations, rather than the precise observation frequency for each map. During all the observations, the PWV was required to be < 2.5 mm (i.e. $\tau_{225\ GHz} < 0.134$).

For consistency, we eventually extract the SPIRE fluxes from the latest versions of the HerMES maps[2] and catalogues. These values can be viewed in Table 3.2, and include the SMA detections (See next Section). As can be seen, later versions of maps and catalogues mean that some sources, such as Lock2, HeLMS35, and HFLS5, were no longer strictly classed as 500 μm risers. However, we include them here as their initial selection was as a 500 μm riser, and investigations by Donevski et al. (2017) and Béthermin et al. (2017) have shown that there can be a significant

[2]Specifically data release 4

contamination of selected 500 μm risers by flux boosted sources with $S_{500} \lessapprox S_{350}$.

By selection, our 34 sources are bright at 500 μm, with five sources that have $S_{500} > 100\ mJy$, the canonical criteria for selecting lensed Herschel sources (Wardlow et al., 2013; Negrello et al., 2017). Several of our sources below this limit are also known to be lensed, such as HFLS3 (Cooray et al., 2014), whilst others have previously been selected as candidate lenses such as Lock2 (Wardlow et al., 2013). Béthermin et al. (2017) meanwhile suggest most $\mathrm{S}_{500} > 60\ mJy$ sources will be single sources, as they claim these will be almost entirely local or lensed galaxies. Half of our sources (17/34) do have this property, and a further 6 sources have $\mathrm{S}_{500} > 40\ mJy$, so we may expect a significant number of our sources to be lensed. Given that most of our observations took place in compact or subcompact array configurations, it is unlikely however that we will be resolving the source (see next Section). The effect of lensing on our results is discussed further in Section 3.4.

3.3 Methods

3.3.1 Interferometry

Rather than directly measuring the real space brightness distribution on the sky, an interferometer measures the interference pattern produced by a number of pairs of apertures. Under certain conditions, namely that a source is spatially incoherent, that the bandwidth is quasi-monochromatic, and that a source is far away, by correlating (multiplying then averaging) the voltage response of each pair of antenna, it is possible to sample the Fourier transform plane (commonly referred to as the visibilities) of the real space brightness distribution. The domain of this Fourier transform plane is known as the UV plane, where U and V give the projected baseline lengths of each antenna pair in terms of the number of wavelengths in the east-west and north-south directions respectively. An interferometer utilises a number of antennae with different baselines, as well as the rotation of the Earth, to sample as much of this plane as possible. The interferometer beamshape can then be thought of as the Fourier transform of the sampling function in the UV plane (i.e. the convolution of the interferometer beam with the true sky brightness distribution is equal to the multiplication of the UV plane sampling function with the visibilities).

In this Section, we will often refer to "dirty" or "clean" maps. As the UV plane will not be fully sampled by our observations, the Fourier transform of the UV plane (i.e. the image plane) will be missing certain Fourier components. This leads to maps with a large number of sidelobes, and is typically refereed to as the "dirty" map. One can further "weight" the samples in the UV plane to reduce sidelobes / improve signal to noise. Two common weighting schemes are the "natural" weighting scheme, which weights each sample in the UV plane by the inverse of the noise variance of each sample, and the "uniform" weighting scheme, which gives a weighting inversely proportional to the sample density (i.e. more dense regions of sample space, typically towards the centre of the UV plane and therefore shorter baselines and lower resolutions). Natural weighting tends to improve signal to noise at the cost of resolution, whilst uniform weighting does the reverse.

The sidelobes in the dirty beam are often problematic, and can make it difficult to understand the images. Though there are an infinite number of solutions to the missing samples in the UV plane, several algorithms have been developed to reproduce the likely "correct" solution, and therefore reproduce the actual image plane. The most common of these is the CLEAN algorithm (Hogbom, 1974). In this algorithm, the highest peak in the dirty map is identified, and a scaled ($<< 1$) version of the beam is removed at this point, with both the position and flux density added to a new blank map, called the CLEANed map. This is repeated, with further points and flux density being added to the CLEANed map, until a pre-defined criterion is met, usually either after a user-specified number of iterations or when the absolute maximum residual in the dirty map falls below a certain user-specified, value. The CLEANed map is then convolved with a model of the beam, which usually assumes the beam can be modeled as the central peak of the beam, further assumed to be a 2 dimensional Gaussian. This produces a map which should then be free of most sidelobes, and is a reasonable representation of the "true" image plane.

3.3.2 Data Reduction

Each of the maps were reduced using the IDL based SMA data reduction package MIR[3], uniformly in the following way. The data were manually inspected, and any location where individual integrations, spectral bands, baselines or antenna suddenly showed significant flux density offsets or phase changes were flagged and removed from the data. The passband calibrators included the bright QSOs 3c279, 3c454.3, 3c84, and BLlac, whilst the flux calibrators included Titan, Uranus, Neptune, Callisto, and Ganymede. Gain calibration was done by periodically observing one to two nearby reasonably bright QSOs with known flux densities at 270 and/or 345 GHz. The total calibration process has a well known error, which is typically around 10%. After calibration, the continuum was generated by averaging all the spectral channels which were not flagged in the inspection step, and the maps were then exported to the data analysis package MIRIAD (Sault et al., 2011) for further reduction.

We used the MIRIAD command INVERT to transform the visibilities into (dirty) maps, choosing a natural weighting (i.e. constant weight to all visibilities) as this maximises the signal to noise of any sources present. We then CLEANed our maps, using 1000 CLEAN iterations. The noise level varies between maps, but on the CLEANed maps was typically around 1.5 $\pm$ 0.5 mJy, with minimum and maximum values of 0.5 mJy and 2.9 mJy respectively. We eventually extract on the dirty maps rather than the CLEANed maps (see next Section), and for the dirty maps our noise values had a mean of 2.2 $\pm$ 0.9 mJy, with minimum and maximum values of 0.8 mJy and 4.9 mJy respectively. The beamshape also varied between maps, and by assuming a Gaussian shape for the central part of the beam, had an average FWHM of 2.5 $\pm$ 0.8 arcsec. At $z = 4$, the expected redshift of our 500 μm risers, this corresponds to 17.5 kpc, and so is unlikely to resolve our sources. Additionally, if multiple sources / signs of lensing such as arcs are within $\sim$ 2.5 arcsec of each other, we would not necessarily resolve them. Experiments were performed using other different weighting schemes and cleaning parameters, both using the data and simulations (see next Section) but we found our above selection generally performed best at recovering the most flux density. These noise levels and beamsizes in

[3] `https://github.com/qi-molecules/sma-mir`

our maps are in reasonable agreement with what Hill et al. (2018) found in their recent SMA reduction of a number of SCUBA-2 selected sources. The resulting dirty maps, the beamshape, and the CLEANed maps for all 34 of our 500 μm risers are shown in Figure 3.1.

3.3.3 Source Extraction

The CLEAN process can bring out noise spikes that, after cleaning, can mimic the appearance of a real source (Glen Petitpas[4], private communication). In Figure 3.2, we replicate this phenomenon and are able to create a 6.5σ detection in the CLEANed map using just random noise. It is therefore important, before extracting sources from our reduced maps, to understand how strong this effect is for different extraction procedures and parameters.

To determine the most reliable method of source extraction, we perform the following steps. First, for each of our 34 maps, we create 1,000 fake maps filled with Gaussian noise. These are then convolved with the beam for that map, and this fake dirty map is scaled until the noise properties match those of the original dirty map (i.e. same mean and standard deviation). For each of our 34 real maps, this provides 1,000 realisations of a map with no sources within it. These 34,000 maps are then CLEANed using the same parameters as in the previous Section, and sources are then extracted from them in the following way. First, the highest SNR peak in the CLEANed map is identified, using the rms error from all the pixels in the map. The flux density, RA, DEC, and SNR in the clean map are all extracted at the position of the source, and the flux error is taken as the global rms error. Additionally, the flux density, SNR and estimate of the error are also extracted from the dirty map at the same position. A flood fill algorithm is then applied at the position of the source, setting all connected pixels with signal to noise ratios in the CLEANed map $> 2\sigma$ to zero. The global rms is *not* recalculated after this process. The next highest signal peak is then identified, until no peaks $> 3\sigma$ are found.

By construction, none of these maps contain any real sources. To determine the best way to extract sources from our real maps, we therefore look to minimise the number of fake sources we

[4]Harvard-Smithsonian Center for Astrophysics, Smithsonian Astrophysical Observatory, Submillimeter Array Project Cambridge, MA 02138 U.S.A.

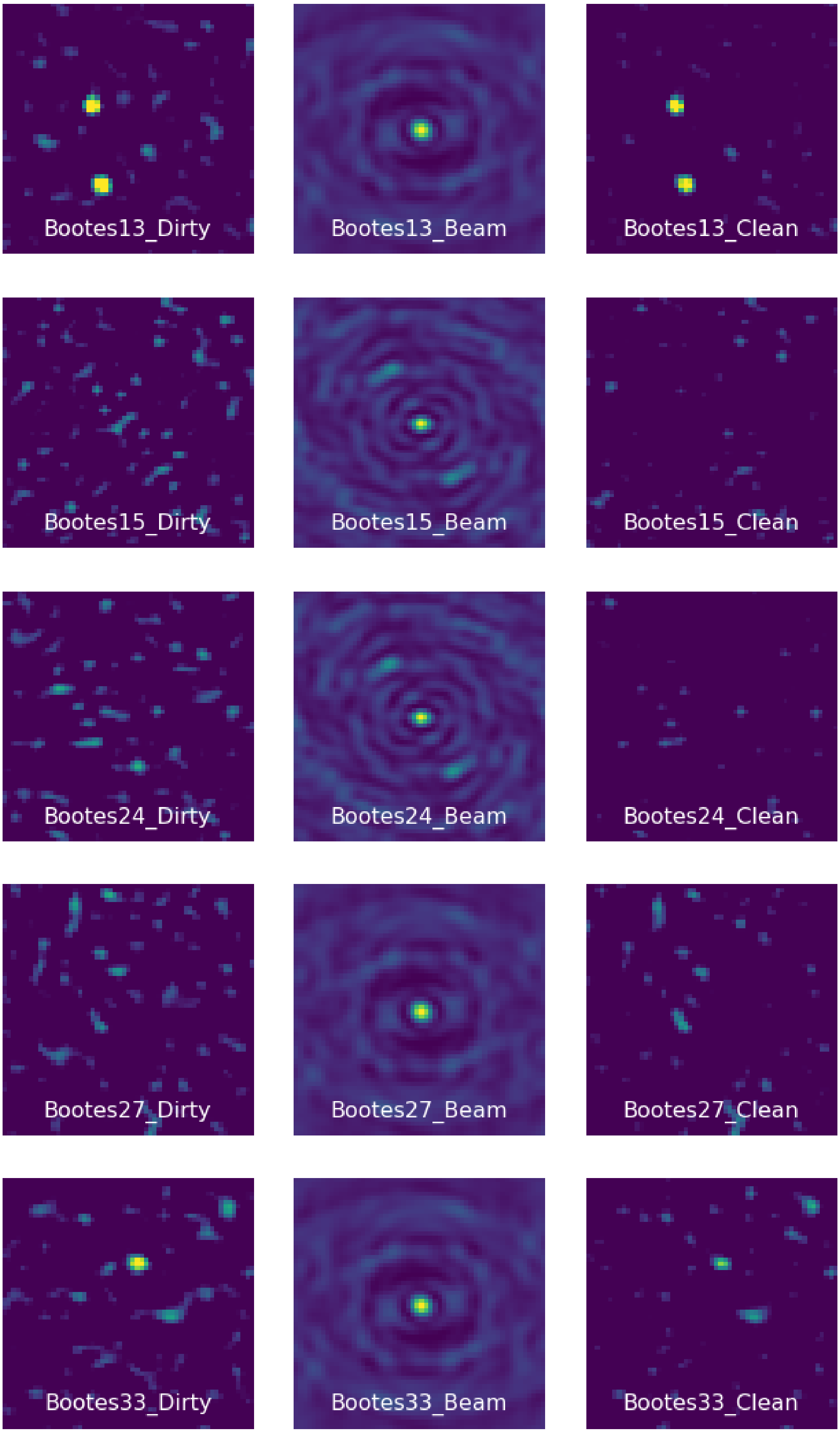

Figure 3.1: Images of the dirty (left), beam (middle) and CLEANed (right) maps of the 34 sources under consideration here. The colour scheme in the dirty and clean maps ranges ranges between 1 and 5σ, using the rms on the dirty map. Maps which include the _COM_ label indicate where we have only included the visibilities from the compact or subcompact array configurations (see text for more details).

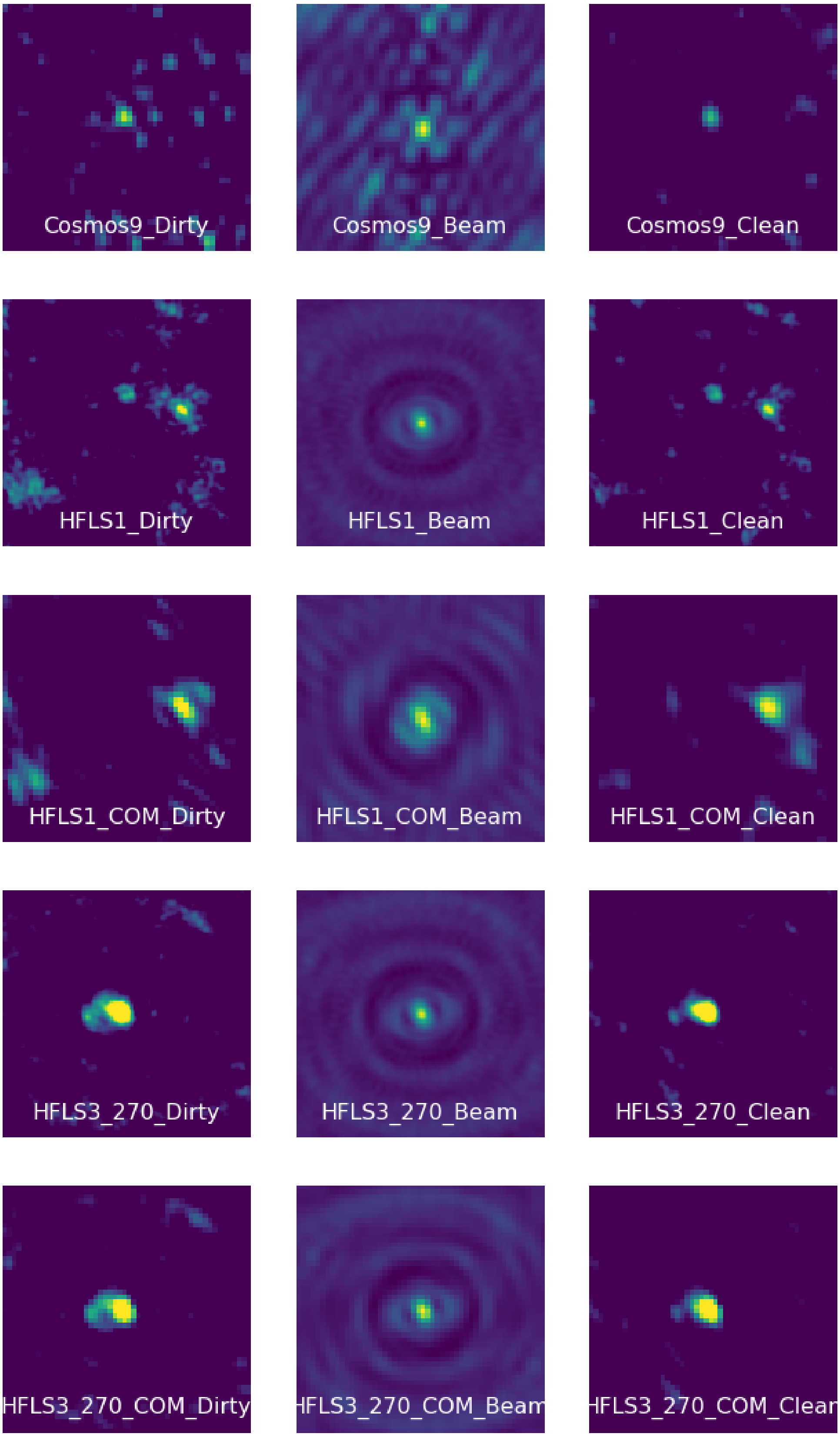

Figure 3.1: **Continued**

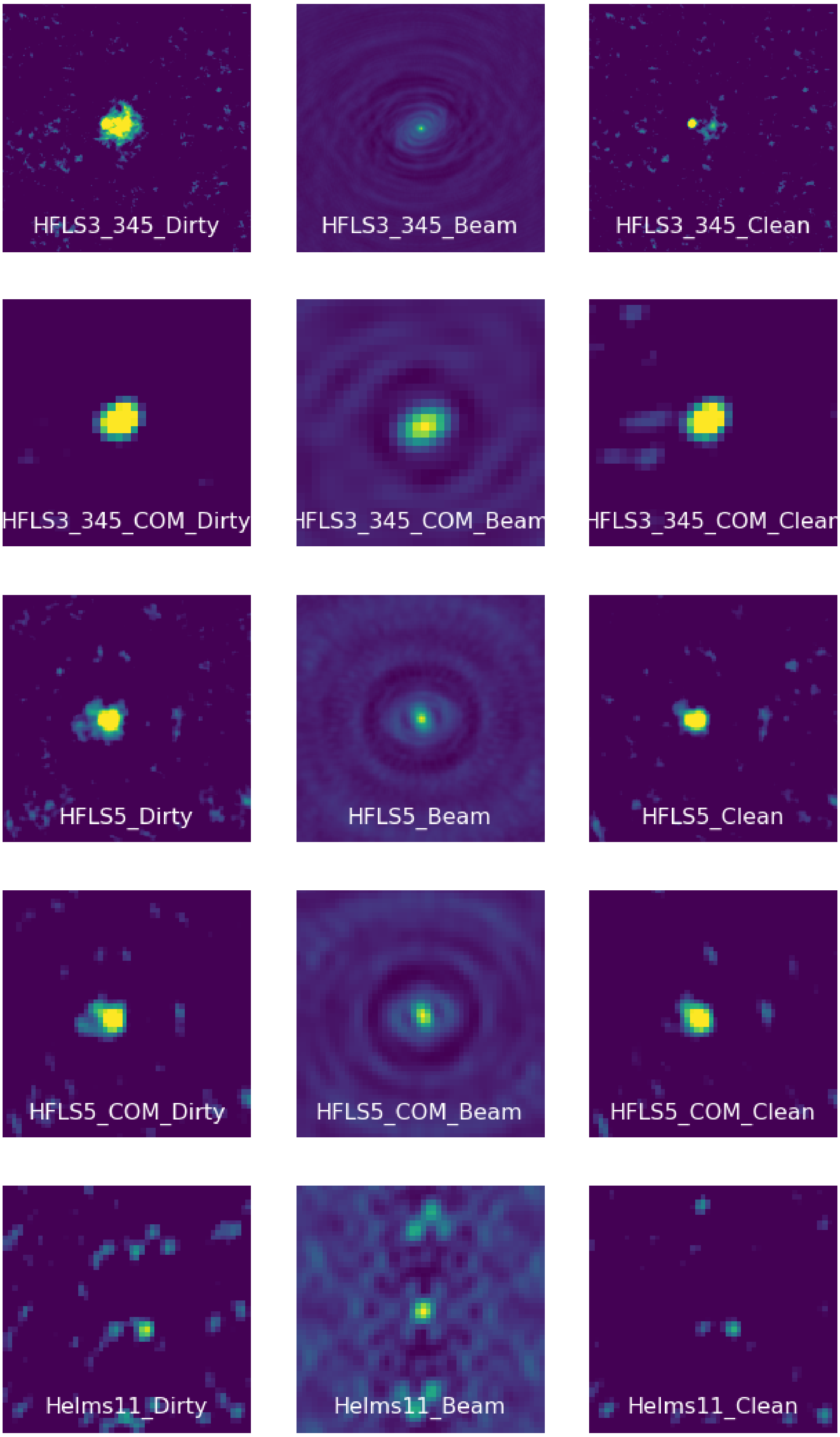

Figure 3.1: **Continued**

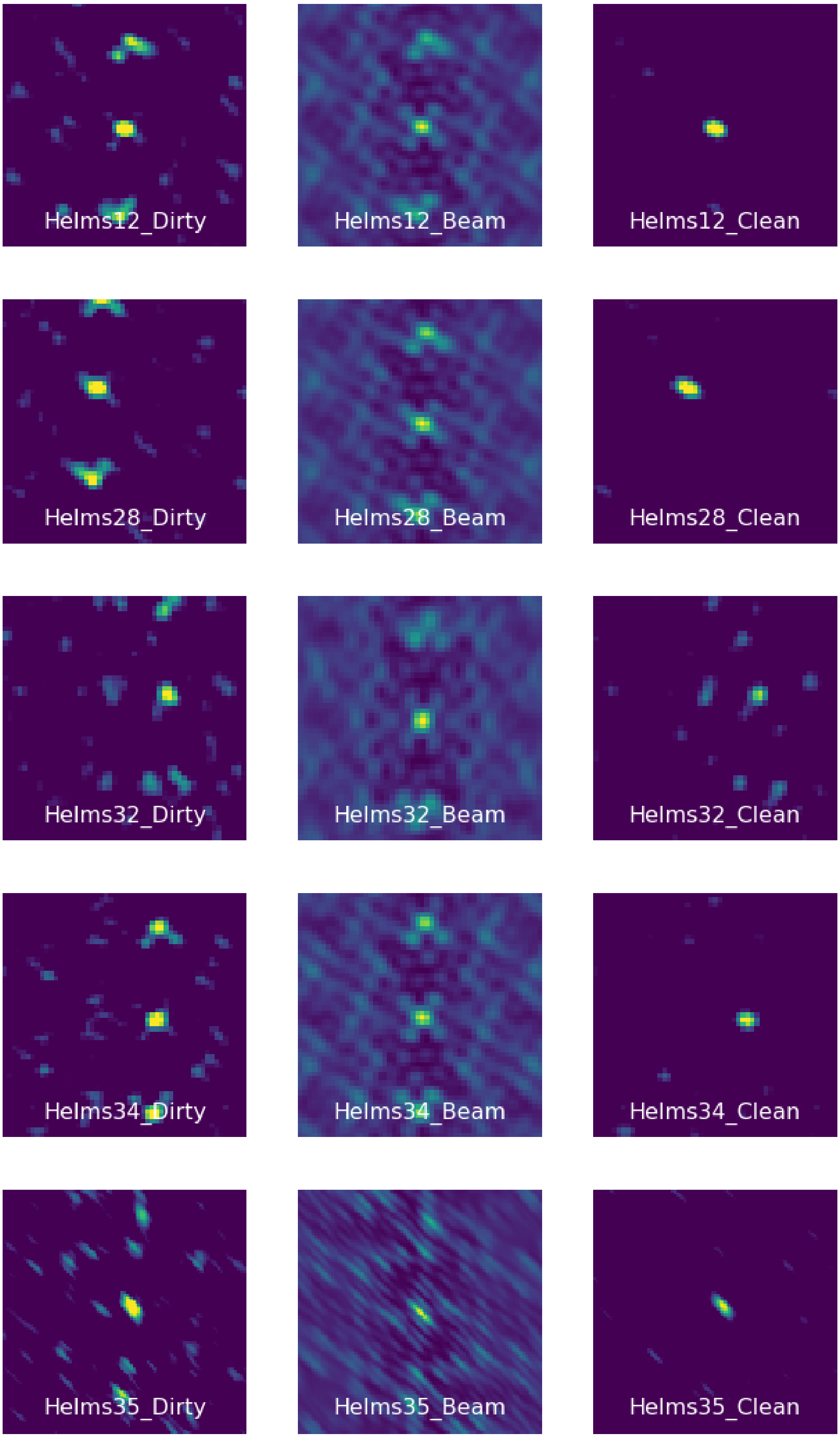

Figure 3.1: **Continued**

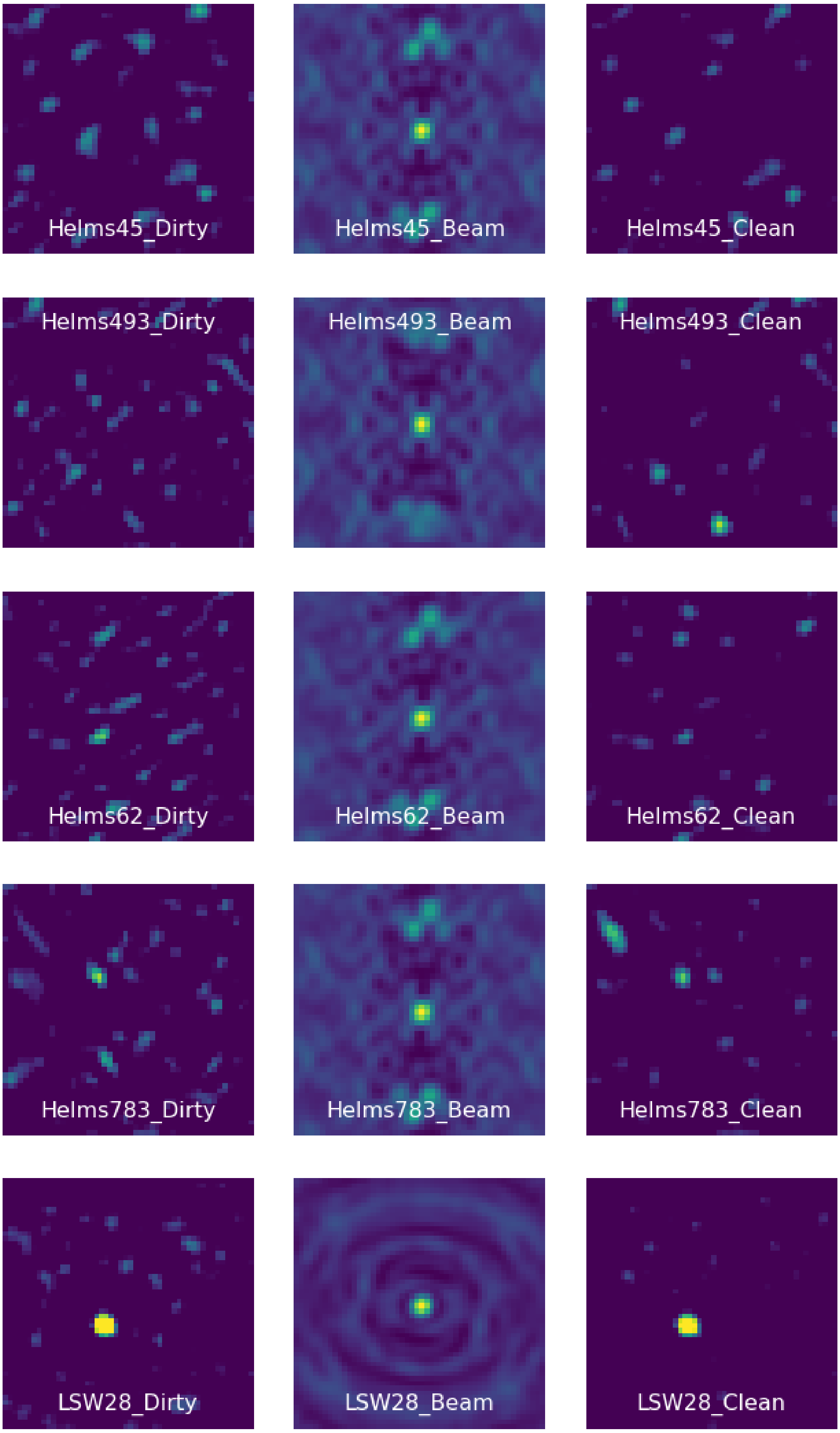

Figure 3.1: **Continued**

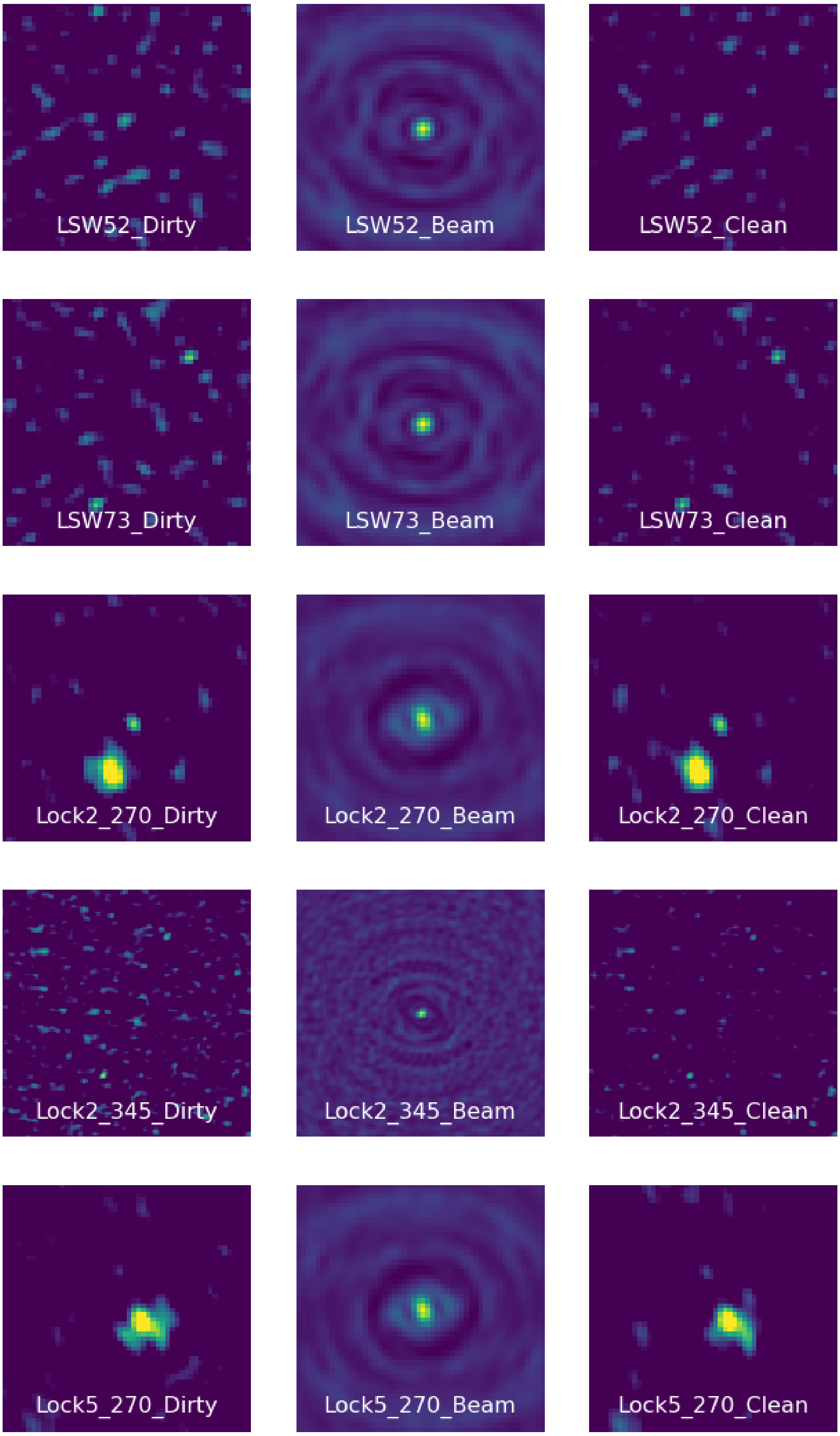

Figure 3.1: **Continued**

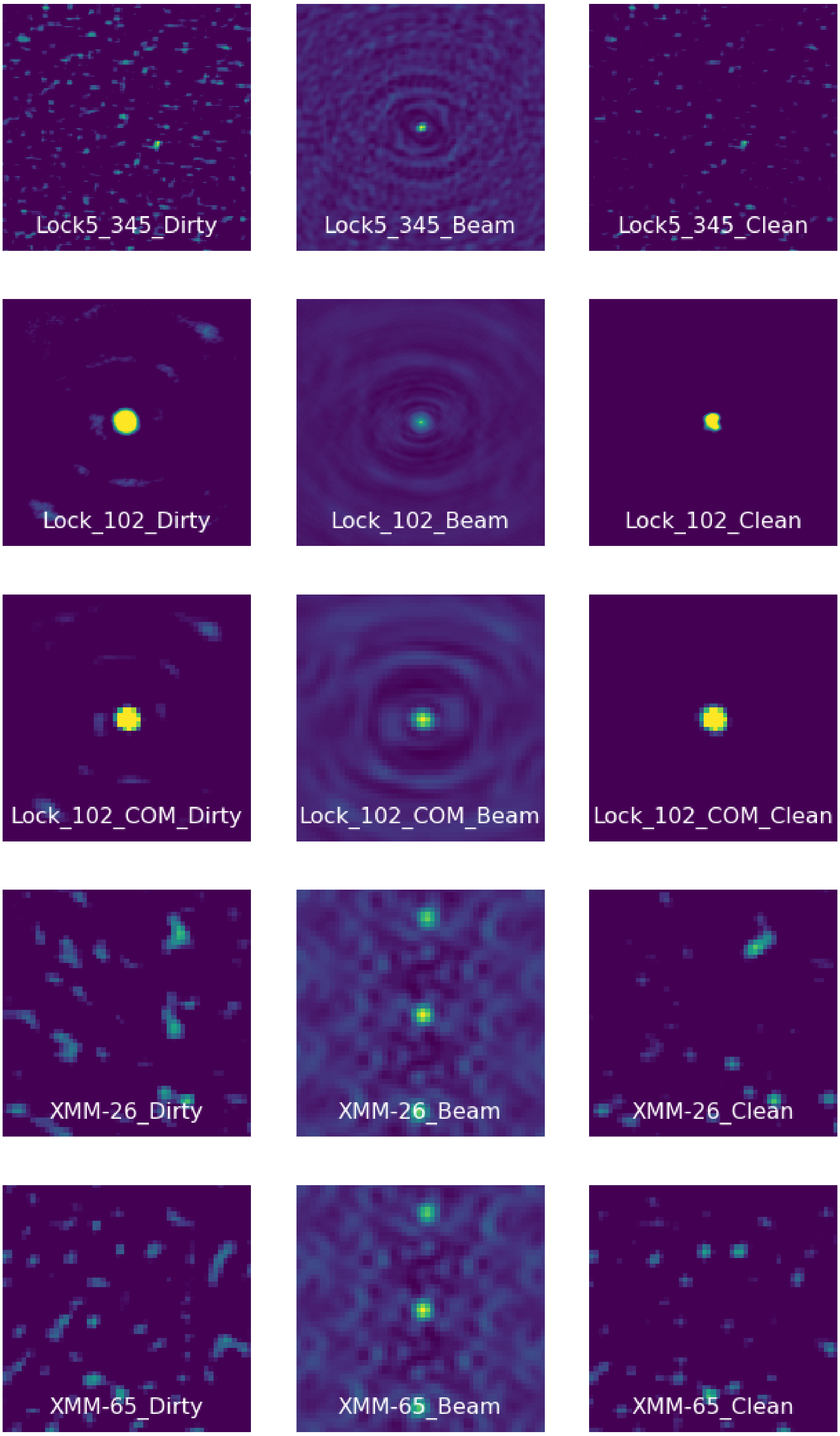

Figure 3.1: **Continued**

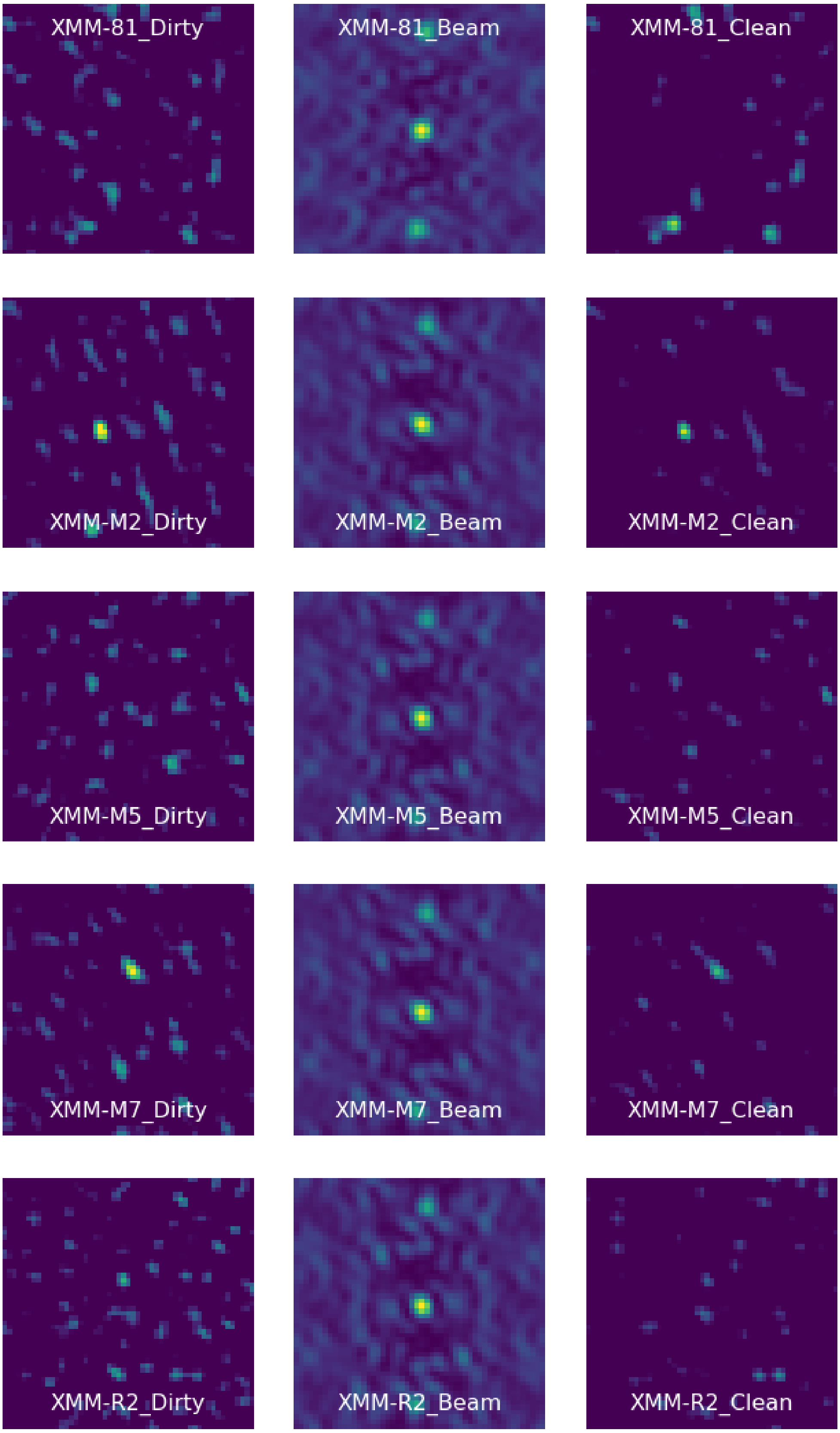

Figure 3.1: **Continued**

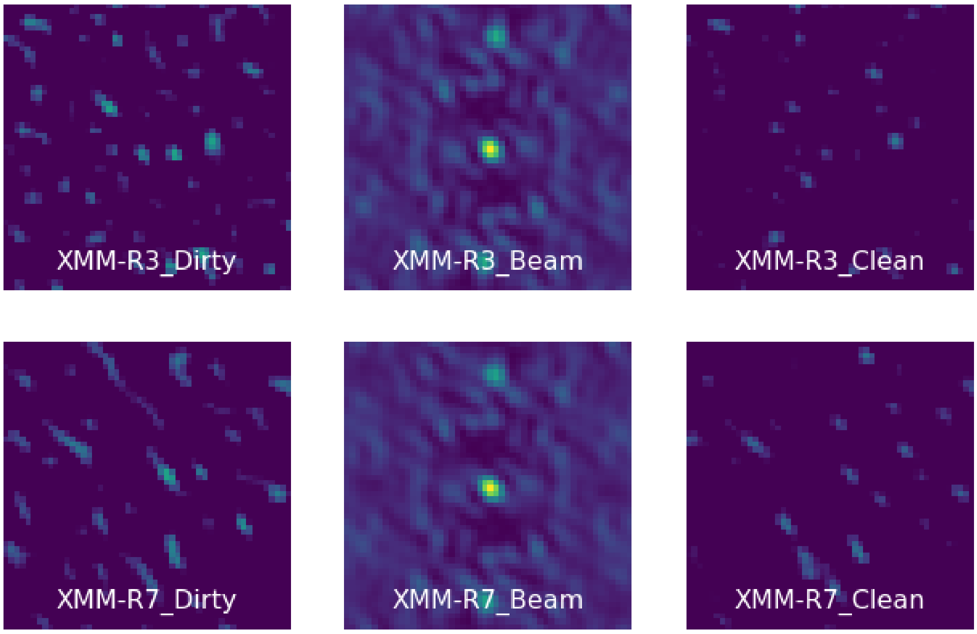

Figure 3.1: **Continued**

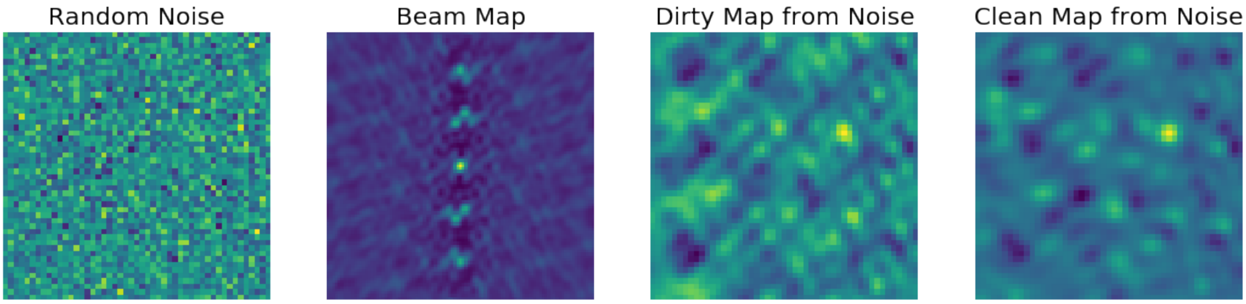

Figure 3.2: A fake source generated from Gaussian noise. *(Left)* Random Gaussian noise with the same properties as the HeLMS62 map. A single 3.5σ pixel is present. *(Middle left)* The HeLMS62 observation beamshape. *(Middle right)*, the random noise on the left convolved with the beam. A 4.0σ detection is now present. (Right) The map after cleaning. The single 3.5σ pixel on the left is now a 6.5σ detection in the CLEANed map.

detect, whilst simultaneously minimising the signal to noise ratio threshold used for inclusion into our catalogue. We examined four separate measurements of the detection strength of a source, one based on the ratio between the peak flux density to the noise in the whole (global) CLEANed map, one on the ratio based on the noise within 1 - 2 beam FWHM radii of the source position, and two similar signal to noise ratios, but using the dirty map instead of the CLEANed map. We found that the global signal to noise ratio measured on the dirty map performed best, with only 0.09% of fake sources detected at $> 5\sigma$, compared to the global and local measurements on the clean map, which had 4 and 16% of fake sources detected at $> 5\sigma$, and the local measurement on the dirty map, which had 2% of fake sources detected at $> 5\sigma$.

On the left of Figure 3.3, we examined the average number of fake sources we detect using our extraction routine, as a function of the signal to noise on the dirty map and for each of the 34 maps individually. As can be seen, there are significant differences between the 34 maps, likely due to the difference in the beamshapes. To ensure good reliability, we choose a cutoff such that there will be, on average, 0.1 fake sources per map. The cutoff that ensures this requirement is met varies between maps, and for each map we use the value corresponding to it, but on average this value is $\sim 3.69\sigma$, where σ gives the global noise on the dirty map. For each of our 34 maps, we therefore repeat the extraction process outlined above, but at the end apply this cutoff. Over our 34 real maps, we would then expect to detect 3.4 ± 1.8 spurious, low S2N sources.

To test our extraction procedure we injected fake sources into our real maps and attempted to recover them. To do this, we took the 34 dirty maps, cloned them each 1,000 times, and injected a point source that had been convolved with the beam into the map, with an injected flux uniformly between 0 and 30 mJy. We required that any injected source was at least 5 arcsec away from any detected source in the map. These maps were then CLEANed using the same procedure as above, and sources extracted from them. Once again there were significant variations between the maps, with maps with more complex beams (i.e. HeLMS28) performing more poorly than beams with better UV coverage (i.e. Bootes13) but we found on average we were able to recover 65.3% of sources. Of the remaining 34.7% of sources, most are faint, with only 6.6% having flux densities > 10 mJy, and usually these are in maps where a bright source is already present, raising the global noise. We additionally used our injected sources to examine two alternative methods for extracting the flux density of sources, by using Gaussian fitting or by fitting a point source to the dirty map (i.e. fitting the beam to the dirty map at the position of the peak pixel). We found that when comparing our injected to extracted flux densities, extracting at the peak position minimised the average difference between the injected and extracted flux densities, compared to both Gaussian fitting and fitting point sources. We note that the injected sources were point sources, and that these alternative methods may be better for resolved sources. However, as we noted in the previous Section, at our resolution we generally do not expect to resolve our sources. On the right of Figure 3.3, we plot the (recovered - injected) to injected flux density ratio of our sources. We find good agreement at injected flux densities $> 10 - 15$ mJy. Below this, the injected flux is within a few standard deviations of the noise values of most of our maps, and whilst the recovered flux density is generally within 2σ of the injected flux, the (recovery - injected) to injected flux density ratio diverges.

In our maps where we additionally have extended or very extended observations, we found that when combining the visibilities from these extended observations and the compact/subcompact observations that our recovered flux was significantly lower than compared to when we only used the compact observations. The precise reasons for this remain unclear, and it may be on these maps we are partially resolving the source, but for now we extract flux densities only using visibilities from compact or subcompact observations. In Figure 3.1, these are indicated with the addition of "_COM_" to the map name.

Map	Detections	D_{map}Lim [mJy]	F250 [mJy]	F350 [mJy]	F500 [mJy]	E250 [mJy]	E350 [mJy]	E500 [mJy]
Bootes13	2.0	4.80	54.11	80.64	81.80	7.77	8.05	8.29
Bootes15	0.0	7.01	51.22	68.27	66.06	6.00	7.00	8.00
Bootes24	0.0	8.98	28.74	49.65	55.83	6.00	7.00	8.00
Bootes27	0.0	3.87	37.84	0.00	52.24	6.00	7.00	8.00
Bootes33	1.0	4.11	49.96	60.92	57.04	8.08	8.71	7.95
Cosmos9	1.0	2.81	20.64	32.94	47.57	6.13	5.85	6.88
HFLS1	1.0	10.40	51.58	82.40	82.78	9.76	10.26	9.67
HFLS3_270	1.0	7.09	15.18	33.42	52.79	6.71	8.00	9.25
HFLS3_345	1.0	11.28	15.18	33.42	52.79	6.71	8.00	9.25
HFLS5	1.0	6.20	24.76	53.02	45.82	8.44	9.24	9.13
HeLMS11	1.0	7.71	83.85	89.59	110.35	15.58	14.86	17.52
HeLMS12	1.0	17.74	76.90	122.46	138.65	16.67	16.61	17.28
HeLMS28	1.0	16.83	91.18	137.84	160.47	14.91	14.16	16.94
HeLMS32	1.0	8.05	36.00	61.45	72.38	15.97	14.76	16.94
HeLMS34	1.0	13.13	66.71	90.66	106.74	14.68	14.40	15.95
HeLMS35	2.0	11.08	54.15	91.00	68.62	15.88	15.52	17.85
HeLMS45	0.0	10.76	32.00	59.00	82.00	14.00	15.00	16.00
HeLMS493	0.0	7.87	35.00	56.00	68.00	14.00	15.00	16.00
HeLMS62	1.0	10.55	35.97	30.58	40.95	27.39	16.99	17.12
HeLMS783	1.0	6.20	42.03	46.62	60.95	14.99	15.02	17.00
LSW28	1.0	6.97	41.03	65.12	66.85	11.80	11.89	13.22
LSW52	0.0	4.34	16.27	32.96	40.16	6.00	7.00	8.00
LSW73	2.0	3.89	19.30	27.37	35.70	8.35	8.57	7.71
Lock2_270	2.0	5.14	41.42	66.99	65.08	7.57	7.86	8.08
Lock2_345	1.0	11.63	41.42	66.99	65.08	7.72	7.99	8.08
Lock5_270	1.0	4.61	17.52	38.12	44.05	8.26	9.14	8.89
Lock5_345	1.0	11.04	17.52	38.12	44.05	8.26	9.14	8.89
Lock_102	1.0	15.35	64.03	105.54	122.73	6.27	6.70	7.08
XMM-26	1.0	7.34	45.73	67.83	81.58	11.89	9.57	8.84
XMM-65	0.0	6.25	0.00	24.59	42.28	6.00	7.00	8.00
XMM-81	0.0	6.79	0.00	9.44	28.54	6.00	7.00	8.00
XMM-M2	1.0	9.36	44.45	54.12	67.60	8.69	9.88	9.41
XMM-M5	0.0	9.06	26.58	43.95	46.14	6.00	7.00	8.00
XMM-M7	1.0	9.81	39.72	60.26	57.63	7.35	8.15	9.31
XMM-R2	0.0	9.22	23.03	32.81	40.25	6.00	7.00	8.00
XMM-R3	0.0	9.00	22.28	34.87	37.64	7.94	8.69	9.72
XMM-R7	0.0	8.07	14.32	24.93	37.32	9.71	9.32	8.96

Table 3.2: The number of detections in each of the 34 maps, including the threshold used for detections on the dirty map, D_{map}Lim. SPIRE flux densities, in mJy, are given by extractions on the SPIRE maps at the positions of the sources. For sources where we have observations at multiple frequencies (HFLS3, Lock2 and Lock5), we split our maps into different frequencies and detect independently in both of them. In HFLS3, Lock2 and Lock5, we observe the source at both 270 GHz and 345 GHz, hence our extracted SPIRE values repeat for these sources.

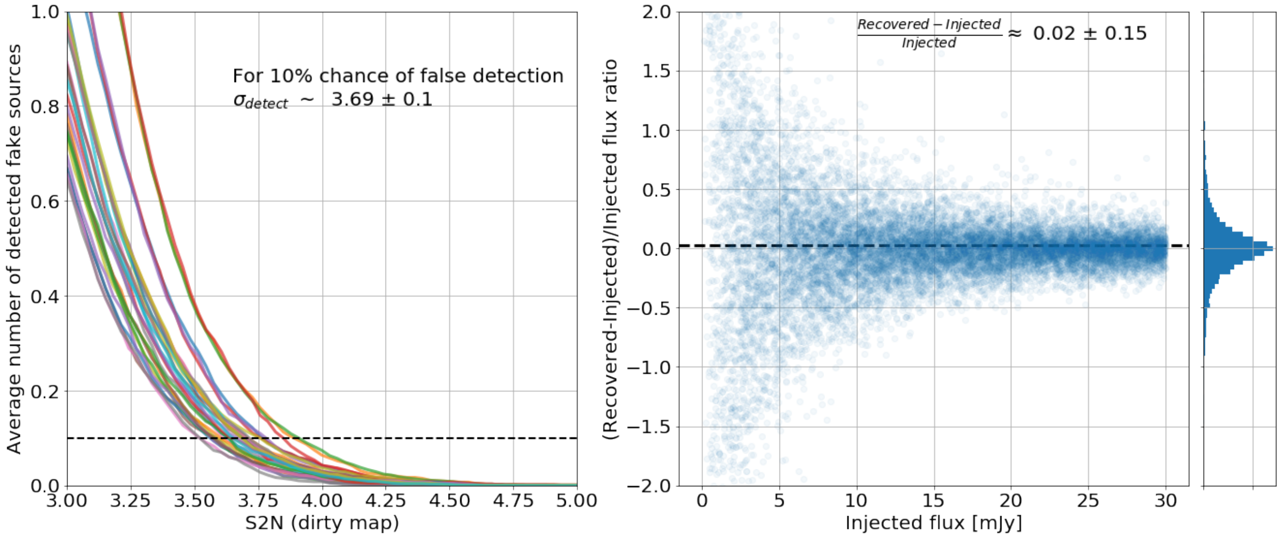

Figure 3.3: *(Left)* The average number of detected fake sources detected as a function of S2N in the dirty map, for each of the 36 maps under consideration here. The coloured lines show the different maps, whilst the horizontal dashed lines shows the S2N required for their to be, on average, 0.1 fake detected sources per map. *(Right)* The recovered / injected flux ratio for fake sources injected into the real maps. The dashed horizontal line shows the mean value of the ratio, as does the text in the top right. The histogram to the right shows the distribution of flux density ratios.

3.3.4 The Detected Sources

Using the procedure outlined above, we then extract sources from our 34 maps, using the parameters derived above. We list the detected sources individual in Table 3.3, whilst in Table 3.2 we list the number of detections per map, alongside the original SPIRE flux densities.

We detect a total of 29 sources across 37 maps (34 maps plus 3 maps observed at both 270 and 345 GHz, where we extract independently in both maps). Of the 37 maps, 12 (35%) have no detections within them, 21 (62%) have a single detection in them, and 4 (12%) have two detections within them, indicating that at these flux density limits and resolutions, most 500 μm risers appear to be single sources. The sample sizes are small, but there is no evidence at these flux densities to suggest a correlation between the number of detections and the detection threshold used in the map, with the two, one, and no detection subsets having mean detection thresholds of 6.2 ± 3.3, 9.4 ± 4.0, and 7.6 ± 2.0 mJy respectively. There are also similar numbers of detections for the 345 GHz and 270 GHz maps, though there are only 13 maps at 345 GHz and 24 at 270 GHz. The flux densities of detected sources range between 2.9 to 35.2 mJy at

Name	RA	DEC	Frequency $[GHz]$	Flux $[mJy]$	Flux_Err $[mJy]$	S2N*	Z
Bootes13ID_1	218.93331	34.79416	265	9.47	0.95	8.19	
Bootes13ID_2	218.93281	34.79787	265	8.48	0.95	7.38	
Bootes33ID_1	217.88329	34.35276	265	4.65	0.86	5.75	
Cosmos9ID_1	150.70492	2.54869	231	2.86	0.47	4.63	
HFLS1_ID_1	257.07377	58.47777	265	14.03	2.26	5.87	4.29
HFLS3_270_ID_1	256.69914	58.77330	270	17.41	1.44	10.02	6.34
HFLS3_345_ID_1	256.69926	58.77330	336	25.06	2.79	8.41	6.34
HFLS5_ID_1	260.20754	59.77442	270	12.45	1.34	8.28	4.44
HeLMS11ID_1	7.40011	2.12036	265	7.64	1.36	4.68	
HeLMS12ID_1	13.24405	6.22189	265	35.17	2.42	7.92	4.37
HeLMS28ID_1	11.04294	1.30615	265	31.19	2.32	7.30	4.17
HeLMS32ID_1	351.14402	-5.41560	265	10.09	1.47	5.66	
HeLMS34ID_1	5.58661	-1.92247	265	20.96	1.71	7.08	5.16
HeLMS35ID_1	5.31452	1.54934	345	14.50	1.21	6.66	
HeLMS35ID_3	5.31506	1.55261	345	4.90	1.21	4.00	
HeLMS62ID_2	13.82280	2.06797	265	8.36	2.00	4.01	
HeLMS783ID_1	10.37588	-2.79840	265	7.08	1.42	4.50	
LSW28ID_1	165.36617	56.32630	265	18.35	1.27	10.34	
LSW73ID_1	164.08463	56.90126	265	4.13	0.84	4.02	
LSW73ID_2	164.07629	56.89420	265	4.03	0.84	4.20	
Lock2_270ID_1	163.29714	56.70437	270	9.49	1.27	6.81	
Lock2_270ID_2	163.29509	56.70212	270	5.63	1.27	4.26	
Lock2_345ID_1	163.29503	56.70220	345	10.75	2.10	4.34	
Lock5_270ID_1	162.88248	56.60535	270	7.80	1.07	6.69	3.36
Lock5_345ID_1	162.88288	56.60542	346	11.92	2.02	4.98	3.36
Lock_102_ID_1	160.21099	56.11496	302	53.15	2.89	13.84	5.29
XMM-26ID_2	36.43590	-2.98359	265	7.67	1.43	3.81	
XMM-M2ID_1	36.31398	-2.78553	345	11.81	1.78	5.70	
XMM-M7ID_1	36.68632	-3.41962	345	9.79	1.73	5.05	

Table 3.3: Properties of our 29 detected sources. The redshift, if known, is given in the final column. * Extracted on the dirty map.

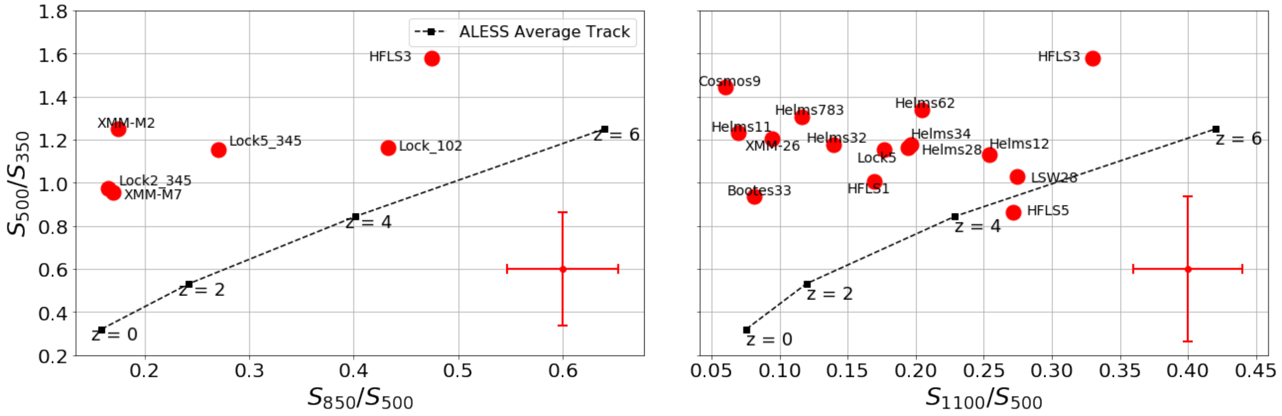

Figure 3.4: The SMA-SPIRE colours of sources where we only detect one counterpart. Names of the source are given next to each point, and typical error bars are given in the bottom right. In black we plot the ALESS average SED (da Cunha et al., 2015), as it would appear at $z = 0$, 2, 4, and 6.

270 GHz, with a mean of 11.8 mJy, and between 4.9 and 53.2 mJy at 345 GHz, with a mean of 17.7 mJy.

For the 17 SPIRE sources with $S_{500} > 60$ mJy, which Béthermin et al. (2017) predict to be almost entirely single sources, we find 12 appear to be single sources, 2 have multiple detections, and 2 have zero detections. The remaining source, Lock2, is ambiguous; we detect one counterpart at 345 GHz but two at 270 GHz. Curiously, the source detected at both 345 GHz and 270 GHz is the fainter of the two sources detected at 270 GHz, with only 5.63 ± 1.27 mJy at 270 GHz compared to the secondary 9.49 ± 1.27 mJy source, which does not have a counterpart at 345 GHz. As we go on to discuss, the maps where we detect no sources are likely be due to multiple faint sources below the detection limit. In this case, we find that of our 17 SPIRE sources with $S_{500} > 60$ mJy, 4 (23%) are actually multiple galaxies. Of the 18 sources in Oteo et al. (2017) with $S_{500} > 60$ mJy, they also find 6 of them (33%) resolve into multiple galaxies, in good agreement with what we find here, and such a high fraction is seemingly in disagreement with Béthermin et al. (2017), who suggest that such sources should be almost entirely comprised of lensed single sources.

In Figure 3.4, we plot the SMA-SPIRE colours of those sources where we detect only one counterpart in the SMA maps. We exclude maps where we detect multiple sources, as assigning the low resolution SPIRE flux to individually resolved sources in the higher resolution SMA maps, given the different frequencies of these observations, is a non-trivial task. We additionally plot the track of the ALESS average SED (da Cunha et al., 2015), as it would appear from z = 0 - 8. Whilst the SPIRE colours alone indicate our sources are significantly red, the SMA-SPIRE colours are not as clear. Whilst many of our sources, such as HFLS1, HFLS3, and Lock5 are within $\sim 1\sigma$ of their true redshift on the ALESS average track, others such as Cosmos9, HeLMS11, and XMM-M2 are significantly fainter in the SMA bands than would be expected. This may be due to these sources being resolved by the SMA, and thus our point source extraction could miss some of the flux. Examination of the maps does not seem to suggest this for most sources however, with the source shape well matched to the beamshape in all sources with the exceptions of HFLS5, Lock2_270, Lock5_270 and Lock_102, which all appear slightly extended even in the compact/subcompact configurations. An additional solution could be that we are in fact not detecting all the sources responsible for the SPIRE flux. If there are multiple undetected sources in the map, then the integrated SMA flux from these could be responsible for the SPIRE flux. Clustering at this scale is discussed extensively in Chapter 2, and we know of at least two bright red Herschel sources which resolve to numerous DSFGs at higher resolution (De Breuck et al., 2017; Oteo et al., 2018).

We can only say with certainty that the maps where we detect 2 sources are definitely multiples; in maps where we detect a single source, there may be a secondary fainter source, and in maps where we detect no sources, we can at best put upper limits to any detection. For maps with one detection, the ratio between the brightest (detected) source and any secondary source can be a maximum of $\frac{S_{Lim}}{S_{Detected}}$, where S_{Lim} is the upper limit for detection, and $S_{Detected}$ is the flux density of the detected source. We find that in this case, any secondary source would have a flux density *at most* between 98% and 28% that of the detected source, with an average of $(63 \pm 19)\%$. These upper limits are reasonably consistent with Donevski et al. (2017), who find that the brightest source that makes up a Herschel detected 500 μm riser contributes around 60% of the 500 μm flux density. However, at these sensitivities our estimates remain upper limits, though we do note that in the four maps where we have two detections the brighter source contributes on average 60% to the total flux density from both sources. For now, the simplest solution to the maps where we detect only one source is that this sole source is responsible for the SPIRE flux, and we move ahead under this assumption. The same cannot be said for those maps where we detect no sources.

Maps Without Detections

In twelve maps, we detect no sources at all. This is surprising; all but one of these maps have Herschel 500 μm flux densities > 40 mJy, and Bootes15, HeLMS493 and HeLMS45 have 500 μm flux densities > 60 mJy, and the detection threshold in these dirty maps is $\sim 7 - 10$ mJy, so it is difficult to explain these non detections as being too faint. Examining Figure 3.1, there is some evidence of a CLEANed source in HeLMS493, with a CLEANed signal to noise ratio of 5.61 and a flux density of 9.85 $\pm$1.76 mJy, but this same does not pass our threshold in the dirty map, with only a signal to noise ratio of 2.1 and a flux density of 4.65 $\pm$2.18 mJy. Numerous (> 2) DSFGs which have the appearance of a single source in the Herschel maps are known (Oteo et al., 2016b, 2018) (see also Section 4.2 in Hill et al. (2018)). To examine roughly how many sources would be needed to reproduce the typical SPIRE flux in the maps where we do not have any SMA detections, we take the ALESS average SED (da Cunha et al., 2015) at redshifts between 4 and 6, and normalise its flux density at 500 μm to 60 mJy. We find that if a single source were responsible for the SPIRE flux, then it should have 345 GHz and 270 GHz flux densities of $\sim$ 24-38 mJy and 14-25 mJy in the two bands respectively, and that we should have detected the source responsible. If the flux were equally split between two sources, we would expect individual SMA flux densities of $\sim$ 12-19 and 7-12 mJy respectively; low, but given the detection limits in Bootes15 and HeLMS493, still detectable. This is not a detailed analysis, but it is suggestive that in at least some of the maps where we do not detect any sources there are > 3 DSFGs separated by between $\sim$ 2 - 20 arcsec (the scales of the SMA and SPIRE beams respectively) If multiple sources are present, deeper integrations would be needed to detect them. The addition of the 32 GHz bandwidth SWARM correlator on the SMA, installed after most of these observations were taken, makes such follow up much easier, and achievable in a reasonably short amount of time.

3.4 Extraction of Physical Properties

In order to extract physical parameters from our sources, we take the measured SPIRE and SMA flux densities, and following the literature convention (Blain, 2002; Magnelli et al., 2012; Bianchi, 2013; Casey et al., 2014), fit them to a single temperature modified blackbody function of the form

$$S_\nu \propto (1 - exp(-\tau_\nu))B_\nu(T), \tag{3.1}$$

where S_ν is the observed flux density at frequency ν, $\tau_\nu = (\frac{\nu}{\nu_0})^\beta$, and gives the optical depth at frequency ν, ν_0 is the frequency at which the optical depth equals unity, and $B_\nu(T) = B_\nu(\nu, T_{dust})$ is the Planck function as a function of temperature T. β, the spectral index, is usually assumed to be β = 1.5 - 2 for SMGs (Blain, 2002; Casey et al., 2014). We do not attempt to split the SPIRE flux densities up in those maps where we detect multiple sources, and do not include these maps in our fits.

To perform our fit, we use the affine invariant Markov Chain Monte Carlo (Goodman and Weare, 2010) ensamble sampler Python package, emcee (Foreman-Mackey et al., 2013) with the following uninformative priors for our parameters: $0 < z \leq 12$, $T_{CMB}(z) \leq T_{dust} \leq 80$, $1 \leq \beta \leq 3$, $1\ \mu m \leq c/\nu_0 \leq 1\ mm$, and $-2 \leq log_{10}(a) \leq 2$, where T_{CMB} gives the CMB temperature at redshift z, and c gives the speed of light. For numerical stability, at each sample we first normalise to the 500 μm observation, and allow the normalisation a to vary from there. In this model, there are then 5 parameters to be fit: The redshift z, the average dust temperature T_{dust}, the spectral index β, ν_0, and an overall normalisation parameter a. We run our sampler with 100 walkers and for 3000 steps and, after manually checking to ensure the model has burnt in, throw away the initial 300 steps as a burn in phase. In Figure 3.5 we show 1,000 single modified blackbody samples from the posterior to show that our samples are in general fitting the data well.

With these models in hand, we now turn to extracting further physical parameters from them. To determine the FIR (42.5 - 122.5 μm) luminosity of sources, we simply integrate under the luminosity SED between these limits. By doing this for all of our samples, we obtain posteriors

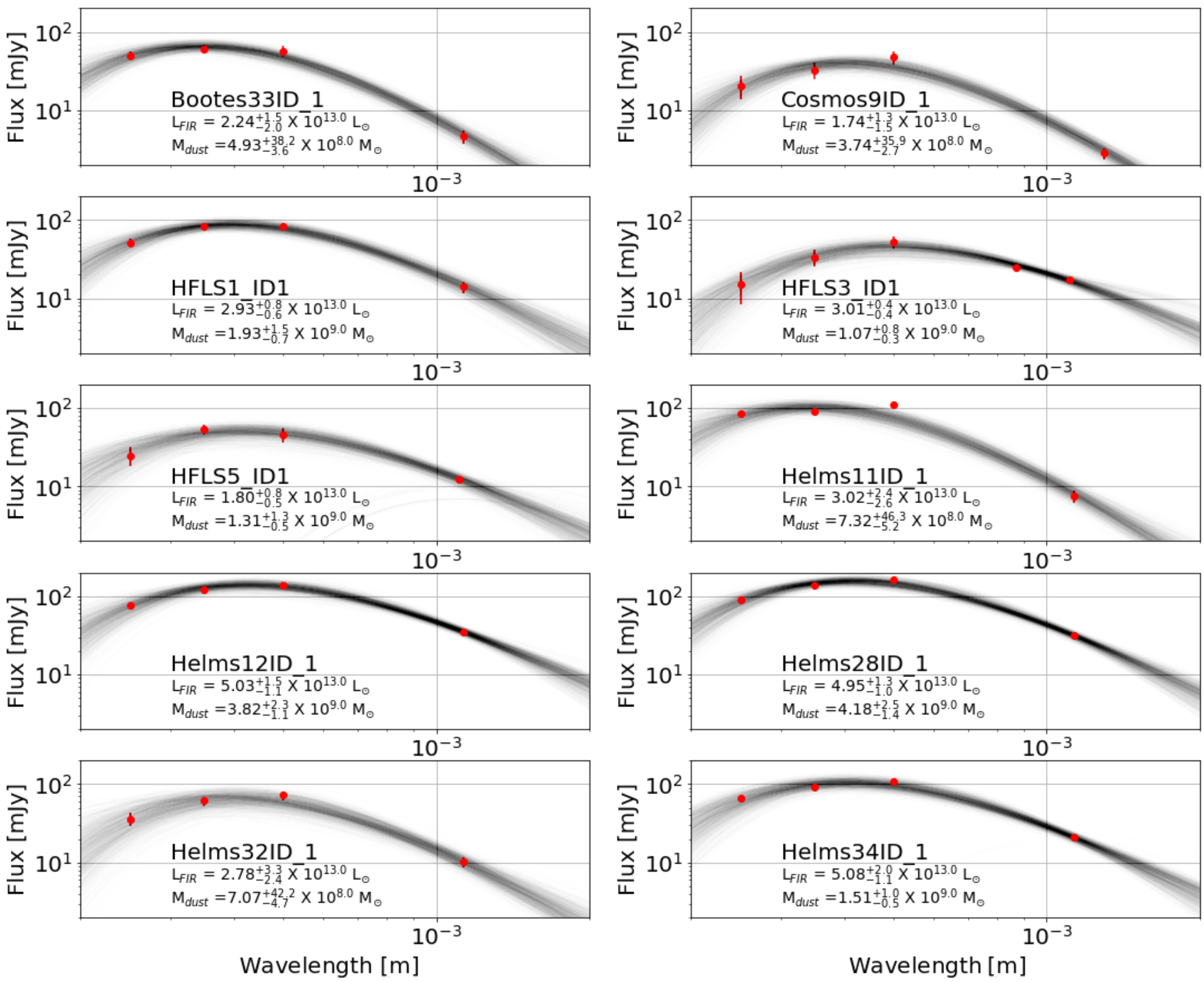

Figure 3.5: Sampled SED fits to the SPIRE and SMA flux densities measured for sources where we only detect a single counterpart to the SPIRE source. The black lines show 1,000 samples after fitting, whilst the red points give the flux densities and errorbars to the observed photometry of each source. Names, estimated FIR luminosities and estimated dust masses are provided as text on each of the plots.

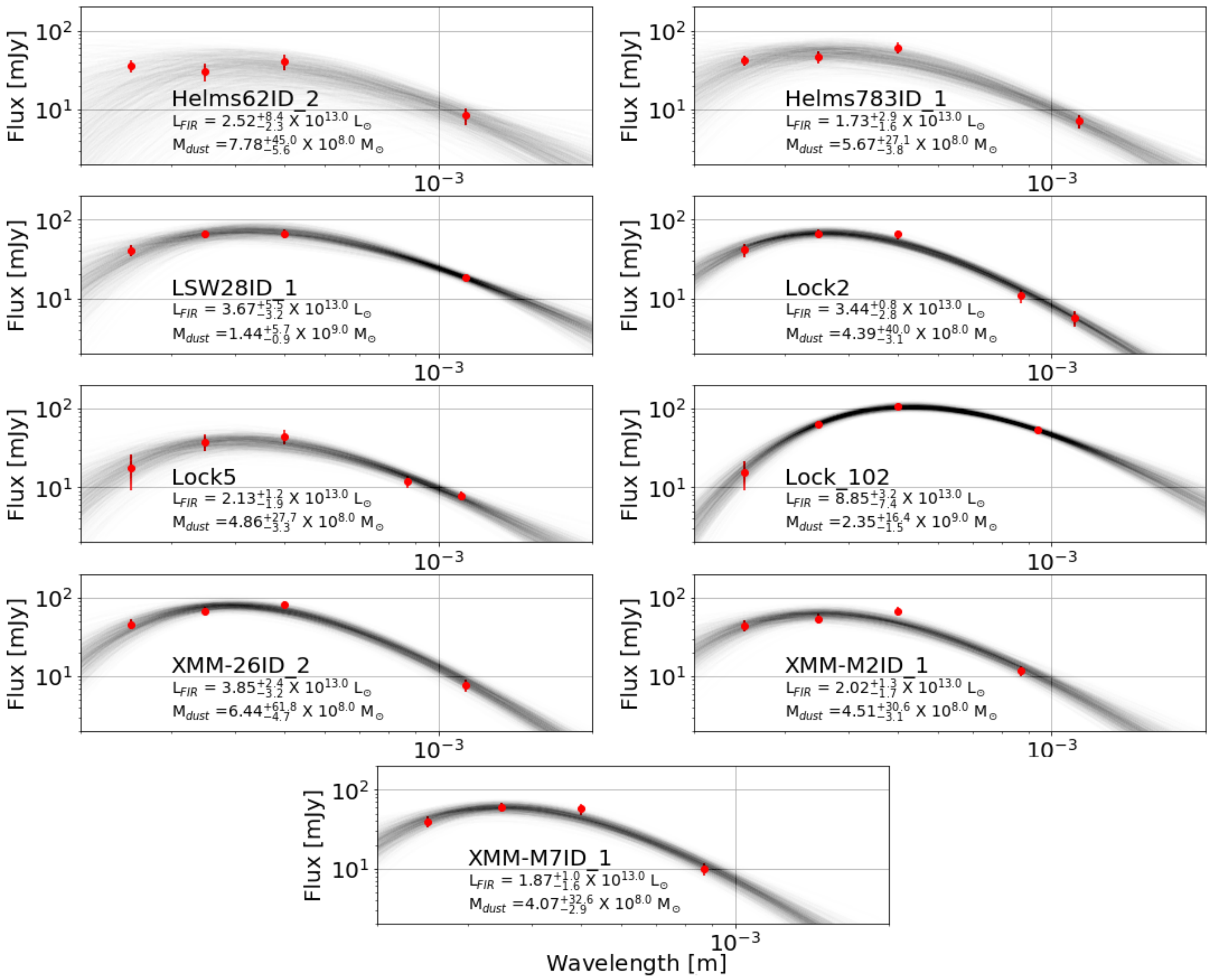

Figure 3.5: Continued

on the luminosities of each of our sources. We can repeat this procedure to determine posteriors on the dust mass, for which we follow Riechers et al. (2013) and use

$$M_{dust} = S_\nu D_L^2[(1+z)\kappa_\nu B_\nu(T)]^{-1}\tau_\nu[1-exp(-\tau_\nu)]^{-1}, \quad (3.2)$$

where S_ν gives the rest-frame flux density at 125 μm, D_L is the luminosity distance, κ_ν is the mass absorption coefficient and is assumed to be $\kappa_\nu = 2.64\ m^2\ kg^{-1}$ at 125 μm (Dunne et al., 2003), and other symbols are defined as before. Finally, we are able to convert the FIR luminosity to a SFR, once again following Riechers et al. (2013) and adopting a top-heavy Chabrier stellar IMF (Chabrier, 2003). We show these results in Table 3.4 we show the median, 14th and 86th percentiles of these distributions for each of our sources.

Some of our sources, such as HFLS3 (Riechers et al., 2013), are well studied elsewhere in the literature. For these sources, we use this extra redshift information to constrain our fits further. However, even when not including the redshift information for HFLS3 (i.e. we also fit the redshift), we get FIR luminosity values of $log_{10}(L_{FIR}/L_\odot) = 13.4^{+0.24}_{-0.73}$ (corresponding to SFRs of $2900^{+2100}_{-2300}\ M_\odot yr^{-1}$) and dust mass estimates of $log_{10}(M_{dust}/M_\odot) = 9.07^{+0.71}_{-0.44}$, in excellent agreement with the results from Riechers et al. (2013), though with larger uncertainties.

Examining the five fitting parameters, the redshift and dust temperature are perfectly degenerate with each another. The β values of our sources have mostly reasonable fits, with most uncertainties around ± 0.3-0.5. The majority of our sources (68%) have median β values above 2.0, with 40% of our sources having median values above $\beta = 2.5$, indicating a reasonably high spectral index for most of our sources. In terms of FIR luminosity, all our sources are observed to be HLIRGs ($log_{10}(L_{FIR}/L_\odot) > 13$). Whilst we do not here correct for lensing, if the magnification on all of our sources is similar to that for HFLS3 of $\mu = 2.2$, 17 of our 29 sources would still be classed as HLIRGS, including HFLS3 itself. This is in reasonably good agreement with Donevski et al. (2017), who find that around 76% of 500 μm risers are HLIRGs even after correction. As can be seen, these generally correspond to SFRs $> 1,000\ M_\odot\ yr^{-1}$.

Name	$log_{10}(L_{FIR}/L_\odot)$	$log_{10}(M_{Dust}/M_\odot)$	β	SFR $[M_\odot yr^{-1}]$
Bootes33ID_1	$13.3^{+0.21}_{-0.76}$	$8.69^{+0.86}_{-0.54}$	$2.57^{+0.29}_{-0.43}$	2200^{+1400}_{-1900}
Cosmos9ID_1	$13.2^{+0.23}_{-0.69}$	$8.57^{+0.94}_{-0.54}$	$2.67^{+0.23}_{-0.38}$	1700^{+1200}_{-1400}
HFLS1	$13.4^{+0.10}_{-0.09}$	$9.29^{+0.23}_{-0.18}$	$1.99^{+0.51}_{-0.47}$	2900^{+700}_{-600}
HFLS3	$13.4^{+0.05}_{-0.06}$	$9.03^{+0.21}_{-0.12}$	$1.51^{+0.56}_{-0.36}$	3000^{+400}_{-400}
HFLS5	$13.2^{+0.15}_{-0.13}$	$9.12^{+0.27}_{-0.18}$	$1.61^{+0.59}_{-0.41}$	1800^{+700}_{-500}
HeLMS11ID_1	$13.4^{+0.24}_{-0.70}$	$8.86^{+0.79}_{-0.50}$	$2.51^{+0.34}_{-0.52}$	3000^{+2200}_{-2400}
HeLMS12ID_1	$13.7^{+0.11}_{-0.09}$	$9.58^{+0.18}_{-0.14}$	$1.53^{+0.58}_{-0.36}$	5000^{+1400}_{-1000}
HeLMS28ID_1	$13.6^{+0.09}_{-0.09}$	$9.62^{+0.18}_{-0.16}$	$1.78^{+0.51}_{-0.41}$	4900^{+1200}_{-900}
HeLMS32ID_1	$13.4^{+0.32}_{-0.75}$	$8.85^{+0.77}_{-0.46}$	$2.20^{+0.53}_{-0.63}$	2800^{+3000}_{-2300}
HeLMS34ID_1	$13.7^{+0.13}_{-0.10}$	$9.18^{+0.20}_{-0.15}$	$1.65^{+0.63}_{-0.42}$	5100^{+1800}_{-1100}
HeLMS62ID_2	$13.4^{+0.60}_{-0.93}$	$8.89^{+0.76}_{-0.53}$	$1.90^{+0.71}_{-0.63}$	2500^{+7400}_{-2200}
HeLMS783ID_1	$13.2^{+0.40}_{-0.88}$	$8.75^{+0.69}_{-0.46}$	$2.03^{+0.62}_{-0.65}$	1700^{+2600}_{-1500}
LSW28ID_1	$13.5^{+0.37}_{-0.78}$	$9.16^{+0.64}_{-0.43}$	$1.53^{+0.62}_{-0.37}$	3700^{+5000}_{-3100}
Lock2	$13.5^{+0.09}_{-0.66}$	$8.64^{+0.92}_{-0.51}$	$2.72^{+0.19}_{-0.32}$	3400^{+800}_{-2700}
Lock5	$13.3^{+0.18}_{-0.79}$	$8.69^{+0.75}_{-0.46}$	$2.04^{+0.58}_{-0.60}$	2100^{+1100}_{-1800}
Lock_102	$13.9^{+0.13}_{-0.69}$	$9.37^{+0.82}_{-0.43}$	$2.11^{+0.48}_{-0.44}$	8800^{+3100}_{-7000}
XMM-26ID_2	$13.5^{+0.19}_{-0.64}$	$8.81^{+0.94}_{-0.53}$	$2.69^{+0.22}_{-0.34}$	3900^{+2200}_{-3000}
XMM-M2ID_1	$13.3^{+0.21}_{-0.68}$	$8.65^{+0.81}_{-0.47}$	$2.51^{+0.35}_{-0.56}$	2000^{+1200}_{-1600}
XMM-M7ID_1	$13.2^{+0.18}_{-0.68}$	$8.61^{+0.87}_{-0.51}$	$2.63^{+0.27}_{-0.45}$	1900^{+1000}_{-1500}

Table 3.4: The derived properties of our sources from fitting single modified blackbodies, *uncorrected for lensing μm*. Lock2 was fitted only using the source detected at both 270 and 345 GHz.

3.5 Discussion

3.5.1 Number Counts

Examining the 270 GHz and 345 GHz flux densities compared to number counts at 1.1 and 850 μm (Oteo et al., 2016a; Aravena et al., 2016; Hatsukade et al., 2016), we find that the sources we detect here are generally among the brightest observed sources expected for the sub-mm galaxy population, with ~ 3 sources expected per deg^2 for the 8 sources with 270 GHz flux densities $> 10\ mJy$. Furthermore, when comparing to the 2 deg^2 simulation by Béthermin et al. (2017), we only find 3 *nearly* 500 μm risers[5] that have $S_{500} > 40\ mJy$, none of which are actually 500 μm risers and all of which are magnified by at least $\mu = 2$. They do however have SFRs, corrected for lensing, of $> 500\ M_\odot\ yr^{-1}$, within 1σ errors of our SFR estimates in Table 3.4.

Our sample selection was heterogeneous, but since all our sources were taken from the HerMES fields, with an area of 280 deg^2, we can place lower limits on the cumulative number counts for flux densities $> 10\ mJy$ at 270 GHz of 0.029 sources deg^{-2}. This value is still well within models predicted by Cai et al. (2013) and Béthermin et al. (2012) (see Figure 6 of Hatsukade et al. (2016)). Asboth et al. (2016) meanwhile select 477 SPIRE detected objects across the HeLMS field of the HerMES survey, with the condition that they are both 500 μm risers and that $S_{500} > 52\ mJy$. However, 22 of our 34 maps also pass these criteria, and are effectively a subsample of these complete 477 SPIRE objects, including the 8 with flux densities $> 10\ mJy$ at 270 GHz. If our sample of 8 out of 22 (36%) objects is representative of all 477 objects identified by Asboth et al. (2016), then we can suggest that the number density of 500 μm risers with $S_{500} > 52\ mJy$ sources *and* with flux densities $> 10\ mJy$ at 270 GHz is 0.62 sources deg^{-2}. The number counts as estimated by models (Cai et al., 2013) and observations (Scott et al., 2012) suggest that in total there should be ~ 3 sources deg^{-2} with 1.1 mm flux density $> 10\ mJy$, suggesting that bright, possibly lensed, 500 μm risers may be responsible for a significant fraction, around 20%, of this population.

[5] Using the same $S_{500}/S_{350} > 0.85$ criteria used in Ivison et al. (2016)

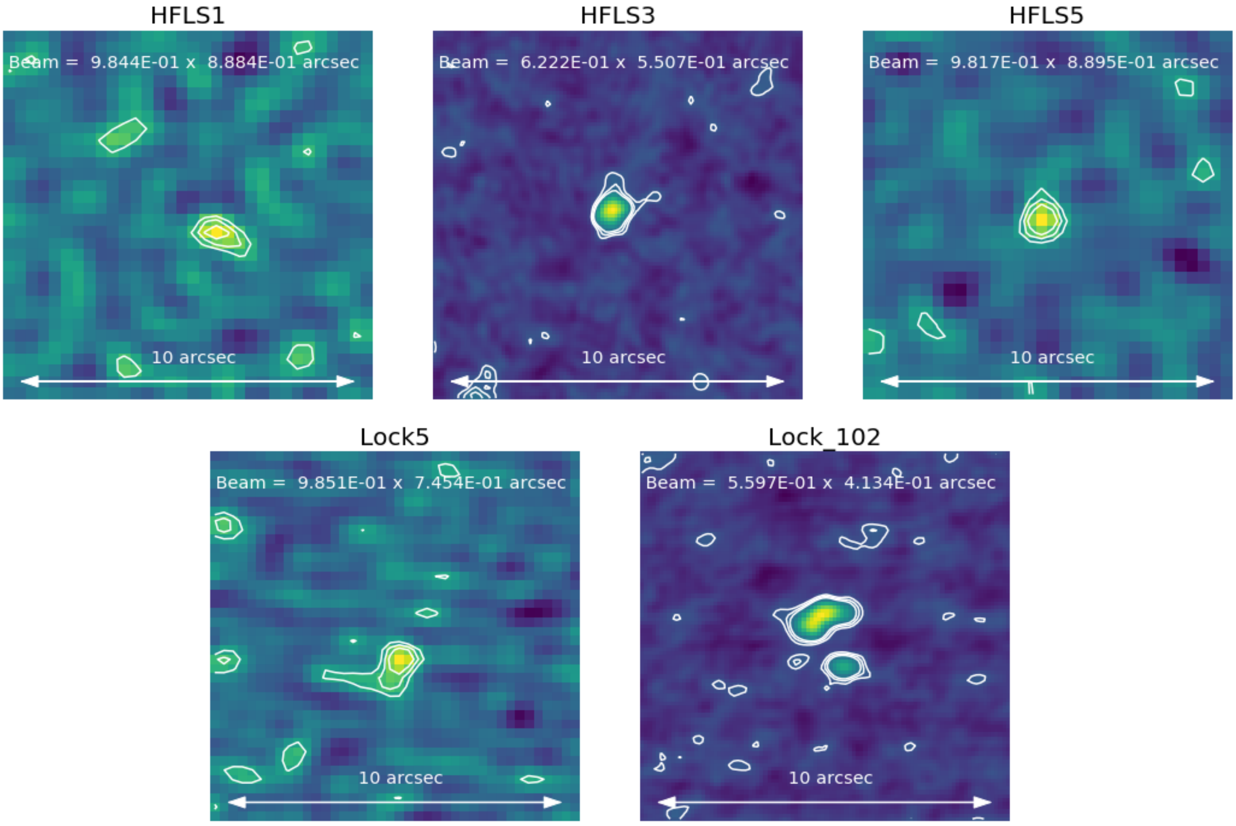

Figure 3.6: Extended (all maps) and very extended (HFLS3 and Lock_102) only) observations on maps where these configurations are available. All maps are 10 arcsec × 10 arcsec. Contours show 2, 3, 4 and 5σ levels. The beam is approximated as a Gaussian, with semi-major and semi-minor axis given in the text at the bottom of each image.

3.5.2 Lensing

At least two of our sources are known lenses (HFLS3 and Lock_102), and 17 of our sources have $S_{500} > 60\ mJy$, which Béthermin et al. (2017) suggest should all be lensed galaxies. However, we only have extended array observations for 6 of our sources (HFLS1, HFLS3, Lock2, HFLS5, Lock5 and Lock_102), and the 2 - 4 arcsecond beamsize in the other compact configurations is unlikely to reveal any arc-like structures. In Figure 3.6, we show those sources where we do have extended or very extended configuration observations. The only source that shows clear arc like structure is Lock_102. The other known lens, HFLS3 with a magnification μ = 2.2 ± 0.3 (Cooray et al., 2014), appears reasonably compact, with small signs of extension to the north, but no obvious indications of lensing. Similar indications of extension are seen in HFLS1 and Lock5, whilst HFLS5 appears compact at the resolution of these maps, indicating it has a diameter < 6.9 *kpc*.

Oteo et al. (2017) in their ALMA examination of 500 μm risers find 40% of their sources display some lensing signature (arcs, elongation or rings). This is significantly higher than what we find here, but this can likely be explained by the superior resolution offered by ALMA, with an average beam FWHM of only 0.12 arcsec, an order of magnitude better than our results here.

3.5.3 Blended Sources

Several publications have claimed, mostly through simulations, that most Herschel sources are blends of multiple galaxies in the large Herschel beam (Cowley et al., 2015; Scudder et al., 2016; Béthermin et al., 2017; Scudder et al., 2018). Whilst Cowley et al. (2015) focused on 850 μm selected sources and Scudder et al. (2016, 2018) focus on 250 μm selected sources, Béthermin et al. (2017) suggest that on average only 60% of a $S_{500} < 60$ mJy Herschel flux density at 500 μm comes from a single source. In this Chapter, we have found a broad population, with both singular and multiple sources both above and below this $S_{500} < 60$ mJy cutoff. The brightest of our sources, $S_{500} > 100$ mJy, do appear to be single sources, but there are also examples like Bootes13, which resolves into 2 sources and has $S_{500} = 82$ mJy, and Bootes15, where we detect no counterparts despite a flux density of $S_{500} = 66$ mJy. As such, these observations alongside those of Oteo et al. (2017) show that both lensed galaxy and multiple galaxies within the beam can be responsible for the brightest 500 μm risers. It is not easy to determine the precise fraction that are lensed vs blended, but our results here seem to suggest that lensing does dominate the bright end with a small contribution from blends. In Figure 3.7, we plot a histogram of the 500 μm Herschel flux density of our sources, as a function of whether we detect any SMA sources in that map. It can clearly be seen that those maps where we do not detect any sources are generally fainter at 500 μm. Therefore, at these depths, our results are similar to Béthermin et al. (2017), that at $S_{500} > 60$ mJy, *most* single dish sources will be lensed, but that there may be a contribution from blended sources.

It should additionally be noted that in 12 of our maps we do not detect any sources whatsoever, despite typical 500 μm flux densities of ~ 50 mJy and in these maps it is perfectly reasonable

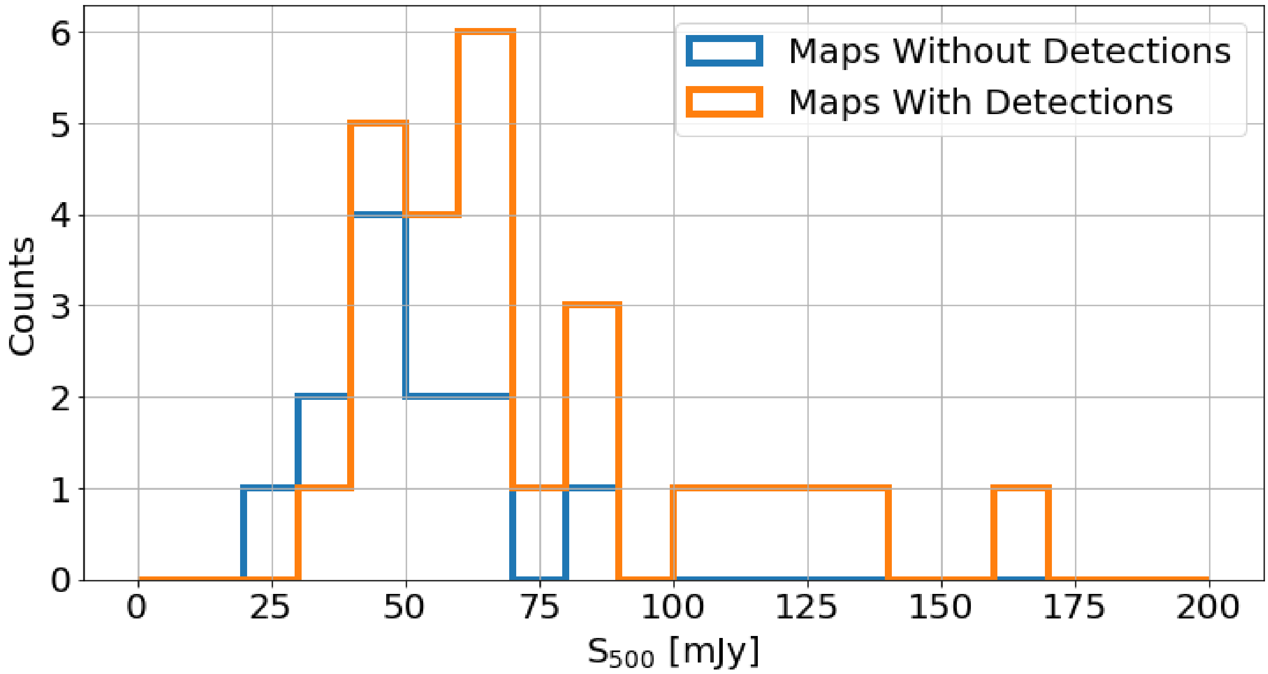

Figure 3.7: The Herschel 500 μm flux density of a source, as a function of whether a source is detected in the SMA map (orange histogram) or not (blue histogram). Bins are of width 20 mJy

that the Herschel flux comes from the integrated flux from many fainter sources. Indeed, Oteo et al. (2017) find the number of detected sources ranges from 1 - 5 in their sample of 44 ultra-reds observed with ALMA.

3.5.4 Extreme Luminosities

The sources discussed in this Chapter additionally appear to represent some of the most luminous objects in the Universe, with observed FIR luminosities typically well above $10^{13} L_{\odot}$. Even allowing for a magnification μ of $\mu = 2.8$, the majority of our sources would still be classed as HLIRGs, and in the single case where we do have magnification estimates (HFLS3, (Cooray et al., 2014)), this is indeed the case. In their simulation of the effects of clustering on single dish instruments, Béthermin et al. (2017) limit the maximal starburst to 1,000 $M_{\odot}\ yr^{-1}$. Table 3.4 shows that all of our detected sources have SFRs above this, and though most are within 1σ of this value, some like HeLMS34 are significantly higher than this limit. Whilst many of our sources are likely lensed, and our observations are not at a high enough resolution to determine this, Oteo et al. (2017) with their superior resolution from ALMA determine that many of their sources are in fact intrinsically this luminous, and so our sources may provide further evidence for extreme starbursts in the early Universe. Precisely what might be powering these extreme starbursts remains unclear (Oteo et al., 2017).

3.5.5 Multi-Wavelength Counterparts

We searched the all sky Wide-field Infrared Survey Explorer (WISE, (Wright et al., 2010)) catalogues, which include photometry at 3.4, 4.6, 12 and 22 μm with associated beamsizes of 6, 6, 6 and 12 arcsec respectively, for any evidence of sources within 10 arcsec of our sources, and find 12 of our sources have WISE associations, mostly at 3.4 μm. As we previously discussed, given we believe a significant number of our sources may be lensed, it is difficult to assess whether these counterparts are the true counterpart to our source or are the foreground lens galaxy.

Additionally, whilst many of our sources do not have Spitzer observations, one of our sources XMM-M7, falls into the footprint of the Spitzer Extragalactic Representative Volume survey (SERVS, (Mauduit et al., 2012)). Our interferometric observations allow us cross-match this source to a faint IRAC source at both 3.6 and 4.5 μm (see Figure 3.8), with flux densities of 2.6 $\pm$0.5 and 4.8 $\pm$0.4 mJy and, whilst the relationship between IRAC colours and redshift is a complex one (Yun et al., 2008), the red IRAC colours may suggest a high-z origin for this source.

Future work on this project will involve deep optical / NIR observations on a range of these sources, in particular to attempt to clarify the strength of any lensing that is occurring, in order to constrain the intrinsic FIR luminosity and SFRs of these apparently extreme sources.

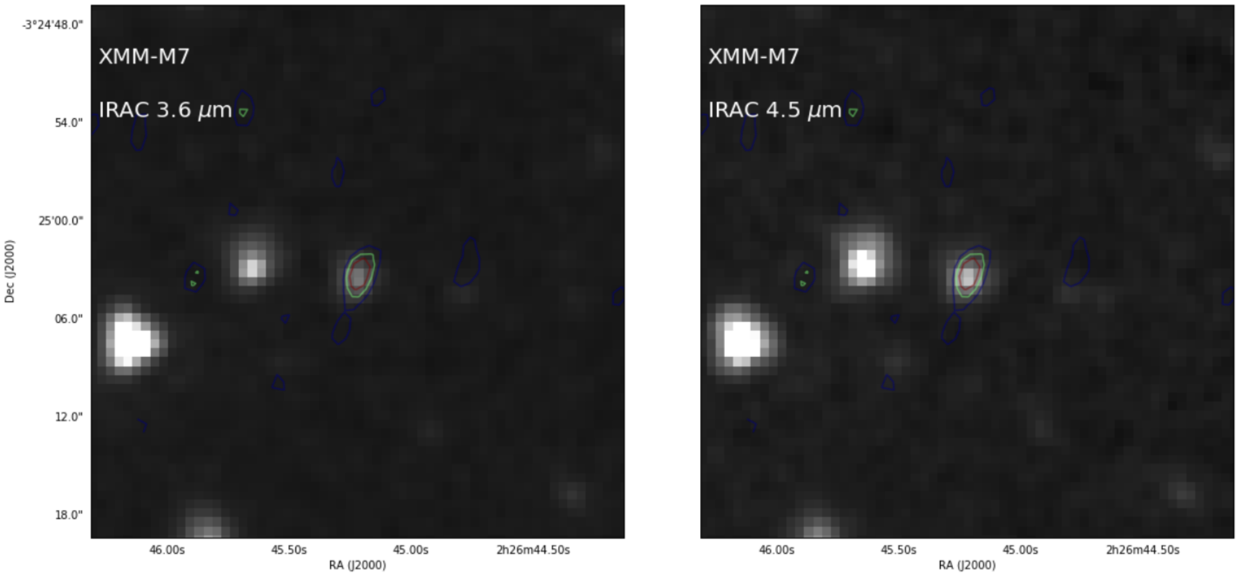

Figure 3.8: Spitzer 3.6 and 4.5 μm imaging of XMM-M7 from the SERVS survey, with contours from our SMA observations overlayed. The contours represent the 2, 3 and 4σ levels in our SMA maps.

3.6 Conclusions

Over a number of years, we have performed high resolution SMA observations on 34 bright and red Herschel sources, the results of which we have presented here. We find that our sources are well modelled as point sources in the compact and subcompact SMA configurations, and therefore place upper limits on the angular sizes of our sources of $\sim 2.5 \pm 0.8$ arcsec. We detect a total of 29 sources across 37 maps. Of the 37 maps, 12 (35%) have no detections within them, 21 (62%) have a single detection in them, and 4 (12%) have two detections. Most of our sources appear to be single sources, though we cannot rule out contributions from any secondary sources, especially in maps with 270 or 345 GHz flux densities lower than expected when compared to well studied local SEDs. In those maps where we do not detect any sources, we postulate that these sources might comprise more than 2 DSFGs, whose integrated flux is responsible for the Herschel flux, similar to the sources discussed in Chapter 2 and in Oteo et al. (2018). We fit single modified blackbodies to all our detected sources and confirm using HFLS3 that our fits are reasonable. Whilst not correcting for lensing, we find that most of our sources are HLIRGs, with associated SFRs $> 1,000\ M_{\odot}\ yr^{-1}$, with dust masses around 10^8 - $10^9\ M_{\odot}$.

At these depths, our results appear consistent with the literature, which suggests that the brightest red Herschel sources are likely lenses, and are responsible for 100% of the Herschel flux, whilst fainter sources can be ascribed to multiple galaxies within the Herschel beam, but which are not detected by our SMA observations. Future observations should take place either with ALMA or the newly upgraded SMA, in order to confirm the nature of those maps where we detect no sources.

"Thus, for instance, when we see the effect of the condensation of the sun's rays in the focus of a burning lens, it seems to be natural to suppose, that every one of the united rays contributes its proportional share to the intensity of the heat which is produced;" - William Herschel, Phil. Trans. R. Soc. Lond. 1800 90, 255-283, published 1 January 1800.

Chapter 4

SPIRE dropouts

4.1 Introduction and Motivation

The discovery of a significant number of DSFGs in the distant Universe over 20 years ago (Hughes et al., 1998) led to significant changes in galaxy formation and evolutionary theories (Blain, 2002; Casey et al., 2014). Even-so, the high-redshift ($z > 3-4$) subset of these galaxies remain poorly constrained, despite two decades of study. Questions still remain about whether DSFGs significantly contribute to the global SFR-density at z > 3 (Rowan-Robinson et al., 2016; Liu et al., 2017; Novak et al., 2017) or not (Michałowski et al., 2017; Koprowski et al., 2017). Indeed, recent results highlight this uncertainty by showing that we can neither rule out a negligible or dominant contribution to the global SFR-density from DSFGs at $z > 3.5$ (Casey et al., 2018). Furthermore, models have consistently been unable to reproduce the observed number counts of the red, $z > 4$ SMGs (Dowell et al., 2014; Asboth et al., 2016; Ivison et al., 2016). Whether this mismatch is due to observational issues such as blends or lensed sources (Karim et al., 2013; Scudder et al., 2016; Béthermin et al., 2017; Negrello et al., 2017; Donevski et al., 2017), or due to the assumptions that have gone into the numerical models (Baugh et al., 2005; Valiante et al., 2009; Borgne et al., 2009; Béthermin et al., 2011, 2012, 2017) remains unclear. Given further that, since we expect these sources to evolve into present day elliptical galaxies in massive clusters (Wilkinson et al., 2016), the highest redshift DSFGs likely trace the most massive dark matter halos in the early Universe, and therefore the statistical characterisation of this population is a key goal for observational astronomers.

Despite an extremely negative k-correction in the sub-mm, mm, and to a lesser degree the FIR (which should lead to $S_\nu(z) \propto$constant across $z = 1 - 8$ in these bands), only a handful of DSFGs at z $\geq$ 4 have spectroscopic confirmation (Capak et al., 2008; Coppin et al., 2009; Daddi et al., 2008; Riechers et al., 2010; Cox et al., 2011; Capak et al., 2011; Combes et al., 2012; Walter et al., 2012; Riechers et al., 2013; Dowell et al., 2014; Yun et al., 2015; Ivison et al., 2016; Oteo et al., 2016b,c; Asboth et al., 2016; Riechers et al., 2017; Zavala et al., 2017; Strandet et al., 2017; Fudamoto et al., 2017; Marrone et al., 2017). The selection criteria used for these high-z DSFGs is varied; some are selected through FIR colours (Riechers et al., 2013; Dowell et al., 2014; Asboth et al., 2016; Ivison et al., 2016; Zavala et al., 2017), whilst others use mm selection (Strandet et al., 2017), and still others sub-mm wavelengths (Walter et al., 2012). Even after candidate selection, spectroscopic confirmation remains difficult, often requiring counter-part identification in optical, near/mid infrared or radio bands, which do not benefit from the extremely negative k-correction the sub-mm and mm bands do.

This bias towards spectroscopic / photometric redshifts for only low redshift sources is routinely seen in the literature, especially for SMGs[1]. One of the earliest examinations of the SMG redshift distribution comes from Chapman et al. (2005), who search for 1.4 GHz radio counterparts to a parent sample of 150 SCUBA selected SMGs, and spectroscopically identify 73 sources with a median redshift of z = 2.3, and an interquartile range between z = 1.7 - 2.8. Around $\sim$ 35% of their SMGs do not have a radio counterpart, and the authors postulate these are likely to be at $z > 3$ SMGs (see Figure 4 of Chapman et al. (2005)). These results are generally consistent with later results from both Wardlow et al. (2011) and Simpson et al. (2017) (see also (Smith et al., 2017)). Wardlow et al. (2011) derive 17-band optical to MIR photometric redshift for 74 SMGs with robust radio (56 counterparts), 24 μm (52 counterparts), or SPITZER IRAC (14 counterparts) identifications, finding a median redshift of $z = 2.2 \pm 0.1$, with an interquartile range of z = 1.8 - 2.7. Simpson et al. (2017) meanwhile use ALMA 870 μm continuum imaging to precisely locate the position of 52 SMGs from the UKIDSS Ultra

[1]To remind the reader, SMGs are typically galaxies selected in sub-mm bands, usually around 850 μm.

Deep Survey (UDS) field (Lawrence et al., 2006; Geach et al., 2017). They use deep optical - radio imaging to fit photometric redshifts to these 52 sources using 11 band photometry, finding a median redshift of $z = 2.65 \pm 0.13$, but once again find that $\sim 30\%$ of SMGs are too faint at optical/NIR wavelengths to derive accurate photometric redshifts, and again postulate these are likely at $z > 3$.

Consistently, around 30% of SMGs have no counterparts in these literature studies, and are routinely assumed to be high-redshift, with little further examination. More recent surveys at mm wavelengths such as the South Pole Telescope (SPT, Carlstrom et al., 2011) survey (Vieira et al., 2013) find redshift distributions which contrast with previous findings. The redshift distribution of DSFGs selected at 1.4 mm, with a sample of 39 sources with spectroscopic redshifts, has a medium redshift of $z = 3.9 \pm 0.4$ (Vieira et al., 2013; Weiß et al., 2013; Strandet et al., 2016), with 46% of sources at $z > 4$, both significantly higher than previously found. Correcting for the fact that their sample is likely entirely comprised of lensed galaxies, which biases their sample to $z > 1.5$ (see Vieira et al. (2013) for more details), they find an intrinsic DSFG redshift distribution median of $z = 3.1 \pm 0.3$. Miettinen et al. (2015) find similar results for a selection of 30 sources selected at 1.1 mm.

Arguably the most successful selection technique for high-z DSFGs has been the selection of SPIRE 500 μm riser sources ($S_{500} > S_{350} > S_{250}$), discussed extensively in Chapter 3. This selection has led to spectroscopic confirmation of numerous $z > 4$ DSFGs (Dowell et al., 2014; Asboth et al., 2016; Ivison et al., 2016), and two $z > 6$ sources (Riechers et al., 2013; Zavala et al., 2017). Whilst impressive, it should be noted that these results are taken from over 1000 deg^2 of Herschel-SPIRE data, and effectively set lower limits for the number counts of SPIRE detectable $z > 6$ DSFGs of $\gtrsim 2 \times 10^{-3}$ deg^{-2}. Furthermore, given the confusion limited 3σ SPIRE detection threshold of around 20 - 30 mJy, a source must still be, in general, highly luminous ($\sim 10^{13}$ $L_\odot$) to be detected by SPIRE at $z > 4$, a problem which is exacerbated at higher redshifts. Indeed, both of the two SPIRE detected $z > 6$ DSFGs (Riechers et al., 2013; Zavala et al., 2017) are observed to have luminosities $> 10^{13}$ $L_\odot$ (though both are additionally lensed, and only HFLS3 has a FIR luminosity intrinsically $> 10^{13}$ $L_\odot$).

Until recently, limited field sizes and depths at sub-mm and mm wavelengths have meant that systematic searches for the rarer $z > 4$ DSFG and SMG population have been restricted to 500 μm risers, lensed sources, or serendipitous discovery. Now, however, with larger ~ 1 deg^2 surveys at 850 μm such as the S2-CLS and S2-COSMOS surveys (Geach et al., 2017), which overlap with the larger Herschel-SPIRE extragalactic fields, new colour selections can be made. Perhaps the most obvious high-z selection is to extend the 500 μm risers to 850 μm risers ($S_{850} > S_{500}$). At a minimum, this would require detection at both 850 μm and at least in the 500 μm band of SPIRE to ensure the riser condition is fulfilled. To date, only one spectroscopically confirmed 850 μm riser is known, ADFS-27 at $z = 5.655$ (Riechers et al., 2017), indicating this selection is reasonably successful at selecting the highest redshift DSFGs. However, ADFS-27 is only just detected at 500 μm in SPIRE[2], with a flux density of $S_{500} = 24.0 \pm 7.5$, and is not detected in either of the other two SPIRE bands.

As we go on to show in this chapter, numerous 850 μm selected sources are not only not detected at other optical, near/mid-infrared or radio wavelengths, but are additionally undetected by SPIRE. These "SPIRE dropouts" (detected at 850 μm but not in any of the three SPIRE bands) are difficult to explain. Assuming a reasonable dust temperature of 30 - 80 K, if these sources are at $z << 3$ then we can assume the SPIRE and sub-mm bands probe regions of the SED well represented by the Rayleigh-Jeans law[3]. Assuming a luminosity proportional to a single temperature modified blackbody, We would then expect to detect them in SPIRE as $S_\lambda \propto \lambda^{-4+\beta}$, where β is the dust spectral index. A detection at 850 μm would therefore generally indicate a detection in at least the 250 μm band, as we would expect the 250 μm band to be $\left(\frac{250\mu m}{850\mu m}\right)^{-4+\beta} \sim 10 - 40$ times brighter than the 850 μm band, assuming a β value between 1 and 2. Given that we do not, it implies that the peak of the thermal emission must lie near 500 μm - 850 μm, and that the Rayleigh-Jeans law approximation does not hold. This condition is fulfilled if the source is either at high-redshift, has a cool dust temperature, or a combination of the two. As we will go on to show, around 30% of SMGs appear to be SPIRE dropouts. The nature of these dropouts is uncertain, but the two simplest explanations are

[2]When including a constant confusion noise of 7 mJy, typical of the SPIRE maps (Dowell et al., 2014; Asboth et al., 2016)

[3]I.e. $B(\lambda, T) \approx \frac{2ck_BT}{\lambda^4+\beta}$.

that this population is either very high redshift, with a median redshift higher than the 500 μm risers, or that they represent a cooler population hitherto undiscovered at $z > 4$. Both of these solutions are interesting in their own right, and indicate that these dropouts are worthy of further study.

In this Chapter, we detail NGP6_D1, a serendipitous SPIRE dropout first identified in 2014, and our subsequent follow up. This "SPIRE dropout" has photometry consistent with an 850 μm riser ($S_{250} < S_{350} < S_{500} \lesssim S_{850}$), similar to the $z = 5.655$ Riechers et al. 2017 object, and could be a $z > 6$ DSFG. However, given the difference in detection limits between the large *Herschel* survey fields and the SCUBA-2 surveys, it is also possible that NGP6_D1 is a lower luminosity ($L_{FIR} \sim 10^{12}\ L_{\odot}$), low dust temperature ($T_{dust} \sim 30$K) source at an intermediate redshift of $z \sim 4$. Nevertheless, the system is unlikely to be at $z < 2$, as, given its SCUBA-2 flux, we would expect to detect it in the shorter wavelength SPIRE bands. Therefore, NGP6_D1 represents an example of either a population of intermediate redshift SMG with a low dust temperature which have been missed by *Herschel*-SPIRE, or a population of $z > 6$ SMGs. Here we present the subsequent observations on this source, and attempt to determine its likely properties. Throughout this chapter, we assume the concordance Λ-CDM cosmology, with $H_0 = 67.74$ km $s^{-1}\ Mpc^{-1}$, $\Omega_\Lambda = 0.69$ and $\Omega_m = 0.31$.

4.2 Serendipitous Discovery of NGP6_D1

As part of a follow up program of the protocluster candidates identified in Chapter 2, we obtained SCUBA-2 observations on several candidate proto-clusters located in the North Galactic Pole (NGP) field of H-ATLAS. A full description of the observations, as well as their implications for the protocluster candidates detailed in Chapter 2 will be in a forthcoming paper (Cheng et al. in preperation), but here we briefly describe the key points the the data acquisition and reduction. These observations typically tracked out a CV_DAISY pattern[4], reaching a uniform 1σ rms of $\sim 3\ mJy$ over an approximate 2 arcmin radius circle. The main SCUBA-2 beam is approximately a Gaussian with a FWHM of 13.0 arcsec. The observations took place

[4]See http://www.eaobservatory.org/jcmt/instrumentation/continuum/scuba-2/observing-modes/

between April 8th and April 12th 2013, with each protocluster candidate field being observed for roughly 2 hours. The atmospheric opacity varied between $\tau_{225\ GHz} = 0.05 - 0.12$ (0.83 - 2.5 mm PWV), and correspond to atmospheric transmission of between 67-77% in the 850 μm band. The data were reduced using the SMURF SCUBA-2 pipeline (Chapin et al., 2013), where separate observation blocks were combined to form a single map. These maps were then convolved with a matched filter, which maximises the signal to noise ratio for unresolved sources in a map with significant confusion noise (Chapin et al., 2011). Finally, the maps are converted from their native pW unit to Jy by multiplying by the standard SCUBA-2 850 μm Flux Conversion Factor (FCF) of 537 Jy/pW. After cropping to both remove edge effects and to give a roughly uniform noise level across the map, a signal to noise map was constructed by dividing the flux density in each pixel by the standard deviations of all the pixels across the map. Sources were then searched for by locating peaks in the signal to noise map above 3.5σ (See Cheng et al, in preperation for more details).

In the map which corresponds to the Planck compact source PLCKER857 G077.25+80.72, which we hereafter refer to as NGP6, we detected a source at position RA:13:22:57.91, and Dec:+33:24:14.05, at a 4.9σ level, with 850 μm flux density of 12.3 $\pm$ 2.5. Examining the Herschel-SPIRE maps at the position of this SCUBA-2 source, we find no evidence of any emission, with measured flux densities of -2.31 $\pm$ 5.54, 2.30 $\pm$ 5.84 and 7.49 $\pm$ 7.35 mJy at 250, 350 and 500 μm respectively, where we calculated errors by taking the estimated instrumental error at the position of our SCUBA-2 source, and adding this in quadrature to an estimate of the confusion noise, as recommended and given in Smith et al. (2017). As this source is absent from the SPIRE bands, we refer to it as a SPIRE dropout, and gave it the identification NGP6_D1 (NGP6, dropout 1). To check that our source was likely real and not a noise spike in a particular observation, we bootstrapped our data, repeatedly randomly discarding half the data and re-reducing it, and found that in all cases we still found at least a 3σ detection of NGP6_D1. We plot an image of NGP6_D1 at 850 μm and in the three SPIRE bands in Figure 4.1.

What is the nature of NGP6_D1? In Figure 4.2 we plot the expected 250, 350 and 500 μm flux density of the ALESS average SED (da Cunha et al., 2015) as a function of redshift, normalising

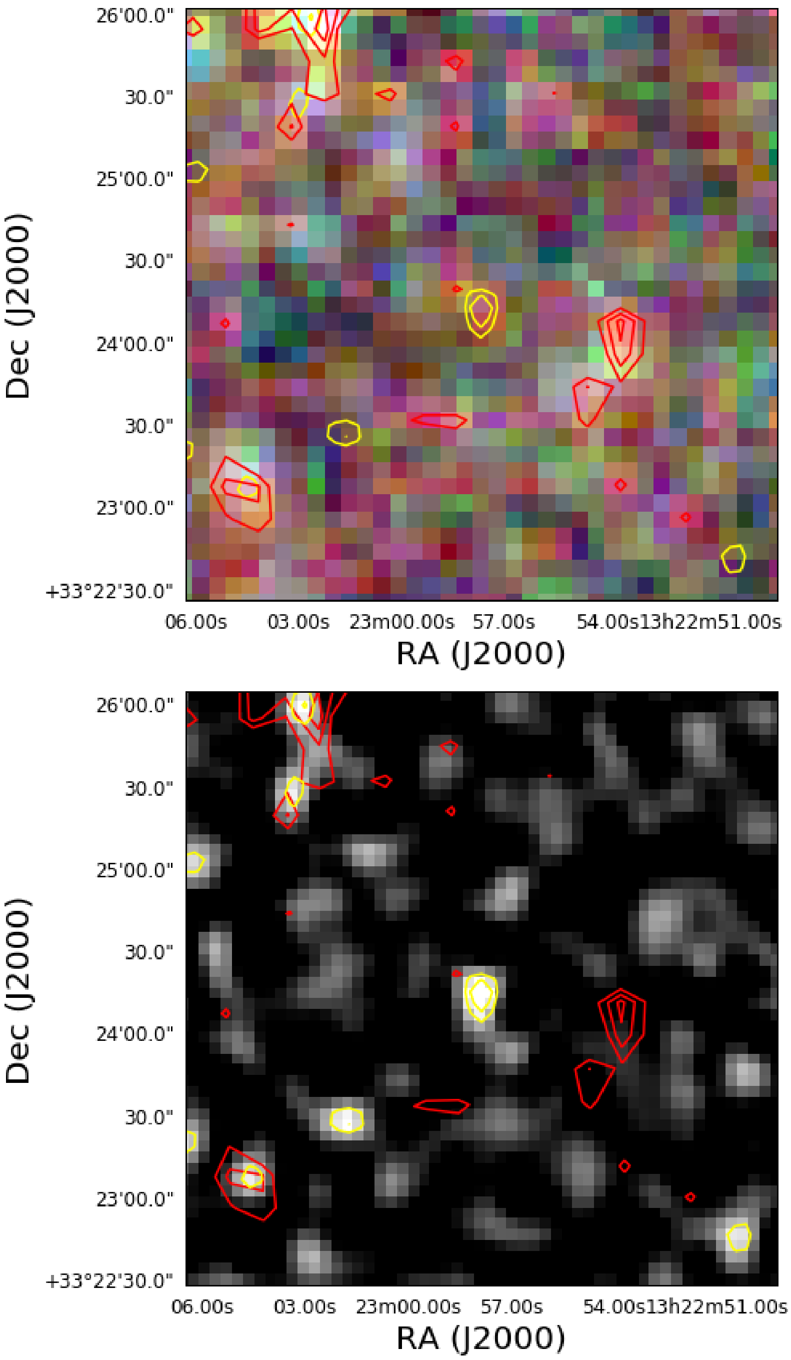

Figure 4.1: *(Top)* A 2".5 × 2".5 RGB (500, 350 and 250 μm) Herschel-SPIRE image of the region around NGP6_D1. Red contours show the 3, 4 and 5σ detection levels for the 500 μm band, whilst yellow contours show the 3, 4 and 5σ detection levels for the SCUBA-2 850 μm band. *(Bottom)* The SCUBA-2 image of the same region, with contours indicating the same as the top image.

the 850 μm flux density each time to 12.3 mJy, the observed flux density of NGP6_D1. Figure 4.2 shows that, if NGP6_D1 has a similar SED to the average ALESS SMG SED and lies at $z \lesssim 4$, we would expect to detect it to a 3σ level in at least the 350 or 500 μm SPIRE band. Furthermore, if it is at $z < 3.5$, we would expect to detect it in all 3 SPIRE bands. Even if NGP6_D1 lies at $z \sim 5$, we would expect to marginally detect (S/N > 2) it in both the 350 and 500 μm bands. However, in no SPIRE band do we even detect NGP6_D1 marginally, and thus we estimated it likely either had an SED intrinsically different to other known sources, such as a much cooler dust SED, or that it was likely at $z > 5$. Experiments were also performed using several other templates, including Arp 220 and several from the Polletta et al. (2007) SWIRE library of DSFG SEDs. These templates and their effect on our conclusions are discussed in more detail in Section 4.5.1, but in all cases only marginal differences were seen and our conclusions here remain unchanged.

4.3 Photometric Observations

Given the reasonably high flux density at 850 μm and lack of detections in the SPIRE bands, we initiated a large multi-wavelength follow up program to characterise NGP6_D1. In this Section, we detail those efforts, focusing on the photometric observations, whilst in Section 4.4 we detail our spectroscopic analysis. A summary of our photometric observations is given in Table 4.1.

4.3.1 SMA

NGP6_D1 was observed using the Sub-Millimeter Array (SMA)[5] in extended configuration, at 870 μm and 1.1 mm on March 29^{th} 2015 and November 21^{st} 2014 respectively for one track each (Project ID: 2014A-S092). The bandpass calibrator was 3c84, while 1310+323, and 1224+213 were used as gain calibrators and Callisto was used as the flux calibrator. The data was reduced

[5]For a more extensive discussion on the SMA, see Chapter 3.

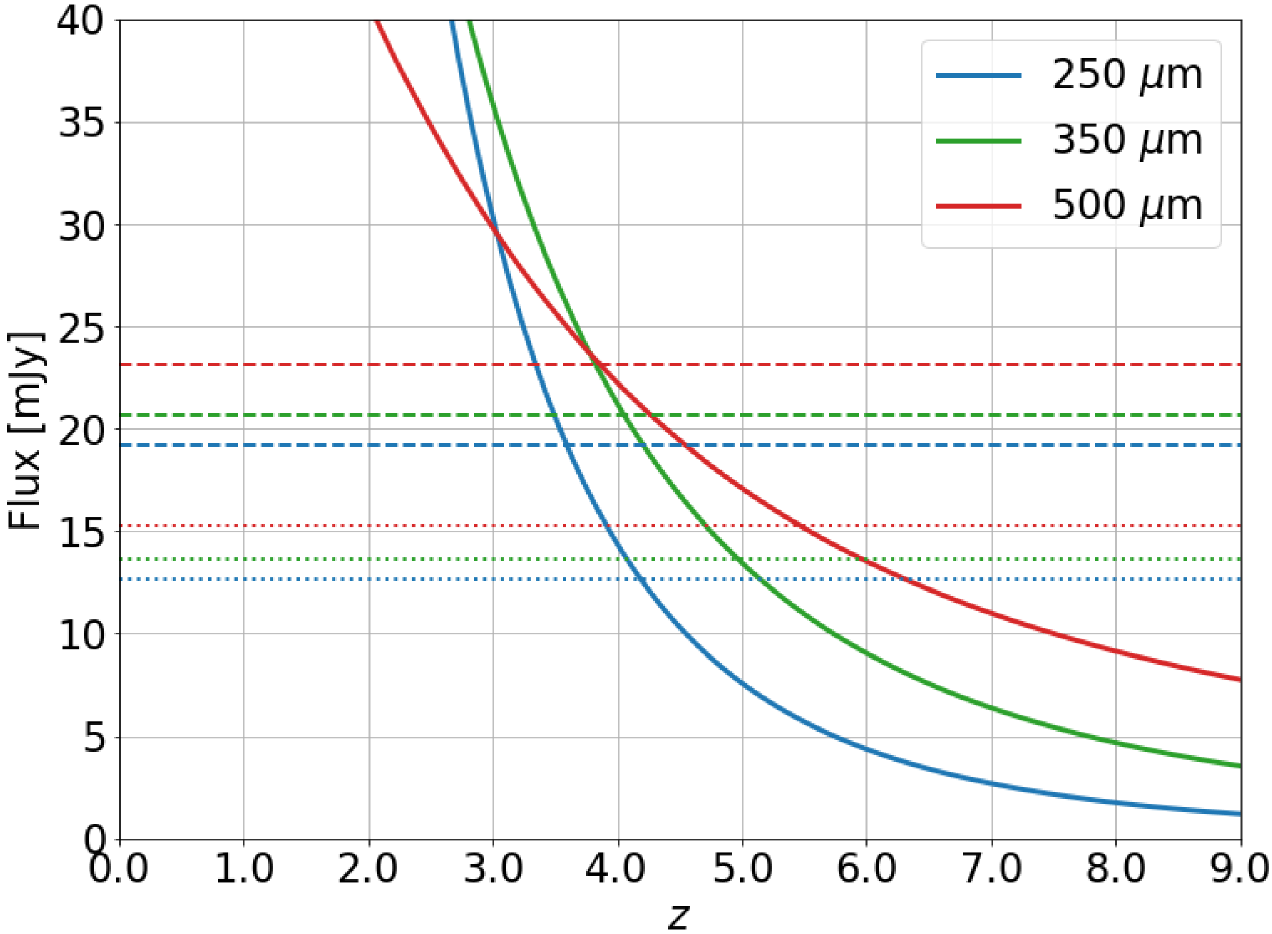

Figure 4.2: In solid lines, the expected 250 (blue), 350 (green) and 500 (red) μm flux densities of the average ALESS sub-millimetre SED as a function of redshift, normalising the 850 μm flux density in each case to the observed 850 μm flux density of NGP6_D1. The dashed horizontal lines show the 3σ SPIRE detection limit, including confusion noise, whilst the dotted horizontal lines show the 2σ marginal detection threshold, with colours referencing the same SPIRE band as the solid lines.

Table 4.1: The FIR, sub-mm, mm and radio photometry of NGP6_D1. Flux densities are given in mJy. These measurements come from Herschel-SPIRE (250, 350, 500 μm), SMA (870 μm, 1.1 mm), NOEMA (2.8 mm), and VLA (6 GHz). SPIRE values are included rather than placing an upper limit, as these are used for template fitting in Section 4.5.1 to constrain the peak of the thermal emission.

Band	Flux [mJy]
250 μm	-3.3 ± 4.2
350 μm	3.0 ± 4.4
500 μm	7.7 ± 8.9
850 μm	12.3 ± 2.5
870 μm	9.3 ± 1.6
1.1 mm	5.9 ± 1.1
1.25 mm	3.97 ± 0.43
2 mm	1.04 ± 0.12
2.8 mm	0.60 ± 0.04
6 GHz	$(1.69 \pm 0.4) \times 10^{-2}$

with a combination of both IDL and MIRIAD using natural weighting to optimise the point-source sensitivity. The smaller 870 μm synthesised beam had semi-major and semi-minor axis of 0".78 × 0".47 and the maps reached 1σ rms of 1.31 and 1.36 mJy in the 870 μm and 1.1 mm bands respectively.

In both maps, a single source was identified at position RA:13:22:57.842, and Dec:+33:24:16.56, 2.5 arcsec away from the nominal SCUBA-2 position and well within the SCUBA-2 beam FWHM. The beamsize corresponds to a physical area of $\sim$ 18 kpc^2 at $z = 1$, and $\sim$ 7 kpc^2 at $z = 6$, both well above the typical physical sizes of SMGs of 1 - 4 kpc^2 (Simpson et al., 2015), indicating NGP6_D1 is likely unresolved at this resolution. The measured flux densities were 8.03 ± 1.31 mJy and 5.96 ± 1.36 mJy at 870 μm and 1.1 mm respectively. The final SMA S/N map of NGP6_D1 in the 345 GHz band is plotted in Figure 4.3, and demonstrates clearly that NGP6_D1 is both well detected, and a single source which corresponds to the SCUBA-2 position. The Herschel measured flux densities at the position of the SMA source are -3.34 ± 4.16 mJy, 2.98 ± 4.42 mJy, and 7.70 ± 8.90 mJy in the three SPIRE bands.

At 870 μm, there is some small tension between this observation and the original SCUBA-2 observation, though this disappears if we take into account the $\sim$ 20% flux boosting expected in the SCUBA-2 maps at 5σ (Geach et al., 2017).

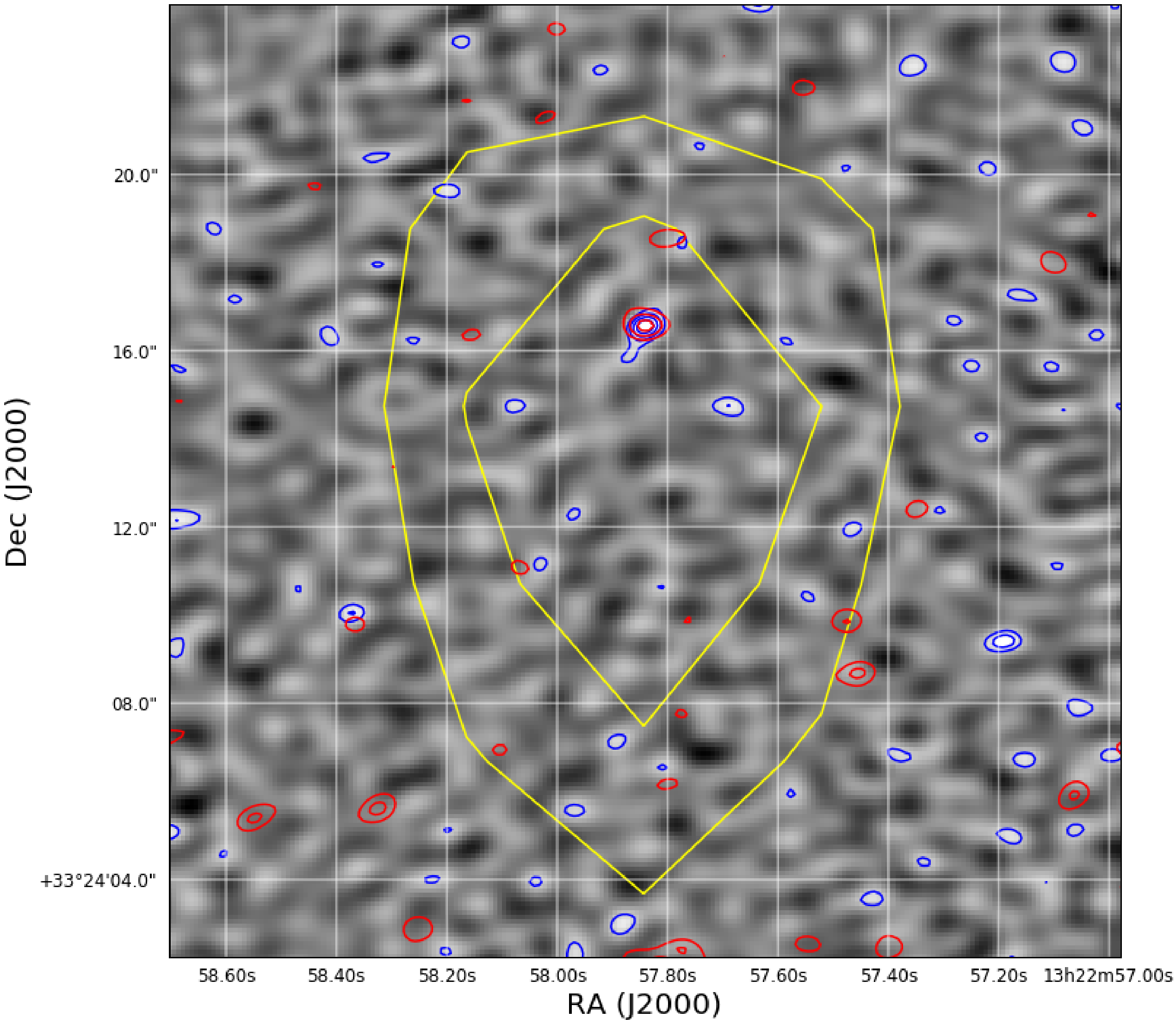

Figure 4.3: The SMA 345 *GHz* (870 μm) map of NGP6_D1, overlaid with SCUBA-2 S/N contours (yellow) in steps of 3, 4, and 5σ, and SMA 870 μm S/N contours (blue) and SMA 1.1 *mm* contours (blue), both in steps of 2, 3, 4, and 5σ.

4.3.2 NIKA

NGP6_D1 was observed on the IRAM 30m telescope using the NIKA (Monfardini et al., 2010) instrument at 1.25 and 2 mm (beamsizes of 12 and 17.5 arcsec) between the 8^{th} and 9^{th} of February 2015 (Project ID: 227-14) for 2 hours, reaching rms values of ~ 0.4 mJy and 0.1 mJy in the two bands respectively. Tau values ranged between $\tau_{225\ GHz} = 0.01$ and 0.28 and with an average of 0.15, but this was generally split between a high opacity $\tau_{225} > 0.1$ and low opacity $\tau_{225} < 0.1$ grouping. The data were reduced by the NIKA team's pipeline, using a "point source oriented" reduction. A single source was found at the position of the SMA object, with a 1.25 mm flux density of 3.97 ± 0.43 mJy and a 2 mm flux density of 1.04 ± 0.12 mJy. The fluxes were found to be consistent when using only the high tau or low tau datasets, but there remains a 10 - 15% uncertainty on the flux calibration. The 1.25 mm flux from NIKA appears inconsistent with the 1.1 mm flux from the SMA, with the SMA 1.1 mm measurement 50% higher than the NIKA 1.25 mm measurement.

4.3.3 VLA

The region around NGP6_D1 was observed by the Very Large Array (VLA) on 17 December 2016 (Project ID VLA/2016-00-110, PI David Clements) for 1.75 hours. This observation was in C-band (6 GHz, 50 mm), and in A-configuration, with a synthesised beamwidth of $0\farcs33 \times 0.33\farcs33$. For bandpass and flux calibration, 3C286 (1331+305) was used, whilst J1310+3220 was the phase calibrator. Data were reduced using the Common Astronomy Software Application (CASA) package (McMullin et al., 2007), version 4.7.0. Small amounts of radio frequency interference (expected to be around $\sim 15\%$) were detected and flagged automatically during the reduction process. The field is cleaned using Briggs (robust) weighting, with a robust parameter of 0, to provide a good balance between angular resolution and sensitivity to all sources in the field. These radio observations were taken on a number of protocluster candidates, and the full results will be presented in a future paper [Chen et al. in prep].

We examined the map around the position of NGP6_D1, and plot this map in Figure 4.4 and

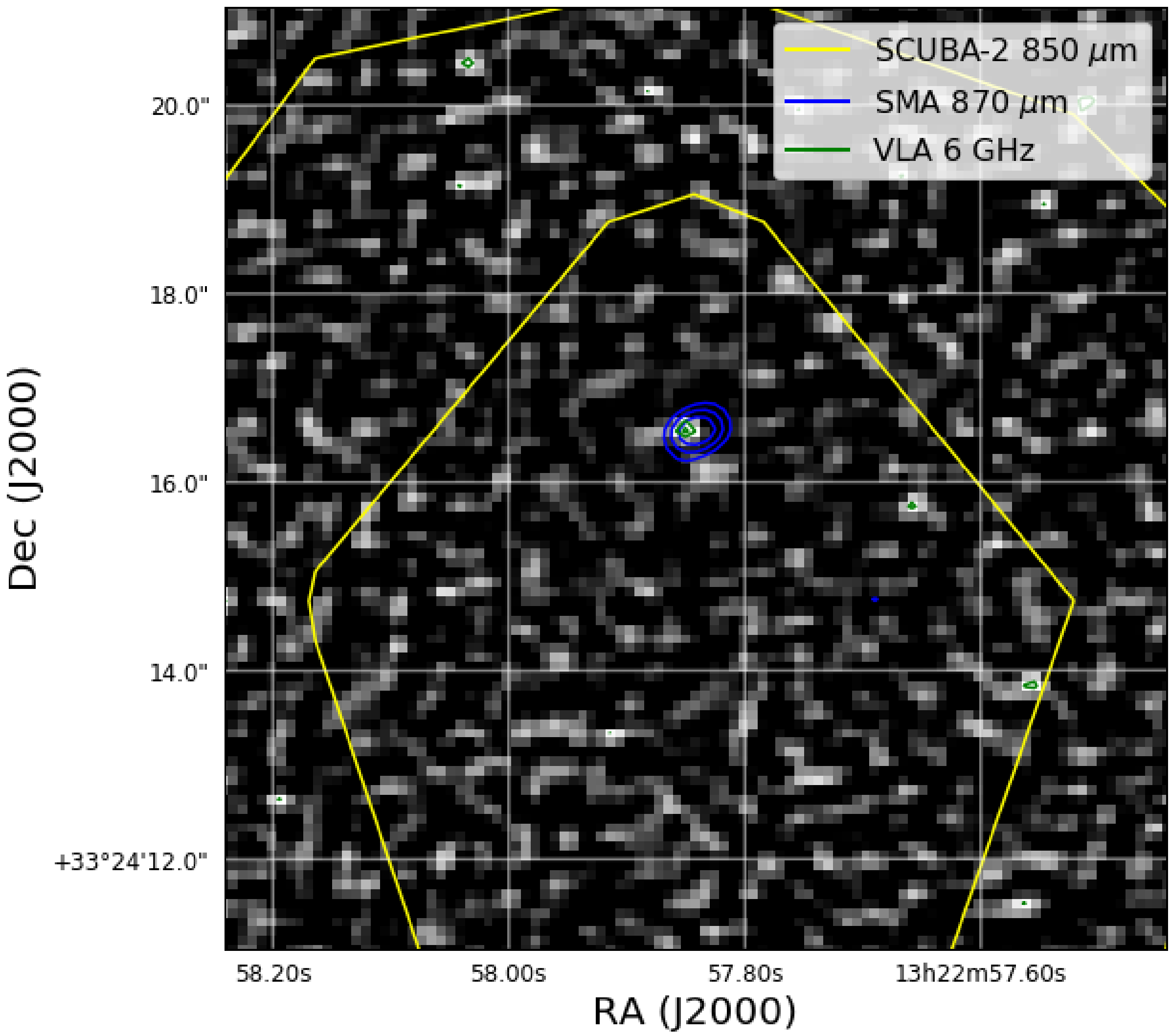

Figure 4.4: A 10" × 10" VLA 6 GHz map of the region surrounding NGP6_D1. SCUBA-2 contours are shown in yellow, in blue are contours from the SMA 870 μm map, and in green are VLA 6 GHz contours. All three contours sets start at a 3σ level, with a step size of 1σ

detected a 4.5σ source, with a 6 GHz flux density of 16.9 ± 3.7 μJy, with a position only 0.05" from the SMA position of NGP6_D1. Assuming the radio emission is concurrent with the FIR emission, our VLA map localises our source to a 0".33 × 0".33 area on the sky.

4.3.4 SDSS, UKIDSS and WISE

The area around NGP6_D1 was observed in both the Sloan Digital Sky Survey (SDSS, (Abolfathi et al., 2017)) and UKIRT Infrared Deep Sky Survey (UKIDSS, (Lawrence et al., 2006; Warren et al., 2006)) in the optical and near-infrared (NIR). These observations reached ap-

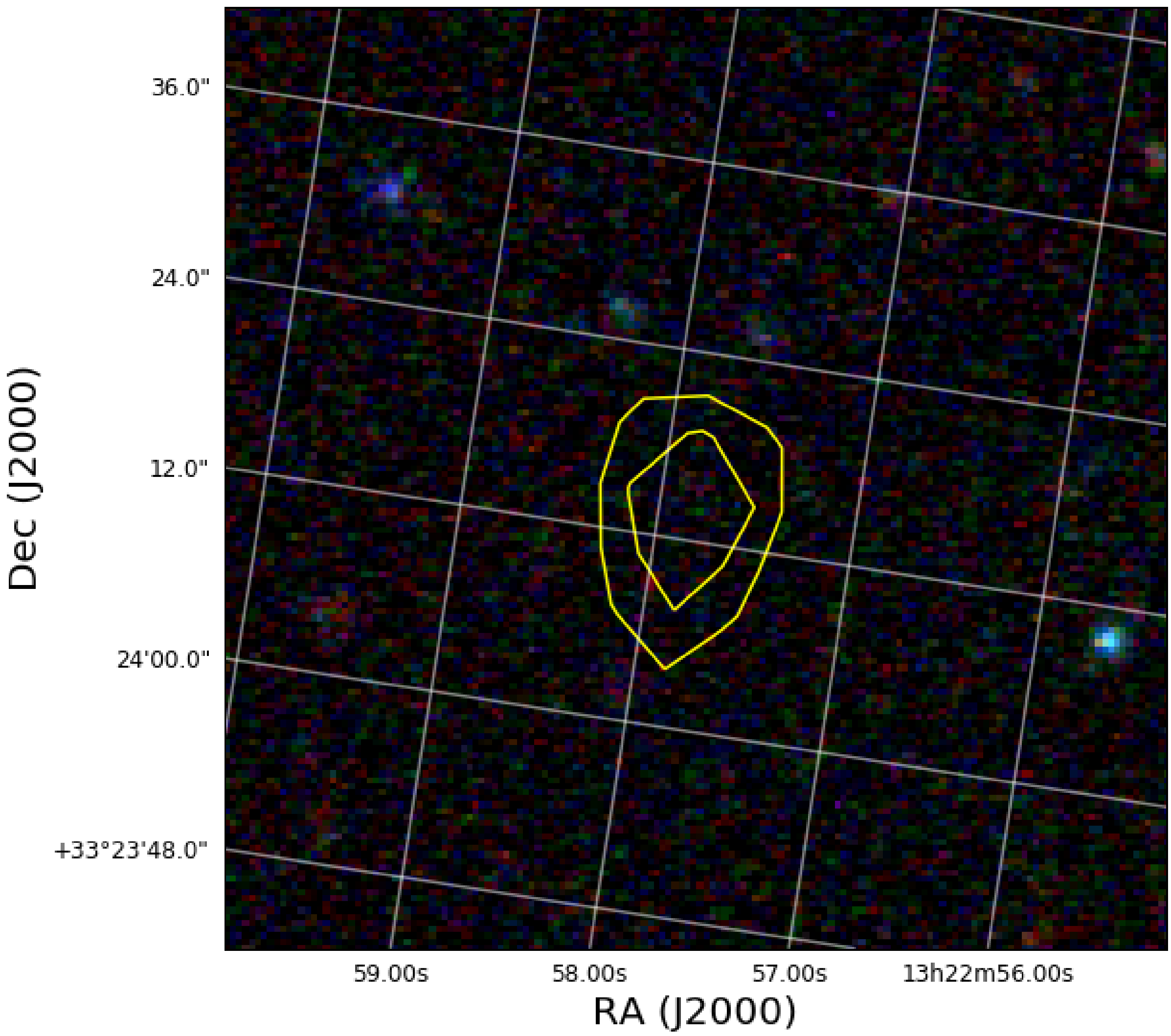

Figure 4.5: A 1' × 1' optical RGB (i, r, g) map of the region surrounding NGP6_D1. SCUBA-2 contours are shown rather than SMA, so as not to obscure the precise location of NGP6_D1.

proximate AB magnitude limits of $u : 22.0$, $g : 22.2$, $r : 22.2$, $i : 21.3$ and $z : 20.5$ in SDSS, and Vega limits of $Y : 20.2$, $J : 19.6$, $H : 18.8$, and $Ks : 18.2$ from UKIDSS. An optical/NIR image of the region surrounding NGP6_D1 from these datasets is shown in Figure 4.5. Though there are two SDSS galaxies approximately 8 and 11 arcsec to the north of the SMA positions of NGP6_D1, there is no current evidence of any optical counterpart, or indication that NGP6_D1 is being lensed by any foreground source. We do note however that deeper images in the optical / NIR may change this. As we do not detect our source in the optical / NIR, even in the Ks band, it supports our supposition that NGP6_D1 is at high redshift.

We also searched for any evidence of NGP6_D1 in the Wide-field Infrared Survey Explorer

(WISE, (Wright et al., 2010)). No evidence of any source was found in any of the WISE maps, with 5σ point source upper limits of 0.068, 0.098, 0.86, and 5.4 mJy for the four WISE bands at 3.6, 4.6, 12.0 and 22.0 μm. Therefore the shortest wavelength with a secure detection of NGP6_D1 remains the SCUBA-2 850 μm detection.

4.4 Spectroscopic Observations

Through both photometric analysis and template fitting (see Section 4.5 for more details), we estimate that the most likely redshift for NGP6_D1 is between z = 5.5 - 7.6. To ascertain a redshift, we opted to target ^{12}CO lines (hereafter referenced as simply CO). The CO(J = 1 - 0) transmission occurs at a rest-frame frequency of 115.27 GHz ($\sim$ 2600 μm), with subsequent CO(J = n - (n-1)) transmissions taking place at n $\times$ 115.27 GHz. At $z > 5$, we would therefore expect adjacent CO lines to be spaced out by $<$ 20 GHz. Such "blind" (having poor prior constraints on the redshift of the source) redshift searches on SMGs have been performed before, and to a reasonable level of success (Dannerbauer et al., 2014; Fudamoto et al., 2017). In this Section, we report on our spectroscopic observations of NGP6_D1 using both the RSR and EMIR instruments, and our resulting spectra from both instruments are shown in Figure 4.6.

4.4.1 RSR

The Redshift Search Receiver (RSR, Erickson et al. 2007, Goeller 2008) is a wide-band 3 mm spectrometer on the 50-m Large Millimetre Telescope (LMT, Hughes et al. (2010)) in Mexico. It has a spectral resolution of 31 MHz or $\sim$ 100 $km\ s^{-1}$ at 92 GHz, and a total instantaneous frequency coverage of 38 GHz from 73 to 111 GHz. The RSR follow-up of NGP6_D1 was conducted in the Early Science phase on January 29 and February 1-3,7 and 8 2016, with a 32-m dish configuration which provided a spatial resolution of 25 arcsec at 92 GHz, well above the expected size of NGP6_D1. As above, we expect at least one line to lie within our bandwidth, and in most cases two, with the exception of a small gap between z = 0.65 and z = 1 where no CO lines would appear within our observed bandwidth.

The opacity $\tau_{225\ GHz}$ ranged between 0.10 and 0.27 with an average $T_{sys} \sim 100$ K over the 6 observation nights. The total on-source integration time on NGP6_D1 was 9 hours (108 spectra × 300 seconds each). Pointing corrections were made observing 1224+213 or 1310+323, every hour.

The individual observations were reduced by Emmaly Aguilar[6], and Fourier transformed, baselined and co-added using the DREAMPY (Data REduction and Analysis Methods in PYthon2) package written by Gopal Narayanan. The final spectrum was obtained by co-adding the best data, defined as all the individual spectra which do not have large structure systematics in the baseline due to low frequency noise. After co-addition the data are smoothed with a 3 channel boxcar filter. Additionally, we smooth the co-added spectrum to match a velocity resolution of 500 km s^{-1}, typical of other high-z DSFGs (Riechers et al., 2013; Bothwell et al., 2013; Aravena et al., 2016; Zavala et al., 2017; Strandet et al., 2017; Yang et al., 2017). To convert from antenna temperature to flux units we use a factor of 6.4 Jy/K for $\nu \leq 92$ GHz and 7.6 Jy/K for $\nu > 92$ GHz (Gomez-Ruiz et al., 2017). Figure 4.6 shows the RSR processed spectrum, alongside the EMIR spectrum, where the average RMS over the full band coverage, after smoothing to velocity widths of 500 km s^{-1}, is 0.46 mJy. There is a $> 3\sigma$ feature detected at 104.28 GHz, and a second line marginally detected to a 2.84σ level at 83.2 GHz. This could reasonably correspond to a $z \sim 4.53$ SMG, and template cross-correlation analysis (i.e. Yun et al. (2015)) suggests a combined detection S/N of 5.5 in support of this redshift solution. However, neither candidate line is detected in EMIR (see next Section), and there are additionally two frequencies that are negatively detected as strongly as this. At the time of writing, investigation and additional follow up into the possible redshift solution seen in the RSR spectrum are ongoing, but for now we must conclude that we are not yet detecting any lines in the RSR spectrum.

[6]Instituto Nacional de Astrofísica, Óptica y Electrónica (INAOE), Luis Enrique Erro 1, Sta. Ma. Tonantzintla, 72840 Puebla, México

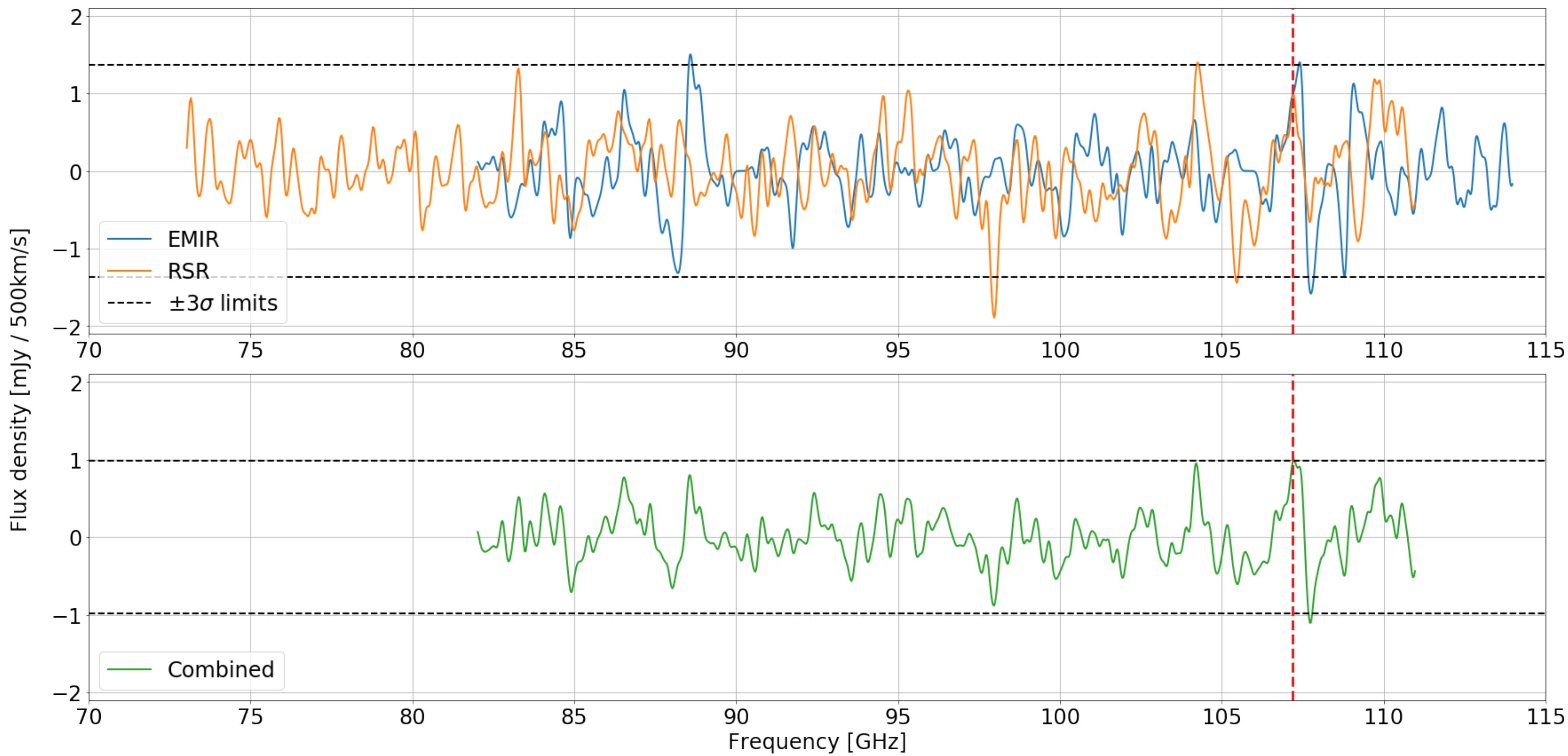

Figure 4.6: *(Top)* The RSR spectrum (blue) and EMIR spectrum (orange) over a $\sim 32\ GHz$ bandwidth. The dashed lines show the $\pm 3\sigma$ rms values for both RSR and EMIR, which differ by only 0.002 mJy. The EMIR spectra is taken from the FTS200 backend. The horizontal dashed lines shows a margianal line seen in both the RSR and EMIR spectrum at $\sim 107.2\ GHz$. *(Bottom)* The resultant spectra when combining both the RSR and EMIR spectra, with the dashed lines once again indicating the $\pm 3\sigma$ rms values.

4.4.2 EMIR

NGP6_D1 was observed for a total of 61 hours on the EMIR (Carter et al., 2012) instrument on the IRAM 30m telescope (Project ID: 199-15). Two setups covered a total of 31 GHz (83 - 114GHz) of frequency space to an rms of 0.06 mK ($\sim 0.42\ mJy$), with two small 1GHz gaps at 90 and 105.5 GHz due to different set ups. The observations ran from the 14^{th} of March to the 20^{th} of March 2016, with $\tau_{225\ GHz}$ values varying from 0.01 to 0.5, with an average of $\tau_{225} \sim 0.2$. The data were reduced using CLASS and Python, and smoothing our data to between 100 and 500 $km\ s^{-1}$, we achieved an rms of between 0.1 and 0.06 mK, corresponding to a line sensitivity of 0.7 - 0.42 mJy. In Figure 4.6, we reproduce our spectrum, smoothed to a velocity width of 500 km s^{-1}. We detect two $\sim 3\sigma$ peaks, one at 88.58 GHz and a second at 107.4 GHz. These two lines would not correspond to any pair of CO lines, and we therefore believe they are likely related to the noise[7]. However, the second line approximately corresponds to a 2σ peak in the RSR spectrum.

4.4.3 NOEMA

As both EMIR and the RSR marginally detect a line at 107.4 GHz independently of one another, we obtained Directors Discretionary Time (DDT) on the The NOrthern Extended Millimetre Array (NOEMA, Guilloteau et al. (1992); Chenu et al. (2016)) to attempt to confirm this line.

The NOEMA Interferometer is a millimetre array located on the Plateau de Bure in the French Alps. A spectral line scan carried out in January 2017 (DDT E16AD: PI J. Greenslade) with 7 (20^{th} January 2017) and 8 antennae (21^{st} January 2017) in D configuration to search for the possible line at $\sim 107.4\ GHz$. The Wide-X receiver offers a bandwidth of 3.6 GHz. The data were calibrated through observations of standard bandpass (3C84, 1055+018), phase/amplitude (1328+307, J1310+323) and flux calibrators (LKHA101, MWC349) and reduced with the

[7]Comments from the time allocation committee at the time raised the question as to whether the noise would continue to integrate down with rms $\propto 1/\sqrt{t}$ given the length of the integration. Whether it does or not remains uncertain.

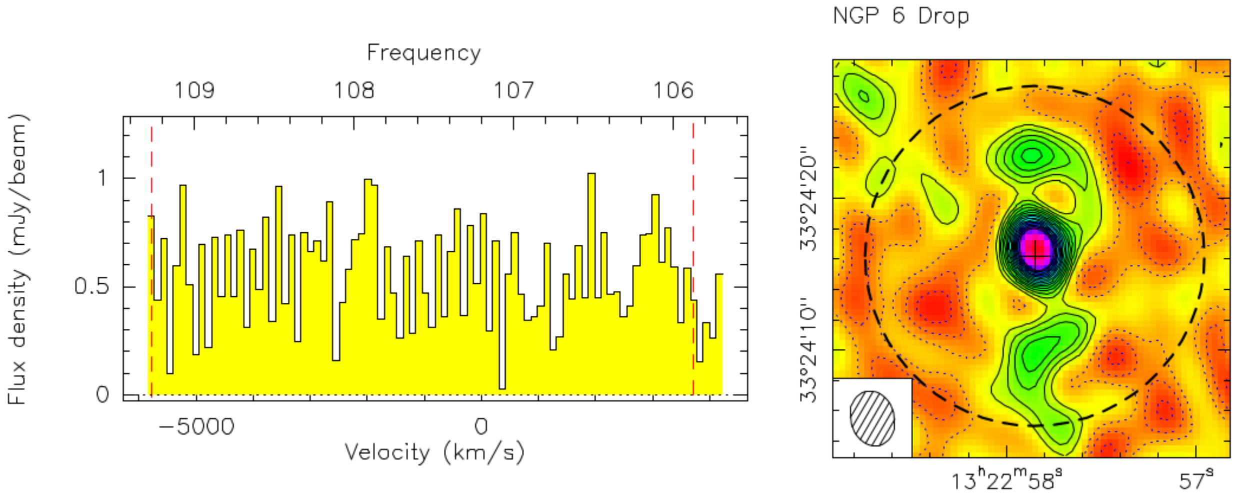

Figure 4.7: (Left) The NOEMA spectra surrounding the candidate line at 107.2 GHz. (Right) The dirty map of NGP6_D1. The northern and southern sidelobes seen are artefacts from the beamshape of NOEMA, and do not represent emission. Contours are in steps of $1\sigma = 0.24$ Jy km s^{-1} beam^{-1}

GILDAS software packages CLIC and MAP. The FWHM of the beam was $3''.8 \times 3''.0$ at 107.4 GHz. The continuum and spectrum is shown in Figure 4.7.

No line was found at 107.2 GHz, indicating the candidate line was just a noise spike, and highlighting the difficulty in obtaining spectroscopic redshift confirmations of these faint sub-mm sources. However, we did detected the continuum emission of NGP6_D1 at $S_{107.2\ GHz} = 0.56 \pm 0.03$ mJy, an 18.6σ detection. The derived position is at RA= 13:22:57.837 DEC= +33:24:16.61 (J2000), only $0.4''$ away from the pointing center (SCUBA-2 position), and only 0.05” from the SMA position.

4.5 Photometric Analysis

Obtaining accurate photometric redshifts from FIR and sub-mm data alone is notoriously difficult. Not only are there no obvious redshift indicators such as the Lyman or Balmer breaks within the FIR/sub-mm region of a typical galaxy SED, but additionally there is a perfect degeneracy between the dust temperature and the redshift of a source (Blain, 2002), such that template fitting is highly uncertain. In this Section, we explore using both fitting templates

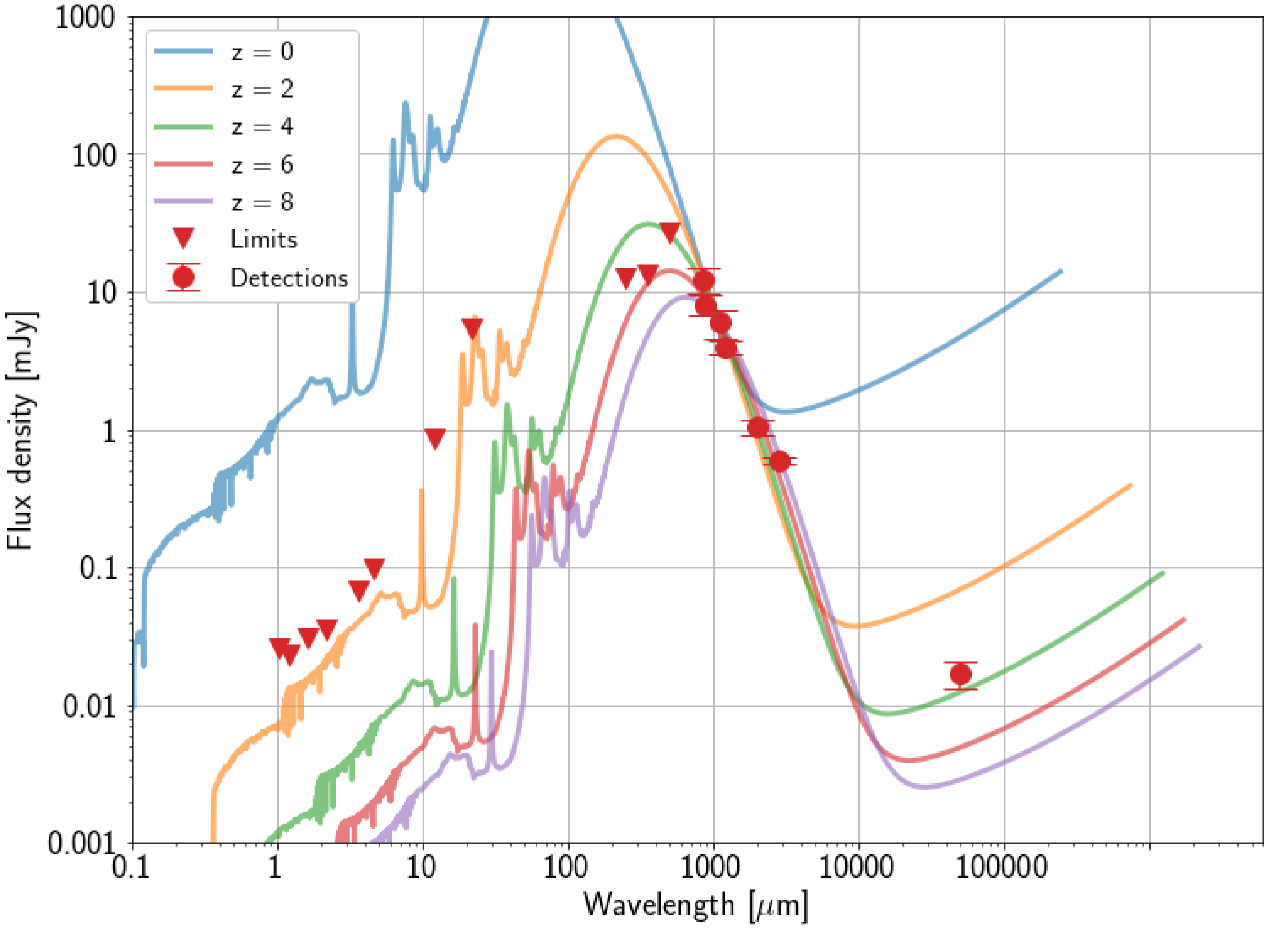

Figure 4.8: The ALESS average SED, as it would appear at $z = 0$, 2, 4, 6, and 8 if normalised each time to the observed 1.1 *mm* flux density of NGP6_D1. The red triangles shows photometric bands where we only have upper limits, whilst the points with errorbars show where we have $>3\sigma$ detections.

and fitting single modified blackbody functions to the photometric data from NGP6_D1, in order to determine its likely redshift, luminosity, and SFR.

4.5.1 Template Fitting

Well studied local ULIRGs and SMGs are often used as templates when fitting photometric redshifts, under the assumption that the template SED is well matched to the underlying SED of the source (Ivison et al., 2016; Ikarashi et al., 2017; Duivenvoorden et al., 2018). Under this assumption, in Figure 4.8, we take the ALESS average SED as it would appear at a variety of redshifts from 0 to 8, and normalise it to the observed 1.1 *mm* flux density of NGP6_D1, to provide a rough guide as to its likely redshift. Tests using different choice of normalisation band provided similar results. Our optical/NIR upper limits rule out a redshift solution much below $z = 2$, whilst the Herschel upper limits are not consistent with a $z < 4$ solution. Furthermore, the 6 GHz VLA detection suggests a redshift $z < 4$, at odds with the SPIRE upper limits. This radio excess is discussed further in Section 4.7.

Whilst a single template may not accurately reflect the SED of a single source, a broad range of templates that span a larger range of parameter space will likely capture the true uncertainty in the redshift of a source[8]. To estimate the redshift of NGP6_D1, we utilise eight templates with a broad range of properties: Cosmic Eyelash (Ivison et al., 2010; Swinbank et al., 2010; Danielson et al., 2010), ALESS average (da Cunha et al., 2015), Arp 220 (Rangwala et al., 2011), M82, NGC 6090, IRAS 20551-4250, IRAS 22491-1808, and two sources with known AGN, Mrk 231, and a QSO template. The last six of these are all from the Polletta et al. 2007 library of SEDs.

In Figure 4.9, we plot the best fit redshift and normalisation for each of the eight templates. We use the photometry given in Table 4.1, excluding the radio point; not all templates include radio data. In each case and for each template, we minimize the χ^2 between the template and our data, allowing both the normalisation amplitude and redshift to vary. This gives, for each template, a best fit redshift for NGP6_D1. To obtain a likely redshift range, we take both the template with the lowest best fit redshift and the template with the highest best fit redshift, and use this range as the likely redshift range appropriate for NGP6_D1. We stress this is specifically *not* an error range, which would slightly extend this range beyond its limits, but is a range of best fit redshifts, given a broad range of templates from the literature.

For NGP6_D1, the best fit redshift ranges from a minimum of $z = 5.88$ to a maximum of $z = 8.33$, with a mean and median redshift estimate from all the templates around $z \sim 6.9$. Assuming the true redshift lies somewhere within this range, this implies that NGP6_D1 is likely one of the highest redshift DSFGs found to date. The reduced χ^2 values range between $\chi^2_\nu = 0.125$ - 0.24, indicating that in all cases we are generally over-fitting the models. This

[8]It is worth noting however that this assumption is not always valid, even when using numerous templates; Ikarashi et al. (2017) fit SMGs from a parent sample of 185 SED templates, and whilst able to accurately fit most of their sources, they are still unable to find a good fit for HFLS3, which they ascribe to HFLS3's warm dust temperature (Section 4.1 and 4.3 of Ikarashi et al. (2017).

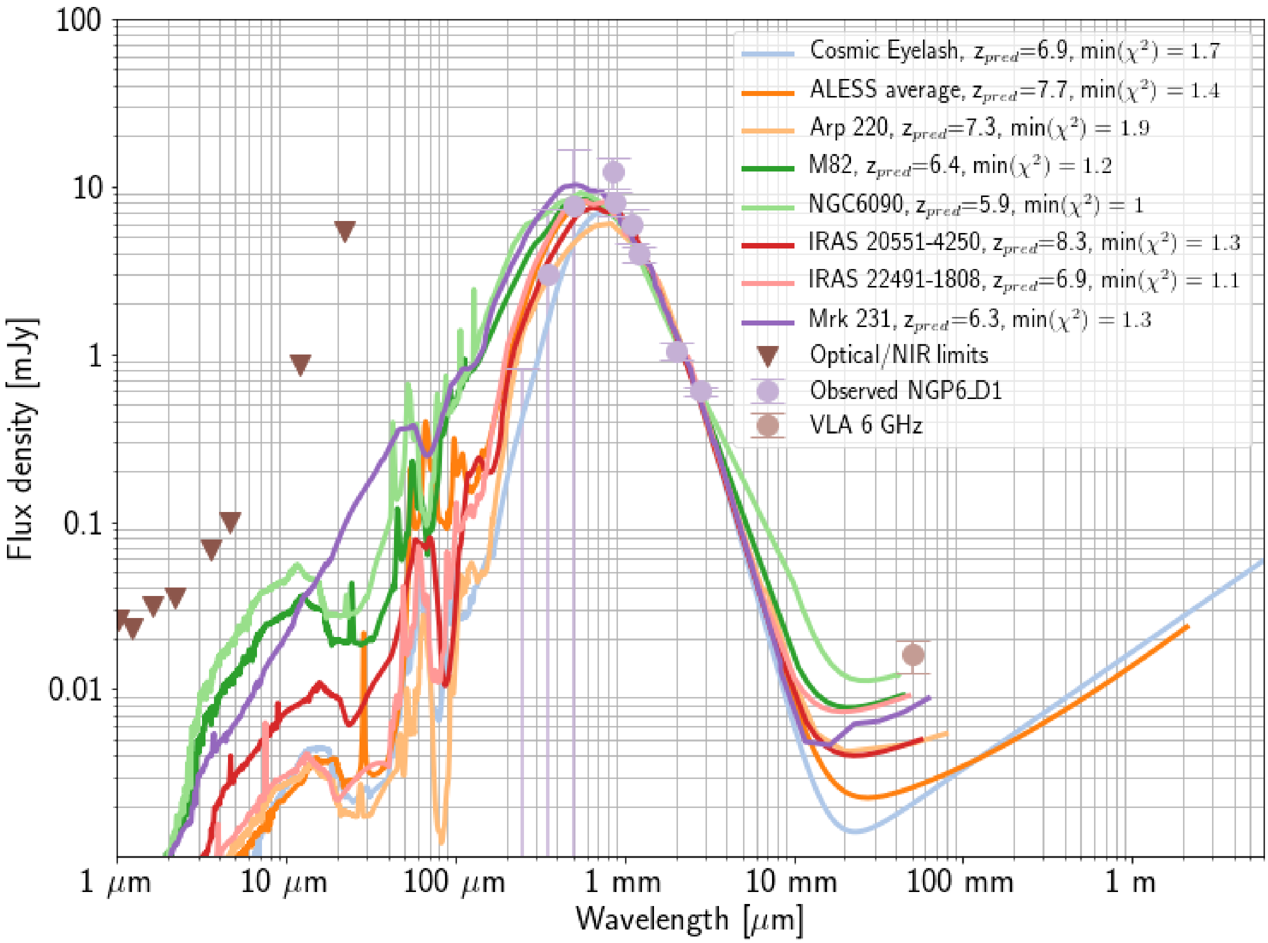

Figure 4.9: The best fit redshift and amplitude for eight templates fit to the photometry of NGP6_D1. The solid coloured lines show the different templates, whilst the legend shows the best fit redshift and minimum χ^2. The grey points with errorbars show the photometry used in the fits, the pink point shows the radio point not used in the fit, and the brown triangles show the optical / NIR upper limits.

is not surprising given the lack of informative features in the long wavelength tail of the dust SED; a single detection in the optical, near-infrared, or mid-infrared would significantly aid in constraining the true redshift.

However, does such a fit generally contain the true redshift of the source? In Figure 4.10 we plot the results of our fitting procedure to a number of well known high-z sources in the literature, as well as a selection of lower redshift sources from the BLAST survey (Chapin et al., 2011). The data used for fitting in each case broadly matches those we have for NGP6_D1 (i.e. the Herschel SPIRE bands plus a number of sub-mm and mm bands where available). As can be seen, in almost all cases the true redshift is contained within the min-max range given by the fits. The only exceptions to this, excluding the BLAST sources which are generally only detected in 1 -

2 FIR bands, are SPT-0311-58 (Strandet et al., 2017), and LSW 20 (Dowell et al., 2014), which are under and over predicted respectively. The reasons for these discrepancies are not clear; both are 500 μm risers, and both have dust temperatures between $\sim 40 - 60$K[9]. These errors indicate the inherent difficulty in fitting photo-zs from templates, but it is encouraging that all the other $z > 3$ sources are well fit by our choice of templates. Nevertheless, the possibility that NGP6_D1 could be similar to LSW-20 or SPT0311-58, and possibly at a lower or higher redshift than predicted cannot be discarded.

Comparing the predictions for NGP6_D1 to the other high-z literature DSFGs, it is clear that NGP6_D1 is predicted to lie at a higher redshift than all other known sources. Its low redshift estimate at $z = 5.9$ is already higher than the highest redshift estimate for all but 6 sources. Its high redshift estimate at $z = 8.3$ is higher than any other high redshift estimate for any other source. As detailed above, there are many uncertainties to these fits, but in general fitting to templates favours a high-z $z > 5$ solution for NGP6_D1.

4.5.2 Fitting Modified Blackbodies

Whilst fitting photometric data to templates is valid if the template SED is well matched to the source SED, Section 4.5.1 has shown that it is difficult to capture the inherent uncertainty in this process. To capture the true uncertainty, we need to utilise a physically motivated model to reproduce the FIR SED of NGP6_D1. Within the literature, this has often been done by assuming the FIR spectrum is well represented by a single dust temperature modified blackbody (Blain, 2002; Magnelli et al., 2012; Bianchi, 2013; Casey et al., 2014). This model usually takes the form:

$$S_\nu \propto (1 - exp(-\tau_\nu))B_\nu, \tag{4.1}$$

where S_ν is the observed flux density at frequency ν, $\tau_\nu = (\frac{\nu}{\nu_0})^\beta$, and gives the optical depth at frequency ν, ν_0 is the frequency at which the optical depth equals unity, and $B_\nu = B_\nu(\nu, T_{dust})$

[9]It is important to note that SPT0311-58 is poorly fit by a single temperature, and indeed Strandet et al. (2017) use a two-component model, with a cold and warm dust temperature of 36 ± 7 K and 115 ± 54 K respectively.

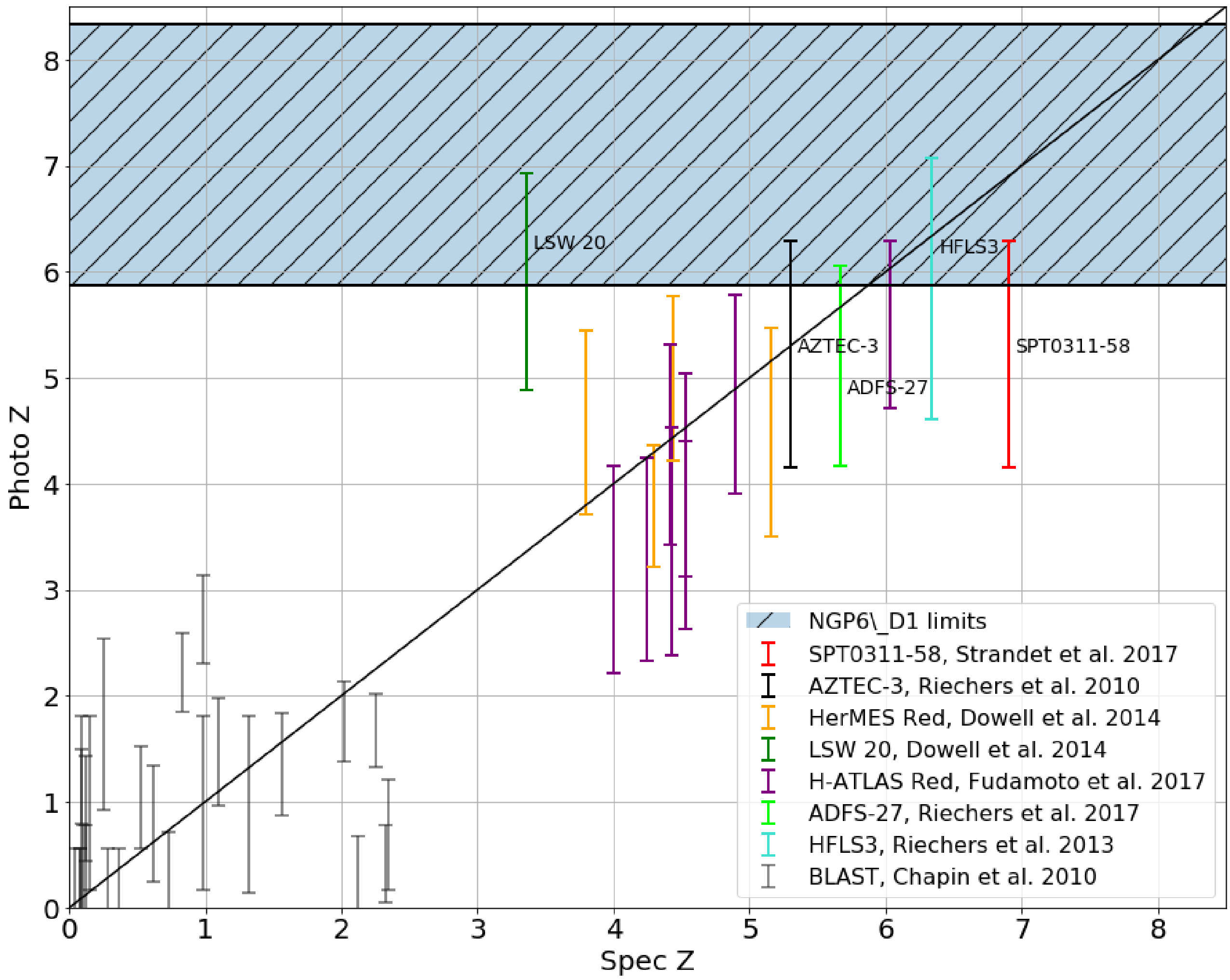

Figure 4.10: A comparison between the photometric and spectroscopic redshift of a variety of literature DSFGs, with photometric redshift fit using the method described in Section 4.5.1. Origins of the data are shown in the legend, whilst several well known DSFGs are labelled with text to their right. The blue shaded region represents the photometric redshift estimate for NGP6_D1.

is the Planck function. β, is usually assumed to be β = 1.5 - 2 for SMGs (Blain, 2002; Casey et al., 2014).

This relatively simple model makes some questionable assumptions, primarily that the dust emission can be well approximated by a single dust temperature[10]. Furthermore, this model often cannot reproduce the Wien side of the FIR SED of SMGs (Blain et al., 2003; Magnelli et al., 2010), though this is less of a problem for us here as we have no observations in this region. However, it is the defacto model primarily used in the literature, and allows us to easily compare its results to other literature sources. In this model, there are 5 parameters to be fit: The redshift z, the average dust temperature T_{dust}, the dust emissivity β, ν_0, and an overall normalisation parameter a.

Similarly to Dowell et al. (2014) and Asboth et al. (2016), we use the affine invariant Markov Chain Monte Carlo (Goodman and Weare, 2010) ensamble sampler PYTHON package, EMCEE (Foreman-Mackey et al., 2013). We use the following uninformative priors for our parameters: $0 < z \leq 12$, $T_{CMB}(z) \leq T_{dust} \leq 80$, $1 \leq \beta \leq 3$, $1\ \mu m \leq c/\nu_0 \leq 1\ mm$, and $-2 \leq log_{10}(a) \leq 2$, where T_{CMB} gives the CMB temperature at redshift z, and c gives the speed of light. For numerical stability, at each sample we first normalise to the 850 μm observation, and allow the normalisation a to vary from there. Tests showed the choice of normalisation band did not drastically affect our final results. The redshift, normalisation, and ν_0 priors are broad and chosen as it is unlikely these parameters lie outside this range; the temperature prior was chosen to ensure the dust temperature is above the CMB temperature, and generally reflects the known distribution of dust temperatures in DSFGs (Chapman et al., 2005; Casey et al., 2014; Clements et al., 2018), and the β prior is typical of what is found in the literature (Bianchi, 2013; Casey et al., 2014). We ran experiments using different and more informative priors, but found that in general we were often reproducing our prior, justifying our choice of an uninformative prior.

To perform our fit, we use 100 walkers over 10,000 steps, throwing away the first 1,000 samples in each chain as a burn-in phase and manually examining the chains to ensure that the samples have fully burnt-in. Figure 4.11 shows the results of the fit, using the same photometry data

[10]See Strandet et al. (2017) for an example where this is clearly not the case

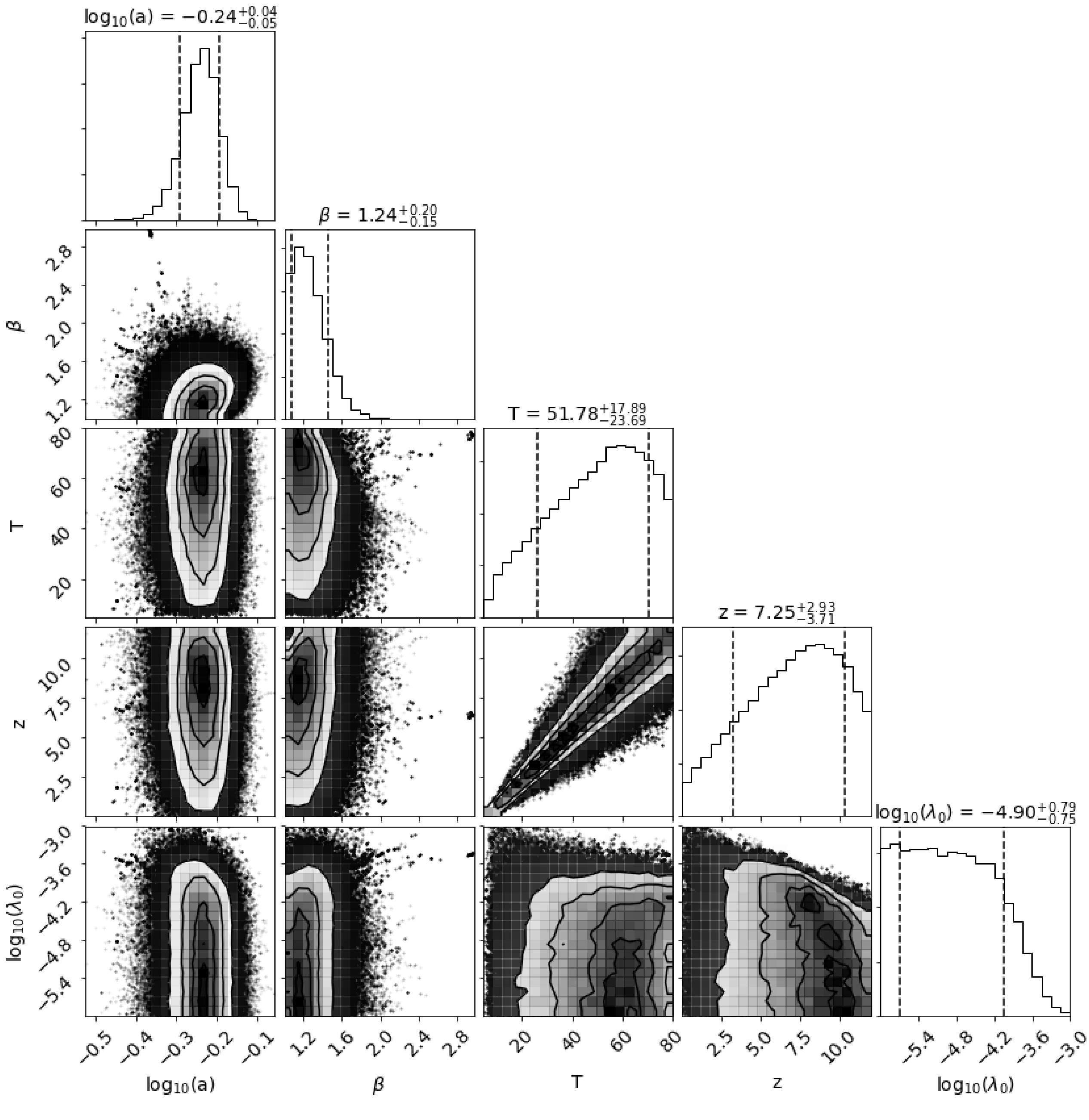

Figure 4.11: A corner plot showing the samples and marginalised posteriors obtained after fitting the model described in Equation 4.1 to the photometry from NGP6_D1. Median values are given above each parameter, whilst errors are taken from the 14th and 86th percentile of each marginalised posterior. The vertical dashed lines also show the 14th and 86th percentiles.

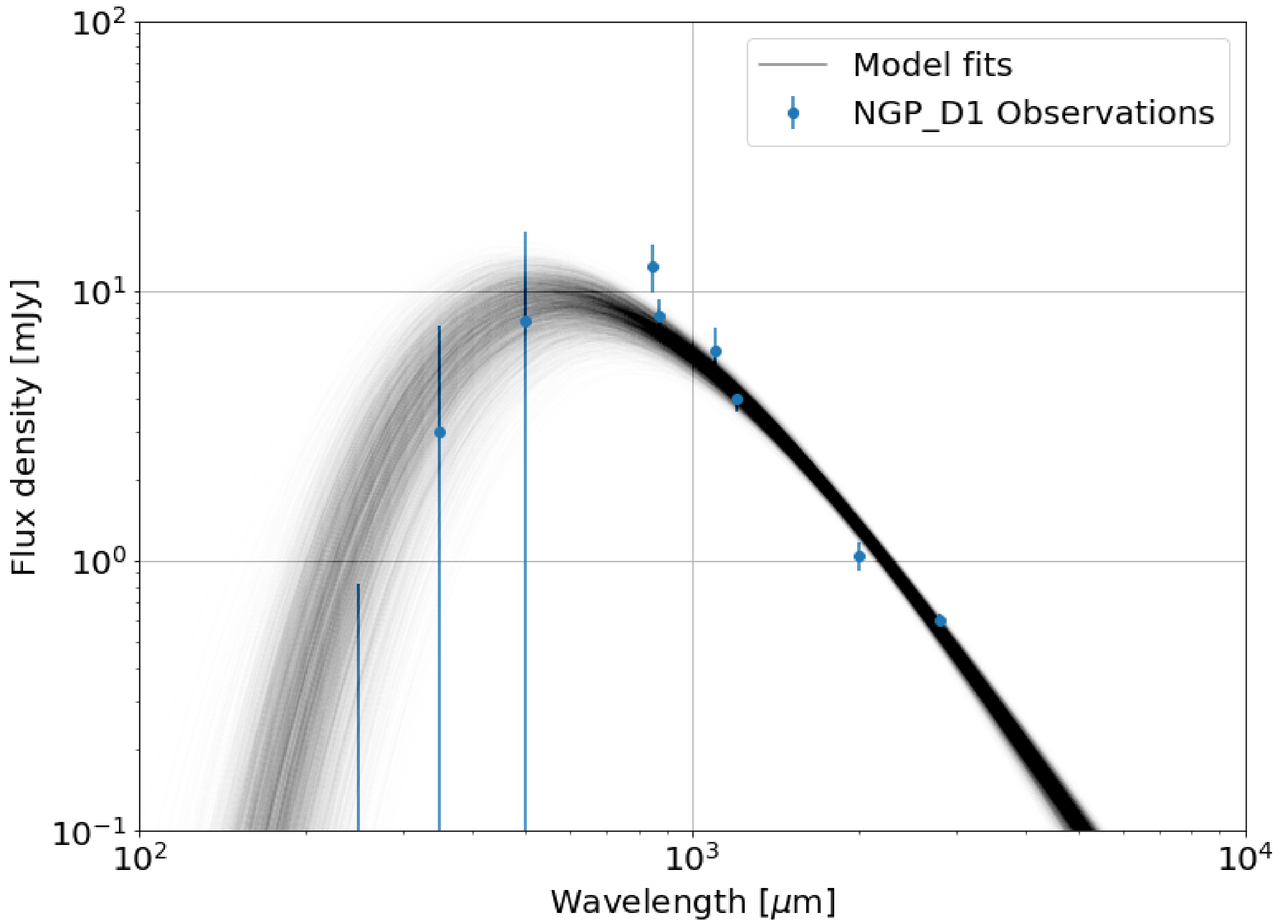

Figure 4.12: 3000 randomly chosen model fits from Section 4.5.2, compared to observations of NGP6_D1

in Section 4.5.1. The temperature-redshift degeneracy can clearly be seen, and indicates that, as expected, we are unable to constrain either the redshift or temperature individually. The ν_0 parameter generally favours $c/\nu_0 < 100\mu$m, indicating that our fits are well matched by an optically thin model. Our normalisation suggests, like the SMA observation, that the observed SCUBA-2 flux density of NGP6_D1 is higher than its true value. The β values are lower than many other $z > 4$ sources in the literature (Riechers et al., 2013; Fudamoto et al., 2017), but within the expected range (though removing the NIKA data can raise this value, as is shown in Section 4.5.3). In Figure 4.12, we plot 3000 single modified blackbody fits to the model, with parameters chosen at random from the samples in the posterior. As expected, most of the uncertainty lies in the SPIRE bands, where our constraints are weakest.

Figure 4.11 shows the posteriors on the parameters used in the model fits, but several further properties can be derived from these samples. These include the $T_{dust}/(1 + z)$ parameter, the FIR luminosity of NGP6_D1, and the dust mass. We calculate the FIR luminosity by integrating between 42.5 and 122.5 μm on the resulting rest-frame FIR SED produced using the parameters from each of the 9,000 samples shown in Figure 4.11. For the dust mass, we follow Riechers et al. (2013) and use

$$M_{dust} = S_\nu D_L^2[(1+z)\kappa_\nu B_\nu(T)]^{-1}\tau_\nu[1 - exp(-\tau_\nu)]^{-1}, \tag{4.2}$$

where S_ν gives the rest-frame flux density at 125 μm, D_L is the luminosity distance, κ_ν is the mass absorbtion coefficient and is assumed to be $\kappa_\nu = 2.64$ m^2kg^{-1} at 125 μm (Dunne et al., 2003). In Figure 4.13 we show our results. This method was also tested on photometry from HFLS3 (Riechers et al., 2013), excluding the redshift, and we found that the literature values of these parameters was generally within the 14th - 86th percentiles of our predictions.

Turning to the parameters and those results derived from them, here we compare our results for NGP6_D1 to other objects in the literature. The $T_{dust}/(1+z)$ parameter of NGP6_D1 is generally lower than those seen in the 500 μm risers seen in Table 3 of Dowell et al. (2014) and Figure 8 of Asboth et al. (2016), which have typical values around 9 - 12, with only one source, FLS 32 in Dowell et al. (2014), having a comparable $T_{dust}/(1+z) = 6.7 \pm 3$ value. Our results are however generally consistent with the $z > 4$ Ivison et al. (2016) selected sources, of which the current spectroscopically confirmed sources are listed in Fudamoto et al. (2017), and have an average $T_{dust}/(1+z)$ parameter of 6.05 $\pm$0.44, in much better agreement with our results here. The spectroscopically confirmed Chapman et al. (2005) sources fit temperatures to their sources using single temperature modified blackbodies, though unlike here they fix their β value to $\beta = 1.5$. They find a mean $T_{dust}/(1+z)$ of 12.3 $\pm$ 3.0, once again significantly higher than we have found for NGP6_D1, with no sources where $T_{dust}/(1+z) < 8$. The redshift distribution of their sources is also limited to $z < 4$, with most of their sources at $2 < z < 3$. The predicted FIR luminosity of NGP6_D1 is reasonably well constrained, with $log_{10}(L_{FIR}) = 12.71^{+0.20}_{-0.78}$, where the errors give the 14th and 86th percentiles of the posterior distribution. These values suggest NGP6_D1 is likely a ULIRG, and if it is at $z > 4$ as our evidence suggests, likely one of the least luminous detected $z > 4$ DSFGs to date (see Table 7 of Fudamoto et al. (2017) for a

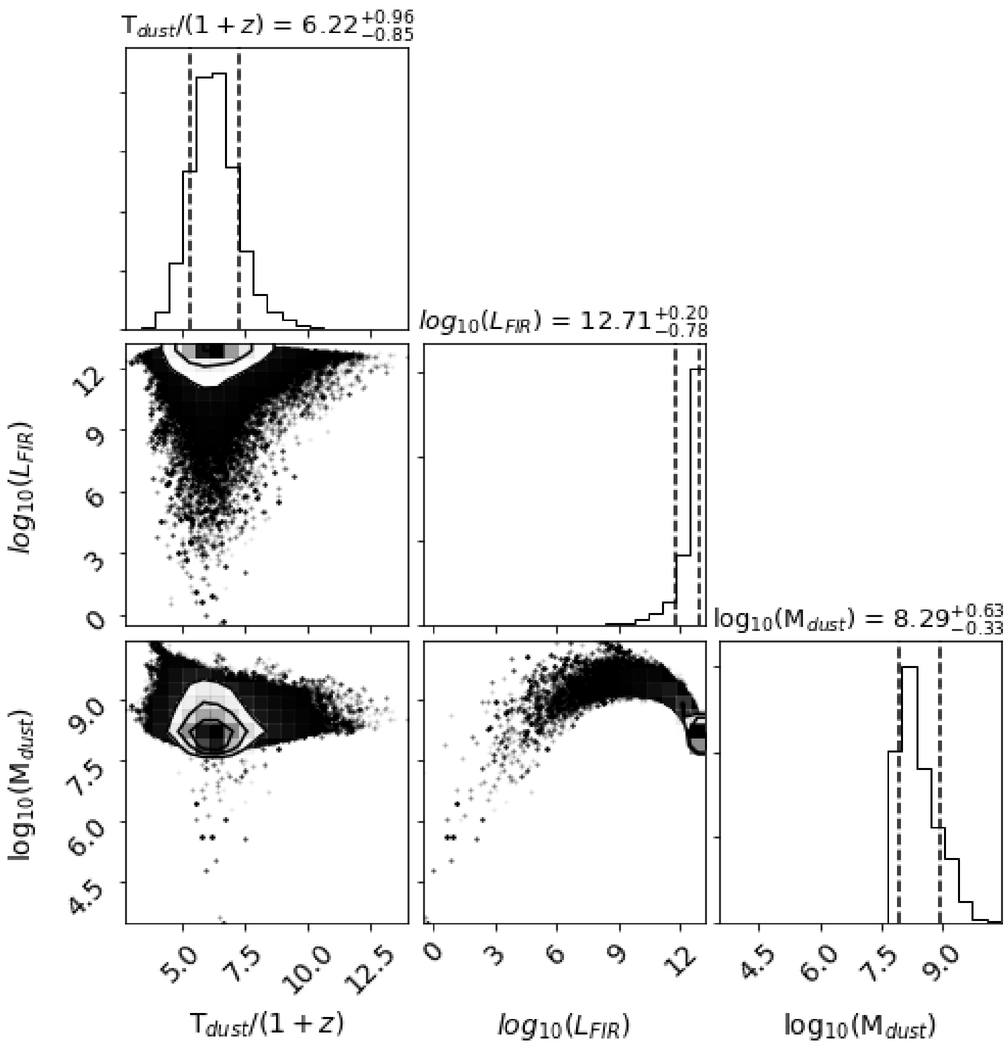

Figure 4.13: Derived parameters for NGP6_D1, using the samples from Figure 4.11

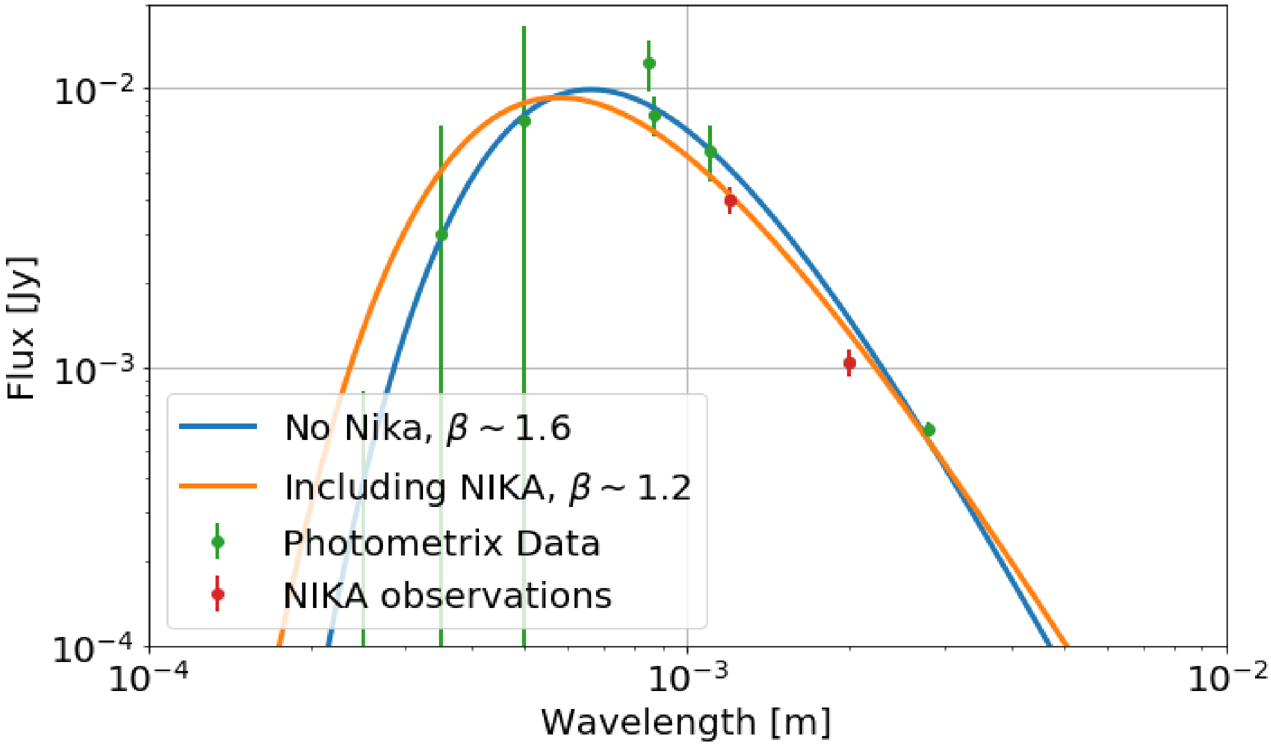

Figure 4.14: Plotting the best fit single modified blackbody models to the data when including the NIKA data (orange line), and excluding it (blue line)

comparison of several literature $z > 4$ DSFGs and their derived properties) and may be more representative of the more general $z > 4$ DSFG population. We convert this FIR luminosity to a SFR by using Equation 4 of Kennicutt (1998), and converting to a Kroupa IMF by dividing by 1.5, as described in Schiminovich et al. (2007) (see also Hayward et al. (2014)). This gives

$$SFR[M_{\odot}\ yr^{-1}] = 1 \times 10^{-10} L_{FIR}\ [L_{\odot}], \tag{4.3}$$

which leads to a predicted SFR for NGP6_D1 of $512^{+301}_{-426}\ M_{\odot}\ yr^{-1}$. This value is an order of magnitude lower than almost all other $z > 4$ DSFGs (see Table 7 of Fudamoto et al. (2017)), with the key exception of HDF 850.1 (Walter et al., 2012), which has a SFR corrected for lensing (using the magnification estimated by Neri et al. (2014)) of $\sim 530\ M_{\odot}\ yr^{-1}$. We note that HDF 850.1 is also the only other SPIRE dropout in Table 7 of Fudamoto et al. (2017).

The predicted dust mass for NGP6_D1 is between 10^8 and $10^9\ M_{\odot}$, slightly lower than but comparable to other literature values (Table 6 of Fudamoto et al. (2017)). Of the 6 dust masses presented by Fudamoto et al. (2017), only one (G09-83808c) is as low as the predicted value for NGP6_D1, and this one source is additionally gravitationally lensed by a factor of 8.2 ± 0.3 (Oteo et al., 2017).

4.5.3 The NIKA Observations

During the course of our analysis, it became apparent that the NIKA fluxes appeared systematically lower than expected by a factor of ~ 1.5. Examination of the processed data, $\tau_{225\ GHz}$ values during the observations, and observing logs do not suggest issues or any likely origin for any possible systematic errors. The data were taken during a shared-risk mode, and the pipelines to reduce the raw data are no longer available, so it is not possible to re-reduce the data. Nevertheless, comparison to data taken at other wavelengths appear to indicate a systematic offset well beyond the reported errors, as can be seen in the zoom in on the sub-mm and mm photometry of NGP6_D1 (Figure 4.14).

Because of these discrepancies, we also ran our sampler without the NIKA data included to see what effects it has on our results. The resultant predicted SED is compared to the results when including the NIKA data in Figure 4.14. Despite the difference in shape, the derived parameters are similar, though parameters are slightly higher when excluding the NIKA data. Both models are consistent with an optically thin model (i.e for all observed frequencies observations $\frac{\nu}{\nu_0} << 1$), have similar derived FIR luminosities ($\log_{10}(L_{FIR}/L_{\odot}) = 12.87^{+0.24}_{-0.87}$ when excluding the NIKA data), and similar predicted dust masses ($\log_{10}(M_{dust}/M_{\odot}) = 8.87^{+0.78}_{-0.49}$ when excluding). The only clear differences are in the derived β values, which are $\beta = 1.23^{+0.20}_{-0.15}$ when including the NIKA data but $\beta = 1.80^{+0.53}_{-0.38}$ when excluding the NIKA data, and in the $\mathrm{T}_{dust}/(1+z)$ parameters, which when including the NIKA data are $\mathrm{T}_{dust}/(1+z) = 6.22^{+0.96}_{-0.85}$ compared to $\mathrm{T}_{dust}/(1+z) = 4.86^{+1.38}_{-1.18}$ without. Additionally, the reduced χ^2 values for the median sampled parameters is $\chi^2_{red} = 3.95$ when including the NIKA data, but 2.62 when excluding it, indicating marginally better fits. This can be seen graphically in Figure 4.14, which clearly shows that the NIKA data are systematically lower than expected from fitting, but this difference does not appear to be having a significant effect on most of the derived parameters for NGP6_D1, and more data are needed, ideally at wavelengths where the two models significantly disagree (i.e.

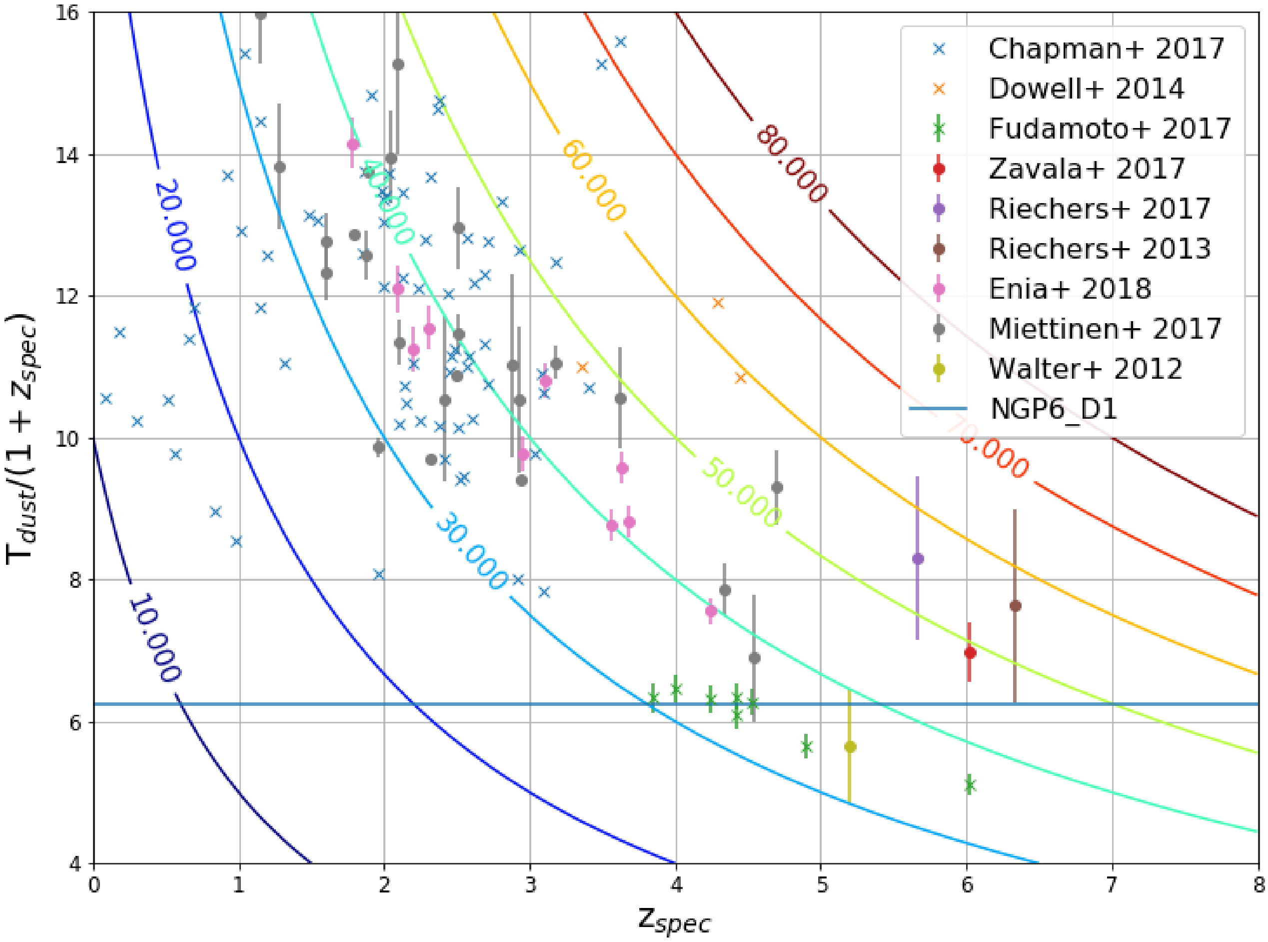

Figure 4.15: Spectroscopically confirmed redshifts to $T_{dust}/(1+z)$. Crosses mark sources where temperatures are fit through template fitting, whilst filled circles indicate sources which use single modified blackbodies. Contours show lines of constant temperature. The horizontal blue line indicates the best fit $T_{dust}/(1+z)$ for NGP6_D1.

potentially SCUBA-2 450 μm observations). For now, we continue to include the NIKA data, but we note that it is possible that β values may be higher, whilst $T_{dust}/(1+z)$ values might be lower.

4.5.4 The Statistics of $T_{dust}/(1+z)$

In Figure 4.15, we plot the $T_{dust}/(1+z)$ parameter for a range of DSFGs with either spectroscopic confirmation or accurate photometric redshifts. We also plot the median $T_{dust}/(1+z)$ value derived for NGP6_D1 to make comparisons. Most DSFGs have temperatures between 30 and 50 K, and those detected at redshifts $\lesssim 3$ appear to be slightly cooler than those detected at $z > 4$. Given the $T_{dust}/(1+z)$ value for NGP6_D1, if it has a similar 30 - 50K dust temperature to other literature sources, it once again implies a $z > 4$ solution.

In Figure 4.16, we again plot z vs $T_{dust}/(1 + z)$, but this time overplot the IR luminosity required for a source at that redshift and temperature, if that source had a 500 μm flux density of 21 mJy (i.e. just detected in SPIRE). We do the same on the right for 850 μm, and 10 mJy. These limits are chosen as they represent the typical detection limits for both the SPIRE 500 μm band and SCUBA-2 at 850 μm, and therefore a source with this temperature and redshift must be at least this FIR luminous to be detected by either instrument. Focusing initially on the 500 μm plot, the top right is uninhabited as very large areas would need to be surveyed to find a source this luminous due to the steepness of the IR luminosity function. The bottom left on the other hand is unoccupied as no LIRG/ULIRG like sources appear to have temperatures << 30K. Of key importance to NGP6_D1 and other SPIRE dropouts is the IR luminosity requirements of a $z > 4$ source if it is to be detected in the SPIRE 500 μm band; for a typical DSFG dust temperature, a source will, in general, need to possess HLIRG like luminosities in order for it to be detected in SPIRE. Indeed, of the few $z > 5$ confirmed SPIRE sources, most have observed IR luminosities $> 10^{13}$ $L_{\odot}$[11] (Riechers et al., 2013; Fudamoto et al., 2017; Riechers et al., 2017; Strandet et al., 2017). Sources selected at 850 μm however do not have this requirement, and ULIRG like sources that may be missed by SPIRE can be selected at 850 μm. HDF 850.1 (Walter et al., 2012), a purely 850 μm selected source and indeed a SPIRE dropout itself, is a good example of a high-z, lower temperature and lower luminosity source. This suggests that sources like NGP6_D1, HDF 850.1 and indeed the SPIRE dropouts in general, may be better representations of the less luminous, more populous $z > 4$ DSFGs, a population that Figure 4.16 suggests SPIRE would have difficulty in detecting.

4.6 Spectroscopic Analysis

In this Section, we explore the implications of the upper limits on our spectroscopic observations, examine whether a non-detection is expected compared to other high-z DSFGs, and derive upper limits to the gas mass of NGP6_D1.

[11]Uncorrected for lensing.

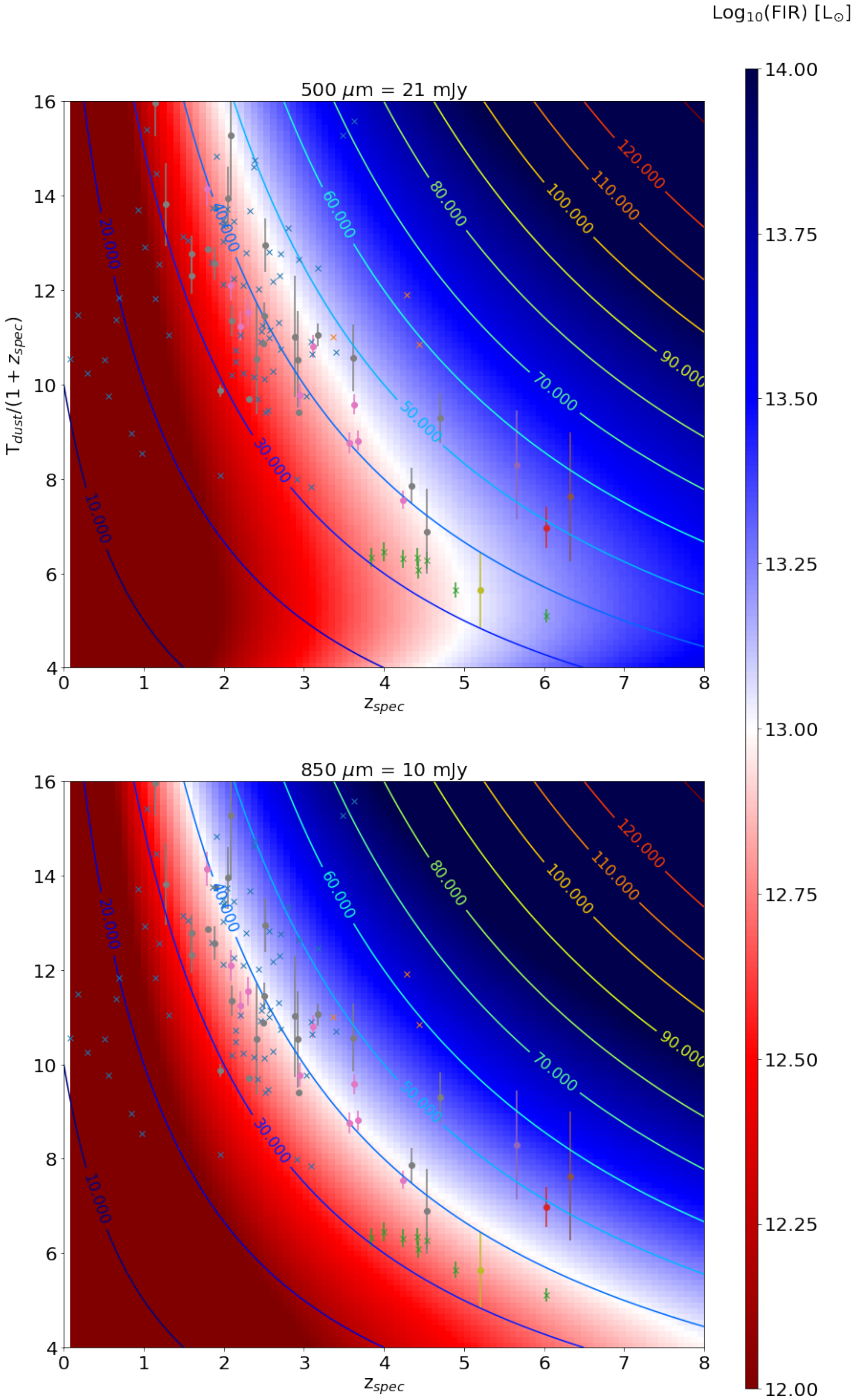

Figure 4.16: *(Top)* The same plot as Figure 4.15, whilst the background colours indicate the required $\log_{10}$ IR luminosity of a source at that redshift, temperature, and a flux density of 21 mJy at 500 μm, the approximate 3σ limit of SPIRE. *(Bottom)* The same as on the top, but this time for a flux density of 10 mJy at 850 μm, the approximate 4-5σ detection limit of many SCUBA-2 observations. Colours correspond to the colourbar shown to the right of both plots.

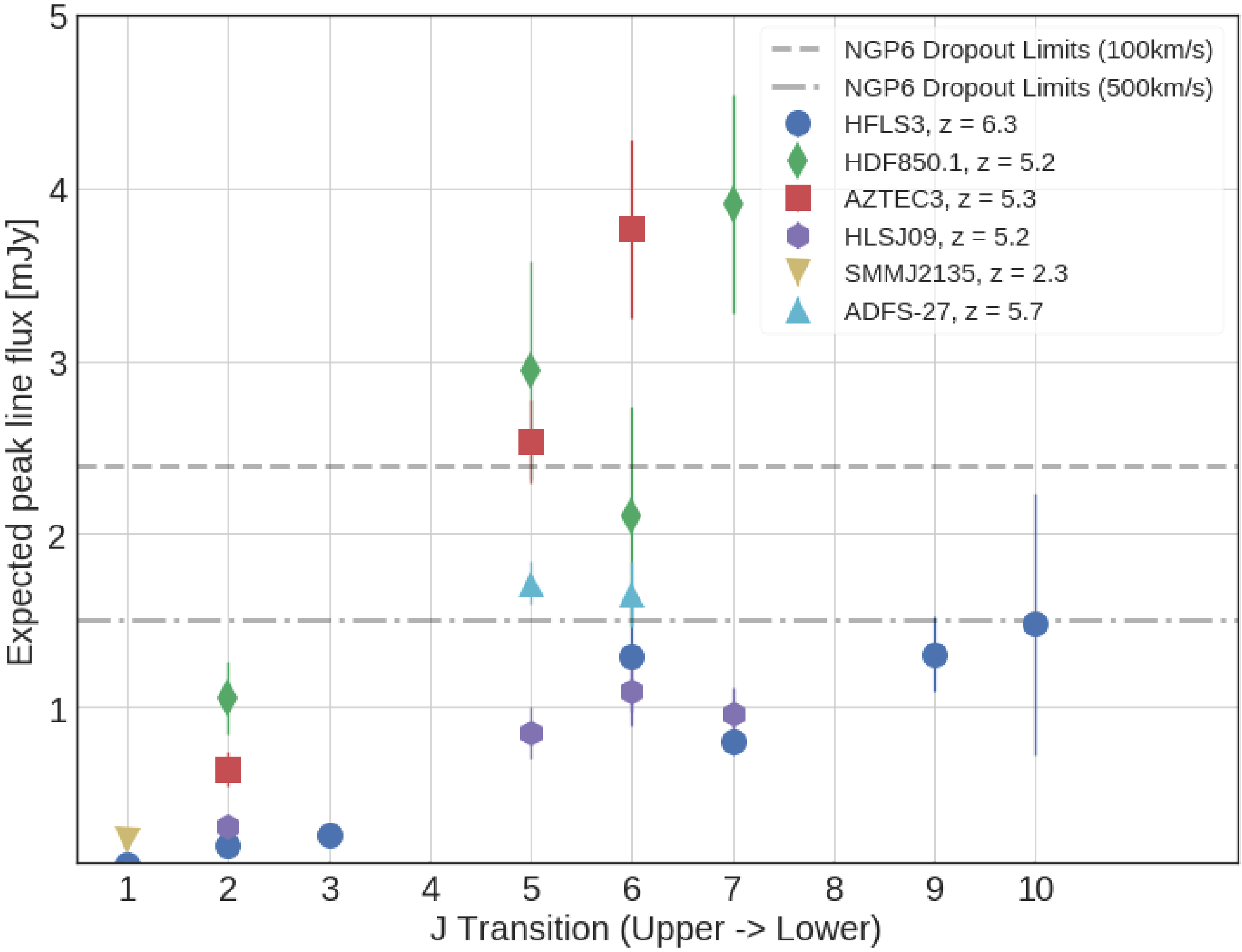

Figure 4.17: The expected peak line flux of the CO line transitions of NGP6_D1, as estimated by several well studied high-z DSFGs and indicated using the different coloured markers. The dashed line shows the upper limits at 100 $km\ s^{-1}$, whilst the dot dashed line shows the upper limits at 500 $km\ s^{-1}$

4.6.1 Literature CO Values

We estimated the expected CO line flux densities for NGP6_D1 by multiplying the observed 850 μm flux density of NGP6_D1 by the CO line flux to 850 μm continuum ratio in several other high redshift DSFGs. In Figure 4.17, we plot these estimates for six well studied SMGs, as well as the upper limits of our EMIR and RSR observations.

At the redshifts estimated from template fitting in Section 4.5.1, between 72 - 114 GHz we expect to see the CO(5-4) - CO(8-7) transitions. These are typically the brightest CO lines seen in DSFGs (see Figure 4.17). Given no detection, we place 3σ upper limits of 2.4 mJy at a resolution of 100 $km\ s^{-1}$ and 1.5 mJy at a resolution of 500 $km\ s^{-1}$. Figure 4.17 suggests we can rule out a CO line flux in NGP6_D1 that is similar to AZTEC3 (Riechers et al., 2010) or HDF 850.1 (Walter et al., 2012). We may be able to marginally rule out a line flux similar to ADFS-27 (Riechers et al., 2017), under the assumption that the line widths in NGP6_D1 are $\sim 500\ km\ s^{-1}$. We cannot however rule out an SLED similar to HLSJ09 (Combes et al., 2012) or HFLS3 (Riechers et al., 2013). Our observations therefore approach the limits where we can indicate that NGP6_D1 is CO deficient compared to other high-z DSFGs, but at this stage we are not able to make this claim. Further observations are ongoing. Our results underscore the difficulty associated with these kind of blind spectral line searches. For instance, Fudamoto et al. 2017 performed spectral scans on 21 objects using NOEMA and/or ALMA, but only secured redshifts for 7. Where they detected no lines, they estimate peak line fluxes of ~ 1.7 mJy, similar to our upper limits here. The other possibility is that it is the lower or higher CO transitions that lie in our bandwidth, which are generally fainter. We find this unlikely though, as we have consistently found that the data disfavour a $z < 4$ solution, ruling out the lower transitions, whilst the higher transitions would require our source to be at $z > 8$ and therefore intrinsically highly luminous.

4.6.2 CO(1-0) Estimates

CO(1-0) has often been used as a proxy for the molecular gas mass in a galaxy (Solomon and Vanden Bout, 2005), as CO is both abundant and possesses readily observable transitions. The conversion factor α_{CO}, relating the CO line luminosity $L^{'}_{CO}$ to the total molecular gas mass M_{H_2}, is given by

$$M_{H_2} = \alpha_{CO}\ L'_{CO(1-0)}. \tag{4.4}$$

A large range of values for α_{CO} have been found for a wide variety of galaxies, from ~ 0.1 to $\lesssim 10$. For SMGs, α_{CO} has generally been found to be $\alpha_{CO} = 0.4 - 1$ (Tacconi et al., 2008; Magnelli et al., 2012; Hodge et al., 2012; Fu et al., 2013; Bothwell et al., 2013), but there remain large uncertainties, and the applicability of α_{CO} to high redshift systems continues to be debated (Papadopoulos et al., 2012). According to Equation 6 of Bothwell et al. (2013)

(derived originally in Solomon and Vanden Bout (2005)), the CO luminosity is given by

$$L'_{CO} = (3.25 \times 10^7)\ I_{CO}\ \Delta\nu\ \nu_{obs}^{-2}\ D_L^2\ (1+z)^{-3}, \tag{4.5}$$

where $I_{CO}\ \Delta\nu$ gives the velocity integrated line flux in $Jy\ km\ s^{-1}$, L'_{CO} is the CO line luminosity in units of $K\ km\ s^{-1}\ pc^2$, ν_{obs} is the observed frequency of the line, and D_L is the luminosity distance to the source in Mpc. To derive upper limits on the gas mass, we first follow Equation 7 of Bothwell et al. (2013):

$$I_{CO} < 3RMS_{channel}\sqrt{\Delta V_{co} d\nu}, \tag{4.6}$$

where $RMS_{channel}$ gives the RMS error on each channel (in this case 0.46 mJy), ΔV_{co} gives the typical line width for CO, and dν gives the bin width, both of which we take as 500 km s^{-1}. We calculate this over a redshift range $z = 2-10$, and for the $CO(J = N \rightarrow (N-1))/CO(J = 1-0)$ conversion ratios listed in Table 4 of Bothwell et al. (2013), using only the $4-3$ and higher conversion ratios listed. Equation 4.5 is a function of redshift, which is poorly constrained by our results for NGP6_D1. However, the uncertainty due to redshift is sub-dominant to the uncertainty from which of the $CO(J = N \rightarrow (N-1))/CO(J = 1 \rightarrow 0)$ conversation ratios we use, given our redshift range. As such, we estimate an L'_{CO1-0} luminosity upper limit of $(1.1 \pm 0.35) \times 10^{11}\ K\ km\ s^{-1}\ pc^2$ for NGP6_D1. Assuming an α_{CO} conversion ratio of 1.0 $M_\odot\ (K\ km\ s^{-1}\ pc^2)^{-1}$, this leads to a molecular gas mass upper limit for NGP6_D1 of $(1.1 \pm 3.5) \times 10^{11}\ M_\odot$.

In Figure 4.18, we plot our estimated CO upper limits against the estimates of the FIR luminosity of NGP6_D1, and include a number of other spectroscopically confirmed sources for comparison. We also plot the predicted L_{FIR} - L'$_{CO}$ relation proposed by Greve et al. (2014). With our current upper limits on the L_{CO} luminosity, we find that our independent L_{FIR} estimates are consistent with the observed scatter in the L_{FIR} - L_{CO} relation.

Comparing this with results from Section 4.5.2, we find our molecular gas mass upper limits imply an upper limit to the gas depletion time, $\tau_{dep} = M_{H2}/SFR$ of ~100 - 1000 Myr, depending

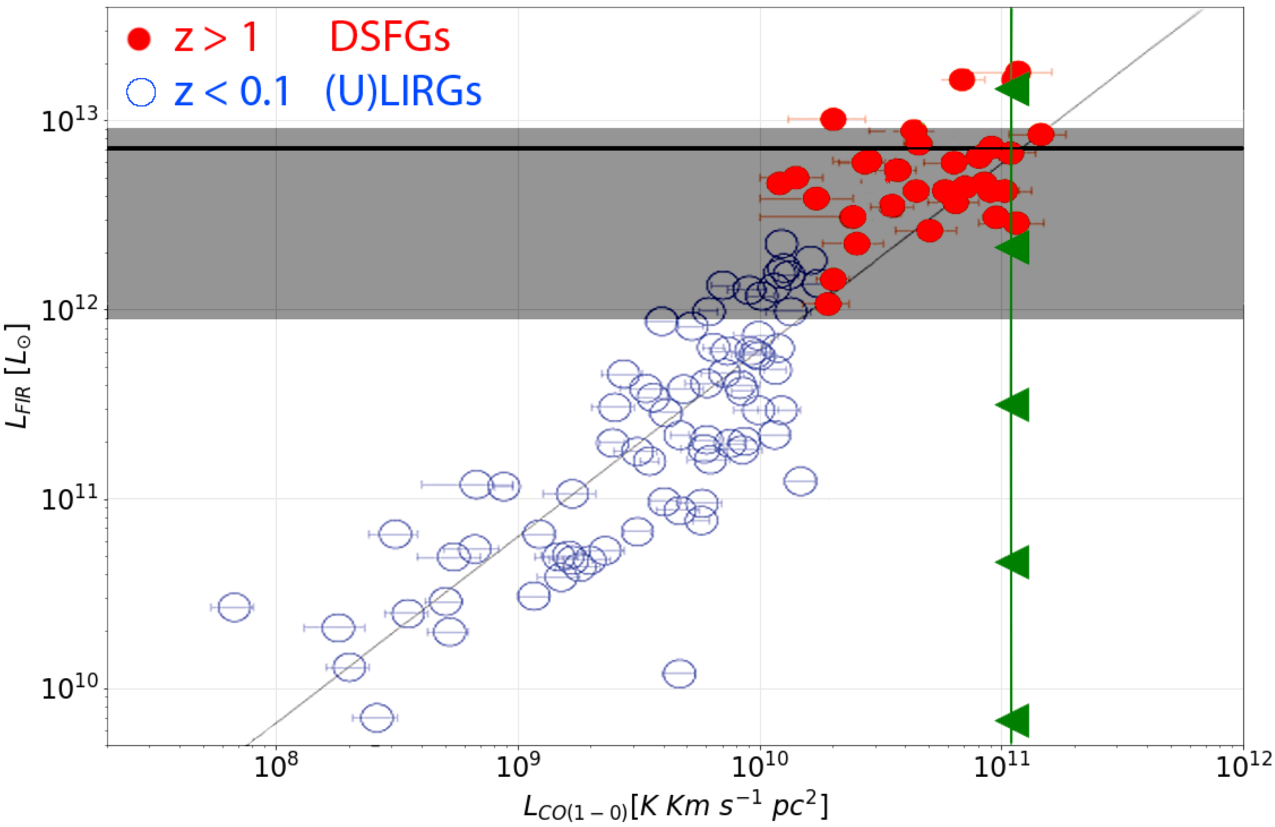

Figure 4.18: The L_{FIR} to L_{CO} correlation for LIRGS at $z < 0.1$ (blue open circles), and for $z > 1$ DSFGs (red filled circles). The limits for both the L_{FIR} and $L_{CO(1-0)}$ for NGP6_D1 are shown as the grey shaded region (the mean is shown as a thick black horizontal line) and green left-facing triangles respectively. The solid diagonal line shows the parameterized $L_{CO(1-0)} - L_{FIR}$ relation proposed by Greve et al. (2014).

on whether we use the lower or upper estimate of the SFR of NGP6_D1, and a median value of 214 Myr. The uncertainty in these upper limits straddles the ~ 100 Myr depletion times seen in SMGs and the ~ 1 Gyr depletion times seen in normal[12] $z > 1$ galaxies (Tacconi et al., 2010; Bothwell et al., 2013; Carilli and Walter, 2013). Additionally, our estimated upper limits on the gas mass provide an upper limit to the molecular gas to dust ratio of ~ 500, using the medium estimated values for both the dust and gas mass upper limits, indicating we are approaching the range of values seen in other high-z SMGs, typically around 100 (Bothwell et al., 2013).

4.7 Radio FIR Correlation

An observed strong correlation exists between the FIR and radio luminosities of a wide variety of galaxies (Helou et al., 1985; Condon et al., 1991; Condon, 1992; Yun et al., 2001; Sargent et al., 2010). The precise mechanisms of this correlation are unclear, but it is thought that the massive, hot stars are responsible; during their lifetimes, these stars primarily emit UV radiation, readily absorbed and re-radiated by dust in the FIR, whilst at the end of their lifetimes they die in supernova explosions which produce the relativistic electrons responsible for synchrotron radiation (Helou and Bicay, 1993; Lacki et al., 2010). Here, we examine whether we can use our radio detection of NGP6_D1 and the FIR-radio correlation to gain another independent measure of the FIR luminosity of NGP6_D1.

Helou et al. 1985 defined the ratio of the FIR to radio luminosities as

$$q = Log_{10}(L_{FIR} \;/\; 3.75 \times 10^{12}\ W) - Log_{10}(L_{1.49\ GHz} \;/\; W\ Hz^{-1}), \tag{4.7}$$

where L_{FIR} is the FIR luminosity of a galaxy, and $L_{1.49\ GHz}$ is its monochromatic luminosity at rest frame 1.49 GHz. Thus, we first must convert our observed frame 6 GHz flux density to its rest frame 1.49 GHz flux density. We model the radio emission as $S_\nu \propto \nu^\alpha$, where we explicitly assume $\alpha = -0.8$, typical of what has been used in the literature. As the redshift of NGP6_D1 is uncertain, we simply take a redshift grid between 0.1 and 10, with step sizes of $\Delta z = 0.1$.

[12] I.e. not mergers or quasars, which are more typically studied at $z > 1$

We then use Equation 4.7 to compute L_{FIR}, assuming a q value of 2.3 ± 0.2, typical of what is found for a wide variety of galaxy types (Condon, 1992), including SMGs (Michałowski et al., 2010; Thomson et al., 2014). We plot our results as a function of redshift in Figure 4.19.

The FIR-radio correlation predicts a FIR luminosity $log_{10}(L_{FIR}) \gtrsim 13.5\ L_{\odot}$ at $z \sim 6$, higher than derived in Section 4.5.2. If we assume that the redshift estimates from template fitting are correct, then this discrepancy can be explained if NGP6_D1 is moderately radio-loud, implying the potential presence of an AGN in a dusty galaxy at $z \sim 6$. However, these templates may be overestimating the redshift of NGP6_D1. The 2σ lines seen in the RSR spectrum, but not seen in the EMIR spectrum, would correspond to $z \sim 4.5$, but even in this case the predicted FIR luminosity is significantly higher than expected from our fitting procedures. If there is no AGN component, the fitting procedure and FIR-radio correlation predict a redshift $z \sim 2.8$, which we have already ruled out as we would likely have detected NGP6_D1 in SPIRE.

4.8 Discussion

4.8.1 Comparison to the Literature

In this Section, we compare NGP6_D1 to other dropout-like sources in the literature. Only recently have large surveys at 850 μm been completed, so few examples of 850 μm risers or SPIRE dropouts have been published to date.

Ikarashi et al. 2017 identify and characterise two sources, selected partially on the basis of their faint SPIRE emission. These sources both are undetected in SPIRE, but are both detected by SCUBA-2 at 850 μm and ALMA at 1.1 mm, with flux densities of ~ 4.5 and ~ 3.0 mJy each in the respective bands. One source, ASXDF1100.053.1, is further detected by the VLA at 6 GHz, with a flux density of $4.5 \pm 1.1\ \mu\ Jy$. Compared to NGP6_D1, these sources are $4\times$ as faint at 850 μm, despite neither NGP6_D1 or either of the Ikarashi et al. 2017 sources being detected in SPIRE. Furthermore, NGP6_D1 is $4\times$ brighter at 6 GHz compared to ASXDF1100.053.1. Indeed, if we repeat our analysis in Section 4.7 on ASXDF1100.053.1, we find it has an estimated

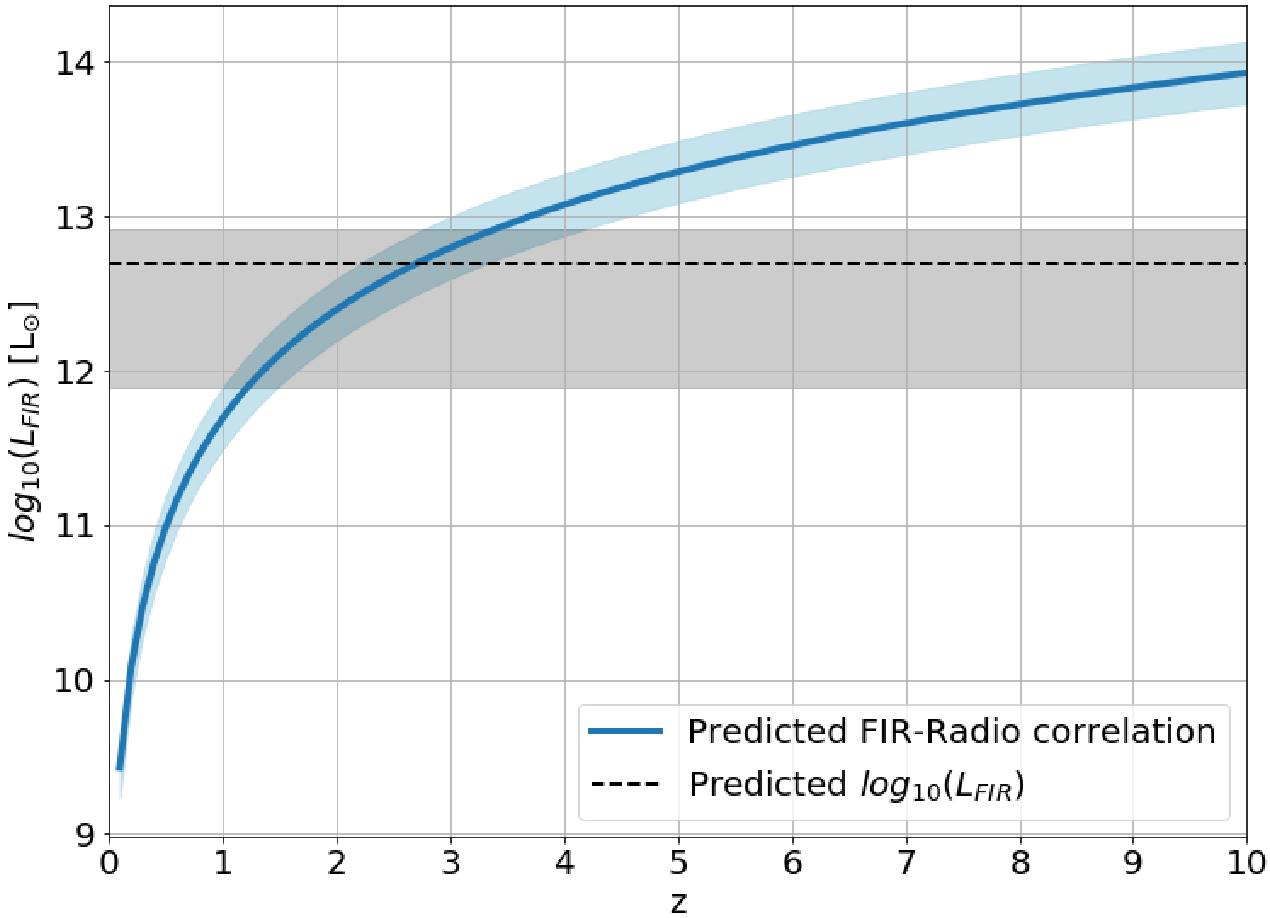

Figure 4.19: The predicted FIR luminosity of NGP6_D1, based on its radio flux density and the FIR-radio correlation. The blue line shows the predicted FIR luminosity given $q = 2.3$, whilst the blue shaded region covers the ± 0.2 rms scatter typically seen on q. The dashed black line shows the predicted FIR luminosity from Figure 4.13, whilst the shaded black region shows the 14^{th} - 86^{th} percentiles on that luminosity.

FIR luminosity consistent with estimates from the FIR-radio correlation, unlike NGP6_D1.

Boone et al. 2013 found a SPIRE-dropout during APEX/Laboca follow up in the Herschel Lensing Survey (Egami et al., 2010). They conclude that it is possibly a low luminosity source ($L_{FIR} < 10^{12}\ L_{\odot}$) at z > 4 that is being lensed, possibly multiple times, by the brightest cluster galaxy in AS1063 (RXC J2248.7-4431). They further postulate this dropout source may be associated with an optically detected z = 6.107 system. Further follow up work by Boone et al. 2015 reveals numerous dropout sources amongst the Herschel Lensing Survey fields, with ALMA and NOEMA programs being further undertaken to discover the nature of these sources. The key difference between NGP6_D1 and the dropouts found in the Herschel Lensing Surveys is that there is no evidence that NGP6_D1 is being lensed by any structure. It is too early to say whether this is because NGP6_D1 represents a more intrinsically luminous population of dropouts, whereas the lensed dropouts may represent the more general population of z > 4 DSFGs, but it is clear from our work here that such dropouts are not limited to the lensing fields alone.

4.8.2 What do the SPIRE Dropouts Represent?

Given what we have learned about this well studied SPIRE-dropout, here we briefly examine other populations that may be analogous to SPIRE dropouts like NGP6_D1. We particularly focus on whether the SPIRE-dropouts are similar to other known populations of DSFGs, or whether they represent a unique type of luminous but cool DSFG, hitherto missed by previous surveys and through selection biases.

The 850 μm risers ($S_{250} < S_{350} < S_{500} < S_{850}$, though often just the last criterion of $S_{500} < S_{850}$ is used due to a lack of detection in the shorter wavelength SPIRE bands) may represent a population of DSFGs at redshifts $z > 6$ (Ikarashi et al., 2017; Riechers et al., 2017). The theory behind this is similar to the 500 μm riser population (Dowell et al., 2014; Asboth et al., 2016; Ivison et al., 2016); at $z \geq 6$ their rest-frame $\sim 100\ \mu m$ peak of dust emission would be redshifted into the 850 μm band. A source bright enough to be detected at both 850 and 500 μm would then be classed as an 850 μm riser. This population potentially relates to NGP6_D1;

a source with a 500 μm flux density below the nominal SPIRE detection threshold, but which is still detected at 850 μm would be classed as a SPIRE dropout.

Few confirmed 850 μm risers are known. As part of a follow up of 500 μm risers, Riechers et al. (2017) discovered ADSF-27, a binary HLIRG 850 μm riser. It has a spectroscopically confirmed redshift of $z = 5.655$ and a luminosity of 2.4×10^{13} $L_{\odot}$. Despite this high luminosity, ADFS-27 is only just bright enough to be detected in the SPIRE bands, and indeed of ∼1000 deg^2 of SPIRE extragalactic field area, only $\sim$ 100 deg^2 reach depths deep enough to detect ADFS-27-like objects (Riechers et al., 2017). Riechers et al. (2017) further suggest that the surface density of 850 μm risers could be as low as 9×10^{-3} deg^{-2}, if ADFS-27 remains the only 850 μm riser amongst the SPIRE-only detected 500 μm risers. The rarity of 850 μm risers is supported by Ivison et al. (2016), who followed up a sample of 109 red SPIRE sources from the H-ATLAS survey with SCUBA-2, and found no source was an 850 μm riser.

A key difference between the Ivison et al. (2016) sample and ADFS-27 however is the flux density at 500 μm; whilst the Ivison et al. (2016) sample had a minimum 500 μm flux density of 30 mJy from completeness considerations, the 500 μm flux of ADFS-27 is only 24.0 ± 2.7 mJy. Indeed, HDF-850.1 (Walter et al., 2012), the only other well studied SPIRE dropout, is undetected in SPIRE, with a 500 μm flux density < 21 mJy. What luminosity would a typical DSFG have to be in order to be detected in SPIRE at ($S_{500} > 30$ mJy), and be an 850 μm riser ($S_{850} > S_{500}$)? In the top panel of Figure 4.20 we plot the luminosity, redshift and dust temperature a source would require in order to be detected in both SPIRE at 500 μm and SCUBA-2 at 850 μm, whilst also having $S_{850} > S_{500}$. We would not expect to see many 850 μm risers at $z < 4$, as they would require cold dust temperatures of $<$ 30K, and would generally be ULIRGS from $z = 2 - 4$. Using Equation 4.2 these requirements would lead to dust masses $> 10^{10} M_{\odot}$, 2 orders of magnitude higher than seen typically in the literature (da Cunha et al., 2015). At $z > 5$ however, we would also expect sources to be rare, as only the most luminous HLIRG and above systems with dust temperatures of 40 - 50K would be detected as 850 μm risers. These results seem to contrast with the observed $T_{dust}/(1+z)$ of ADFS-27, with $T_{dust}/(1+z) = 8.3$ at $z = 5.655$. However it should be noted that ADFS-27 is a merger of two systems, at a distance of around 10 kpc from one another. Even though they are at the same redshift, it is possible to construct a viable 850 μm riser SED; experiments show that fitting dual single modified black bodies to the two components of ADFS-27, with ~20 K and ~50 K dust temperatures respectively, can accurately reproduce the observed SED of the dual system.

Additionally, the SPIRE dropouts may be fainter analogues to the 500 μm risers; a 500 μm riser too faint to be detected in the SPIRE bands may still be detected at 850 μm due to the different depths SPIRE and typical 850 μm instruments reach. In the bottom panel of Figure 4.20, we plot a SPIRE dropout with a 850 μm flux density of 10 mJy. We further indicate where, in the plot of $T_{dust}/(1+z)$ vs z, such a source would be detected in SPIRE (and therefore not a dropout), where it is a fainter version of a 500 μm riser, and where it is a fainter version of an 850 μm riser. For a source with an 850 μm flux density of 10 mJy, about half of the parameter space would not be detected in SPIRE, including ULIRGS with $z \gtrsim 4$ and/or $T_{dust} < 50$ K sources.

Finally, comparing the two panels of Figure 4.20, it is immediately apparent that the SPIRE dropouts cover a much larger range of parameter space compared to the 850 μm risers seen in the top panel. Furthermore, they are better at detecting the general population; they are able to detect sub-HLIRG objects with dust temperatures 30 - 50 K, similar to the general population seen in Chapman et al. (2005) and Miettinen et al. (2017) in Figure 4.15. The 850 μm risers on the other hand, are limited to HLIRG-like objects at $z > 5$, and below $z = 4$ are limited to cold $T_{dust} < 30$ K objects. We have shown here that the SPIRE dropouts provide excellent access to the $z > 5$ Universe, and likely probe the more general ULIRG population of DSFGs at these redshifts, unlike the 500 μm and 850 μm risers, which are limited to sources at the high-end of the FIR luminosity function. If the trends seen at $z = 2 - 3$ in Figure 4.15, that *most* SMGs have dust temperatures $\sim$ 30 - 50 K, continues to $z > 4$, then the SPIRE dropouts could well represent a population of medium dust temperature (T_{dust} = 30 - 50 K), ULIRG-like objects at $z > 4$. This kind of source would be inaccessible in the optical/NIR without the benefit of negative k-correction, and additionally inaccessible in SPIRE due to the faint emission at observed frame FIR wavelengths.

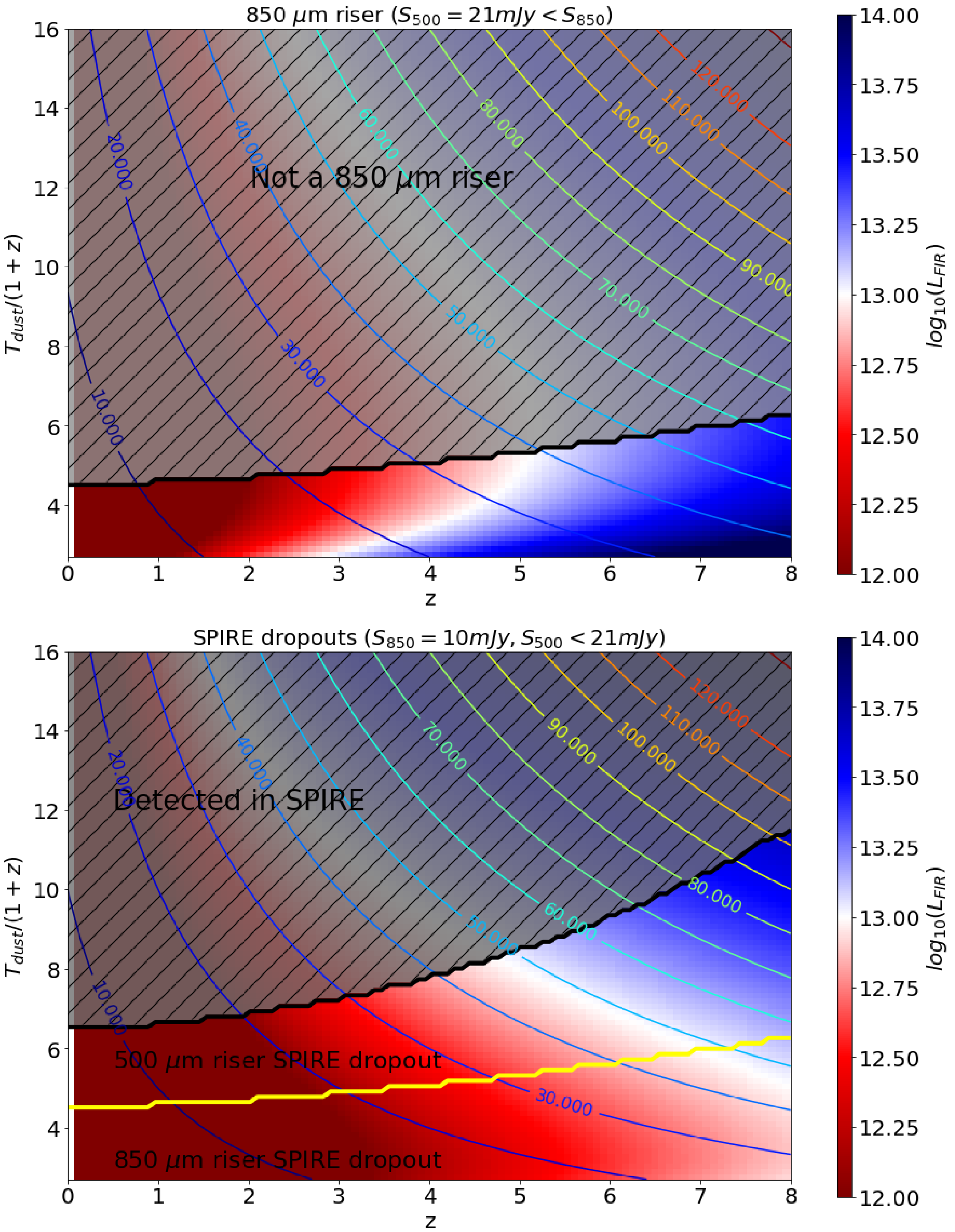

Figure 4.20: *(Top)*: $T_{dust}/(1+z)$ against z for a single modified blackbody with $\beta = 2.$ and $\nu_0 = 100\mu$m, normalised to $S_{500} = 21$ mJy. The shaded region shows where this source is *not* a 850 μm riser, whilst the background colours show the luminosity of such a source as a function of z and T_{dust}. *(Bottom)*: The same as the top, but for a SPIRE dropout with normalisation $S_{850} = 10$ mJy. The shaded region shows where the source is *not* a SPIRE dropout, whilst the yellow line separates out SPIRE dropouts which are also 500 μm risers from those which are 850 μm risers. The lower y limit is constrained by the CMB temperature as $y = 2.73 \times (1+z)$, whilst the upper is chosen to broadly fit sources from the literature.

4.8.3 SPIRE Dropouts Number Counts

Figure 4.20 suggests that SPIRE dropouts should be significantly more populous than 850 μm risers; the polygon that forms from the constraints that 20 K $< T_{dust} <$ 80 K, and the approximate "knee" of the $z > 2$ DSFG luminosity function[13] at around 10^{13} $L_{\odot}$ (Casey et al., 2014)[14] encompasses a much larger area of parameter space for the SPIRE dropouts compared to the 850 μm risers.

Both the high-z solution to SPIRE dropouts and the cooler, $\sim$ 30 K population at $z \sim 4$ make SPIRE dropouts a population worthy of study in their own right, especially since both these solutions are generally inaccessible from SPIRE alone. We therefore examined two of the largest extragalactic surveys at 850 μm with significant Herschel-SPIRE survey overlaps, in order to determine the approximate number of SPIRE dropouts per deg^2.

Initially, we searched for dropouts among the maps and catalogues from the observed 1 deg^2 COSMOS field of the SCUBA-2 COSMOS Survey (S2COSMOS). S2COSMOS was designed to complete the work started in S2CLS (Geach et al., 2017), and reach a uniform 1σ rms error of 1.2 mJy across 2 deg^2 in the COSMOS field. The S2COSMOS catalogues require a 4.0σ detection for a source to be included in the catalogues, with a typical 1σ value of 1.06 ± 0.35 mJy at 850 μm. We then matched these catalogues to catalogues from Herschel to search for any dropouts among the 1207 detected SCUBA-2 objects. For the Herschel catalogues, we used the HerMES (Oliver et al., 2012) DR2 SUSSEXtractor (Wang et al., 2013) catalogues, which are based on a peak finder algorithm, and assume Gaussian shaped beam FWHMs of 18.15, 25.15 and 36.3 arcsec at 250, 350 and 500 μm respectively. No attempt is made at cross-matching between bands, and three separate catalogues are made for the three SPIRE bands individually. Using a search radius of 13.0 arcsec, equivalent to the beamsize of SCUBA-2, we cross-match the S2COSMOS sources with each of the three Herschel-SPIRE catalogues. We find 264 sources which have no Herschel match in any of the three bands, a dropout fraction of 21.8%. If we use

[13] No 850 μm riser nor SPIRE dropout has a dust temperature above 20 K below this redshift

[14] The shape, evolution and modelling of the DSFG luminosity function is a topic worthy of at least its own chapter, but a detailed examination is beyond the scope of this discussion. We refer the interested reader to Gruppioni et al. (2017); Koprowski et al. (2017), and the references therein for a more thorough examination of this topic.

the beamsize from the Herschel 500 μm band of 35.2 arcsec, we still find 64 dropouts (5.3%). Regardless of the precise beamsize, we find that a significant number of SCUBA-2 sources are dropouts. In Figure 4.21 we examine both the normalised and deboosted flux density distribution and normalised SNR distribution of the dropout sources when using the 13 arcsec search radius compared to the general population. We find that the flux distributions of the dropouts and of the general population are broadly similar, with median values of 3.9 and 4.5 mJy respectively, standard deviations of 1.5 and 2.1 mJy, with a long tail stretching towards higher flux densities. This suggests that the dropouts are not merely the faint population of 850 μm detected sources, but are a unique population of SMGs that remain undetected by Herschel. Examining the SNR distribution, we find that 62.5% of dropouts have a low SNR (σ between 4 and 5), compared to the general population, which has 54% in this range. This may imply that a number of the dropouts are noise spikes, but 37.5% have a SNR > 5 and, as we have shown here, at least some of the dropout population consists of real sources. We can get an approximate sense of the number counts of bright dropouts; we detect five dropouts with flux densities at 850 $\mu m > 8$ mJy over ~ 2 deg^2, corresponding to a source density of 2.5 ± 1.1 sources deg^{-2}, comparable to the 3.3 ± 0.8 bright red (S500 > $30mJy$) 500 μm riser sources found by Dowell et al. (2014). One of these five bright dropouts is additionally identified by Oteo et al. [in preparation] as an ultra-red galaxy, $S2COSMOSJ095748{+}015843$, with significantly red 1.2 mm / 850 μm colours, further supporting the idea that these dropout sources are likely at $z > 4$. To check for consistency, all these previous results were compared against the published S2CLS results, and found to be consistent.

These results are further confirmed by Aguilar et al, in preparation. They make a comparison between AzTEC detected sources (i.e. S/N > 3.5 at 1.1 mm) that were selected as 500 μm risers or SPIRE dropouts on three well observed blank fields: GOODS-S, GOODS-N and COSMOS (270 sources on ∼0.86 deg^2 in total). They found that 10% of AzTEC sources were 500 μm risers while ∼30% were classed as SPIRE dropouts, similar to the results we found using the S2CLS. After identification through radio-IRAC-CANDELS counterpart analysis and sub-mm SED fitting, they suggest that more than 50% of each of the populations is at z>4. These results are in excellent agreement, not only with our cursory examination of the S2COSMOS,

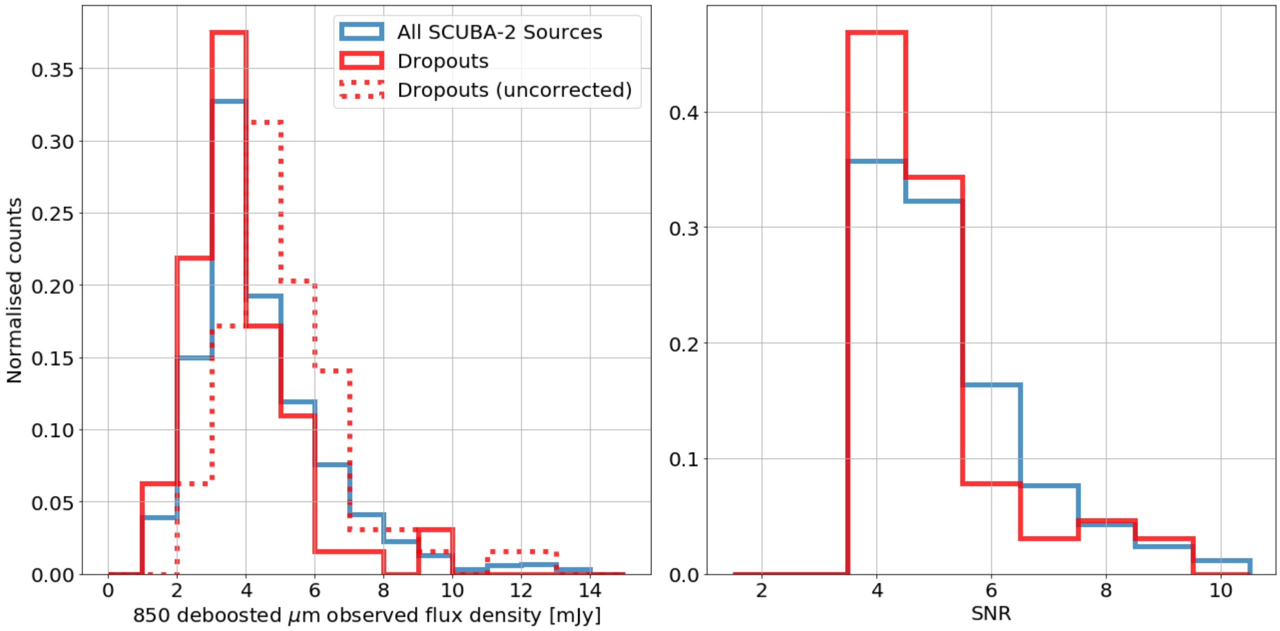

Figure 4.21: *Left)* The number counts of both all detected SCUBA-2 sources in S2COSMOS (blue solid line), and dropouts (red dashed line showing sources uncorrected for boosting, red solid line for sources corrected for boosting. Bins have widths of 1 mJy. *Right)* The SNR for the detections of both all detected S2COSMOS sources and dropouts.

but also with the predictions in Figure 4.20, and the large numbers of these objects hint towards the detection of a significant number of "normal" DSFGs at $z > 4$, compared to the extreme sources detected by SPIRE (Riechers et al., 2013; Dowell et al., 2014; Strandet et al., 2017; Zavala et al., 2017; Riechers et al., 2017)

4.9 Conclusions

NGP6_D1 is a serendipidously detected SPIRE dropout, strongly detected at 850 μm but not detected in any shorter wavelength bands. Interferometric observations confirm it to be a single source, with no evidence for any optical or NIR emission, or nearby likely foreground lensing sources. No $> 3\sigma$ detected lines are seen in the spectrum of NGP6_D1 across 32 GHz of bandwidth, and the redshift remains unknown. The degeneracy between the temperature and redshift of NGP6_D1 prevents us from constraining either of these parameters strongly, whilst the luminosity and dust mass are reasonably well constrained, and suggest NGP6_D1 is a ULIRG like object, with a dust mass $\sim 10^8$ - 10^9 $M_\odot$ and a SFR of ~ 500 $M_\odot$ yr^{-1}.

Template fitting over a range of galaxy types suggests the redshift of NGP6_D1 is most likely between $z = 5.8$ and 8.3. The FIR-radio correlation predicts redshifts much lower than this, not consistent with our lack of detections in SPIRE, and implies the presence of a possible AGN in this galaxy. The upper limits on the gas mass of NGP6_D1 suggest a maximum of $M_{H2} < (1.1 \pm 3.5) \times 10^{11}\ M_{\odot}$, consistent with a gas-to-dust ratio of $\sim$ 100 - 1000.

The SPIRE dropouts account for $\sim$ 20% of all SCUBA-2 detected sources, but have similar flux density distributions to the general population. We have examined the parameter space, and have determined that these dropouts likely represent ULIRG like objects at $z > 4$, with dust temperatures around 30 - 50 K, comparable to those seen at $z = 2 - 3$. These results are consistent with HDF 850.1 (Walter et al., 2012), one of the few other well studied SPIRE dropouts, as well as the SPIRE dropout identified by Ikarashi et al. (2017), though these sources do not have spectroscopic redshifts yet. SPIRE dropouts are likely the best way to access this population; it is generally faint and undetected in the Herschel bands, and at a high enough redshift that sources are not likely to be detected in the optical/NIR/radio bands which do not benefit from the negative k-correction seen in the sub-mm.

"We should probably think it highly absurd, if it were asserted that many of them had but little concern in the combustion, or vitrification, which follows, when an object is put into that focus."

- William Herschel, Phil. Trans. R. Soc. Lond. 1800 90, 255-283, published 1 January 1800.

Chapter 5

Conclusion

Elements of this work, including Figure 5.1, appear in Zotti et al. (2018)

5.1 Summary of Thesis Achievements

Chapter 1 of this thesis set out a series of clear observational goals which could aid our understanding of high-z DSFGs. These included the characterisation of the environments of high-z DSFGs by searching for overdensities and evidence of large scale structures associated with them, high resolution imaging of $z > 4$ DSFGs in order to determine their multiplicity and affirm their extremely large luminosities, and utilising new techniques to discover larger samples of $z > 6$ galaxies with which the luminosity function can be further constrained.

Chapter 2 detailed our examination of large scale structure and protoclusters associated with what appear to be $z = 2 - 3$ DSFGs. By cross-matching Herschel and Planck data, we identified 27 candidate high-z protoclusters which are overdense in 250, 350, or 500 μm sources. Their red colours favour a redshift around 2 - 3, whilst simple blackbody fits suggest total cluster SFRs on the order to 1,000 - 10,000 $M_{\odot}\ yr^{-1}$. Finding such overdensities is unexpected, given the assumed dynamical timescale of DSFGs, unless one invokes either simultaneous triggering of these DSFGs or cold gas inflow from the cosmic web. Comparison to simulations suggest that even in our most conservative estimates, the FIR flux density of these protoclusters is 5 $\times$ greater than expected.

In Chapter 3, we detail our interferometric follow up over a number of years of 34 500 μm risers, likely to lie at $z > 4$. Of these 34, 62% appear to be single sources, 12% are confirmed to be multiple sources, and in the remaining 35% of the fields we detect no sources at all. We infer these are also likely multiples. We make no effort to correct for lensing, and indeed only one of our sources shows clear signs of lensing at the resolution of our observations. We further find that 500 μm risers are responsible for perhaps 20% of all $S_{1.1mm} > 10\ mJy$ sources, suggesting a high-z origin for a significant fraction of this population. We find that our sources have observed flux densities consistent with HLIRGs, with associated SFRs $> 1,000\ M_{\odot}\ yr^{-1}$.

Finally, Chapter 4 introduced a new technique for targeting $z > 6$ DSFGs by searching for sources bright at 850 μm, but faint in the 3 Herschel-SPIRE bands. It details the extensive follow up of one of these SPIRE-dropouts, including both photometric and spectroscopic observations, and we find it is likely a ULIRG somewhere between z = 5.8 and 8.3, has a gas mass $< 1.1 \times 10^{11}\ M_{\odot}$, a dust mass $\sim 10^{8}$ - $10^{9}\ M_{\odot}$, and appears to host a radio excess, suggestive of AGN activity. We find these SPIRE dropouts account for $\sim$ 20% of all SCUBA-2 detected sources, and whilst the faint-end may include more examples of $z = 2 - 3$ DSFGs, the bright end may represent a population of ULIRGs at $z \gtrsim 6$ with warm, 30 - 50 K, dust temperatures.

5.2 Future Work

5.2.1 Future Protocluster Detection

The cross-matching performed in Chapter 2 required low resolution Planck all sky data and higher resolution imaging from Herschel. The area that could be surveyed for protoclusters was therefore limited to the areas surveyed by Herschel. Future missions such as the Cosmic Origins Explorer (CoRE (Delabrouille et al., 2017)), an all sky microwave and sub-mm survey of the whole sky, will likely not only be able to create similar catalogues to the Planck catalogues of compact sources, but have resolutions high enough to resolve individual overdensities across the whole sky.

In Figure 5.1, we simulate how one of our protoclusters would appear on the sky if imaged by CORE. This work appears in De Zotti et al. (2016). At the time the mission design had several options, with the CORE150 design hosting a 1.5m mirror and the CORE100 design hosting a 1m mirror, which correspond to approximate resolutions of 1 - 2 arcmin at $\sim 800\ GHz$. As can be seen, these resolution improvements over Planck allow overdensities on scales of a few arcmin to be detected directly, and contaminants removed without the need for higher resolution data. Furthermore, the cores of clusters in formation, expected only to extend on several hundred *kpc* scales, can be directly detected and located by CORE. Finally, the estimated 30x improvement in sensitivity from CORE will allow fainter overdensities to be studied; in Chapter 2 we found numerous objects that we were not able to classify. If these are overdensities of fainter objects, CORE should be able to detect them. Whilst CORE was not selected for further review, future CMB missions with bands in the FIR and sub-mm with similar resolutions should achieve similar results.

As part of our follow up program on the sources identified in Chapter 2, we successfully applied for 56 hours of SPITZER time (P.I. A. Cooray) to follow up the 27 protoclusters candidiates detailed in Chapter 2 at 3.6 and 4.5 μm. These observations will help reveal any NIR overdensities associated with the Herschel clusters, and alongside sub-mm and radio observations which we have already taken on several of these clusters (Cheng et al. in prep), will enable us to identify the correct counterparts to the Herschel sources. Spectroscopy on one of the sources in the Bootes protocluster candidate has also revealed spectral lines (Cheng et al. in prep). Follow up on other sources within this prototcluster candidate is ongoing.

5.2.2 The Optical/NIR Environments Around 500 μm Risers

Whilst Chapter 3 was able to detail the high resolution sub-mm and mm properties of 500 μm risers, the optical and NIR properties remain uncertain. As they likely lie at $z > 4$, such optical / NIR counterparts are expected to be faint, and only deep maps will be able to detect them.

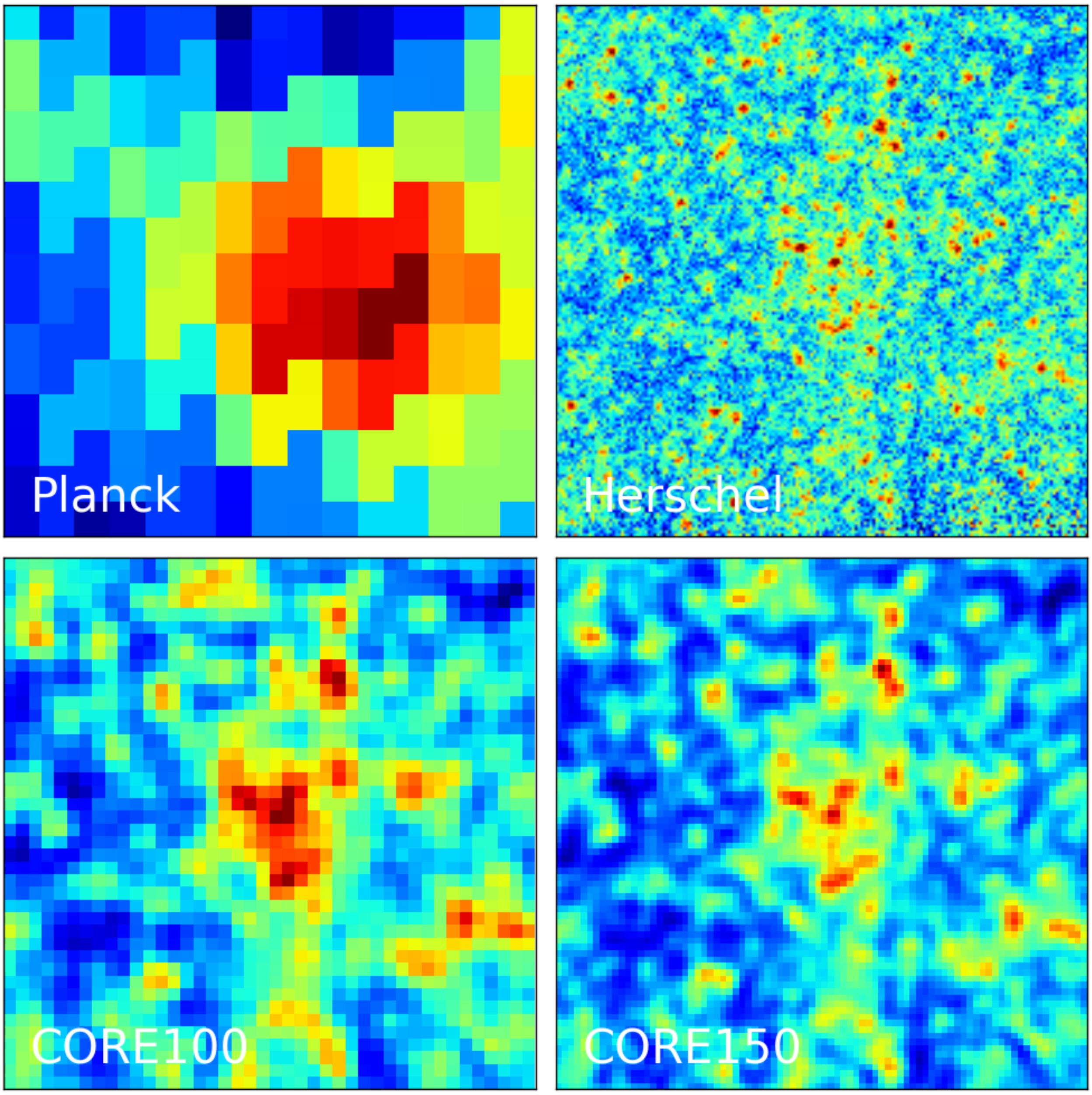

Figure 5.1: 25 x 25 arcmin cutouts of one of our protocluster candidates at 350 μm (857 GHz), as viewed by Planck (top left), Herschel (top right), the proposed CORE 100 (bottom left) and CORE 150 missions (bottom right).

However, $z > 4$ sources are expected to be rare in the optical / NIR maps, so the detection of a $z > 4$ optical / NIR source concurrent with the position of 500 μm riser may indicate a correct counterpart.

Investigations are ongoing into this, using the Spitzer Extragalactic Representative Volume Survey (SERVS, Mauduit et al. (2012)) in the XMM-LSS field. Recently, accurate photo-z's containing 12 band photometry (Nyland et al., 2017) have been provided for this field. The XMM-LSS field also contains a number of 500 μm risers. In Figure 5.2, we take 9 500 μm risers in the XMM-LSS field, associate them with the highest photometric redshift optical / NIR source within the Herschel beam, and plot both the optical, NIR, and SPIRE flux densities directly on top of several templates. It should be noted that *the only fitting performed is to redshift the template to the photo-z, and normalise the template to the 500 μm flux density.* Whilst in some cases the resultant SED is dubious, in most cases the SED fits surprisingly well to the template. Future proposals are aiming to confirm the optical/NIR counterparts are the correct ones, and demonstrate the viability of this approach.

5.2.3 SPIRE dropouts in the JINGLE fields

Ivison et al. (2016) found that the progenitors to the z > 6 QSOs are probably beyond the grasp of Herschel. Our results from Chapter 4 are generally in agreement with this, specifically Figure 4.20 which finds that unless the progenitors to these $z > 6$ QSOs are extremely luminous with $L_{FIR} > 10^{13.5} L_{\odot}$, it is unlikely that Herschel will be able to detect any of them. Despite our best efforts, the redshift of NGP6_D1 remains unknown. Partially, the difficulty in establishing a redshift is due to its high declination, and therefore inaccessibility to ALMA. We therefore searched for other dropout sources in the JCMT dust and gas In Nearby Galaxies Legacy Exploration (JINGLE, Saintonge et al. in prep) survey. JINGLE surveyed 190 local Herschel selected galaxies at 850 μm, as well as integrated CO measurements for a subset of 75 galaxies, in order to constrain the gas and dust properties of these galaxies. The large map sizes mean the total area surveyed is close to $\sim 2\ deg^2$, albeit with very heterogeneous depths. We examined the backgrounds in each of these maps, and detected a further SPIRE dropout with

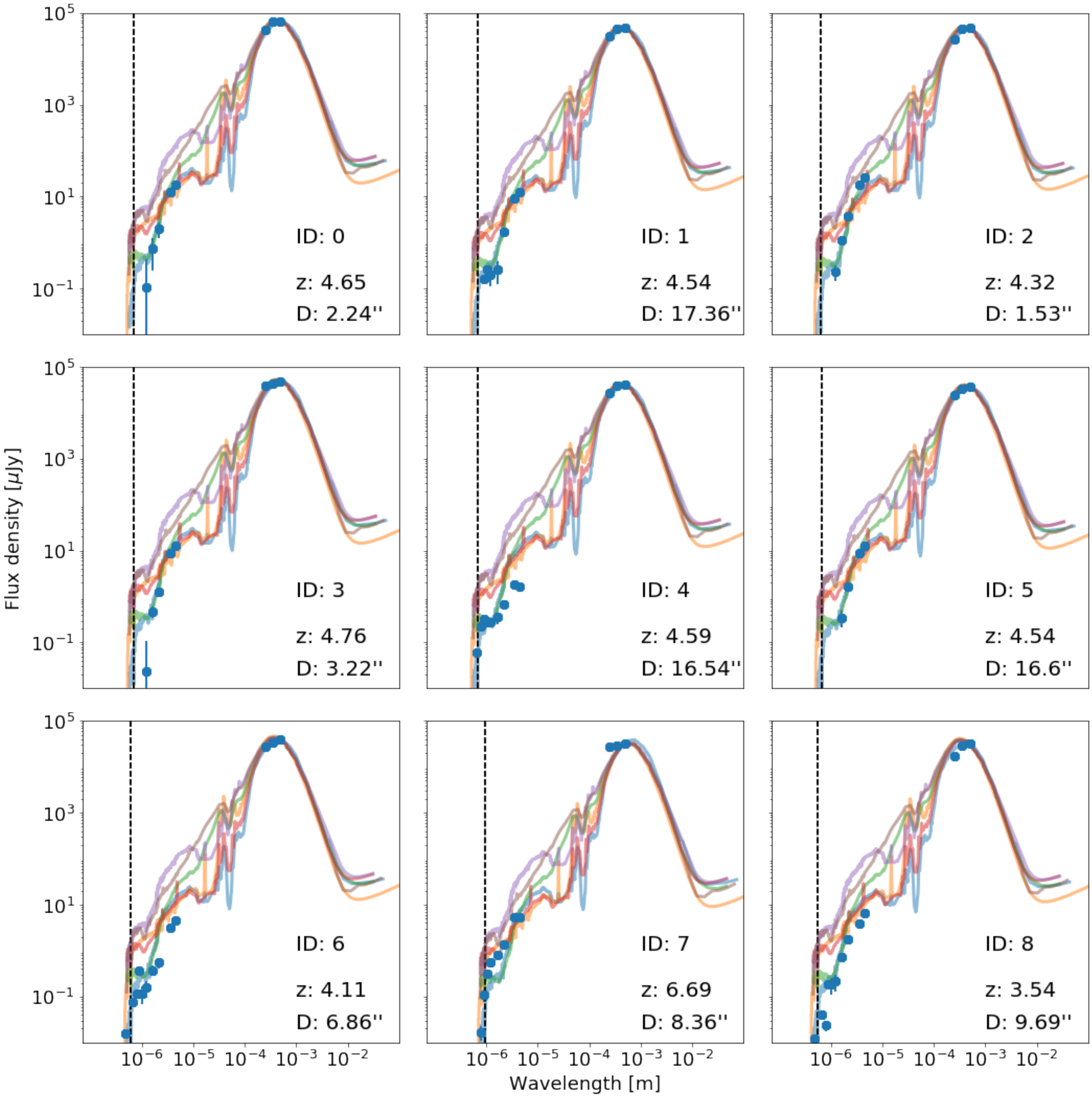

Figure 5.2: Cross-matching 500 μm risers in the XMM-LSS field with photo-z > 3.5 IRAC selected sources. Points show observed data, whilst the coloured lines show different model SEDs. Each model is first redshifted to the redshift of the IRAC source, and then normalised to the 500 μm flux. The dashed vertical lines shows the predicted location of the Lyman-break. The ID, redshift, and offset between the centre of the SPIRE 500 μm beam and the IRAC sources are given in each box.

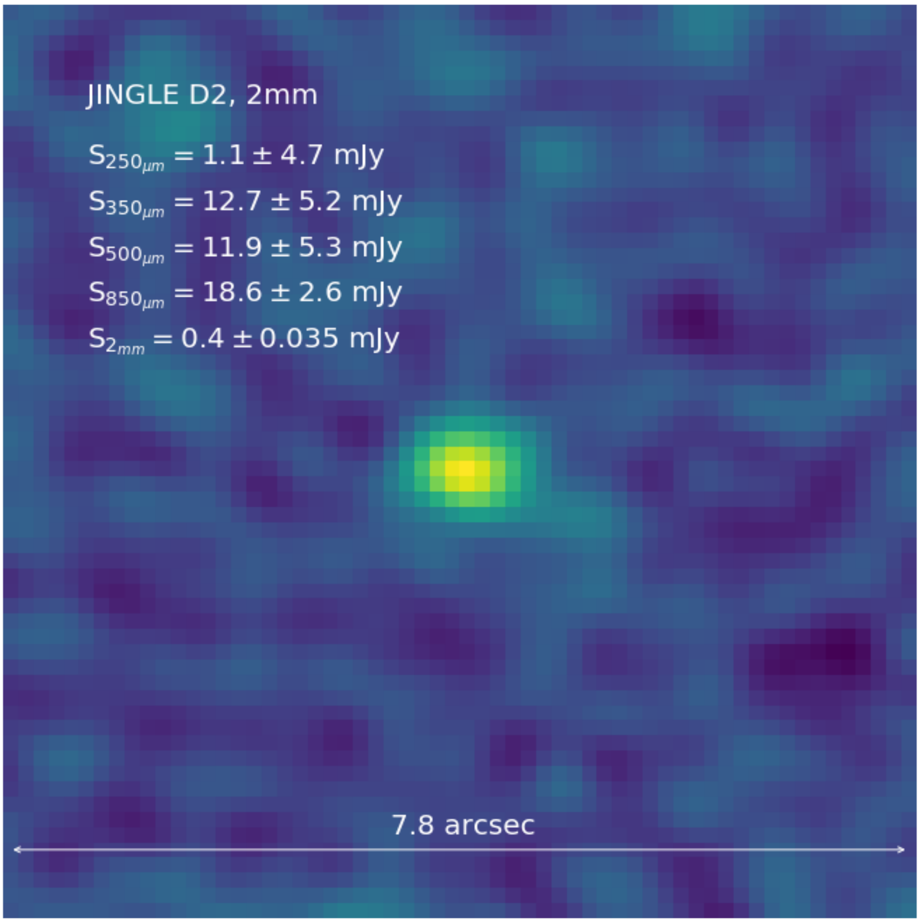

Figure 5.3: a 7.8 arcsec x 7.8 arcsec region around the SPIRE dropout JINGLE D2 at 2 mm. Various flux densities of the source are given in the top left. No other $> 4\sigma$ source is detected in the map, indicating that JINGLE D2 is a single source.

$S_{850\mu m} = 18.6 \pm 2.6\ mJy$, once again indicating a source bright at 850 μm but undetected in Herschel.

We obtained ALMA time to image this source at 2mm, and detected a single source with a flux density of $0.4 \pm 0.035\ mJy$, which we show in Figure 5.3. The source appears to be a single source, and no evidence of lensing from any arcs / rings is apparent, despite a synthesised beam of 0.8 arcsec $\times$ 0.6 arcsec (FWHM). Since this source is accessible by ALMA, future work will be on spectroscopically confirming the redshift of this source, and understanding whether the SPIRE dropouts represent a high-z population or a cool dust population at lower redshift.

5.3 Concluding Remarks

The field of DSFGs has come a long way in the last 20 years, and has significantly changed our understanding of galaxy formation and evolution. We now understand that half of all energy from stellar nucleosynthesis has been reprocessed by dust, and that the majority of this took place at $z = 2 - 3$ in extremely luminous and prodigiously star forming galaxies, which are very rare today. These galaxies are likely go on to to form the present day elliptical galaxies that exist in massive galaxy clusters, and so the epoch of DSFGs may represent the epoch of the formation of galaxy clusters and their constituents. Still, there remain significant questions about the role DSFGs play above $z > 4$. How much they contribute to the cosmic star formation rate density, what their maximum luminosities may be, how significant mergers may be, the spatial density of such sources, the process by which DSFGs transition into elliptical galaxies, and how groups of DSFGs interact, all remain difficult questions to answer. This thesis provides both targets and techniques to help answer some of these questions, as well as speculation into the theory behind how some of these processes take place. However, it remains difficult to work in the FIR due to the large beamsizes associated with single dish instruments, and the small field of view offered by typical interferometers. The large, deep surveys and targeted follow up required to answer these questions will form a key part of the next decade of DSFG studies. The near - mid term future of FIR and sub-mm observations will have to be ground based. Whilst JWST should be able to probe the stellar kinematics of these sources, there are no more space based missions planned for the sub-mm or FIR for at least the next decade. The next planned missions for instance include the Space Infrared Telescope for Cosmology and Astrophysics (SPICA, Swinyard and Nakagawa (2009)) planned for a 2032 launch, or the Origins Space Telescope (OST[1]), for a 2035 launch. As such, observations will be limited to the atmospheric windows accessible from the ground at 450 μm, 850 μm, and in the mm. The legacy value of Herschel will continue to support these observations for at least the next 10 years.

[1] `https://asd.gsfc.nasa.gov/firs/docs/`

"In this case, radiant heat will at least partly, if not chiefly, consist, if I may be permitted the expression, of invisible light; that is to say, of rays coming from the sun, that have such a momentum as to be unfit for vision." - William Herschel, Phil. Trans. R. Soc. Lond. 1800 90, 255-283, published 1 January 1800. The first paper to report the discovery of infrared light.

Acknowledgements

Herschel is an ESA space observatory with science instruments provided by European-led Principal Investigator consortia and with important participation from NASA. This research has made use of the NASA/IPAC Extragalactic Database (NED), which is operated by the Jet Propulsion Laboratory, California Institute of Technology, under contract with the National Aeronautics and Space Administration. The research leading to these results has received funding from the European Unions Horizon 2020 research and innovation programme under grant agreement No 730562 [RadioNet]. Based on observations obtained with Planck (http://www.esa.int/Planck), an ESA science mission with instruments and contributions directly funded by ESA Member States, NASA, and Canada. The Herschel-ATLAS is a project with Herschel, which is an ESA space observatory with science instruments provided by European-led Principal Investigator consortia and with important participation from NASA. The H-ATLAS website is `http://www.h-atlas.org/` U.S. participants in Herschel ATLAS acknowledge support provided by NASA through a contract issued from JPL. This research has made use of data from HerMES project (`http://hermes.sussex.ac.uk/`). HerMES is a Herschel Key Programme utilising Guaranteed Time from the SPIRE instrument team, ESAC scientists and a mission scientist. The HerMES data was accessed through the Herschel Database in Marseille (HeDaM -`http://hedam.lam.fr`) operated by CeSAM and hosted by the Laboratoire dAstrophysique de Marseille. HerMES DR3 was made possible through support of the Herschel Extragalactic Legacy Project, HELP (`http://herschel.sussex.ac.uk`). This work made extensive use of the Starlink Table/VOTable Processing Software, TOPCAT (Taylor, 2005). GAMA is a joint European-Australasian project based around a spectroscopic campaign using the Anglo-Australian Telescope. The GAMA input catalogue is based on data taken from the Sloan Digital Sky Survey and the UKIRT Infrared Deep Sky Survey. Complementary imaging of the GAMA regions is being obtained by a number of independent survey programmes including GALEX MIS, VST KiDS, VISTA VIKING, WISE, Herschel-ATLAS, GMRT and ASKAP providing UV to radio coverage. GAMA is funded by the STFC (UK), the ARC (Australia), the AAO, and the participating institutions. The GAMA website is `http://www.gama-survey.org/`. This research made use of Astropy, a community-developed core Python package for Astronomy (The Astropy Collaboration et al., 2013) The author acknowledges support from STFC, in part through grant numbers ST/N000838/1 and ST/K001051/1. The James Clerk Maxwell Telescope is operated by the East Asian Observatory on behalf of The National Astronomical Observatory of Japan; Academia Sinica Institute of Astronomy and Astrophysics; the Korea Astronomy and Space Science Institute; the Operation, Maintenance and Upgrading Fund for Astronomical Telescopes and Facility Instruments, budgeted from the Ministry of Finance (MOF) of China and administrated by the Chinese Academy of Sciences (CAS), as well as the National Key R&D Program of China (No. 2017YFA0402700). Additional funding support is provided by the Science and Technology Facilities Council of the United Kingdom and participating universities in the United Kingdom and Canada. This work is based on observations carried out under project number E16AD, 077-17 and 199-15 with the IRAM NOEMA Interferometer and 30m telescope. IRAM is supported by INSU/CNRS (France), MPG (Germany) and IGN (Spain). This paper makes use of the following ALMA data: ADS/JAO.ALMA#2017.1.00773.S. ALMA is a partnership of ESO (representing its member states), NSF (USA) and NINS (Japan), together with NRC (Canada), MOST and ASIAA (Taiwan), and KASI (Republic of Korea), in cooperation with the Republic of Chile. The Joint ALMA Observatory is operated by ESO, AUI/NRAO and NAOJ. The author wishes to express his thanks for support and assistance from the JINGLE collaboration, the S2-CLS, and S2COSMOS. The Submillimeter Array is a joint project between the Smithsonian Astrophysical Observatory and the Academia Sinica Institute of Astronomy and Astrophysics and is funded by the Smithsonian Institution and the Academia Sinica. This research has made use of NASA's Astrophysics Data System Bibliographic Services This research made use of APLpy, an open-source plotting package for Python hosted at `http://aplpy.github.com`. The author wishes to recognize and acknowledge the very significant cultural role and reverence that the summit of Maunakea has always had within the indigenous Hawaiian community. We are most fortunate to have the opportunity to conduct observations from this mountain. Finally, the author wishes to express his utmost thanks and gratitude to all the

unsung heroes of support staff, administrators, software developers, cleaners, editors, drivers, maintenance staff and a thousand others who are rarely mentioned, but without whom none of this work would even be remotely possible.

Bibliography

B. Abolfathi, et al. *eprint arXiv:1707.09322*, 2017.

B. Acke, et al. *Astronomy & Astrophysics, Volume 540, id.A125, 9 pp.*, 540, 2012. ISSN 0004-6361. doi:10.1051/0004-6361/201118581.

P. A. R. Ade, et al. *Astronomy & Astrophysics*, 594:A13, 2016. ISSN 0004-6361. doi:10.1051/0004-6361/201525830.

N. Aghanim, et al. *Astronomy & Astrophysics*, 582:A30, 2015. ISSN 0004-6361. doi:10.1051/0004-6361/201424790.

A. Amblard, et al. *Astronomy and Astrophysics, Volume 518, id.L9, 5 pp.*, 518, 2010. ISSN 0004-6361. doi:10.1051/0004-6361/201014586.

S. K. Andrews, S. P. Driver, L. J. M. Davies, C. d. P. Lagos, and A. S. G. Robotham. *Monthly Notices of the Royal Astronomical Society*, 474(1):898–916, 2018. ISSN 0035-8711. doi:10.1093/mnras/stx2843.

M. Aravena, et al. *Monthly Notices of the Royal Astronomical Society*, 457:4406–4420, 2016. ISSN 0035-8711. doi:10.1093/mnras/stw275.

V. Asboth, et al. *Monthly Notices of the Royal Astronomical Society, Volume 462, Issue 2, p.1989-2000*, 462:1989–2000, 2016. doi:10.1093/mnras/stw1769.

S. P. Bamford, et al. *MNRAS*, 393(4):1324–1352, 2009. doi:10.1111/j.1365-2966.2008.14252.x.

C. M. Baugh, et al. *Monthly Notices of the Royal Astronomical Society*, 356(3):1191–1200, 2005. ISSN 00358711. doi:10.1111/j.1365-2966.2004.08553.x.

S. V. W. Beckwith, et al. *The Astronomical Journal, Volume 132, Issue 5, pp. 1729-1755.*, 132:1729–1755, 2006. ISSN 0004-6256. doi:10.1086/507302.

E. Bertin and S. Arnouts. *Astronomy and Astrophysics Supplement Series*, 117(2):393–404, 1996. ISSN 0365 0138. doi:10.1051/aas:1996164.

B. Bertincourt, et al. *Astronomy & Astrophysics*, 588:A107, 2016. ISSN 0004-6361. doi: 10.1051/0004-6361/201527313.

M. Béthermin, H. Dole, G. Lagache, D. Le Borgne, and A. Penin. *Astronomy & Astrophysics*, 529:A4, 2011. ISSN 0004-6361. doi:10.1051/0004-6361/201015841.

M. Béthermin, et al. *The Astrophysical Journal*, 757(2):L23, 2012. ISSN 2041-8205. doi: 10.1088/2041-8205/757/2/L23.

M. Béthermin, et al. *eprint arXiv:1703.08795*, 2017.

H. Beuther, et al. *The Astrophysical Journal, Volume 616, Issue 1, pp. L31-L34.*, 616:L31–L34, 2004. ISSN 0004-637X. doi:10.1086/423670.

S. Bianchi. *Astronomy & Astrophysics, Volume 552, id.A89, 5 pp.*, 552, 2013. ISSN 0004-6361. doi:10.1051/0004-6361/201220866.

A. Blain. *Physics Reports*, 369(2):111–176, 2002. ISSN 03701573. doi:10.1016/S0370-1573(02)00134-5.

A. W. Blain, V. E. Barnard, and S. C. Chapman. *Monthly Notices of the Royal Astronomical Society*, 338(3):733–744, 2003. ISSN 00358711. doi:10.1046/j.1365-8711.2003.06086.x.

A. W. Blain, S. C. Chapman, I. Smail, and R. Ivison. *The Astrophysical Journal*, 611(1):52–58, 2004a. ISSN 0004-637X. doi:10.1086/422026.

A. W. Blain, S. C. Chapman, I. Smail, and R. Ivison. *The Astrophysical Journal*, 611(2):725–731, 2004b. ISSN 0004-637X. doi:10.1086/422353.

F. Boone, et al. *Astronomy & Astrophysics, Volume 559, id.L1, 5 pp.*, 559, 2013. ISSN 0004-6361. doi:10.1051/0004-6361/201322552.

F. Boone, et al. *Proceedings of the International Astronomical Union*, 11(A29B):818–819, 2015. ISSN 1743-9213. doi:10.1017/S1743921316006931.

D. L. Borgne, D. Elbaz, P. Ocvirk, and C. Pichon. *Astronomy and Astrophysics, Volume 504, Issue 3, 2009, pp.727-740*, 504:727–740, 2009. ISSN 0004-6361. doi:10.1051/0004-6361/200809945.

M. S. Bothwell, et al. *Monthly Notices of the Royal Astronomical Society*, 429:3047–3067, 2013. ISSN 0035-8711. doi:10.1093/mnras/sts562.

R. S. Bussmann, et al. *The Astrophysical Journal, Volume 779, Issue 1, article id. 25, 26 pp. (2013).*, 779, 2013. ISSN 0004-637X. doi:10.1088/0004-637X/779/1/25.

A. M. Bykov, et al. *Space Science Reviews*, 188(1-4):141–185, 2015. doi:10.1007/s11214-014-0129-4.

Z.-Y. Cai, et al. *The Astrophysical Journal, Volume 768, Issue 1, article id. 21, 24 pp. (2013).*, 768, 2013. ISSN 0004-637X. doi:10.1088/0004-637X/768/1/21.

D. Calzetti and Daniela. *Secular Evolution of Galaxies, by Jesús Falcón-Barroso, and Johan H. Knapen, Cambridge, UK: Cambridge University Press, 2013, p.419*, page 419, 2013.

P. Capak, et al. *The Astrophysical Journal Letters, Volume 681, Issue 2, article id. L53, pp. (2008).*, 681, 2008. ISSN 0004-637X. doi:10.1086/590555.

P. L. Capak, et al. *Nature*, 470(7333):233–5, 2011. ISSN 1476-4687. doi:10.1038/nature09681.

C. Carilli and F. Walter. *Annual Review of Astronomy and Astrophysics*, 51(1):105–161, 2013. ISSN 0066-4146. doi:10.1146/annurev-astro-082812-140953.

J. E. Carlstrom, et al. *Publications of the Astronomical Society of the Pacific*, 123(903):568–581, 2011. ISSN 00046280. doi:10.1086/659879.

M. Carter, et al. *Astronomy & Astrophysics*, 538:A89, 2012. ISSN 0004-6361. doi:10.1051/0004-6361/201118452.

C. M. Casey. *The Astrophysical Journal, Volume 824, Issue 1, article id. 36, pp. (2016).*, 824, 2016. ISSN 0004-637X. doi:10.3847/0004-637X/824/1/36.

C. M. Casey, D. Narayanan, and A. Cooray. *Physics Reports*, 541(2):45161, 2014. ISSN 03701573. doi:10.1016/j.physrep.2014.02.009.

C. M. Casey, et al. *The Astrophysical Journal, Volume 761, Issue 2, article id. 140, 24 pp. (2012).*, 761, 2012. ISSN 0004-637X. doi:10.1088/0004-637X/761/2/140.

C. M. Casey, et al. *The Astrophysical Journal*, 808(2):L33, 2015. ISSN 2041-8213. doi:10.1088/2041-8205/808/2/L33.

C. M. Casey, et al. *eprint arXiv:1805.10301*, 2018.

G. Chabrier. *Publications of the Astronomical Society of the Pacific*, 115(809):763–795, 2003. ISSN 0004-6280. doi:10.1086/376392.

E. L. Chapin, et al. *Monthly Notices of the Royal Astronomical Society*, 411(1):505549, 2011. ISSN 00358711. doi:10.1111/j.13652966.2010.17697.x.

E. L. Chapin, et al. *Monthly Notices of the Royal Astronomical Society*, 430(4):2545–2573, 2013. ISSN 1365-2966. doi:10.1093/mnras/stt052.

S. C. Chapman, A. W. Blain, I. Smail, and R. J. Ivison. *The Astrophysical Journal*, 622(2):772–796, 2005. ISSN 0004-637X. doi:10.1086/428082.

S. C. Chapman, et al. *The Astrophysical Journal*, 691(1):560–568, 2009. ISSN 0004-637X. doi:10.1088/0004-637X/691/1/560.

C.-C. Chen, et al. *The Astrophysical Journal*, 799(2):194, 2015. ISSN 1538-4357. doi:10.1088/0004-637X/799/2/194.

J.-Y. Chenu, et al. *IEEE Transactions on Terahertz Science and Technology*, 6(2):223–237, 2016. ISSN 2156-342X. doi:10.1109/TTHZ.2016.2525762.

Y.-K. Chiang, R. Overzier, and K. Gebhardt. *The Astrophysical Journal, Volume 779, Issue 2, article id. 127, 16 pp. (2013).*, 779, 2013. ISSN 0004-637X. doi:10.1088/0004-637X/779/2/127.

D. L. Clements, W. J. Sutherland, R. G. McMahon, and W. Saunders. *Monthly Notices of the Royal Astronomical Society*, 279(2):477–497, 1996. ISSN 0035-8711. doi:10.1093/mnras/279.2.477.

D. L. Clements, et al. *Astronomy and Astrophysics*, 518:L8, 2010. ISSN 0004-6361. doi:10.1051/0004-6361/201014581.

D. L. Clements, et al. *Monthly Notices of the Royal Astronomical Society*, 439(2):1193–1211, 2014. ISSN 0035-8711. doi:10.1093/mnras/stt2253.

D. L. Clements, et al. *Monthly Notices of the Royal Astronomical Society*, 461(2), 2016. ISSN 0035-8711. doi:10.1093/mnras/stw1224.

D. L. Clements, et al. *Monthly Notices of the Royal Astronomical Society*, 475(2):2097–2121, 2018. doi:10.1093/mnras/stx3227.

F. Combes, et al. *Astronomy & Astrophysics, Volume 538, id.L4, 5 pp.*, 538, 2012. ISSN 0004-6361. doi:10.1051/0004-6361/201118750.

J. J. Condon. *Annual Review of Astronomy and Astrophysics*, 30(1):575–611, 1992. ISSN 0066-4146. doi:10.1146/annurev.aa.30.090192.003043.

J. J. Condon, M. L. Anderson, and G. Helou. *The Astrophysical Journal*, 376:95, 1991. ISSN 0004-637X. doi:10.1086/170258.

E. A. Cooke, N. A. Hatch, S. I. Muldrew, E. E. Rigby, and J. D. Kurk. *Monthly Notices of the Royal Astronomical Society*, 440(4):3262–3274, 2014. ISSN 0035-8711. doi:10.1093/mnras/stu522.

A. Cooray. *Royal Society Open Science*, 3(3):150555, 2016. ISSN 2054-5703. doi:10.1098/rsos.150555.

A. Cooray, et al. *The Astrophysical Journal, Volume 790, Issue 1, article id. 40, 10 pp. (2014).*, 790, 2014. ISSN 0004-637X. doi:10.1088/0004-637X/790/1/40.

K. E. K. Coppin, et al. *Monthly Notices of the Royal Astronomical Society*, 395(4):1905–1914, 2009. ISSN 00358711. doi:10.1111/j.1365-2966.2009.14700.x.

W. I. Cowley, C. G. Lacey, C. M. Baugh, and S. Cole. *Monthly Notices of the Royal Astronomical Society*, 446(2):1784–1798, 2014. ISSN 0035-8711. doi:10.1093/mnras/stu2179.

. Cowley, . Lacey, . Baugh, and . Cole. *eprint arXiv:1504.04516*, 2015.

P. Cox, et al. *The Astrophysical Journal, Volume 740, Issue 2, article id. 63, 10 pp. (2011).*, 740, 2011. ISSN 0004-637X. doi:10.1088/0004-637X/740/2/63.

E. da Cunha, et al. *The Astrophysical Journal, Volume 806, Issue 1, article id. 110, 22 pp. (2015).*, 806, 2015. ISSN 0004-637X. doi:10.1088/0004-637X/806/1/110.

E. Daddi, et al. *The Astrophysical Journal, Volume 617, Issue 2, pp. 746-764.*, 617:746–764, 2004. ISSN 0004-637X. doi:10.1086/425569.

E. Daddi, et al. *The Astrophysical Journal, Volume 631, Issue 1, pp. L13-L16.*, 631:L13–L16, 2005. ISSN 0004-637X. doi:10.1086/496918.

E. Daddi, et al. *The Astrophysical Journal, Volume 694, Issue 2, pp. 1517-1538 (2009).*, 694:1517–1538, 2008. ISSN 0004-637X. doi:10.1088/0004-637X/694/2/1517.

E. Daddi, et al. *The Astrophysical Journal Letters, Volume 695, Issue 2, pp. L176-L180 (2009).*, 695:L176–L180, 2009. ISSN 0004-637X. doi:10.1088/0004-637X/695/2/L176.

A. L. R. Danielson, et al. *Monthly Notices of the Royal Astronomical Society, Volume 410, Issue 3, pp. 1687-1702.*, 410:1687–1702, 2010. ISSN 0035-8711. doi:10.1111/j.1365-2966.2010.17549.x.

H. Dannerbauer, et al. *Astronomy & Astrophysics*, 570:A55, 2014. ISSN 0004-6361. doi:10.1051/0004-6361/201423771.

H. Dannerbauer, et al. *eprint arXiv:1701.05250*, 2017. doi:10.1051/0004-6361/201730449.

B. Darvish, et al. *The Astrophysical Journal, Volume 825, Issue 2, article id. 113, 16 pp. (2016).*, 825, 2016. ISSN 0004-637X. doi:10.3847/0004-637X/825/2/113.

J. I. Davies, et al. *Astronomy and Astrophysics*, 518:L48, 2010. ISSN 0004-6361. doi:10.1051/0004-6361/201014571.

J. I. Davies, et al. *Monthly Notices of the Royal Astronomical Society*, 419(4):3505–3520, 2012. ISSN 00358711. doi:10.1111/j.1365-2966.2011.19993.x.

C. De Breuck, T. Miller, and S. Chapman. *Zendo*, 2017. doi:10.5281/ZENODO.830191.

T. de Graauw, et al. *Astronomy and Astrophysics*, 518:L6, 2010. ISSN 0004-6361. doi:10.1051/0004-6361/201014698.

G. De Zotti, et al. *Journal of Cosmology and Astroparticle Physics, Issue 06, article id. 018, (2015).*, 6, 2015. ISSN 1475-7516. doi:10.1088/1475-7516/2015/06/018.

G. De Zotti, et al. *eprint arXiv:1609.07263*, 2016.

J. Delabrouille, et al. *eprint arXiv:1706.04516*, 2017.

J. T. Dempsey, et al. *Monthly Notices of the Royal Astronomical Society, Volume 430, Issue 4, p.2534-2544*, 430:2534–2544, 2013. ISSN 0035-8711. doi:10.1093/mnras/stt090.

E. Diolaiti, et al. *Proc. SPIE Vol. 4007, p. 879-888, Adaptive Optical Systems Technology, Peter L. Wizinowich; Ed.*, 4007:879–888, 2000. ISSN 0277-786X. doi:10.1117/12.390377.

H. Dole, et al. *Astronomy and Astrophysics*, 451(2):417–429, 2006. ISSN 0004-6361. doi:10.1051/0004-6361:20054446.

D. Donevski, et al. *eprint arXiv:1709.00942*, 2017.

D. Donevski, et al. *Astronomy & Astrophysics*, 614:A33, 2018. ISSN 0004-6361. doi:10.1051/0004-6361/201731888.

C. D. Dowell, et al. *The Astrophysical Journal*, 780(1):75, 2014. ISSN 0004-637X. doi:10.1088/0004-637X/780/1/75.

B. Draine. *Annual Review of Astronomy and Astrophysics*, 41(1):241–289, 2003. ISSN 0066-4146. doi:10.1146/annurev.astro.41.011802.094840.

A. Dressler. *The Astrophysical Journal*, 236:351, 1980. doi:10.1086/157753.

S. P. Driver, et al. *Monthly Notices of the Royal Astronomical Society*, 413(2):971–995, 2011. ISSN 00358711. doi:10.1111/j.1365-2966.2010.18188.x.

S. Duivenvoorden, et al. *Monthly Notices of the Royal Astronomical Society*, 477(1):1–17, 2018. ISSN 13652966. doi:10.1093/mnras/sty691.

L. Dunne, S. A. Eales, and M. G. Edmunds. *Monthly Notices of the Royal Astronomical Society*, 341(2):589–598, 2003. ISSN 00358711. doi:10.1046/j.1365-8711.2003.06440.x.

S. Eales, et al. *Publications of the Astronomical Society of the Pacific*, 122(891):499–515, 2010. ISSN 0004-6280. doi:10.1086/653086.

E. Egami, et al. *The Astrophysical Journal Supplement Series, Volume 154, Issue 1, pp. 130-136.*, 154:130–136, 2004. ISSN 0067-0049. doi:10.1086/423322.

E. Egami, et al. *Astronomy and Astrophysics, Volume 518, id.L12, 5 pp.*, 518, 2010. ISSN 0004-6361. doi:10.1051/0004-6361/201014696.

P. R. M. Eisenhardt, et al. *The Astrophysical Journal*, 684(2):905–932, 2008. ISSN 0004-637X. doi:10.1086/590105.

D. Elbaz, et al. *Astronomy & Astrophysics*, 384(3):848–865, 2002. ISSN 0004-6361. doi: 10.1051/0004-6361:20020106.

D. Elbaz, et al. *Astronomy and Astrophysics, Volume 468, Issue 1, June II 2007, pp.33-48*, 468:33–48, 2007. ISSN 0004-6361. doi:10.1051/0004-6361:20077525.

B. H. C. Emonts, et al. *Science, Volume 354, Issue 6316, pp. 1128-1130 (2016).*, 354:1128–1130, 2016. ISSN 0036-8075. doi:10.1126/science.aag0512.

H. Engel, et al. *The Astrophysical Journal*, 724(1):233–243, 2010. ISSN 0004-637X. doi: 10.1088/0004-637X/724/1/233.

N. Erickson, G. Narayanan, R. Goeller, and R. Grosslein. In A. Baker, J. Glenn, A. Harris, J. Mangum, and M. Yun, editors, *From Z-Machines to ALMA: (Sub)Millimeter Spectroscopy of Galaxies*, volume 375 of *Astronomical Society of the Pacific Conference Series*, page 71. 2007.

D. J. Fixsen, E. Dwek, J. C. Mather, C. L. Bennett, and R. a. Shafer. *The Astrophysical Journal*, 508(1):12, 1998. ISSN 0004-637X. doi:10.1086/306383.

I. Flores-Cacho, et al. *Astronomy & Astrophysics*, 585:A54, 2016. doi:10.1051/0004-6361/201425226.

D. Foreman-Mackey, D. W. Hogg, D. Lang, and J. Goodman. 2013.

H. Fu, et al. *The Astrophysical Journal*, 753(2):134, 2012. ISSN 0004-637X. doi:10.1088/0004-637X/753/2/134.

H. Fu, et al. *Nature*, 498(7454):338–341, 2013. ISSN 0028-0836. doi:10.1038/nature12184.

Y. Fudamoto, et al. *Monthly Notices of the Royal Astronomical Society, Volume 472, Issue 2, p.2028-2041*, 472:2028–2041, 2017. ISSN 0035-8711. doi:10.1093/mnras/stx1956.

F. Galliano. 2004.

J. E. Geach, et al. *Monthly Notices of the Royal Astronomical Society, Volume 432, Issue 1, p.53-61*, 432:53–61, 2013. ISSN 0035-8711. doi:10.1093/mnras/stt352.

J. E. Geach, et al. *Monthly Notices of the Royal Astronomical Society, Volume 452, Issue 1, p.502-510*, 452:502–510, 2015. ISSN 0035-8711. doi:10.1093/mnras/stv1243.

J. E. Geach, et al. *Monthly Notices of the Royal Astronomical Society, Volume 465, Issue 2, p.1789-1806*, 465:1789–1806, 2017. ISSN 0035-8711. doi:10.1093/mnras/stw2721.

R. Genzel, et al. *The Astrophysical Journal*, 498(2):579–605, 1998. ISSN 0004-637X. doi:10.1086/305576.

R. D. George, et al. *Monthly Notices of the Royal Astronomical Society: Letters, Volume 436, Issue 1, p.L99-L103*, 436:L99–L103, 2013. ISSN 0035-8711. doi:10.1093/mnrasl/slt122.

R. Gispert, G. Lagache, and J. L. Puget. Implications of the cosmic infrared background for light production and the star formation history in the Universe. Technical report, 2000.

R. Goeller. *A wideband analog correlating spectrometer for millimeter astronomy.* Ph.D. thesis, University of Massachusetts Amherst, 2008.

A. Gomez-Ruiz, et al. *ArXiv e-prints*, 2017.

J. Goodman and J. Weare. *Communications in Applied Mathematics and Computational Science*, 5(1):65–80, 2010. ISSN 2157-5452. doi:10.2140/camcos.2010.5.65.

G. L. Granato, et al. *Monthly Notices of the Royal Astronomical Society*, 450(2):1320–1332, 2015. ISSN 0035-8711. doi:10.1093/mnras/stv676.

J. Greenslade, et al. *Monthly Notices of the Royal Astronomical Society, Volume 476, Issue 3, 21 May 2018,*, 2018. ISSN 0035-8711. doi:10.1093/mnras/sty023.

T. R. Greve, et al. *The Astrophysical Journal*, 756(1):101, 2012. ISSN 0004-637X. doi:10.1088/0004-637X/756/1/101.

T. R. Greve, et al. *The Astrophysical Journal, Volume 794, Issue 2, article id. 142, 16 pp. (2014).*, 794, 2014. ISSN 0004-637X. doi:10.1088/0004-637X/794/2/142.

M. J. Griffin, et al. *Astronomy and Astrophysics*, 518:L3, 2010. ISSN 0004-6361. doi:10.1051/0004-6361/201014519.

C. Gruppioni, et al. *Monthly Notices of the Royal Astronomical Society*, 432(1):23–52, 2013. ISSN 1365-2966. doi:10.1093/mnras/stt308.

C. Gruppioni, et al. *eprint arXiv:1710.02353*, 2017.

. Guilloteau, et al. *Astronomy and Astrophysics (ISSN 0004-6361)*, 262:624–633, 1992.

B. Gullberg, et al. *The Astrophysical Journal, Volume 859, Issue 1, article id. 12, 12 pp. (2018).*, 859, 2018. ISSN 0004-637X. doi:10.3847/1538-4357/aabe8c.

J. E. Gunn, J. G. Hoessel, and J. B. Oke. *The Astrophysical Journal*, 306:30, 1986. ISSN 0004-637X. doi:10.1086/164317.

J. Hao, et al. *The Astrophysical Journal Supplement Series*, 191(2):254–274, 2010. ISSN 0067-0049. doi:10.1088/0067-0049/191/2/254.

K. C. Harrington, et al. *Monthly Notices of the Royal Astronomical Society, Volume 458, Issue 4, p.4383-4399*, 458:4383–4399, 2016. ISSN 0035-8711. doi:10.1093/mnras/stw614.

I. Harrison and P. Coles. *Monthly Notices of the Royal Astronomical Society*, 421:L19–L23, 2011. ISSN 0035-8711. doi:10.1111/j.1745-3933.2011.01198.x.

B. Hatsukade, et al. *Publications of the Astronomical Society of Japan*, 68(3):36, 2016. ISSN 0004-6264. doi:10.1093/pasj/psw026.

M. G. Hauser and E. Dwek. *Annual Review of Astronomy and Astrophysics*, 39(1):249–307, 2001. ISSN 0066-4146. doi:10.1146/annurev.astro.39.1.249.

M. G. Hauser, et al. *The Astrophysical Journal*, 508(1):106–122, 1998. ISSN 0004-637X. doi:10.1086/306382.

C. C. Hayward, et al. *Monthly Notices of the Royal Astronomical Society*, 428(3):2529–2547, 2012. ISSN 0035-8711. doi:10.1093/mnras/sts222.

C. C. Hayward, et al. *Monthly Notices of the Royal Astronomical Society, Volume 434, Issue 3, p.2572-2581*, 434:2572–2581, 2013. ISSN 0035-8711. doi:10.1093/mnras/stt1202.

C. C. Hayward, et al. *Monthly Notices of the Royal Astronomical Society*, 445(2):1598–1604, 2014. ISSN 1365-2966. doi:10.1093/mnras/stu1843.

G. Helou and M. D. Bicay. *The Astrophysical Journal*, 415:93, 1993. doi:10.1086/173146.

G. Helou, B. T. Soifer, and M. Rowan-Robinson. *The Astrophysical Journal*, 298:L7, 1985. ISSN 0004-637X. doi:10.1086/184556.

D. Herranz, et al. *Astronomy & Astrophysics*, 549, 2013.

R. C. Hickox, et al. *Monthly Notices of the Royal Astronomical Society*, 421(1), 2012. ISSN 00358711. doi:10.1111/j.1365-2966.2011.20303.x.

R. Hill, et al. *Monthly Notices of the Royal Astronomical Society*, 477(2):2042–2067, 2018. ISSN 0035-8711. doi:10.1093/mnras/sty746.

P. T. P. Ho, J. M. Moran, and K. Y. Lo. *The Astrophysical Journal*, 616(1):L1–L6, 2004. ISSN 0004-637X. doi:10.1086/423245.

J. A. Hodge, et al. *The Astrophysical Journal*, 760(1):11, 2012. ISSN 0004-637X. doi:10.1088/0004-637X/760/1/11.

J. A. Hodge, et al. *The Astrophysical Journal*, 768(1):91, 2013. ISSN 0004-637X. doi:10.1088/0004-637X/768/1/91.

J. A. Hodge, et al. *The Astrophysical Journal, Volume 833, Issue 1, article id. 103, 15 pp. (2016).*, 833, 2016. ISSN 0004-637X. doi:10.3847/1538-4357/833/1/103.

J. A. Hogbom. *Aperture Synthesis with a Non-Regular Distribution of Interferometer Baselines*, volume 15. EDP Sciences [etc.], 1974.

D. W. Hogg, I. K. Baldry, M. R. Blanton, and D. J. Eisenstein. *eprint arXiv:astro-ph/0210394*, 2002.

W. S. Holland, et al. *Monthly Notices of the Royal Astronomical Society*, 303(4):659672, 1999. ISSN 00358711. doi:10.1046/j.13658711.1999.02111.x.

W. S. Holland, et al. *Monthly Notices of the Royal Astronomical Society*, 430(4):2513–2533, 2013. ISSN 0035-8711. doi:10.1093/mnras/sts612.

P. F. Hopkins, L. Hernquist, T. J. Cox, and D. Kereš. *The Astrophysical Journal Supplement Series*, 175(2):356–389, 2008. ISSN 0067-0049. doi:10.1086/524362.

D. Hughes, et al. In *Ground-based and Airborne Telescopes III*, volume 7733 of *procspie*, page 773312. 2010. doi:10.1117/12.857974.

. Hughes, et al. *Nature*, 394(6690):241–247, 1998. doi:10.1038/28328.

C.-L. Hung, et al. *The Astrophysical Journal, Volume 826, Issue 2, article id. 130, 10 pp. (2016).*, 826, 2016. ISSN 0004-637X. doi:10.3847/0004-637X/826/2/130.

P. D. Hurley, et al. *Monthly Notices of the Royal Astronomical Society, Volume 464, Issue 1, p.885-896*, 464:885–896, 2016. ISSN 0035-8711. doi:10.1093/mnras/stw2375.

M. T. Huynh, et al. *Monthly Notices of the Royal Astronomical Society*, 467(1):stx156, 2017. ISSN 0035-8711. doi:10.1093/mnras/stx156.

S. Ikarashi, et al. *The Astrophysical Journal, Volume 835, Issue 2, article id. 286, 15 pp. (2017).*, 835, 2017. ISSN 0004-637X. doi:10.3847/1538-4357/835/2/286.

R. J. Ivison, et al. *Astronomy and Astrophysics, Volume 518, id.L35, 5 pp.*, 518, 2010. ISSN 0004-6361. doi:10.1051/0004-6361/201014548.

R. J. Ivison, et al. *Monthly Notices of the Royal Astronomical Society*, 425(2):1320–1331, 2012. ISSN 00358711. doi:10.1111/j.1365-2966.2012.21544.x.

R. J. Ivison, et al. *The Astrophysical Journal, Volume 772, Issue 2, article id. 137, 15 pp. (2013).*, 772, 2013. ISSN 0004-637X. doi:10.1088/0004-637X/772/2/137.

R. J. Ivison, et al. *APJ*, 832(1), 2016. ISSN 0004-637X. doi:10.3847/0004-637X/832/1/78.

A. Karim, et al. *Monthly Notices of the Royal Astronomical Society*, 432(1):2–9, 2013. ISSN 0035-8711. doi:10.1093/mnras/stt196.

Y. Kato, et al. *Monthly Notices of the Royal Astronomical Society, Volume 460, Issue 4, p.3861-3872*, 460:3861–3872, 2016. ISSN 0035-8711. doi:10.1093/mnras/stw1237.

R. C. Kennicutt. *Annual Review of Astronomy and Astrophysics*, 36(1):189–231, 1998. ISSN 0066-4146. doi:10.1146/annurev.astro.36.1.189.

R. C. Kennicutt and N. J. Evans. *Annual Review of Astronomy and Astrophysics*, 50(1):531–608, 2012. ISSN 0066-4146. doi:10.1146/annurev-astro-081811-125610.

R. C. Kennicutt, et al. *The Astrophysical Journal*, 703(2):1672–1695, 2009. ISSN 0004-637X. doi:10.1088/0004-637X/703/2/1672.

D.-C. Kim. *Thesis (PH.D.)–UNIVERSITY OF HAWAII, 1995.Source: Dissertation Abstracts International, Volume: 56-05, Section: B, page: 2676.*, 1995.

M. P. Koprowski, et al. *Monthly Notices of the Royal Astronomical Society, Volume 471, Issue 4, p.4155-4169*, 471:4155–4169, 2017. ISSN 0035-8711. doi:10.1093/mnras/stx1843.

A. Kovacs, et al. *The Astrophysical Journal, Volume 650, Issue 2, pp. 592-603.*, 650:592–603, 2006. ISSN 0004-637X. doi:10.1086/506341.

A. Kravtsov and S. Borgani. *Annual Review of Astronomy and Astrophysics*, 50:353–409, 2012. ISSN 0066-4146. doi:10.1146/annurev-astro-081811-125502.

C. G. Lacey, et al. *Monthly Notices of the Royal Astronomical Society*, 462(4):3854–3911, 2016. ISSN 0035-8711. doi:10.1093/mnras/stw1888.

B. C. Lacki, T. A. Thompson, and E. Quataert. *The Astrophysical Journal*, 717(1):1–28, 2010. ISSN 0004-637X. doi:10.1088/0004-637X/717/1/1.

G. Lagache, J.-L. Puget, and H. Dole. *Annual Review of Astronomy & Astrophysics, vol. 43, Issue 1, pp.727-768*, 43:727–768, 2005. ISSN 0066-4146. doi:10.1146/annurev.astro.43.072103.150606.

A. Lawrence, et al. *Monthly Notices of the Royal Astronomical Society, Volume 379, Issue 4, pp. 1599-1617.*, 379:1599–1617, 2006. ISSN 0035-8711. doi:10.1111/j.1365-2966.2007.12040.x.

E. Le-Floc'h, et al. *The Astrophysical Journal, Volume 632, Issue 1, pp. 169-190.*, 632:169–190, 2005. ISSN 0004-637X. doi:10.1086/432789.

L. Levenson, et al. *Monthly Notices of the Royal Astronomical Society*, 409:83–91, 2010. doi:10.1111/j.1365-2966.2010.17771.x.

A. J. R. Lewis, et al. *eprint arXiv:1711.08803*, 2017.

T. C. Licquia and J. A. Newman. *The Astrophysical Journal, Volume 806, Issue 1, article id. 96, 20 pp. (2015).*, 806, 2014. ISSN 0004-637X. doi:10.1088/0004-637X/806/1/96.

D. Liu, et al. *eprint arXiv:1703.05281*, 2017.

C. J. Lonsdale, D. Farrah, and H. E. Smith. In *Astrophysics Update 2*, pages 285–336. Springer Berlin Heidelberg, 2006. doi:10.1007/3-540-30313-8_9.

P. A. A. Lopes, et al. *The Astronomical Journal*, 128(3):1017–1045, 2004. ISSN 0004-6256. doi:10.1086/423038.

M. López-Caniego, et al. *Monthly Notices of the Royal Astronomical Society*, 370(4):2047–2063, 2006. ISSN 00358711. doi:10.1111/j.1365-2966.2006.10639.x.

C.-J. Ma, et al. *The Astrophysical Journal*, 806(2):257, 2015. ISSN 1538-4357. doi:10.1088/0004-637X/806/2/257.

P. Madau and M. Dickinson. *Annual Review of Astronomy and Astrophysics, vol. 52, p.415-486*, 52:415–486, 2014. ISSN 0066-4146. doi:10.1146/annurev-astro-081811-125615.

P. Madau, L. Pozzetti, and M. Dickinson. *The Astrophysical Journal*, 498(1):106–116, 1998. ISSN 0004-637X. doi:10.1086/305523.

S. J. Maddox, et al. 2017.

M. Maercker, et al. *Astronomy & Astrophysics, Volume 586, id.A5, 12 pp.*, 586, 2015. ISSN 0004-6361. doi:10.1051/0004-6361/201527128.

B. Magnelli, et al. *Astronomy and Astrophysics*, 518:L28, 2010. ISSN 0004-6361. doi:10.1051/0004-6361/201014616.

B. Magnelli, et al. *Astronomy & Astrophysics, Volume 528, id.A35, 18 pp.*, 528, 2011. ISSN 0004-6361. doi:10.1051/0004-6361/200913941.

B. Magnelli, et al. *Astronomy & Astrophysics*, 548:A22, 2012. ISSN 0004-6361. doi:10.1051/0004-6361/201220074.

B. Magnelli, et al. *Astronomy & Astrophysics, Volume 553, id.A132, 22 pp.*, 553, 2013. ISSN 0004-6361. doi:10.1051/0004-6361/201321371.

D. P. Marrone, et al. *Nature, Volume 553, Issue 7686, pp. 51-54 (2018).*, 553:51–54, 2017. ISSN 0028-0836. doi:10.1038/nature24629.

J. C. Mauduit, et al. *Publications of the Astronomical Society of the Pacific, Volume 124, Issue 917, pp. 714 (2012).*, 124:714, 2012. ISSN 0004-6280. doi:10.1086/666945.

A. Mayer, et al. *Astronomy & Astrophysics, Volume 531, id.L4, 4 pp.*, 531, 2011. ISSN 0004-6361. doi:10.1051/0004-6361/201117203.

J. P. McMullin, B. Waters, D. Schiebel, W. Young, and K. Golap. *CASA Architecture and Applications*, volume 376. Astronomical Society of the Pacific (ASP), 2007.

M. Michałowski, J. Hjorth, and D. Watson. *Astronomy and Astrophysics*, 514:A67, 2010. ISSN 0004-6361. doi:10.1051/0004-6361/200913634.

M. J. Michałowski, et al. *Monthly Notices of the Royal Astronomical Society*, 469(1):492–515, 2017. ISSN 0035-8711. doi:10.1093/mnras/stx861.

O. Miettinen, et al. *Astronomy & Astrophysics*, 577:A29, 2015. ISSN 0004-6361. doi:10.1051/0004-6361/201425032.

O. Miettinen, et al. *Astronomy & Astrophysics*, 606:A17, 2017. ISSN 0004-6361. doi:10.1051/0004-6361/201730762.

J. W. Miles, J. R. Houck, T. L. Hayward, and M. L. N. Ashby. *The Astrophysical Journal*, 465:191, 1996. ISSN 0004-637X. doi:10.1086/177412.

G. K. Miley, et al. *The Astrophysical Journal*, 650(1):L29–L32, 2006. ISSN 0004-637X. doi:10.1086/508534.

T. B. Miller, C. C. Hayward, S. C. Chapman, and P. S. Behroozi. *Monthly Notices of the Royal Astronomical Society*, 452:878–883, 2015. ISSN 0035-8711. doi:10.1093/mnras/stv1267.

M. A. Miville Deschenes and G. Lagache. *The Astrophysical Journal Supplement Series*, 157(2):302:323, 2005. ISSN 0067 0049. doi:10.1086/427938.

A. Monfardini, et al. *Astronomy and Astrophysics*, 521:A29, 2010. ISSN 0004-6361. doi:10.1051/0004-6361/201014727.

S. I. Muldrew, N. A. Hatch, and E. A. Cooke. *Monthly Notices of the Royal Astronomical Society*, 452(3):2528–2539, 2015. ISSN 0035-8711. doi:10.1093/mnras/stv1449.

S. I. Muldrew, N. A. Hatch, and E. A. Cooke. *Monthly Notices of the Royal Astronomical Society*, 473(2):2335–2347, 2018. ISSN 0035-8711. doi:10.1093/mnras/stx2454.

H. Murakami, et al. *Publications of the Astronomical Society of Japan*, 59(sp2):S369–S376, 2007. ISSN 0004-6264. doi:10.1093/pasj/59.sp2.S369.

M. Negrello, et al. *Monthly Notices of the Royal Astronomical Society*, 358(3):869–874, 2005. ISSN 0035-8711. doi:10.1111/j.1365-2966.2005.08783.x.

M. Negrello, et al. *Monthly Notices of the Royal Astronomical Society*, 470(2), 2017. ISSN 13652966. doi:10.1093/mnras/stx1367.

J. E. Nelan, et al. *The Astrophysical Journal*, 632(1):137–156, 2005. ISSN 0004-637X. doi:10.1086/431962.

R. Neri, D. Downes, P. Cox, and F. Walter. *Astronomy & Astrophysics*, 562:A35, 2014. ISSN 0004-6361. doi:10.1051/0004-6361/201322528.

G. Neugebauer, et al. *The Astrophysical Journal*, 278:L1, 1984. ISSN 0004-637X. doi:10.1086/184209.

H. T. Nguyen, et al. *Astronomy and Astrophysics, Volume 518, id.L5, 5 pp.*, 518, 2010. ISSN 0004-6361. doi:10.1051/0004-6361/201014680.

A. G. Noble, et al. *Monthly Notices of the Royal Astronomical Society: Letters*, 436(1):L40–L44, 2013. ISSN 1745-3925. doi:10.1093/mnrasl/slt108.

M. Novak, et al. *Astronomy & Astrophysics, Volume 602, id.A5, 17 pp.*, 602, 2017. ISSN 0004-6361. doi:10.1051/0004-6361/201629436.

K. Nyland, et al. *The Astrophysical Journal Supplement Series*, 230(1):9, 2017. ISSN 1538-4365. doi:10.3847/1538-4365/aa6fed.

S. J. Oliver, et al. *Monthly Notices of the Royal Astronomical Society*, 424(3):1614–1635, 2012. ISSN 00358711. doi:10.1111/j.1365-2966.2012.20912.x.

I. Oteo, M. A. Zwaan, R. J. Ivison, I. Smail, and A. D. Biggs. *The Astrophysical Journal*, 822(1):36, 2016a. ISSN 1538-4357. doi:10.3847/0004-637X/822/1/36.

I. Oteo, M. A. Zwaan, R. J. Ivison, I. Smail, and A. D. Biggs. *The Astrophysical Journal, Volume 837, Issue 2, article id. 182, 9 pp. (2017).*, 837, 2016b. ISSN 0004-637X. doi:10.3847/1538-4357/aa5da4.

I. Oteo, et al. *The Astrophysical Journal, Volume 827, Issue 1, article id. 34, 11 pp. (2016).*, 827, 2016c. ISSN 0004-637X. doi:10.3847/0004-637X/827/1/34.

I. Oteo, et al. *In prep*, 2017.

I. Oteo, et al. *The Astrophysical Journal*, 856(1):72, 2018. doi:10.3847/1538-4357/aaa1f1.

S. Ott, H. S. Centre, and E. S. Agency. *Astronomical Data Analysis Software and Systems XIX*, 434:139, 2010. ISSN 1050-3390.

R. A. Overzier. *The Astronomy and Astrophysics Review*, 24(1):14, 2016. ISSN 0935-4956. doi:10.1007/s00159-016-0100-3.

R. A. Overzier, et al. *The Astrophysical Journal, Volume 637, Issue 1, pp. 58-73.*, 637:58–73, 2006. ISSN 0004-637X. doi:10.1086/498234.

P. P. Papadopoulos, P. van der Werf, E. Xilouris, K. G. Isaak, and Y. Gao. *The Astrophysical Journal*, 751(1):10, 2012. ISSN 0004-637X. doi:10.1088/0004-637X/751/1/10.

J. Pardo, J. Cernicharo, and E. Serabyn. *IEEE Transactions on Antennas and Propagation*, 49(12):1683–1694, 2001. ISSN 0018926X. doi:10.1109/8.982447.

G. Patanchon, et al. *The Astrophysical Journal, Volume 681, Issue 1, article id. 708-725, pp. (2008).*, 681, 2008. ISSN 0004-637X. doi:10.1086/588543.

H. Patel, et al. *Monthly Notices of the Royal Astronomical Society*, 428(1):291–306, 2013. ISSN 0035-8711. doi:10.1093/mnras/sts013.

E. A. Pearson, et al. *Monthly Notices of the Royal Astronomical Society, Volume 435, Issue 4, p.2753-2763*, 435:2753–2763, 2013. ISSN 0035-8711. doi:10.1093/mnras/stt1369.

G. L. Pilbratt, et al. *Astronomy and Astrophysics*, 518:L1, 2010. ISSN 0004-6361. doi:10.1051/0004-6361/201014759.

A. Pillepich, et al. *Monthly Notices of the Royal Astronomical Society*, 475(1):648–675, 2018. ISSN 0035-8711. doi:10.1093/mnras/stx3112.

P. Planck Collaboration, et al. *Astronomy & Astrophysics*, 536:A7, 2011. ISSN 0004-6361. doi:10.1051/0004-6361/201116474.

P. Planck Collaboration, et al. *Astronomy & Astrophysics*, 571:A28, 2014. ISSN 0004-6361. doi:10.1051/0004-6361/201321524.

P. Planck Collaboration, et al. *Astronomy & Astrophysics, Volume 594, id.A26, 39 pp.*, 594, 2015a. ISSN 0004-6361. doi:10.1051/0004-6361/201526914.

P. Planck Collaboration, et al. *Astronomy & Astrophysics, Volume 594, id.A27, 38 pp.*, 594, 2015b. ISSN 0004-6361. doi:10.1051/0004-6361/201525823.

P. Planck Collaboration, et al. *Astronomy & Astrophysics, Volume 594, id.A28, 28 pp.*, 594, 2015c. ISSN 0004-6361. doi:10.1051/0004-6361/201525819.

P. Planck Collaboration, et al. *Astronomy & Astrophysics, Volume 582, id.A30, 29 pp.*, 582, 2015d. ISSN 0004-6361. doi:10.1051/0004-6361/201424790.

P. Planck Collaboration, et al. *Astronomy & Astrophysics, Volume 596, id.A100, 28 pp.*, 596:A100, 2016. ISSN 0004-6361. doi:10.1051/0004-6361/201527206.

P. Planck HFI Team, et al. *Astronomy and Astrophysics*, 520:A9, 2010. doi:10.1051/0004-6361/200912975.

A. Poglitsch, et al. *Astronomy and Astrophysics*, 518:L2, 2010. ISSN 0004-6361. doi:10.1051/0004-6361/201014535.

M. Polletta, et al. *The Astrophysical Journal, Volume 663, Issue 1, pp. 81-102.*, 663:81–102, 2007. ISSN 0004-637X. doi:10.1086/518113.

J.-L. Puget, et al. *Aap*, 308:L5+, 1996.

C. Ragone-Figueroa, G. L. Granato, G. Murante, S. Borgani, and W. Cui. *Monthly Notices of the Royal Astronomical Society*, 436(2):1750–1764, 2013. ISSN 1365-2966. doi:10.1093/mnras/stt1693.

N. Rangwala, et al. *The Astrophysical Journal, Volume 743, Issue 1, article id. 94, 19 pp. (2011).*, 743, 2011. ISSN 0004-637X. doi:10.1088/0004-637X/743/1/94.

D. A. Riechers, et al. *The Astrophysical Journal Letters, Volume 720, Issue 2, pp. L131-L136 (2010).*, 720:L131–L136, 2010. ISSN 0004-637X. doi:10.1088/2041-8205/720/2/L131.

D. A. Riechers, et al. *Nature*, 496(7445):329–33, 2013. ISSN 1476-4687. doi:10.1038/nature12050.

D. A. Riechers, et al. *eprint arXiv:1705.09660*, 2017.

E. E. Rigby, et al. *Monthly Notices of the Royal Astronomical Society*, 437(2):1882–1893, 2013. ISSN 0035-8711. doi:10.1093/mnras/stt2019.

I. G. Roseboom, et al. *Monthly Notices of the Royal Astronomical Society, Volume 409, Issue 1, pp. 48-65.*, 409:48–65, 2010. ISSN 0035-8711. doi:10.1111/j.1365-2966.2010.17634.x.

I. G. Roseboom, et al. *Monthly Notices of the Royal Astronomical Society, Volume 419, Issue 4, pp. 2758-2773.*, 419:2758–2773, 2011. ISSN 0035-8711. doi:10.1111/j.1365-2966.2011.19827.x.

M. Rowan-Robinson, et al. *Monthly Notices of the Royal Astronomical Society, Volume 461, Issue 1, p.1100-1111*, 461:1100–1111, 2016. ISSN 0035-8711. doi:10.1093/mnras/stw1169.

E. E. Salpeter. *The Astrophysical Journal*, 121:161, 1955. ISSN 0004-637X. doi:10.1086/145971.

D. B. Sanders, E. Egami, S. Lipari, I. F. Mirabel, and B. T. Soifer. *The Astronomical Journal*, 110:1993, 1995. ISSN 00046256. doi:10.1086/117665.

D. B. Sanders, J. M. Mazzarella, D.-C. Kim, J. A. Surace, and B. T. Soifer. *The Astronomical Journal*, 126(4):1607–1664, 2003. ISSN 0004-6256. doi:10.1086/376841.

D. B. Sanders and I. F. Mirabel. *Annual Review of Astronomy and Astrophysics*, 34(1):749–792, 1996. ISSN 0066-4146. doi:10.1146/annurev.astro.34.1.749.

D. B. Sanders, N. Z. Scoville, and B. T. Soifer. *The Astrophysical Journal*, 370:158, 1991. ISSN 0004-637X. doi:10.1086/169800.

M. T. Sargent, et al. *The Astrophysical Journal Supplement, Volume 186, Issue 2, pp. 341-377 (2010).*, 186:341–377, 2010. ISSN 0067-0049. doi:10.1088/0067-0049/186/2/341.

R. J. Sault, P. Teuben, and M. C. H. Wright. *Astrophysics Source Code Library, record ascl:1106.007*, 2011.

D. Schiminovich, et al. *The Astrophysical Journal Supplement Series*, 173(2):315–341, 2007. ISSN 0067-0049. doi:10.1086/524659.

K. S. Scott, et al. *Monthly Notices of the Royal Astronomical Society*, 423(1):575–589, 2012. ISSN 00358711. doi:10.1111/j.1365-2966.2012.20905.x.

N. Scoville, et al. *The Astrophysical Journal Supplement, Volume 206, Issue 1, article id. 3, 26 pp. (2013).*, 206, 2013. ISSN 0067-0049. doi:10.1088/0067-0049/206/1/3.

J. M. Scudder, et al. *Monthly Notices of the Royal Astronomical Society, Volume 460, Issue 1, p.1119-1130*, 460:1119–1130, 2016. ISSN 0035-8711. doi:10.1093/mnras/stw1044.

J. M. Scudder, et al. *eprint arXiv:1807.09790*, 2018.

J. M. Simpson, et al. *The Astrophysical Journal*, 788(2):125, 2014. ISSN 0004-637X. doi:10.1088/0004-637X/788/2/125.

J. M. Simpson, et al. *The Astrophysical Journal*, 807(2):14, 2015. ISSN 1538-4357. doi:10.1088/0004-637X/807/2/128.

J. M. Simpson, et al. *The Astrophysical Journal*, 839(1):58, 2017. ISSN 1538-4357. doi:10.3847/1538-4357/aa65d0.

G. Siringo, et al. *Astronomy and Astrophysics*, 497(3):945–962, 2009. ISSN 0004-6361. doi:10.1051/0004-6361/200811454.

I. Smail, R. J. Ivison, and A. W. Blain. *The Astrophysical Journal*, 490(1):L5–L8, 1997. ISSN 0004637X. doi:10.1086/311017.

I. Smail, R. J. Ivison, A. W. Blain, and J. P. Kneib. *Monthly Notices of the Royal Astronomical Society, Volume 331, Issue 2, pp. 495-520.*, 331:495–520, 2002. ISSN 0035-8711. doi:10.1046/j.1365-8711.2002.05203.x.

I. Smail, et al. *The Astrophysical Journal*, 782(1):19, 2014. ISSN 0004-637X. doi:10.1088/0004-637X/782/1/19.

D. J. B. Smith, C. C. Hayward, M. J. Jarvis, and C. Simpson. *Monthly Notices of the Royal Astronomical Society, Volume 471, Issue 2, p.2453-2462*, 471(2):2453–2462, 2017. ISSN 0035-8711. doi:10.1093/mnras/stx1689.

R. J. Smith, J. R. Lucey, J. Price, M. J. Hudson, and S. Phillipps. *Monthly Notices of the Royal Astronomical Society*, 419(4):3167–3180, 2012. ISSN 00358711. doi:10.1111/j.1365-2966.2011.19956.x.

V. Smolcic, et al. *Astronomy & Astrophysics, Volume 548, id.A4, 34 pp.*, 548, 2012. ISSN 0004-6361. doi:10.1051/0004-6361/201219368.

B. T. Soifer, L. Boehmer, G. Neugebauer, and D. B. Sanders. *The Astronomical Journal*, 98:766, 1989. ISSN 00046256. doi:10.1086/115178.

B. T. Soifer and G. Neugebauer. *The Astronomical Journal*, 101:354, 1991. ISSN 00046256. doi:10.1086/115691.

P. Solomon and P. Vanden Bout. *Annual Review of Astronomy and Astrophysics*, 43(1):677–725, 2005. ISSN 0066-4146. doi:10.1146/annurev.astro.43.051804.102221.

S. M. Stach, et al. 860(2):161, 2018. doi:10.3847/1538-4357/aac5e5.

J. A. Stevens, et al. *Nature*, 425(6955):264–267, 2003. ISSN 0028-0836. doi:10.1038/nature01976.

J. A. Stevens, et al. *Monthly Notices of the Royal Astronomical Society*, 405(4):no–no, 2010. ISSN 00358711. doi:10.1111/j.1365-2966.2010.16641.x.

M. L. Strandet, et al. *The Astrophysical Journal*, 822(2):80, 2016. ISSN 1538-4357. doi:10.3847/0004-637X/822/2/80.

M. L. Strandet, et al. *The Astrophysical Journal Letters, Volume 842, Issue 2, article id. L15, 6 pp. (2017).*, 842, 2017. ISSN 0004-637X. doi:10.3847/2041-8213/aa74b0.

A. M. Swinbank, et al. *Monthly Notices of the Royal Astronomical Society*, 371(1):465–476, 2006. ISSN 00358711. doi:10.1111/j.1365-2966.2006.10673.x.

M. Swinbank, et al. *Nature, Volume 464, Issue 7289, pp. 733-736 (2010).*, 464:733–736, 2010. ISSN 0028-0836. doi:10.1038/nature08880.

M. Swinbank, et al. *Monthly Notices of the Royal Astronomical Society, Volume 438, Issue 2, p.1267-1287*, 438:1267–1287, 2014. ISSN 0035-8711. doi:10.1093/mnras/stt2273.

B. Swinyard and T. Nakagawa. *Experimental Astronomy*, 23(1):193–219, 2009. ISSN 0922-6435. doi:10.1007/s10686-008-9090-0.

L. J. Tacconi, et al. *The Astrophysical Journal*, 640(1):228–240, 2006. ISSN 0004-637X. doi:10.1086/499933.

L. J. Tacconi, et al. *The Astrophysical Journal*, 680(1):246–262, 2008. ISSN 0004-637X. doi:10.1086/587168.

L. J. Tacconi, et al. *Nature*, 463(7282):781–784, 2010. ISSN 0028-0836. doi:10.1038/nature08773.

Y. Tamura, et al. *Nature, Volume 459, Issue 7243, pp. 61-63 (2009).*, 459:61–63, 2009. ISSN 0028-0836. doi:10.1038/nature07947.

M. B. Taylor. *Astronomical Data Analysis Software and Systems XIV - ASP Conference Series*, 347:29–33, 2005.

A. The Astropy Collaboration, et al. *Astronomy & Astrophysics, Volume 558, id.A33, 9 pp.*, 558, 2013. ISSN 0004-6361. doi:10.1051/0004-6361/201322068.

A. P. Thomson, et al. *Monthly Notices of the Royal Astronomical Society*, 442(1):577–588, 2014. ISSN 1365-2966. doi:10.1093/mnras/stu839.

S. Toft, et al. *The Astrophysical Journal, Volume 782, Issue 2, article id. 68, 12 pp. (2014).*, 782, 2014. ISSN 0004-637X. doi:10.1088/0004-637X/782/2/68.

H. Umehata, et al. *The Astrophysical Journal*, 815(1):L8, 2015. ISSN 2041-8213. doi:10.1088/2041-8205/815/1/L8.

E. Valiante, D. Lutz, E. Sturm, R. Genzel, and E. Chapin. *The Astrophysical Journal, Volume 701, Issue 2, pp. 1814-1838 (2009).*, 701:1814–1838, 2009. ISSN 0004-637X. doi:10.1088/0004-637X/701/2/1814.

E. Valiante, et al. *Monthly Notices of the Royal Astronomical Society, Volume 462, Issue 3, p.3146-3179*, 462:3146–3179, 2016. ISSN 0035-8711. doi:10.1093/mnras/stw1806.

J. D. Vieira, et al. *Nature, Volume 495, Issue 7441, pp. 344-347 (2013).*, 495:344–347, 2013. ISSN 0028-0836. doi:10.1038/nature1200.

M. P. Viero, et al. *The Astrophysical Journal Supplement Series*, 210(2):22, 2014. ISSN 0067-0049. doi:10.1088/0067-0049/210/2/22.

F. Walter, et al. *Nature*, 486(7402):233–6, 2012. ISSN 1476-4687. doi:10.1038/nature11073.

L. Wang, et al. *Monthly Notices of the Royal Astronomical Society, Volume 444, Issue 3, p.2870-2883*, 444:2870–2883, 2013. ISSN 0035-8711. doi:10.1093/mnras/stu1569.

T. Wang, et al. *The Astrophysical Journal, Volume 828, Issue 1, article id. 56, 15 pp. (2016).*, 828, 2016. ISSN 0004-637X. doi:10.3847/0004-637X/828/1/56.

W.-H. Wang, L. L. Cowie, A. J. Barger, and J. P. Williams. *The Astrophysical Journal*, 726(2):L18, 2011. ISSN 2041-8205. doi:10.1088/2041-8205/726/2/L18.

W.-H. Wang, et al. *The Astrophysical Journal, Volume 850, Issue 1, article id. 37, 17 pp. (2017).*, 850, 2017. ISSN 0004-637X. doi:10.3847/1538-4357/aa911b.

J. L. Wardlow, et al. *Monthly Notices of the Royal Astronomical Society*, 415(2):1479–1508, 2011. ISSN 00358711. doi:10.1111/j.1365-2966.2011.18795.x.

J. L. Wardlow, et al. *The Astrophysical Journal*, 762(1):59, 2013. ISSN 0004-637X. doi:10.1088/0004-637X/762/1/59.

J. L. Wardlow, et al. *Monthly Notices of the Royal Astronomical Society, Volume 479, Issue 3, p.3879-3891*, 479:3879–3891, 2018. ISSN 0035-8711. doi:10.1093/mnras/sty1526.

S. J. Warren, et al. *Monthly Notices of the Royal Astronomical Society, Volume 375, Issue 1, pp. 213-226.*, 375:213–226, 2006. ISSN 0035-8711. doi:10.1111/j.1365-2966.2006.11284.x.

A. Weiß, et al. *The Astrophysical Journal*, 767(1):88, 2013. ISSN 0004-637X. doi:10.1088/0004-637X/767/1/88.

M. Wenger, et al. *Astronomy and Astrophysics Supplement, v.143, p.9-22*, 143:9–22, 2000. ISSN 0365-0138. doi:10.1051/aas:2000332.

T. Wiklind, et al. *The Astrophysical Journal, Volume 785, Issue 2, article id. 111, 19 pp. (2014).*, 785, 2014. ISSN 0004-637X. doi:10.1088/0004-637X/785/2/111.

A. Wilkinson, et al. *Monthly Notices of the Royal Astronomical Society, Volume 464, Issue 2, p.1380-1392*, 464:1380–1392, 2016. ISSN 0035-8711. doi:10.1093/mnras/stw2405.

G. W. Wilson, et al. *Monthly Notices of the Royal Astronomical Society*, 386(2):807–818, 2008. ISSN 0035-8711. doi:10.1111/j.1365-2966.2008.12980.x.

A. Wootten and A. Thompson. *Proceedings of the IEEE*, 97(8):1463–1471, 2009. ISSN 0018-9219. doi:10.1109/JPROC.2009.2020572.

E. L. Wright, et al. *The Astronomical Journal, Volume 140, Issue 6, article id. 1868-1881 (2010).*, 140, 2010. ISSN 0004-6256. doi:10.1088/0004-6256/140/6/1868.

C. Yang, et al. *Astronomy & Astrophysics, Volume 608, id.A144, 41 pp.*, 608, 2017. ISSN 0004-6361. doi:10.1051/0004-6361/201731391.

J. D. Younger, et al. *The Astrophysical Journal*, 688(1):59–66, 2008. ISSN 0004-637X. doi: 10.1086/591931.

T. T. Yuan, et al. *The Astrophysical Journal Letters, Volume 795, Issue 1, article id. L20, 6 pp. (2014).*, 795, 2014. ISSN 0004-637X. doi:10.1088/2041-8205/795/1/L20.

M. S. Yun, N. A. Reddy, and J. J. Condon. *The Astrophysical Journal, Volume 554, Issue 2, pp. 803-822.*, 554:803–822, 2001. ISSN 0004-637X. doi:10.1086/323145.

M. S. Yun, et al. *Monthly Notices of the Royal Astronomical Society*, 389(1):333–340, 2008. ISSN 00358711. doi:10.1111/j.1365-2966.2008.13565.x.

M. S. Yun, et al. *Monthly Notices of the Royal Astronomical Society, Volume 454, Issue 4, p.3485-3499*, 454:3485–3499, 2015. ISSN 0035-8711. doi:10.1093/mnras/stv1963.

J. A. Zavala, et al. *Nature Astronomy*, 2017. ISSN 2397-3366. doi:10.1038/s41550-017-0297-8.

Z.-Y. Zhang, D. Romano, R. J. Ivison, P. P. Papadopoulos, and F. Matteucci. *Nature*, 558(7709):260–263, 2018. ISSN 0028-0836. doi:10.1038/s41586-018-0196-x.

G. D. Zotti, et al. *Journal of Cosmology and Astroparticle Physics*, 2018(4):020–020, 2018. ISSN 14757516. doi:10.1088/1475-7516/2018/04/020.

Appendix A

Planck Compact Sources Detected in the Herschel Extragalactic Fields

Here we include a list of all our *Planck* compact sources that lie in the Herschel fields discussed in 2.

Table A.1: Compact sources and their identifications from the *Planck* 857 GHz catalogues of compact sources. σ values give the strength of the overdensity at the 3 SPIRE wavelengths.

Name	RA	DEC	Associations	Planck 857 Flux [mJy]	σ_{250}	σ_{350}	σ_{500}
PCCS1 857 G014.92-58.26	336.635	-32.177	Cluster Candidate	302 ± 239	1.88	1.96	4.36
PCCS1 857 G354.81-79.56	3.049	-33.228	Cluster Candidate	1014 ± 233	1.67	2.23	3.25
PLCKERC857 G257.09-87.10	15.233	-29.122	Cluster Candidate	2403 ± 198	3.52	3.02	3.25
PLCKERC857 G014.99-59.64	338.260	-32.139	Cluster Candidate	943 ± 115	3.12	1.96	4.36
PLCKERC857 G239.13-78.19	25.333	-31.786	Cluster Candidate	1110 ± 145	2.72	1.68	3.25
PLCKERC857 G017.86-68.67	348.790	-30.591	Cluster Candidate	1657 ± 167	2.92	3.76	5.05
PLCKERC857 G007.34-65.24	345.366	-35.103	Cluster Candidate	920 ± 132	3.32	3.52	3.25
PCCS1 857 G252.98-85.59	16.749	-29.910	Cluster Candidate	619 ± 817	1.88	2.76	3.25
PCCS1 857 G058.69+81.03	202.258	30.712	Cluster Candidate	845 ± 298	1.45	1.68	4.01
PCCS1 857 G058.53+82.57	200.607	30.124	Cluster Candidate	827 ± 197	1.45	2.23	4.36
PLCKERC857 G062.48+78.89	204.276	32.142	Cluster Candidate	814 ± 109	0.77	2.50	3.25
PLCKERC857 G063.13+78.00	205.172	32.621	Cluster Candidate	912 ± 169	2.10	3.52	3.25
PLCKERC857 G027.36+84.83	198.608	26.510	Cluster Candidate	792 ± 93	2.52	3.27	4.01
PLCKERC857 G042.54+81.51	202.358	28.224	Cluster Candidate	1697 ± 251	1.67	3.76	4.01
PLCKERC857 G149.81+50.11	158.364	59.196	Cluster Candidate	1249 ± 131	5.38	4.47	4.71
PCCS1 857 G089.66+36.10	256.828	60.449	Cluster Candidate	886 ± 194	3.32	2.76	2.01
PCCS1 857 G085.48+43.36	244.657	55.771	Cluster Candidate	748 ± 128	2.72	3.27	3.64
PLCKERC857 G095.44+58.94	216.128	52.936	Cluster Candidate	1141 ± 176	4.65	5.80	2.44
PCCS1 857 G238.20+42.27	150.845	1.469	Cluster Candidate	712 ± 269	4.28	3.76	2.01
PLCKERC857 G060.37+66.55	218.579	35.559	Cluster Candidate	1241 ± 151	1.00	4.47	5.70
PLCKERC857 G261.89-40.69	70.168	-53.734	Cluster Candidate	795 ± 134	3.32	4.47	3.64
PCCS1 857 G088.71+81.15	198.869	34.314	Lens Candidate	427 ± 159	0.29	0.17	-0.04
PCCS1 857 G076.18+79.96	201.639	33.732	Lens Candidate	282 ± 397	-1.25	-1.64	0.54
PCCS1 857 G044.43+78.90	205.288	28.791	Lens Candidate	512 ± 233	0.05	0.17	2.01
PCCS1 857 G151.39-61.73	25.907	-1.783	Lens Candidate	445 ± 274	-2.43	-1.24	0.54
PCCS1 857 G060.81+67.75	217.103	35.421	(Lens) HERMES J142823.9+352619	424 ± 323	0.05	1.96	1.55
PCCS1 857 G231.57+30.82	138.393	-0.610	(Lens) H-ATLAS J091331.3-003642	730 ± 251	1.45	0.80	2.01
PCCS1 857 G266.28+58.43	174.648	0.841	(Lens) H-ATLAS J113833.3+004909	643 ± 402	0.77	1.10	0.54
PCCS2 857 G270.56+58.54	176.637	-0.187	(Lens) H-ATLAS J114637.9-001132	1148 ± 337	0.77	2.76	2.44
PLCKERC857 G047.32+82.53	201.116	28.742	(Lens) H-ATLAS J132426.9+284452	1303 ± 152	2.31	1.96	3.25
PCCS2 857 G052.27+77.90	206.125	30.506	(Lens) H-ATLAS J134429.4+303036	355 ± 250	-0.98	-0.50	0.54
PCCS2 857 G148.42+53.62	164.478	57.516	(Lens) HERMES J105751.1+573027	223 ± 382	-1.82	-1.64	-0.70
PCCS1 857 G229.23+33.59	139.710	2.532	(Lens) H-ATLAS J091840.8+023047	1991 ± 530	0.05	1.10	1.06

Name	RA	DEC	Associations	Planck 857 Flux [mJy]	σ_{250}	σ_{350}	σ_{500}
PCCS1 857 G131.83-60.95	17.168	1.619	(QSO) LBQS 0106+0119	657 ± 269	-3.83	-2.54	-1.52
PCCS1 857 G226.34+23.23	129.496	-0.560	(QSO) SDSS J083800.68-003306.0	1311 ± 429	-0.20	-0.16	1.06
PCCS1 857 G020.48-64.90	344.405	-29.622	(Star) Formalhaut	986 ± 244	0.05	0.49	0.54
PLCKERC857 G167.74-57.97	34.836	-2.970	(Star) Omicron Cet	4751 ± 167	6.07	-3.07	N/A
PLCKERC857 G250.12-80.58	21.755	-32.540	(Star) R Scl	1292 ± 138	-0.45	-1.24	1.06
PCCS1 857 G272.66-83.32	16.856	-32.835	2MASX J01072341-3249443	863 ± 666	-1.82	-2.07	1.06
PCCS2 857 G134.60-61.96	18.318	0.416	2MASX J01131527+0026137	964 ± 316	-0.98	-1.24	-0.70
PCCS1 857 G160.59-56.74	32.432	0.285	2MASX J02094125+0015587	877 ± 375	-0.71	-0.86	-0.70
PCCS1 857 G086.97+83.70	197.220	32.155	2MASX J13085045+3209540	638 ± 382	-0.45	0.17	0.54
PLCKERC857 G068.89+81.23	201.226	32.027	2MASX J13250973+3200520	1802 ± 183	2.31	1.68	2.86
PCCS1 857 G072.04+80.82	201.311	32.661	2MASX J13251511+3240167	418 ± 247	0.53	2.23	3.64
PLCKERC857 G070.09+80.54	201.794	32.555	2MASX J13265837+3232115	1692 ± 240	2.10	2.50	2.44
PLCKERC857 G070.52+80.05	202.236	32.880	2MASX J13285668+3252436	1167 ± 108	-0.20	0.80	1.55
PCCS1 857 G083.03+45.68	241.642	53.444	2MASX J16063296+5326319	473 ± 316	1.67	-0.50	0.54
PCCS2 857 G006.33-68.95	349.882	-34.656	2MASX J23192682-3437467	423 ± 249	0.05	1.10	1.06
PCCS2 857 G357.79-75.05	357.949	-34.938	2MASX J23514878-3455460	574 ± 252	0.05	0.80	0.54
PLCKERC857 G355.57-75.22	358.468	-35.353	2MASX J23534806-3520536	875 ± 110	0.29	2.50	2.01
PCCS1 857 G223.04-78.74	25.492	-28.536	2MFGC 01281	774 ± 431	1.45	1.10	1.06
PCCS1 857 G267.52+59.32	175.659	1.264	2MFGC 09181	333 ± 448	0.53	1.68	0.54
PLCKERC857 G307.24-86.67	12.570	-30.442	AM 0047-304	1052 ± 179	-0.20	1.68	1.06
PCCS1 857 G249.29-87.97	14.713	-28.318	AM 0056-283	261 ± 393	0.29	0.17	1.06
PLCKERC857 G219.43-78.58	25.709	-27.835	AM 0140-280	871 ± 123	1.45	0.80	1.06
PLCKERC857 G274.04+60.90	179.271	1.115	CGCG 013-010	1448 ± 110	-0.45	-0.16	-0.04
PLCKERC857 G281.52+60.68	182.564	-0.463	CGCG 013-092	1237 ± 173	3.12	1.39	3.25
PCCS2 857 G341.22+56.12	213.070	-0.617	CGCG 018-077	1027 ± 338	0.05	0.49	-0.70
PCCS1 857 G344.28+57.82	213.472	1.731	CGCG 018-084	628 ± 407	0.77	2.23	1.06
PCCS1 857 G223.97+26.09	130.926	2.720	CGCG 033-001	546 ± 347	-0.98	0.80	2.01
PLCKERC857 G066.56+83.87	198.767	30.394	CGCG 160-170	1056 ± 152	2.10	1.10	1.06
PCCS1 857 G085.81+43.85	243.702	55.859	CGCG 276-004	650 ± 160	3.90	3.76	1.06
PCCS1 857 G137.65-62.31	19.639	-0.222	CGCG 385-062	997 ± 384	1.22	1.39	0.54
PLCKERC857 G126.90-63.28	14.644	-0.473	Cirrus	2763 ± 313	-0.98	-0.50	-0.04
PLCKERC857 G131.56-63.86	16.650	-1.251	Cirrus	5438 ± 921	-1.25	-0.86	-0.04
PLCKERC857 G159.09-55.91	32.175	1.433	Cirrus	1422 ± 240	-2.43	-1.24	0.54
PLCKERC857 G147.26-60.62	24.521	0.022	Cirrus	2196 ± 238	-1.53	-1.24	-0.04
PLCKERC857 G145.33-60.97	23.513	0.028	Cirrus	1786 ± 280	-0.20	-0.16	-1.52

Name	RA	DEC	Associations	Planck 857 Flux [mJy]	σ_{250}	σ_{350}	σ_{500}
PLCKERC857 G131.96-63.35	16.898	-0.770	Cirrus	1666 ± 252	-1.25	-0.86	0.54
PCCS1 857 G139.80-62.24	20.627	-0.395	Cirrus	1592 ± 940	-0.98	-0.50	-0.04
PCCS2 857 G138.41-61.22	20.244	0.760	Cirrus	797 ± 246	-0.20	-0.16	1.55
PCCS1 857 G140.38-62.74	20.756	-0.948	Cirrus	1380 ± 440	-1.82	-1.24	0.54
PLCKERC857 G144.37-59.70	23.488	1.385	Cirrus	1753 ± 125	-0.98	-0.50	-0.04
PLCKERC857 G139.61-62.17	20.562	-0.302	Cirrus	3445 ± 363	-1.25	-1.24	-1.52
PLCKERC857 G136.06-63.48	18.682	-1.210	Cirrus	5603 ± 395	-2.43	-3.07	N/A
PLCKERC857 G126.28-63.31	14.363	-0.478	Cirrus	4489 ± 469	-1.82	-1.24	-0.70
PLCKERC857 G126.80-63.90	14.564	-1.080	Cirrus	2997 ± 369	-2.75	-2.07	-0.70
PCCS1 857 G131.08-64.08	16.415	-1.436	Cirrus	2188 ± 709	-3.83	-2.54	-1.52
PCCS1 857 G134.53-63.43	18.021	-1.026	Cirrus	1365 ± 1889	-1.82	-1.64	1.06
PCCS1 857 G131.85-64.10	16.745	-1.507	Cirrus	3259 ± 1192	-1.53	-1.24	-0.70
PLCKERC857 G287.82+60.54	185.491	-1.463	Cirrus	2124 ± 240	2.31	3.52	4.36
PLCKERC857 G266.26+58.99	174.940	1.323	Cirrus	1277 ± 211	-1.82	-0.86	0.54
PLCKERC857 G224.73+23.79	129.253	0.998	Cirrus	2289 ± 293	-1.53	-0.86	0.54
PLCKERC857 G231.25+32.05	139.284	0.279	Cirrus	1804 ± 324	3.12	3.02	4.01
PLCKERC857 G224.33+24.38	129.583	1.602	Cirrus	2928 ± 421	0.05	0.49	2.01
PLCKERC857 G231.43+32.10	139.413	0.173	Cirrus	2807 ± 430	3.71	3.76	6.01
PLCKERC857 G230.97+32.31	139.381	0.614	Cirrus	1539 ± 280	1.45	0.80	-0.70
PLCKERC857 G226.70+24.89	131.101	-0.013	Cirrus	2090 ± 194	1.45	1.96	1.55
PLCKERC857 G227.26+24.72	131.206	-0.540	Cirrus	3180 ± 438	1.22	1.39	1.55
PCCS1 857 G228.60+29.58	135.998	0.919	Cirrus	1417 ± 348	0.29	1.39	1.55
PLCKERC857 G227.24+24.51	131.018	-0.629	Cirrus	2761 ± 387	0.29	1.96	2.86
PLCKERC857 G223.40+22.96	127.935	1.659	Cirrus	2072 ± 314	-0.20	-0.50	0.54
PLCKERC857 G224.70+24.60	129.940	1.415	Cirrus	2905 ± 317	1.67	1.39	2.01
PLCKERC857 G227.58+24.57	131.222	-0.863	Cirrus	3136 ± 276	2.10	1.68	3.64
PCCS1 857 G223.74+24.66	129.572	2.213	Cirrus	2091 ± 654	3.32	1.96	2.01
PCCS1 857 G230.39+34.28	140.794	2.074	Cirrus	572 ± 542	-3.45	-3.07	N/A
PCCS1 857 G223.82+24.63	129.580	2.127	Cirrus	1622 ± 282	3.12	3.27	2.44
PLCKERC857 G227.75+30.24	136.180	1.886	Cirrus	3524 ± 482	0.77	1.68	3.25
PLCKERC857 G231.38+32.24	139.511	0.291	Cirrus	2477 ± 435	2.10	1.68	2.44
PLCKERC857 G226.98+26.25	132.398	0.454	Cirrus	2375 ± 315	1.00	1.10	1.06
PCCS1 857 G017.51-71.04	351.544	-30.537	DUKST 470-030	425 ± 331	0.05	1.39	1.06
PCCS1 857 G311.06-73.30	9.640	-43.622	ESO 242- G 021	901 ± 288	3.32	-2.07	2.01
PCCS1 857 G310.95-73.87	9.817	-43.064	ESO 242- G 023	1400 ± 212	2.52	2.23	2.01

Name	RA	DEC	Associations	Planck 857 Flux [mJy]	σ_{250}	σ_{350}	σ_{500}
PCCS1 857 G357.76-75.78	358.749	-34.602	ESO 349- G 005	543 ± 285	-1.25	0.17	2.01
PCCS1 857 G356.25-76.69	359.917	-34.481	ESO 349- G 016	762 ± 199	0.29	1.96	1.06
PCCS1 857 G353.76-79.19	2.809	-33.594	ESO 349- G 038	426 ± 214	0.05	-0.16	0.54
PCCS1 857 G259.62-82.44	18.996	-32.491	ESO 352- G 030	822 ± 421	1.00	2.23	2.44
PCCS1 857 G254.41-81.05	20.825	-32.826	ESO 352- G 063	487 ± 382	0.29	0.80	0.54
PCCS1 857 G255.18-80.62	21.138	-33.184	ESO 352- G 071	592 ± 281	1.67	1.96	0.54
PLCKERC857 G249.83-79.43	22.942	-33.109	ESO 353- G 009	2089 ± 155	0.29	0.80	1.55
PLCKERC857 G014.32-65.00	344.602	-32.225	ESO 406- G 035	1014 ± 133	0.29	0.49	1.55
PLCKERC857 G009.50-65.08	344.981	-34.238	ESO 406- G 039	1309 ± 108	-0.45	1.39	1.55
PLCKERC857 G006.28-68.56	349.426	-34.774	ESO 407- G 014	1298 ± 113	1.22	1.68	2.01
PCCS2 857 G010.95-86.53	9.204	-28.379	ESO 410- G 027	438 ± 324	-0.20	0.49	1.55
PLCKERC857 G359.78-81.31	4.324	-31.617	ESO 410-IG 006	953 ± 135	0.29	1.39	3.25
PCCS1 857 G319.26-85.76	11.467	-31.190	ESO 411- G 010	583 ± 169	0.53	0.80	0.54
PCCS1 857 G294.36-85.05	13.727	-32.017	ESO 411- G 030	655 ± 288	0.29	1.39	1.55
PCCS1 857 G253.13-83.53	18.632	-31.186	ESO 412- G 021	1131 ± 293	0.29	1.96	1.55
PLCKERC857 G247.41-81.38	21.212	-31.758	ESO 413- G 004	1175 ± 176	0.05	2.23	2.01
PLCKERC857 G224.07-79.17	24.988	-28.697	ESO 413- G 016	1065 ± 112	0.77	0.49	0.54
PCCS1 857 G220.52-79.20	24.999	-28.031	ESO 413- G 018	662 ± 172	0.77	0.80	1.06
PCCS1 857 G225.10-55.12	52.480	-28.776	ESO 418- G 007	249 ± 208	3.32	2.50	2.01
PLCKERC857 G016.48-57.99	336.338	-31.350	ESO 467-IG 055	1533 ± 130	2.10	0.80	1.06
PLCKERC857 G018.03-66.69	346.485	-30.616	ESO 469- G 011	1120 ± 139	1.22	0.49	1.55
PCCS1 857 G015.37-71.81	352.513	-31.131	ESO 470- G 013	606 ± 290	0.53	0.17	3.25
PCCS1 857 G014.42-76.50	357.958	-30.619	ESO 471- G 028	929 ± 196	1.00	2.23	2.86
PCCS2 857 G221.37-54.48	52.830	-26.558	ESO 482- G 001	749 ± 301	3.71	1.68	2.44
PCCS1 857 G354.65+51.85	221.871	1.035	FGC 1806	827 ± 308	-0.71	1.10	1.55
PCCS1 857 G054.16+67.86	217.596	32.944	Holm 657	448 ± 159	0.53	3.27	2.01
PCCS1 857 G231.90+31.90	139.457	-0.267	IC 0531	723 ± 196	-0.98	-0.50	0.54
PCCS1 857 G140.74+87.22	191.881	29.768	IC 0821	730 ± 156	1.22	1.10	0.54
PCCS1 857 G002.19+85.13	197.459	24.566	IC 0854	389 ± 233	-0.45	-0.86	1.55
PLCKERC857 G008.90+84.11	198.768	24.611	IC 0860	2052 ± 156	1.22	2.76	2.86
PLCKERC857 G082.93+80.60	200.138	34.133	IC 0883	2553 ± 147	1.88	1.96	1.55
PLCKERC857 G339.69-83.51	8.275	-32.249	IC 1554	1159 ± 103	-0.71	0.17	1.55
PCCS1 857 G251.82-84.57	17.754	-30.448	IC 1637	560 ± 214	-0.71	-0.16	1.55
PLCKERC857 G262.57-82.60	18.537	-32.645	IC 1657	1848 ± 180	0.53	1.39	2.01
PLCKERC857 G225.15-79.05	25.095	-28.911	IC 1720	1835 ± 165	1.22	1.68	2.01

Name	RA	DEC	Associations	Planck 857 Flux [mJy]	σ_{250}	σ_{350}	σ_{500}
PCCS1 857 G057.74+87.73	195.192	28.061	IC 4040	434 ± 182	0.05	0.49	0.54
PLCKERC857 G010.62-64.19	343.834	-33.887	IC 5262	1032 ± 103	2.52	3.02	2.86
PLCKERC857 G010.78-64.76	344.509	-33.744	IC 5271	3848 ± 142	0.29	0.80	0.54
PCCS2 857 G326.23-88.15	12.029	-28.817	IRAS F00456-2904NE	69 ± 238	-0.71	-0.86	-0.04
PLCKERC857 G054.78+83.32	199.972	29.432	KUG 1317+296	1213 ± 137	2.92	4.47	2.44
PCCS1 857 G071.66+80.96	201.211	32.531	KUG 1322+328	702 ± 308	-1.82	-0.16	-0.04
PCCS1 857 G071.93+78.54	203.576	33.925	KUG 1331+342	931 ± 230	1.00	1.68	2.44
PLCKERC857 G052.87+68.36	217.091	32.397	KUG 1426+326	1257 ± 112	-0.20	0.49	1.55
PLCKERC857 G059.17+66.46	218.822	35.114	KUG 144+353	999 ± 112	-0.98	-3.07	N/A
PCCS1 857 G062.57+78.53	204.657	32.303	MCG +06-30-064	787 ± 402	0.05	1.39	2.86
PCCS1 857 G007.78-77.44	359.471	-31.822	MCG -05-01-015	565 ± 205	-0.98	-0.50	2.01
PCCS2 857 G246.27-80.51	22.202	-32.029	MCG -05-04-040	1013 ± 280	-0.45	-0.16	1.55
PLCKERC857 G060.85+67.13	217.836	35.598	MGC +06-32-056	1018 ± 98	-0.71	3.52	2.01
PCCS1 857 G354.13-78.58	2.152	-33.871	NGC 0010	1353 ± 254	0.05	-0.16	-0.04
PCCS2 857 G349.11-81.94	5.973	-32.536	NGC 0101	1108 ± 193	-0.98	-0.50	-0.70
PLCKERC857 G340.47-81.55	6.689	-33.686	NGC 0115	809 ± 115	-1.25	-0.50	1.55
PCCS1 857 G339.08-82.27	7.416	-33.262	NGC 0131	853 ± 308	0.05	0.49	2.01
PLCKERC857 G338.28-82.37	7.594	-33.246	NGC 0134	23887 ± 439	-0.98	-2.07	0.54
PLCKERC857 G021.83-86.13	8.571	-27.807	NGC 0150	4604 ± 197	-0.45	1.39	1.06
PLCKERC857 G355.57-86.04	9.248	-29.482	NGC 0174	2143 ± 140	-0.45	0.17	-0.04
PLCKERC857 G299.12-85.91	13.176	-31.206	NGC 0289	7416 ± 175	-0.20	1.10	3.64
PLCKERC857 G256.92-85.55	16.558	-30.168	NGC 0378	1441 ± 129	-0.20	-0.50	1.06
PLCKERC857 G250.46-84.78	17.641	-30.222	NGC 0418	1684 ± 96	0.29	0.17	-0.04
PLCKERC857 G239.77-85.12	17.847	-29.242	NGC 0423	1708 ± 150	1.00	0.80	3.25
PLCKERC857 G134.22-61.41	18.236	0.986	NGC 0428	2791 ± 271	-1.25	-0.86	-0.70
PCCS1 857 G136.33-63.11	18.878	-0.876	NGC 0450	1955 ± 484	-1.82	-2.07	0.54
PLCKERC857 G138.92-60.96	20.544	0.946	NGC 0493	2074 ± 124	-2.43	-1.24	-0.04
PCCS1 857 G140.00-62.69	20.601	-0.856	NGC 0497	1304 ± 347	-0.98	0.17	1.06
PCCS2 857 G140.57-59.63	21.679	2.025	NGC 0550	823 ± 351	-3.45	-2.54	-1.52
PCCS1 857 G144.85-62.07	22.933	-0.927	NGC 0585	1159 ± 175	-3.09	-2.54	N/A
PLCKERC857 G229.07-80.28	23.581	-29.418	NGC 0613	17227 ± 296	0.53	1.96	2.01
PCCS1 857 G145.82-60.22	24.002	0.655	NGC 0622	307 ± 489	-2.43	-2.07	-0.70
PLCKERC857 G230.65-79.17	24.769	-29.916	NGC 0639	2319 ± 149	-1.25	-0.16	1.06
PCCS2 857 G155.97-57.96	29.671	0.528	NGC 0768	820 ± 198	-1.53	-0.86	-0.70
PCCS1 857 G157.99-58.08	30.536	-0.112	NGC 0800	420 ± 205	-4.25	-3.07	-0.70

Name	RA	DEC	Associations	Planck 857 Flux [mJy]	σ_{250}	σ_{350}	σ_{500}
PCCS1 857 G163.10-57.02	33.414	-0.715	NGC 0856	267 ± 266	-3.83	-3.07	-1.52
PCCS1 857 G163.48-56.94	33.631	-0.767	NGC 0863	238 ± 508	-2.75	-2.07	-0.70
PLCKERC857 G172.21-60.84	34.680	-6.625	NGC 0881	1825 ± 122	5.73	0.80	4.01
PCCS2 857 G170.56-57.15	36.526	-3.314	NGC 0881	693 ± 211	2.10	2.76	2.86
PLCKERC857 G171.77-59.54	35.402	-5.523	NGC 0895	3736 ± 155	7.08	0.17	8.04
PLCKERC857 G263.34-41.83	67.913	-54.603	NGC 1617	2213 ± 98	7.08	8.04	5.05
PLCKERC857 G152.29+53.37	161.355	55.964	NGC 3353	1200 ± 114	4.47	-3.70	2.01
PLCKERC857 G148.24+52.44	163.020	58.417	NGC 3408	813 ± 100	3.12	1.96	2.01
PLCKERC857 G149.59+53.66	163.650	56.986	NGC 3445	846 ± 92	3.52	4.47	2.01
PLCKERC857 G147.66+53.84	165.363	57.677	NGC 3488	746 ± 103	4.47	4.93	2.44
PLCKERC857 G263.84+57.55	173.088	0.810	NGC 3720	1669 ± 167	-0.45	0.17	2.44
PCCS1 857 G272.55+58.08	177.350	-1.083	NGC 3907B	807 ± 521	-1.53	-1.24	0.54
PLCKERC857 G277.37+59.21	180.100	-1.104	NGC 4030	16747 ± 287	-2.43	-1.24	-0.04
PLCKERC857 G280.29+58.41	181.218	-2.397	NGC 4079	2204 ± 150	-0.71	-0.16	1.06
PCCS1 857 G140.19+86.20	191.549	30.749	NGC 4676	618 ± 252	0.29	-0.16	-0.70
PCCS1 857 G125.67+83.96	192.515	33.158	NGC 4719	460 ± 200	-1.25	-0.50	1.55
PLCKERC857 G294.85+88.35	192.603	25.497	NGC 4725	11974 ± 574	4.09	5.59	8.04
PCCS1 857 G125.12+88.34	192.787	28.781	NGC 4738	854 ± 172	1.45	1.10	0.54
PLCKERC857 G306.37+88.63	192.950	25.769	NGC 4747	1862 ± 113	1.00	1.39	1.06
PLCKERC857 G101.57+88.05	193.667	28.933	NGC 4793	5552 ± 140	-1.53	-0.86	-0.04
PCCS1 857 G070.45+88.15	194.517	28.240	NGC 4848	443 ± 216	0.29	-0.86	0.54
PLCKERC857 G050.58+87.80	195.227	27.775	NGC 4911	1105 ± 136	1.00	0.80	2.01
PCCS1 857 G052.56+87.66	195.344	27.890	NGC 4921	335 ± 211	0.05	1.10	1.55
PLCKERC857 G077.99+86.90	195.363	29.295	NGC 4922	900 ± 166	0.29	1.39	0.54
PLCKERC857 G044.43+86.76	196.446	27.728	NGC 4961	1367 ± 134	-0.45	0.17	1.06
PLCKERC857 G064.15+86.19	196.580	29.051	NGC 4966	1158 ± 135	0.77	1.39	2.01
PLCKERC857 G057.61+85.56	197.459	28.903	NGC 5000	842 ± 96	-0.45	-0.86	1.06
PLCKERC857 G063.78+85.05	197.738	29.578	NGC 5004	1247 ± 133	0.29	1.39	2.01
PLCKERC857 G351.34+83.78	197.903	22.914	NGC 5012	3810 ± 103	0.05	-1.24	-0.70
PCCS1 857 G352.22+83.55	198.157	22.827	NGC 5012A	322 ± 171	-0.45	-1.24	1.06
PLCKERC857 G001.00+84.43	198.030	24.092	NGC 5016	1676 ± 101	-2.12	-0.16	1.55
PLCKERC857 G079.49+83.41	198.186	31.811	NGC 5025	1053 ± 168	-0.45	-2.07	-1.52
PLCKERC857 G041.82+85.07	198.362	27.783	NGC 5032	1140 ± 144	0.53	1.10	3.64
PLCKERC857 G069.61+83.37	199.052	30.948	NGC 5056	1332 ± 132	0.29	1.96	2.01
PCCS2 857 G069.35+83.06	199.376	31.095	NGC 5065	610 ± 253	-0.45	0.49	2.01

Name	RA	DEC	Associations	Planck 857 Flux [mJy]	σ_{250}	σ_{350}	σ_{500}
PLCKERC857 G047.31+83.73	199.772	28.515	NGC 5081	912 ± 101	0.05	0.49	-0.04
PLCKERC857 G033.44+82.97	200.742	26.971	NGC 5116	1142 ± 139	-0.71	-2.07	0.54
PCCS2 857 G044.42+82.93	200.732	28.316	NGC 5117	408 ± 175	-2.75	-2.07	-0.70
PLCKERC857 G066.66+80.62	202.057	32.034	NGC 5166	1051 ± 135	-0.45	1.10	0.54
PCCS2 857 G060.66+80.72	202.448	31.115	NGC 5187	580 ± 308	-0.71	-0.86	-0.70
PLCKERC857 G037.10+79.78	204.351	27.403	NGC 5251	1252 ± 108	1.67	1.96	2.86
PLCKERC857 G042.48+79.19	204.986	28.397	NGC 5263	1877 ± 86	0.05	-0.50	0.54
PCCS1 857 G340.43+55.75	212.898	-1.165	NGC 5496	984 ± 240	-2.75	-2.07	-0.04
PLCKERC857 G345.11+54.84	215.605	-0.395	NGC 5584	3308 ± 171	0.05	0.17	-0.04
PCCS1 857 G060.74+67.53	217.376	35.455	NGC 5646	669 ± 183	0.53	1.68	2.44
PLCKERC857 G060.27+67.38	217.606	35.319	NGC 5656	2721 ± 146	2.31	-2.07	2.86
PLCKERC857 G353.15+54.45	219.422	2.288	NGC 5690	5662 ± 198	-0.98	-0.50	-0.04
PCCS1 857 G350.17+52.42	219.462	-0.406	NGC 5691	1125 ± 263	-0.45	0.49	0.54
PLCKERC857 G350.46+51.85	219.962	-0.716	NGC 5705	1538 ± 196	-1.53	-0.86	0.54
PLCKERC857 G351.01+52.11	220.048	-0.298	NGC 5713	7124 ± 222	0.05	-1.24	1.06
PLCKERC857 G351.22+51.97	220.238	-0.320	NGC 5719	4001 ± 226	-1.53	-0.16	-0.04
PLCKERC857 G354.50+52.84	221.113	1.676	NGC 5740	2573 ± 190	-1.53	0.17	0.54
PLCKERC857 G354.96+52.95	221.237	1.951	NGC 5746	9795 ± 306	-0.98	-0.86	0.54
PCCS1 857 G352.89+51.17	221.541	-0.210	NGC 5750	666 ± 270	-2.75	-2.07	-1.52
PLCKERC857 G084.40+43.10	245.453	55.076	NGC 6143	1108 ± 76	2.92	3.27	2.44
PLCKERC857 G012.07-57.79	336.087	-33.692	NGC 7267	1784 ± 88	2.31	2.23	3.25
PLCKERC857 G016.87-58.16	336.545	-31.146	NGC 7277	881 ± 148	3.12	2.50	1.55
PLCKERC857 G019.30-61.60	340.589	-30.054	NGC 7361	1925 ± 89	1.88	1.96	4.36
PLCKERC857 G015.44-75.68	356.965	-30.527	NGC 7755	3690 ± 233	-1.25	-0.16	1.55
PLCKERC857 G004.50-77.17	359.464	-32.592	NGC 7793	26167 ± 806	2.52	4.70	8.04
PCCS2 857 G355.71-77.40	0.734	-34.223	NGC 7812	1160 ± 409	1.67	1.10	2.86
PCCS1 857 G013.37-62.85	342.100	-32.798	Not assigned	392 ± 246	0.77	2.50	2.01
PCCS1 857 G293.47-84.07	14.017	-32.965	Not assigned	138 ± 221	0.05	-0.16	-0.04
PCCS1 857 G230.86-80.29	23.497	-29.712	Not assigned	424 ± 211	1.00	1.68	2.01
PCCS1 857 G343.37-84.34	8.568	-31.364	Not assigned	463 ± 512	0.77	1.39	2.01
PCCS1 857 G338.93-84.48	9.063	-31.535	Not assigned	400 ± 244	0.53	1.10	2.01
PLCKERC857 G259.96-87.61	14.717	-28.862	Not assigned	2320 ± 329	1.00	0.80	0.54
PLCKERC857 G249.60-85.50	17.007	-29.749	Not assigned	1390 ± 215	0.77	0.17	2.01
PCCS2 857 G020.34-88.13	10.807	-27.520	Not assigned	618 ± 412	-1.82	1.39	-0.04
PCCS1 857 G008.30-68.26	348.868	-34.119	Not assigned	99 ± 391	0.05	0.80	1.55

Name	RA	DEC	Associations	Planck 857 Flux [mJy]	σ_{250}	σ_{350}	σ_{500}
PCCS1 857 G004.31-80.79	3.409	-31.217	Not assigned	369 ± 292	0.53	0.80	2.44
PLCKERC857 G013.68-79.70	1.614	-30.071	Not assigned	1066 ± 139	-0.20	1.10	1.55
PLCKERC857 G006.96-67.92	348.604	-34.679	Not assigned	940 ± 106	1.67	1.39	2.44
PLCKERC857 G221.31-79.84	24.273	-28.147	Not assigned	1328 ± 191	2.52	1.96	2.86
PLCKERC857 G222.32-80.00	24.074	-28.312	Not assigned	972 ± 128	2.10	2.50	2.44
PLCKERC857 G244.96-80.43	22.403	-31.874	Not assigned	1367 ± 165	2.31	1.68	2.86
PLCKERC857 G339.76-85.56	9.768	-30.648	Not assigned	1539 ± 223	-0.20	0.80	1.55
PLCKERC857 G272.23-87.16	14.525	-29.560	Not assigned	1843 ± 324	1.67	1.10	2.01
PLCKERC857 G251.68-86.96	15.569	-29.005	Not assigned	2101 ± 362	1.67	2.23	1.55
PCCS1 857 G074.62+80.41	201.406	33.240	Not assigned	425 ± 270	0.77	1.96	1.06
PCCS1 857 G036.04+80.21	203.865	27.230	Not assigned	119 ± 474	-0.20	-1.24	0.54
PCCS1 857 G029.92+79.80	204.218	26.136	Not assigned	515 ± 190	1.88	2.23	2.01
PLCKERC857 G014.88+80.31	202.929	23.771	Not assigned	1243 ± 158	1.45	1.39	1.55
PLCKERC857 G102.51+85.22	194.814	31.592	Not assigned	861 ± 141	0.53	1.68	2.86
PLCKERC857 G077.25+80.72	200.801	33.387	Not assigned	1065 ± 97	2.31	0.80	1.06
PCCS2 857 G069.76+76.61	205.857	34.547	Not assigned	572 ± 297	0.29	0.49	0.54
PLCKERC857 G028.53+83.67	199.905	26.468	Not assigned	1301 ± 166	1.00	2.23	2.86
PCCS1 857 G141.28-60.26	21.848	1.318	Not assigned	565 ± 360	-1.53	-0.86	-1.52
PCCS2 857 G156.60-56.71	30.581	1.448	Not assigned	1033 ± 292	-3.09	-2.07	-0.70
PCCS1 857 G285.70+60.28	184.415	-1.452	Not assigned	463 ± 185	-0.45	0.49	2.01
PCCS1 857 G279.25+59.97	181.268	-0.745	Not assigned	519 ± 259	0.53	1.68	-0.04
PLCKERC857 G230.55+31.91	138.859	0.711	Not assigned	1216 ± 86	-0.45	1.39	2.01
PCCS2 857 G083.61+44.14	243.976	54.260	Not assigned	458 ± 191	2.52	1.68	-0.70
PCCS1 857 G085.24+46.30	239.831	54.712	Not assigned	637 ± 168	2.92	1.39	1.55
PCCS1 857 G222.56-53.84	53.671	-27.130	Not assigned	227 ± 185	0.53	1.68	0.54
PLCKERC857 G224.76-54.44	53.219	-28.497	Not assigned	807 ± 102	2.10	2.23	0.54
PCCS2 857 G007.68-72.90	354.332	-33.190	Not assigned	669 ± 277	-0.20	1.10	1.06
PCCS1 857 G001.66-72.03	354.044	-35.183	Not assigned	392 ± 305	-0.71	1.39	2.44
PCCS1 857 G018.31-71.34	351.866	-30.256	Not assigned	749 ± 360	0.29	1.68	1.55
PCCS1 857 G135.78-62.78	18.701	-0.497	UGC 00793	823 ± 261	-1.25	-0.86	0.54
PCCS1 857 G138.16-60.62	20.265	1.367	UGC 00890	600 ± 374	-2.43	-1.64	-0.04
PCCS1 857 G223.87+23.88	128.948	1.727	UGC 04491	460 ± 288	-2.12	-2.54	-0.70
PCCS1 857 G232.19+31.64	139.373	-0.613	UGC 04915	693 ± 324	0.05	-1.64	1.06
PCCS1 857 G235.51+42.78	150.107	3.372	UGC 05376	1885 ± 222	0.29	0.17	-0.04
PCCS2 857 G268.20+56.69	174.632	-1.175	UGC 06608	489 ± 204	-0.71	-0.50	0.54

Name	RA	DEC	Associations	Planck 857 Flux [mJy]	σ_{250}	σ_{350}	σ_{500}
PCCS1 857 G273.25+60.86	178.907	1.248	UGC 06903	1015 ± 290	-1.53	-0.50	-0.70
PLCKERC857 G108.32+88.72	193.225	28.362	UGC 08017	1183 ± 114	-1.25	0.17	-0.04
PLCKERC857 G101.38+83.79	195.568	32.873	UGC 08145	893 ± 109	2.10	1.68	2.86
PLCKERC857 G091.96+84.28	196.322	31.984	UGC 08179	890 ± 107	1.22	-0.16	1.55
PCCS1 857 G049.28+86.01	197.202	28.184	UGC 08229	676 ± 339	1.22	1.10	2.01
PCCS1 857 G094.47+81.88	197.524	34.185	UGC 08246	308 ± 206	0.05	-0.86	0.54
PCCS1 857 G086.19+81.12	199.259	34.095	UGC 08352	378 ± 249	-1.53	-1.24	-0.70
PLCKERC857 G038.66+84.14	199.435	27.559	UGC 08359	1218 ± 114	1.00	0.80	1.06
PCCS2 857 G006.30+81.88	200.754	23.273	UGC 08409	705 ± 157	0.05	0.80	1.55
PCCS1 857 G063.08+80.40	202.603	31.609	UGC 08498	823 ± 201	-0.98	-0.86	-0.04
PCCS2 857 G075.02+78.38	203.306	34.525	UGC 08536	528 ± 295	-1.82	0.17	0.54
PCCS1 857 G072.04+78.37	203.734	34.039	UGC 08561	1549 ± 299	-0.45	-0.16	0.54
PLCKERC857 G075.27+77.67	203.962	34.989	UGC 08583	1026 ± 129	0.05	0.49	1.55
PCCS1 857 G056.93+78.78	204.845	31.178	UGC 08640	757 ± 371	1.88	0.49	-0.04
PCCS2 857 G071.87+76.53	205.635	35.009	UGC 08681	768 ± 194	0.05	1.68	1.55
PLCKERC857 G051.72+78.22	205.794	30.324	UGC 08685	902 ± 117	0.05	-0.16	1.06
PCCS1 857 G065.77+76.25	206.773	33.889	UGC 08715	965 ± 496	0.05	1.10	1.06
PLCKERC857 G347.77+56.35	215.865	1.720	UGC 09215	1221 ± 146	-1.25	-0.16	1.06
PCCS1 857 G347.54+55.75	216.144	1.172	UGC 09229	888 ± 238	-0.45	0.49	1.55
PCCS1 857 G089.40+34.18	260.751	60.450	UGC 10830	1319 ± 481	4.09	5.37	3.64
PCCS1 857 G088.83+33.68	261.815	60.011	UGC 10870	1074 ± 271	5.38	5.37	2.44
PLCKERC857 G055.79+67.45	217.966	33.623	VV 775	1010 ± 184	0.77	2.50	1.06

Table A.2: Compact sources and their identifications from the *Planck* 545GHz catalogues of compact sources.

Name	RA	DEC	Associations	S_{545} [mJy]	σ_{250}	σ_{350}	σ_{500}
PCCS1 545 G019.76-58.74	337.311	-29.670	Cluster Candidate	225±164	2.92	1.68	3.25
PCCS1 545 G354.79-79.57	3.060	-33.226	Cluster Candidate	335±158	1.22	1.39	3.25
PLCKERC545 G015.45-60.34	339.084	-31.902	Cluster Candidate	607±87	2.72	3.27	4.01
PCCS1 545 G058.72+82.59	200.566	30.136	Cluster Candidate	349±161	1.22	1.39	3.64
PCCS1 545 G027.38+84.85	198.581	26.515	Cluster Candidate	433±136	1.45	2.23	4.01
PCCS1 545 G084.40+81.05	199.569	33.968	Cluster Candidate	387±230	1.88	1.39	3.25
PLCKERC545 G146.77+52.48	164.280	59.031	Cluster Candidate	606±73	4.09	4.93	1.06
PCCS1 545 G222.38-54.39	53.046	-27.117	Cluster Candidate	182±185	2.10	3.02	2.01
PLCKERC545 G060.36+66.56	218.577	35.554	Cluster Candidate	872±114	0.77	4.47	5.70
PLCKERC545 G260.28-39.75	71.996	-52.643	Cluster Candidate	471±46	3.71	3.27	3.25
PCCS1 545 G230.70-79.18	24.755	-29.924	(Galaxy Pair) NGC 0639, NGC 0642	364±208	-1.25	0.17	1.06
PLCKERC545 G270.59+58.54	176.648	-0.199	Lens Candidate	1071±121	0.53	2.76	2.44
PLCKERC545 G047.34+82.51	201.130	28.747	(Lens) H-ATLAS J132427.0+28445	810±106	2.31	1.96	4.01
PLCKERC545 G131.81-60.98	17.158	1.590	(QSO) LBQS 0106+119	1097±99	-4.25	-3.07	-1.52
PCCS1 545 G020.46-64.92	344.427	-29.631	(Star) Formalhaut	401±175	0.29	0.80	0.54
PLCKERC545 G167.74-57.97	34.837	-2.967	(Star) Omicron Cet	1807±111	5.90	-3.07	N/A
PCCS1 545 G160.59-56.75	32.432	0.279	2MASX J02094125+0015587	532±232	-0.71	-0.86	-0.70
PCCS1 545 G355.79+52.97	221.575	2.322	2MASX J14461287+0218372	464±218	1.00	1.39	3.25
PCCS2 545 G351.78+49.90	221.884	-1.622	CGCG 020-017	510±228	0.05	0.17	1.55
PCCS1 545 G139.56-62.17	20.540	-0.296	Cirrus	985±261	-1.25	-1.24	-0.04
PCCS1 545 G144.40-59.72	23.497	1.365	Cirrus	630±178	-1.25	-0.86	-1.52
PLCKERC545 G126.83-63.90	14.574	-1.085	Cirrus	1052±153	-2.43	-1.64	-0.70
PLCKERC545 G126.26-63.31	14.356	-0.480	Cirrus	1415±166	-1.53	-0.86	-0.70
PLCKERC545 G136.06-63.48	18.682	-1.204	Cirrus	1534±159	-2.43	-3.07	N/A
PCCS2 545 G130.16-64.05	16.016	-1.361	Cirrus	571±320	-2.75	-2.54	-0.70
PLCKERC545 G231.44+32.10	139.420	0.174	Cirrus	1137±178	3.71	3.52	6.01
PLCKERC545 G224.70+24.61	129.951	1.422	Cirrus	1064±134	1.22	0.80	2.01
PLCKERC545 G227.27+24.71	131.198	-0.550	Cirrus	1245±223	1.00	1.39	1.55
PLCKERC545 G227.57+24.56	131.215	-0.863	Cirrus	1105±151	2.10	1.68	3.64
PLCKERC545 G227.77+30.23	136.181	1.869	Cirrus	1641±196	0.77	1.68	2.86
PLCKERC545 G230.17+32.05	138.809	1.055	Cirrus	809±78	2.10	2.50	2.86
PLCKERC545 G226.97+26.25	132.394	0.458	Cirrus	1212±159	1.22	0.80	1.06
PCCS1 545 G226.21+24.93	130.906	0.391	Cirrus	729±395	0.05	1.68	2.01

Name	RA	DEC	Associations	S_{545} [mJy]	σ_{250}	σ_{350}	σ_{500}
PCCS2 545 G229.62+28.51	135.540	-0.403	Cirrus	792±227	0.77	0.80	1.06
PCCS1 545 G229.68+30.43	137.202	0.558	Cirrus	447±139	-0.45	-0.16	0.54
PCCS1 545 G228.63+29.60	136.025	0.911	Cirrus	708±232	0.53	1.39	1.55
PCCS1 545 G226.48+23.25	129.579	-0.667	Cirrus	782±241	-0.71	-0.50	-0.04
PLCKERC545 G249.81-79.42	22.951	-33.111	ESO 353- G 009	634±113	0.53	1.10	2.01
PLCKERC545 G085.69+83.35	197.614	32.339	FIRST J131028.6+322054	741±95	0.05	1.39	1.06
PCCS1 545 G009.02+84.14	198.753	24.631	IC 0860	611±170	0.29	1.68	2.86
PCCS1 545 G083.01+80.62	200.117	34.133	IC 088	570±193	2.10	1.68	2.44
PLCKERC545 G262.62-82.60	18.530	-32.649	IC 1657	684±116	-0.20	0.80	2.01
PLCKERC545 G225.13-79.06	25.093	-28.908	IC 1720	826±103	0.77	1.39	2.01
PLCKERC545 G010.79-64.76	344.505	-33.741	IC 5271	1054±89	0.29	0.80	0.54
PCCS1 545 G340.39-81.54	6.686	-33.705	NGC 0115	308±209	-0.98	0.17	1.55
PLCKERC545 G338.28-82.37	7.594	-33.245	NGC 0134	6794±176	-0.71	-1.64	0.54
PLCKERC545 G021.76-86.13	8.576	-27.811	NGC 0150	1495±120	-0.45	1.10	0.54
PCCS1 545 G355.51-86.04	9.248	-29.488	NGC 0174	548±175	-0.71	0.17	-0.04
PLCKERC545 G299.11-85.91	13.178	-31.208	NGC 0289	2411±113	-0.20	1.10	3.64
PCCS1 545 G250.48-84.79	17.631	-30.218	NGC 0418	442±167	0.05	0.17	-0.04
PLCKERC545 G134.20-61.41	18.225	0.982	NGC 0428	984±112	-0.98	-0.50	-0.70
PCCS1 545 G136.34-63.09	18.884	-0.852	NGC 0450	568±241	-1.82	-2.07	-0.04
PLCKERC545 G138.92-60.95	20.546	0.955	NGC 0493	821±122	-2.12	-1.24	-0.04
PCCS1 545 G139.99-62.71	20.591	-0.877	NGC 0497	395±212	-1.25	0.17	1.06
PLCKERC545 G229.08-80.28	23.582	-29.420	NGC 0613	4735±131	0.53	1.96	2.01
PLCKERC545 G171.78-59.55	35.401	-5.527	NGC 0894	1385±96	7.08	0.17	8.04
PLCKERC545 G263.34-41.82	67.925	-54.602	NGC 1617	753±62	7.41	8.21	5.38
PCCS1 545 G263.82+57.53	173.065	0.800	NGC 3720	541±129	-0.98	0.17	2.44
PLCKERC545 G277.36+59.21	180.094	-1.097	NGC 4030	4409±113	-1.53	-0.86	-0.04
PLCKERC545 G280.27+58.42	181.211	-2.382	NGC 4079	897±111	-0.20	0.49	1.55
PLCKERC545 G294.87+88.34	192.603	25.492	NGC 4725	4410±237	4.09	5.80	8.04
PCCS1 545 G305.91+88.64	192.938	25.776	NGC 4747	635±139	0.29	0.80	1.06
PLCKERC545 G101.42+88.06	193.672	28.930	NGC 4793	1505±97	-0.98	-0.50	0.54
PCCS1 545 G044.60+86.76	196.435	27.736	NGC 4961	599±232	-0.71	-0.16	1.06
PCCS1 545 G351.36+83.79	197.896	22.924	NGC 5012	1061±158	0.29	-0.50	-0.04
PCCS1 545 G047.55+83.74	199.755	28.539	NGC 5081	150±146	0.53	0.80	-0.04
PCCS1 545 G042.41+79.20	204.985	28.385	NGC 5263	332±125	-0.45	-0.16	0.54
PCCS1 545 G340.48+55.74	212.924	-1.159	NGC 5496	273±212	-3.45	-2.54	-1.52

Name	RA	DEC	Associations	S_{545} [mJy]	σ_{250}	σ_{350}	σ_{500}
PLCKERC545 G345.12+54.85	215.603	-0.381	NGC 5584	1039±118	0.05	-0.16	-0.04
PLCKERC545 G060.29+67.38	217.604	35.325	NGC 5656	1004±86	2.31	-2.07	2.86
PLCKERC545 G353.14+54.45	219.414	2.290	NGC 5690	1509±127	-1.25	-0.86	-0.04
PCCS1 545 G350.45+51.86	219.958	-0.719	NGC 5705	277±183	-1.25	-0.50	1.06
PLCKERC545 G351.01+52.12	220.047	-0.292	NGC 5713	2041±136	-0.20	-1.64	0.54
PLCKERC545 G351.21+51.96	220.242	-0.327	NGC 5719	1175±174	-2.12	-0.86	-0.04
PCCS1 545 G354.49+52.85	221.100	1.682	NGC 5740	671±202	-1.53	0.17	0.54
PLCKERC545 G354.97+52.95	221.236	1.956	NGC 5746	3095±143	-0.98	-0.86	0.54
PCCS2 545 G088.85+33.67	261.839	60.031	NGC 6381	319±215	4.09	4.93	3.25
PLCKERC545 G012.05-57.77	336.070	-33.700	NGC 7267	599±74	1.88	1.68	2.86
PCCS1 545 G019.27-61.60	340.583	-30.071	NGC 7361	469±118	1.00	0.80	2.86
PLCKERC545 G015.53-75.66	356.945	-30.508	NGC 7755	1203±145	-1.53	-0.86	0.54
PLCKERC545 G004.50-77.17	359.463	-32.593	NGC 7793	9171±378	2.52	4.70	8.04
PLCKERC545 G260.18-87.65	14.678	-28.841	Not assigned	929±160	2.31	1.39	1.06
PCCS1 545 G355.68-75.23	358.461	-35.324	Not assigned	523±109	0.05	1.96	2.01
PCCS1 545 G345.09-79.28	4.114	-34.800	Not assigned	622±160	0.77	1.39	2.44
PLCKERC545 G007.56-64.14	344.024	-35.214	Not assigned	584±75	-4.71	N/A	N/A
PCCS1 545 G006.41-66.96	347.524	-35.106	Not assigned	329±137	1.45	1.10	1.06
PCCS1 545 G012.72-58.67	337.137	-33.320	Not assigned	500±162	1.22	1.96	2.86
PCCS1 545 G011.38-70.82	351.609	-32.552	Not assigned	281±117	-0.20	0.80	1.55
PCCS1 545 G012.89-66.24	346.134	-32.698	Not assigned	587±139	2.52	1.39	2.01
PCCS1 545 G001.76-78.81	1.514	-32.457	Not assigned	560±128	0.05	0.80	1.55
PCCS1 545 G004.26-81.15	3.796	-31.078	Not assigned	314±157	0.53	1.39	2.86
PLCKERC545 G339.86-85.54	9.752	-30.651	Not assigned	929±127	-0.20	0.17	1.55
PCCS1 545 G141.01+88.40	192.294	28.647	Not assigned	176±125	1.22	1.10	1.06
PCCS1 545 G000.99+84.45	198.012	24.103	Not assigned	601±163	-1.82	0.17	1.55
PCCS1 545 G064.37+83.30	199.491	30.466	Not assigned	263±155	-0.98	0.17	0.54
PCCS1 545 G038.35+77.36	207.084	27.603	Not assigned	154±157	0.29	0.49	1.55
PCCS1 545 G129.08+85.56	192.302	31.540	Not assigned	147±138	0.53	0.49	-0.04
PLCKERC545 G149.13+52.95	163.033	57.670	Not assigned	735±109	2.31	2.50	1.55
PCCS1 545 G153.54+52.83	159.776	55.700	Not assigned	310±134	1.22	1.39	-0.04
PCCS1 545 G139.19-61.55	20.525	0.340	Not assigned	575±226	-1.25	-1.64	-0.04
PCCS1 545 G345.78+54.33	216.219	-0.568	Not assigned	260±209	-2.12	-2.07	-0.04
PCCS1 545 G341.61+58.65	211.837	1.610	Not assigned	329±188	1.00	1.10	1.06
PCCS1 545 G354.98+52.33	221.678	1.518	Not assigned	341±207	-0.98	0.80	-0.70

Name	RA	DEC	Associations	S_{545} [mJy]	σ_{250}	σ_{350}	σ_{500}
PCCS1 545 G224.02+26.10	130.951	2.689	Not assigned	367±198	0.05	1.39	2.01
PCCS1 545 G083.80+44.81	242.798	54.211	Not assigned	168±154	1.45	0.80	-0.04
PCCS1 545 G084.81+46.34	239.932	54.413	Not assigned	303±166	1.00	1.96	-0.04
PCCS1 545 G014.03-72.46	353.345	-31.441	Not assigned	277±137	0.05	-0.16	-0.70
PCCS1 545 G007.73-72.26	353.597	-33.347	Not assigned	425±123	1.88	2.50	3.25
PCCS1 545 G009.60-73.01	354.290	-32.619	Not assigned	478±191	2.31	1.68	1.55
PCCS1 545 G285.33+61.23	184.492	-0.489	PKS 1215-002	624±179	-1.25	0.17	0.54
PCCS1 545 G235.53+42.77	150.108	3.361	UGC 05376	548±119	0.53	0.17	-0.04
PCCS1 545 G107.45+88.72	193.246	28.355	UGC 08017	426±154	-0.98	-0.16	-0.70
PCCS1 545 G072.04+78.36	203.750	34.047	UGC 08561	486±206	0.05	0.17	0.54
PCCS1 545 G089.39+34.19	260.727	60.439	UGC 10830	432±253	4.65	5.59	3.64
PCCS1 545 G141.16-61.74	21.377	-0.088	UM 321	557±151	-0.71	-0.16	-0.04